Development of a Rotating Test Facility for the Experimental Characterisation of Turbomachinery Shaft Seals

Pedraza-Valle, Ernesto

Award date:
2020

Awarding institution:
University of Bath

Development of a Rotating Test Facility for the Experimental Characterisation of Turbomachinery Shaft Seals

Ernesto Pedraza-Valle

A thesis submitted for the degree of Doctor of Philosophy

University of Bath

Department of Mechanical Engineering

January 2020

Abstract

In gas turbines, seals that reduce the leakage between high and low pressure regions are critical for improved performance. Damaging rubs between the rotating and stationary parts of turbomachinery shaft seals occur due to thermal and assembly misalignments, and rotordynamic vibration during engine start-up and shut-down transients. These rubs lead to increased seal leakage and hence to reduced overall turbine efficiency and life span. In recent years, compliant seals that allow for variable clearances and a reduced frequency of seal rubs have been developed. The Film Riding Pressure Actuated Leaf Seal (FRPALS) is a non-contacting compliant seal design that maintains a tight clearance between rotating and non-rotating parts, throughout the transient conditions experienced in engines.

The FRPALS concept has been defined and its application formulated in previous reports. Preliminary tests in a two-dimensional model of the seal have also been carried out, demonstrating that the concept works as intended. This thesis presents the research performed in order to advance the new sealing technology towards a system closer to be deployed in industrial applications. The specific milestones achieved during this research are as follows: (i) design and manufacturing of a high-speed rotating test facility for the development of turbomachinery shaft seals, (ii) validation of the test rig and experimental methodology via the characterisation of a four-cavity labyrinth seal, (iii) experimental investigation of a Rayleigh-step annular seal and prediction of the pressure distribution in the clearance of the seal by solving the Reynolds equation for lubrication, and (iv) measurements of the FRPALS blow-down process and leakage performance under stationary conditions.

A novel high-speed rotating test facility for the performance characterisation of turbine shaft seals has been developed. The rig features a 254 mm diameter rotor, capable of rotating at speeds of up to 15,000 rpm (equivalent to rotor surface speeds up to 200 m/s). Pressure drops of up to 3.5 bar can be achieved. One of the main parameters to be measured with the rig are the rotordynamic coefficients of the testing seal. For this, a vibration test is performed to the seal by exciting the casing to which it is attached with an electromagnetic shaker. The rig is also capable of measuring the leakage performance of the seal; the leakage flow is collected downstream of the seal and measured by means of a thermal mass flow meter.

Labyrinth seals are a well-established sealing technology that are normally used in research work as a reference for the assessment of the leakage performance of new sealing technologies under development. Additionally, labyrinth seals have been also widely studied from a stability standpoint. For these reasons, a labyrinth seal has been chosen to perform the first test in the new design rig, validate its capabilities, and debug the experimental methodology used

to calculate the rotordynamic coefficients. The results of the labyrinth seal have value by themselves as it was found that no published data were available for the rotordynamic coefficients of labyrinth seals with less than five cavities. For pressure drops of up to 3.3 bar and rotational speeds of up to 14,600 rpm, the labyrinth seal was found to have an overall stable behaviour with negative cross-coupled stiffness and positive direct damping coefficients. In general terms, increments in pressure drop translated into increments of stiffness and damping, whereas the coefficients decreased as rotational speed increased.

A Rayleigh-step annular seal featuring the same clearance geometry as the FRPALS prototype under study has been characterised. Results of rotordynamic coefficients showed that the cross-coupled stiffness is positive, which has a destabilising effect on the behaviour of the seal. However, the direct damping was found to be large enough to outweigh this effect for large values of rotational speed. In any case, the stability of the Rayleigh-step annular seal was found to be poorer than that of the labyrinth seal for the range of rotational speeds tested. Calculation of discharge coefficients from mass flow rate measurements showed that the Rayleigh-step annular seal had a discharge coefficient twice as large as that of the labyrinth seal, indicating that the Rayleigh step was less effective in restricting the flow.

The steady-state Reynolds equation for gas lubrication has been solved in order to predict the pressure distribution in the clearance of the Rayleigh-step annular seal and the FRPALS. The predictions have been shown to be in good agreement with the experimental pressure data, except for the regions in which the geometry of the clearance changes abruptly. These pressure predictions can be used to inform the design process of the FRPALS. Additionally this is a stepping stone towards the solution of the upgraded transient Reynolds equation which will provide a model for the rotordynamic coefficients.

The measurements performed to investigate the blow-down process of the FRPALS at zero rotational speed are presented. The opening and closing translations of the leaves have been measured using eddy current displacement probes targeting the movable parts of the seal. The seal clearance has been shown to remain constant for a range of applied pressure drops, which indicates the stable operation of the seal, though resulting in contact with the rotor at a pressure drop of 2 bar. Mass flow leakage measurements have also demonstrated the sealing performance of the FRPALS. Comparison of the effective clearance of the FRPALS with that of the labyrinth seal has shown that the FRPALS leaks three times more than the labyrinth seal. However the prototype tested has an interleaf area that can be restricted in order to improve its leakage performance. These measurements show the potential of the seal to film ride subject to design modifications to maintain a more uniform film thickness.

Acknowledgements

I am most grateful to my supervisors James, Carl and Patrick for their guidance, advice and encouragement. It has been a great honour to work with you all.

To the project sponsors, Cross Manufacturing (1938) Ltd., and in particular to Aaron Bowsher and Peter Crudgington, for their technical input. Also, to George Papageorgiou, for his eagerness to help.

The prototype inventor, Clayton Grondahl, is thanked for his enthusiasm and positivity.

Technical acknowledgement is given to Andrew Langley and Terrence Warder for sharing their experience and imparting their advice on the design of the rig and for fabricating all the in-house components. Also, to the technicians in the Instrumentation team for their assistance with the rig data acquisition system.

I would also like to acknowledge the love and support of my family. To my parents, for their unconditional support. To my brother, for always making me laugh.

I am also especially grateful to Laura M., the one who has held my hand through the highs and lows of this PhD. To Anartz, Aitor, Óscar, Adriana, Paula, Sara, Isma, Lamia, Carlos, Laura V., Sonia, Artur, Liam, Mariano, Ioanna, Olivia, Naomi and Laura A., for sharing the experience. Finally, to the guys in the aero-thermo research office, for making the every-day life more enjoyable.

Contents

List of figures

List of tables

Nomenclature

Symbols

Symbol	*Unit*	*Description*
a	m/s	Acceleration of the casing
c	µm	Seal minimum clearance
c_D	-	Discharge coefficient
C_{ij}	(N s)/m	Damping coefficients
$\mathbb{C}_i$		Measured calibration values
$\mathbb{C}_{fit,i}$		Calculated calibration values
D	mm	Seal diameter
e	µm	Effective clearance
f_{ext}	N	Applied force
f_{fluid}	N	Fluid-flow induced excitation force
f_r	N	Radial component of the seal reaction force
f_θ	N	Tangential component of the seal reaction force
F	N	Force
F_{ext}	N	Fourier transform of the applied force
h	µm	Seal clearance distribution
H	-	Non-dimensional clearance distribution (h/c)
H_{ij}	N/m	Frequency response functions (impedances)
j	-	Imaginary unit $(\sqrt{-1})$
K	-	Number of coefficients
K_{ij}	N/m	Stiffness coefficients
L	mm	Axial length of the seal clearance
$\dot{m}$	kg/s	Mass flow rate
M_{stator}	kg	Stator mass
N	-	Number of calibration points
p	bar	Pressure
P	-	Non-dimensional pressure (p/p_a)
Q	$(K^{1/2}$ s)/m	Flow coefficient

R	mm	Seal radius
R	J/(kg K)	Air constant
Re_ϕ	-	Rotational Reynolds number (= $\rho\omega R^2/\mu$)
T	K	Temperature
x	mm	Distance between probes
δx	μm	displacement of stator with respect to the rotor in the x direction
X	μm	Fourier transform of δx
y	mm	Radial movement of FRPALS runner
δy	μm	displacement of stator with respect to the rotor in the y direction
Y	μm	Fourier transform of δy
z	mm	Axial coordinate
z	mm	Axial movement of FRPALS runner
α	°	Seal segment rock angle
γ	-	Heat capacity ratio of air
∂	-	Uncertainty
η	-	Non-dimensional axial coordinate (z/R)
θ	rad	Tangential coordinate
Λ	-	Compressibility number ($=6\mu\omega r^2/p_a c$)
μ	kg/(m s)	Dynamic viscosity
ϕ	(kg $K^{1/2}$)/(Pa m s)	Flow coefficient
ω	rad/s	Angular speed of rotor
ω	rad/s	Angular frequency $(2\pi f)$
Ω	rad/s	Whirling speed

Subscripts

Symbol	*Description*
a	Atmospheric
d	Downstream
u	Upstream
0	Initial
$()^i$	Response ( ) due to excitation in the i direction

Chapter 1: Introduction

1.1 The gas turbine engine

Without any doubt, the gas turbine is considered one of the greatest inventions of the 20th century. The main reason for the success of the gas turbine is its high energy density (ratio between the generated power and the size of the power plant). Another important feature is the large range of output power available. From 50 W micro-turbines for battery replacement, to the 375 MW SGT5-8000H Siemens turbine for electric power generation (see Figure 1.1), these devices have been used as car and train engines, for aircraft and marine propulsion, or in pumping sets for oil and gas transmission pipelines. Such a diverse range of applications has been possible thanks to the technological flexibility and fuel versatility of the gas turbine.

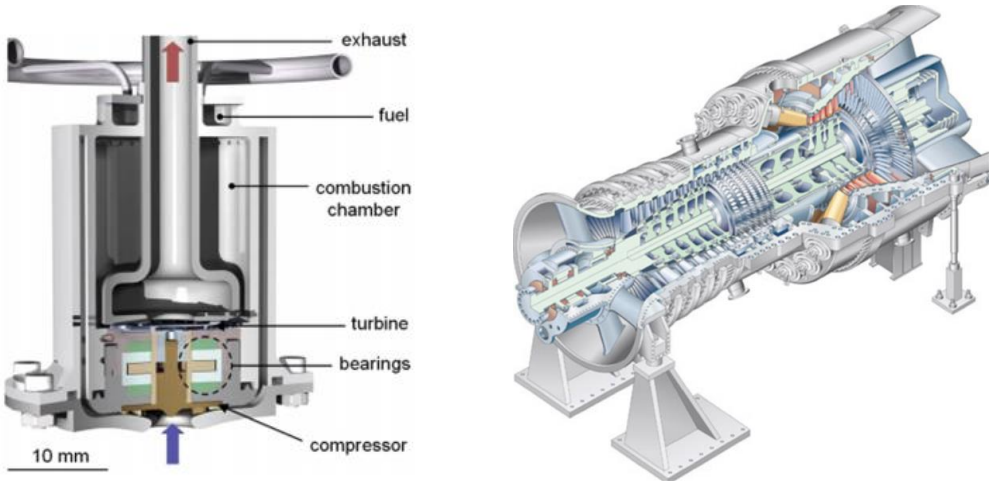

Figure 1.1: Different applications of the gas turbine: (a) concept diagram of the 50 W micro turbine engine by Dessornes et al. [2014] and (b) the 375 MW SGT5-8000H Siemens turbine.

From a historical point of view, the inventions by Sir Frank Whittle and Dr Hans von Ohain in the decade of 1930 are both considered to be the first aircraft gas turbine engines. Whittle patented the first turbojet engine in 1930. It consisted of a centrifugal compressor coupled with an axial turbine, being both components single-stage machines In 1937, a prototype of Whittle's turbojet design was tested in laboratory conditions, proving the feasibility of the concept, and in 1941, it flew for the first time powering the Gloster Pioneer.

Von Ohain, without knowing about Whittle's project, also developed a jet engine and received a patent for his invention in 1935. This engine was used to power the Heinkel He-178 in August 1939, representing the world's first turbojet flight. Also in Germany, the Junkers Jumo 004 was the first engine to be mass-produced. Approximately 6,000 units were used as

the power plant of the Messershmitt M262 at the end of the Second World War. It consisted of an axial machine with a five-stage compressor driven by a two-stage turbine.

The jet engine soon took over the propeller as it allowed planes to fly faster and at higher altitudes. However the first turbo-jet engines had low efficiency and poor reliability and, therefore, it was not until 1952 that the new power plant was used for civil applications. Ever since then, the demand of gas turbines for civilian transport has grown steadily.

Regarding land-based gas turbines, the first concept of a stationary gas turbine was presented by J. Barber in 1791 and the first gas turbine ever built was designed by Stolze in 1872. This turbine had the characteristics of a modern gas turbine: a multistage compressor, a multistage axial turbine and a heat exchanger used to increase the temperature of the compressed air before entering the combustion chamber. However, the efficiency of the compressor was too low and, therefore, the tests performed between 1900 and 1904 were not successful.

The turbine designed by A. Stodola and put into operation in 1939 in Switzerland is regarded as a milestone for stationary gas turbines. It had a power output of 4,000 kW for a turbine entry temperature of 820 K and a cycle efficiency of 17.4 per cent. Since then, the evolution of gas turbines has followed two parallel paths, one corresponding to the development of the aero-engine and the other to the advancement of the stationary gas turbines.

Typical differences between both types of gas turbines exist with respect to the turbine entry temperature, the stage loading and the Mach number level, because of the requirement of longer lifetime for stationary gas turbines. Additionally, land-based gas turbines can use long diffusers to decrease the kinetic outlet energy and thereby increase the overall efficiency because of the lack of weight and space restrictions.

1.2 Gas turbine theory

In spite of the different requirements and restrictions of each application, the reference thermodynamic cycle of every type of gas turbine is the Brayton cycle. The changes that the flow undergoes along this cycle are represented in the *T*-*s* and *p*-*v* diagrams in Figure 1.2. They are:

- **1-2 compression**: Incoming air from atmosphere is compressed over a given pressure ratio.
- **2-3 combustion**: Burning fuel raises the air enthalpy.
- **3-4 expansion**: Air is expanded until the work output is sufficient to drive the compressor.

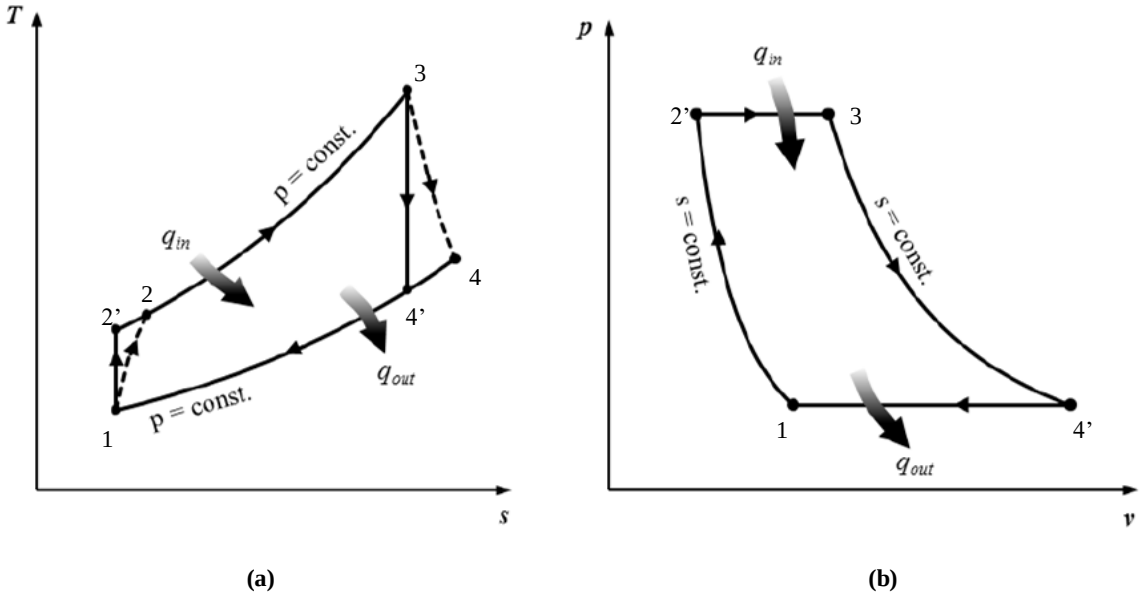

Figure 1.2: (a) Temperature-entropy and (b) pressure-volume diagrams for the Brayton cycle. From Scobie [2014].

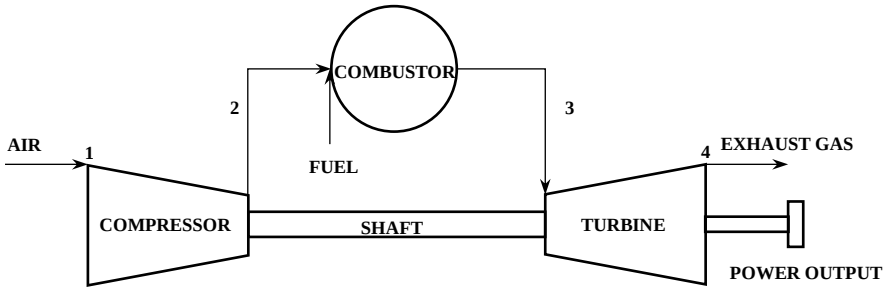

Figure 1.3: Block diagrams of a simple gas turbine system.

Figure 1.3 shows the schematic layout of typical aero and land-based gas turbines.

The processes described above are not isentropic; these non-isentropic changes yield a real cycle that differs from the ideal one. According to Kerrebrock [1992], the deviations from the ideal cycle are due to:

- Variation in gas properties
- Compressor and turbine efficiencies
- Burner efficiency and pressure loss
- Imperfect expansion losses in the nozzle

The thermal efficiency of a gas turbine is defined as the ratio between the net power given by the engine to the air, and the calorific power released in the combustion. When applying this definition of thermal efficiency to the ideal Bryton cycle, it can be demonstrated that it is only a function of the pressure ratio (Saravanamuttoo *et al.* [2001]). However, if the

efficiencies of the compression and expansion processes are taken into account, the expression of the thermal efficiency is now dependent, not only on the compression ratio, but also on the temperature of the air at the entry of the turbine:

$$\eta_{TH} = \frac{W_n}{cL} = \frac{(\eta_t \eta_c t)\left(1 - \frac{1}{p}\right) - (p-1)}{\eta_c(t-1) - (p-1)} \quad 1.1$$

Where η_c, η_t are the efficiencies of the compressor and the turbine, respectively. The factor p determines the maximum compression ratio of the cycle and takes into account the flight condition, if any, and the compressor pressure ratio, π:

$$p = \left(1 - \frac{\gamma - 1}{2} {M_0}^2\right) \cdot \pi^{\frac{\gamma-1}{\gamma}} \quad 1.2$$

The factor t represents the overall temperature increase from the atmosphere (T_0) up to the entry of the turbine:

$$t = \frac{TET}{T_0} \quad 1.3$$

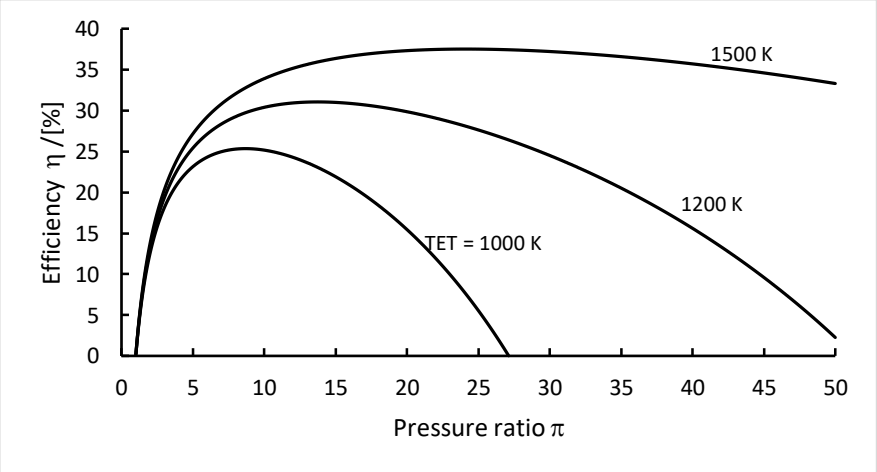

Figure 1.4: Thermal efficiency vs. pressure ratio for different TET.

Figure 1.4 shows the efficiency calculated as per Eq. 1.1, for three different values of the turbine entry temperature (TET) and a range of pressure ratios from 1 to 30. It can be seen that, at a given TET, the efficiency of a gas turbine increases up to a maximum value with the overall pressure ratio. The first aero engines had an overall pressure ratio around 4:1. Nowadays, the value of the pressure ratio for modern civilian engines ranges from 38:1 to 50:1. These values of pressure ratio can be obtained thanks to improvements in materials,

which support higher pressure differences and higher temperatures, to new compressor blades design, with higher aerodynamic efficiency and 3D features that control the secondary flows, and to multi-spool engines.

Additionally, Figure 1.4 shows how, for a constant pressure ratio, the efficiency of a gas turbine increases when the TET increases. Large efforts have been directed towards the increase of the overall temperature ratio. The maximum combustor exit temperature is limited by the turbine blade materials maximum working temperature. The research in this area is mainly focused on obtaining better materials for the turbine vanes and blades, improving the cooling systems, and developing ceramic coatings that are used as thermal barriers.

1.3 Secondary air system

Since the introduction of cooling techniques in the 1960s, the TET has been increased beyond the melting temperature of the turbine material, as shown in Figure 1.5. More specifically, Gülen [2018] states that the most advanced modern engines have a nominal TET of almost 1900 K, whereas the melting point of the single-crystal, nickel-based alloys, used to cast the turbine blades, is 1550 K.

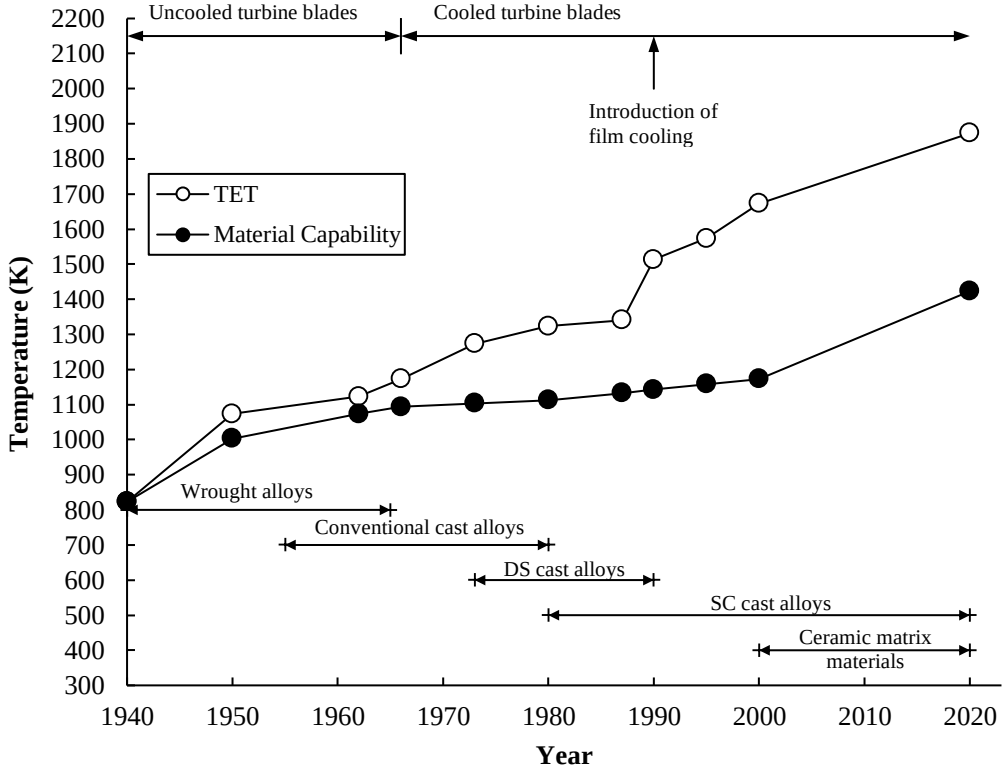

Figure 1.5: The progress of turbine entry temperature. Data from Cumpsty [1997], Hunt [2011] and Gülen [2018].

The air used to cool turbine components is the high-pressure air bled from the compressors. A large amount of work is given to this air during the compression process that is not fully recovered in the expansion process, as the cooling air is not burnt in the combustion chamber and does not pass through every turbine stage. This, in turn, means that using cooling air is not free and has an impact on the thermal efficiency of the engine.

In addition to the compressed air used for cooling purposes, extra air is extracted at different stages along the compression process for different applications; namely, sealing bearing compartments and turbine disc cavities, conditioning of the aircraft cabin, anti-icing, or active clearance control. The complicated network of ducts and passages in charge of delivering the correct amount of cooling and sealing flow at the right pressure level from one part of the engine to another is referred to as the secondary air system. A representation of a typical turbine secondary air system is shown in Figure 1.6.

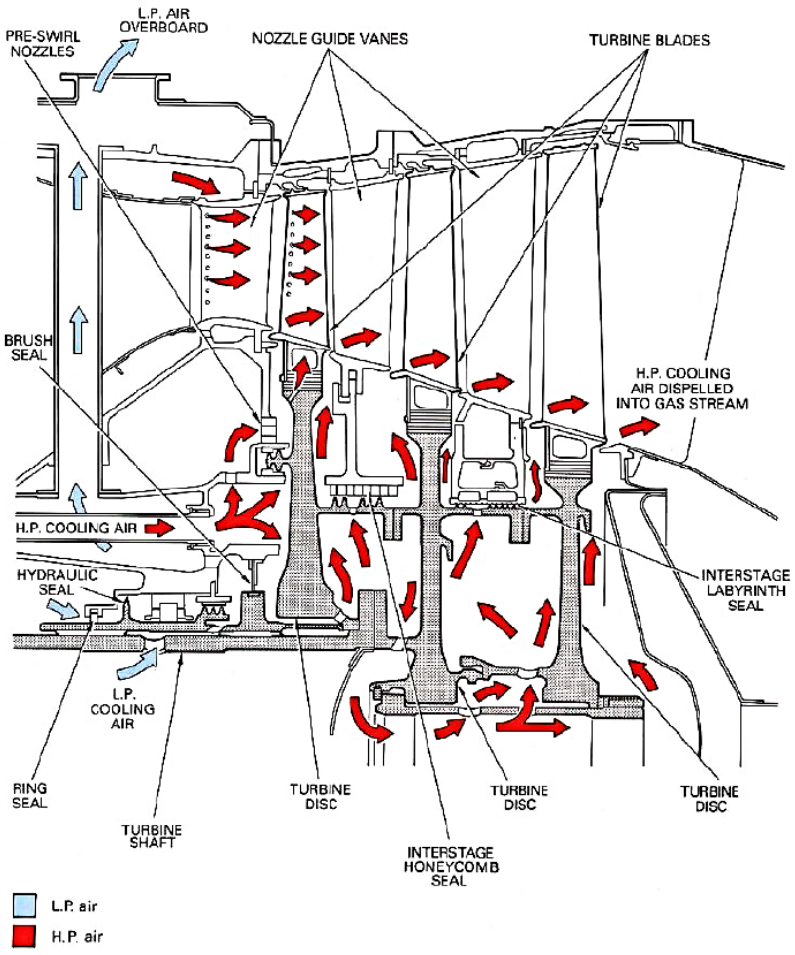

Figure 1.6: Typical turbine secondary air system. From Rolls-Royce [2015].

Because the use of compressed air for cooling and sealing purposes has a cost, the good management of the internal air system is crucial for the overall performance of gas turbines. Chupp *et al.* [2010] states that a reduction of 1% in compressor bleed translates into a reduction of 0.4% in specific fuel consumption (SFC).

The devices used to manage the secondary air system are seals that control the clearance between the rotating and stationary parts of the turbomachines, regulating the amount of flow that leaks between the high pressure and low pressure regions within the engine. Large clearances lead to low cycle efficiencies, flow instability and hot gas ingress into disc cavities. On the contrary, tight clearances lead to reduced coolant flow and rubbing between parts. Both extreme situations lead to lower engine efficiency and life span. Therefore, accurate clearance control is of paramount importance in engine design.

Another important feature of a seal that has to be taken into account during the design stage is its dynamic stability. The air that passes through the clearance of the seal exerts a force on the rotor that have an impact on its dynamic behaviour. In other words, the reaction forces of the leakage air on the rotor can either stabilise or destabilise it.

Together with the optimisation of component aerodynamics, the development of new materials, and the use of novel cooling techniques and thermal barrier coatings, the improvement of seals used to increase the efficiency of the secondary air system represents one of the most important research paths towards higher engine performance.

1.4 The sealing problem in turbomachinery

The research presented in this thesis is focused on the improvement of the sealing technologies. A succinct overview and classification of existing seals, which allows for the understanding of the sealing problem in turbomachinery, is given in this section. For a deeper insight into the state of the art of the seals used in modern engines, the reader is referred to the work by Chupp *et al.*[2006], which reviews conventional dynamic seals to control clearances and advanced seal designs under development at the time.

Figure 1.7 shows a cross section of a modern high-bypass turbofan engine in which all the existing seal locations have been highlighted. These seals have different functions that are crucial for the integrity and efficiency of the engine. They can be classified in two main groups.

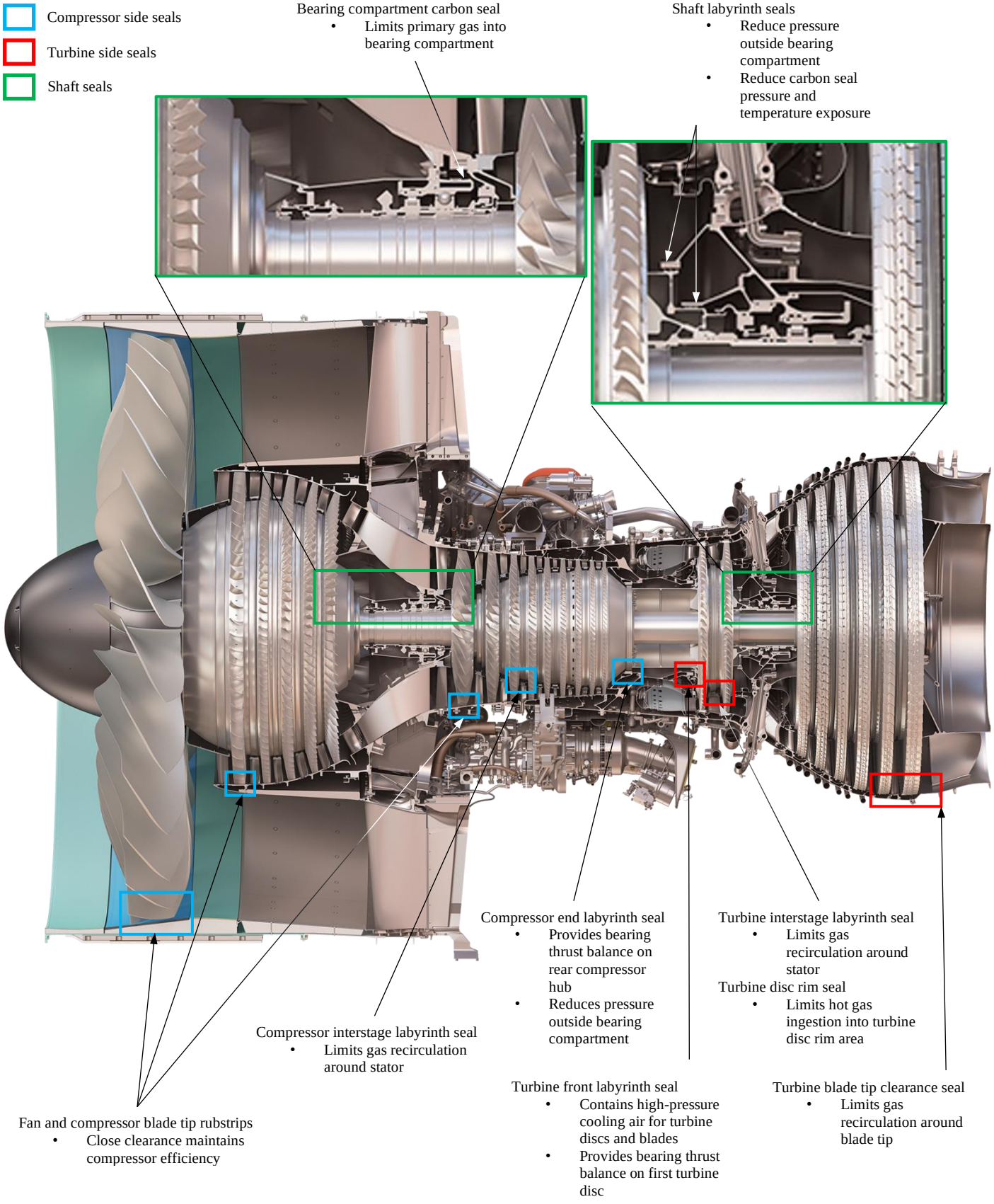

Figure 1.7: Seal location in a modern high-bypass turbofan engine – GP7200.

The first group comprises oil shaft seals, which protect the shaft bearing compartments and sumps from engine debris and stops bearing oil vapour from mixing with the engine main flow, preventing cabin air from poisonous contaminants. Face seals, carbon ring seals and buffer seals are different types of shaft seals.

The second group of seals are referred to as air-to-air seals. These control the flow leakage from high to intermediate- or low- pressure areas and depending on their location and function within the engine, they can be subdivided as follows:

- **Inter-stage seals**: reduce gas recirculation around the stator hub.
- **Turbine disc rim seals**: control the ingestion of hot gas into the inter-disc cavity.
- **Blade tip clearance seals**: reduce secondary flow effects by reducing flow leakage from the blade pressure surface to the suction surface.
- **Balance piston seals**: at the end of the compressor or at the front of the turbine, they balance the pressure difference created in both components and, therefore, reduce the thrust acting on the bearings.
- **Shaft seals**: adapt the pressure and temperature of the air to suitable values for the bearing compartments.

It is worth mentioning that the air-to-air shafts seals are different in configuration and working principle to the oil shaft seals of the first group, but they are known by the same name in the literature as both types of shaft seals are used together as a means to the same final aim of keeping the air flow separated from the oil flow and ensuring the integrity of the bearings. This research focuses on the investigation of the air-to-air shaft seals.

A different classification of the air-to-air seals can be done when looking at the type of boundary existing between the rotating and the static parts of the seal. According to this criterion, there are three groups; namely, non-contacting seals, compliant contacting seals and adaptive non-contacting seals. Figure 1.8 summarises the development of air-to-air seals, and lists their advantages and disadvantages, from the well-established labyrinth seal to the latest seal concepts, yet to be proved.

Labyrinth seals are the most used non-contacting seals in turbomachinery, since they represent a low cost and long life solution that allows reverse rotation. Nevertheless, a high sealing effectiveness implies a tight radial clearance between the static and rotating parts, which also implies a high probability of rub when the rotor runs eccentrically with respect to the stator. In turn, the latter means that in order to prevent from rubbing and wearing, the seal clearances are increased and therefore the performance of this type of seals is diminished. Another drawback of labyrinth seals is the fact that they create destabilising forces that cause the rotor to move away from its centre.

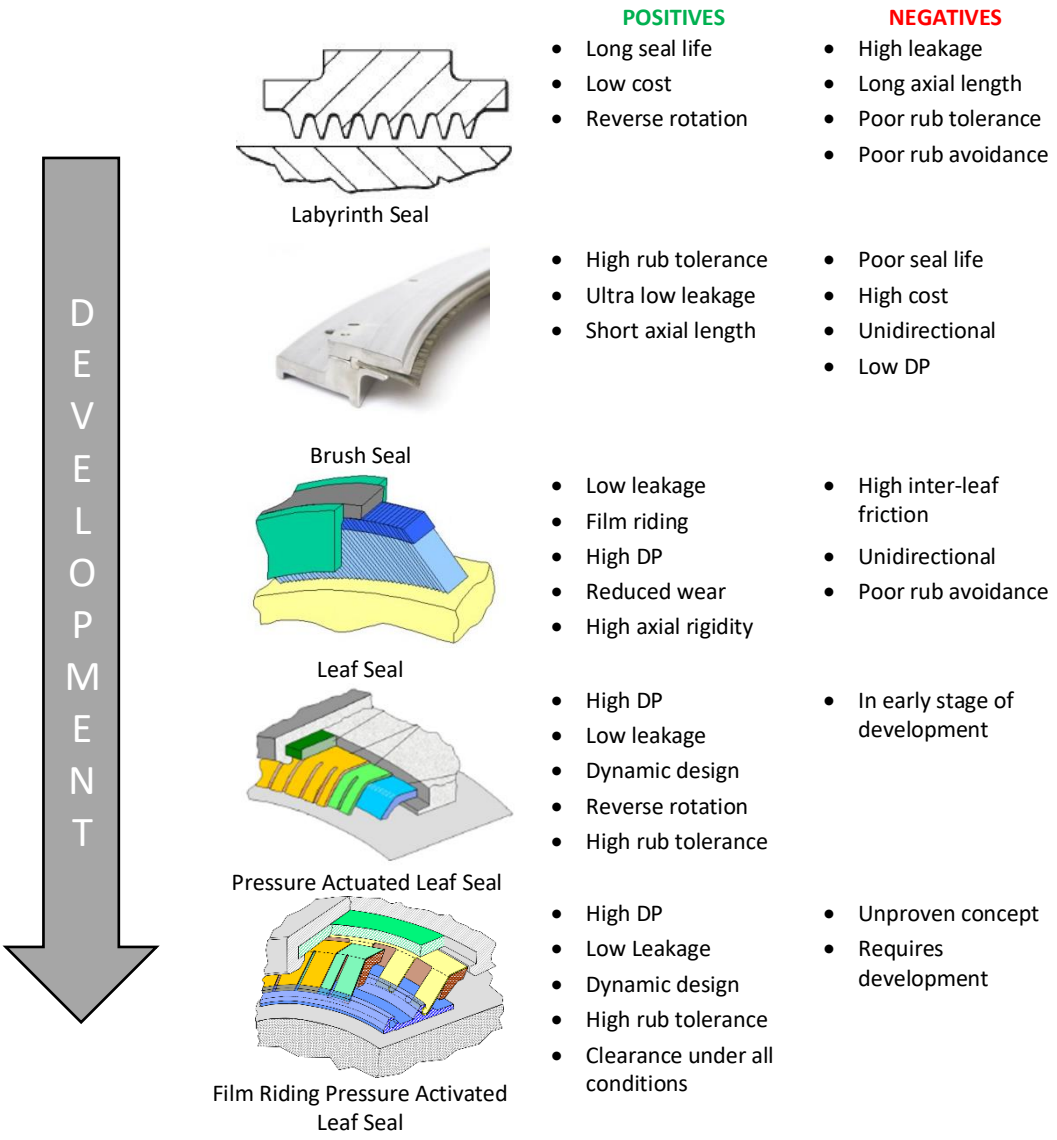

Figure 1.8: Development of different types of shaft seals. Scobie *et al.* [2015].

In compliant contacting seals, the clearance created between the rotor and stator allows for rotor excursions. As a result, both the leakage and the wear of the rotor and seal remain low. The most common seals of this group are brush seals and their performance benefits over labyrinth seals have been demonstrated. Aslan-zada *et al*. [2013] provides a comparative review between both types of seals, including their design, features and results from the studies carried out to improve their performance.

Indeed, brush seals represent a low leakage solution with higher rub tolerances and more favourable rotor-dynamic characteristics than labyrinth seals. However, the bristles suffer from hysteresis, which means that after the bristles are pushed outwards by the rotor they do not recover their initial position and, hence the effective clearance of the seal increases. Because of this problem, brush seals have a short life in comparison with their relative high cost. In addition, brush seals can only run in one direction and can only withstand maximum

pressure differences of 20 bar, approximately, which is lower than the maximum pressure differences across labyrinth seals.

In order to overcome these disadvantages, new compliant seals such as leaf seals (Jahn *et al*. [2008]), shoed brush seals (Delgado *et al.* [2005]) and finger seals (Proctor and Delgado [2004]) have been developed. These seals maintain a tight radial clearance during steady operation and, hence, a high sealing effectiveness. They are characterised as being in contact with the shaft at low rotating speeds and lift away as the speed increases when a hydrodynamic film pressure is generated, which minimises the contact between rotating and static parts. The positive clearance that exists when the hydrodynamic forces separate the sealing elements from the rotor is beneficial for accommodating small rotor misalignments such as thermal growth or manufacturing run-out, which leads to rub reduction.

The latest turbomachinery sealing solutions are referred to as non-contacting adaptive seals and are designed to avoid rubbing under any operating condition. A large clearance between the rotor and the stator exists during start-up and shutdown transients of the engine when the misalignments of the rotor are at their largest. As the pressure inside the engine increases, the sealing elements close down towards the shaft and the clearance decreases. An example of this type of seal is the Film Riding Pressure Activated Leaf Seal (FRPALS) (Grondahl and Dudley [2010]).

1.5 Description of the FRPALS

The FRPALS conceptual design is the subject of a United States Patent (Grondahl *et al*. [2011]) and its feasibility has been evaluated by Grondahl and Dudley [2010]. Large scale, static testing has been carried out by Kirk *et al.* [2016]. However, this new seal concept needs to be proven and optimised at engine conditions before its implementation in real gas turbines. This proof of concept and further development is the goal of this project and is motivated by the fact that this new design represents a superior shaft seal capable of maintaining a small, non-contacting clearance under all transient and steady-state operating conditions.

Figure 1.9 shows a 3-D representation of the FRPALS prototype and identifies the key components making up the seal assembly. Figure 1.10 shows the FRPALS in cross-section. The sealing components are leaves fabricated from shim stock. On one end, the leaves are bent and fitted to the support members. At the other end, they are rolled-up to slide into the grooves machined on the top surface of the hydrodynamic runners (Figure 1.10). Two layers of leaves are used to withstand the differential pressures applied to the seal. The upstream set of leaves are referred to as positioning leaves. Their main function is to keep the runners nearly parallel to the rotor. The gap between the upstream leaves is large enough to let the air pressurise the

interleaf gap. The downstream leaves are the so-called sealing leaves as they stop the flow leaking to the low-pressure side of the seal. Nevertheless, a minimum gap between leaves is needed to allow for movement, which implies that there is a parasitic leakage that has to be taken into account.

The support members are located at the upstream side of the leaves. At the design differential pressure, the leaves lean on the support members and the gap between the seal and the rotor reaches its minimum value. Hydrodynamic runners are assembled at the ends of both the forward and aft rows of leaves. The joints between the runner and the leaves are set to allow the latter to pivot as the seal displaces radially under the effect of the pressure. The inner diameter surface of the runners features a Rayleigh step which generates the required pressure distribution to make the seal film ride. The seal is divided into eight circumferential segments, each of which is fitted with a runner. The eight segments of the seal are enclosed by a backing ring. This structure serves as a means of mounting the FRPALS into the stator.

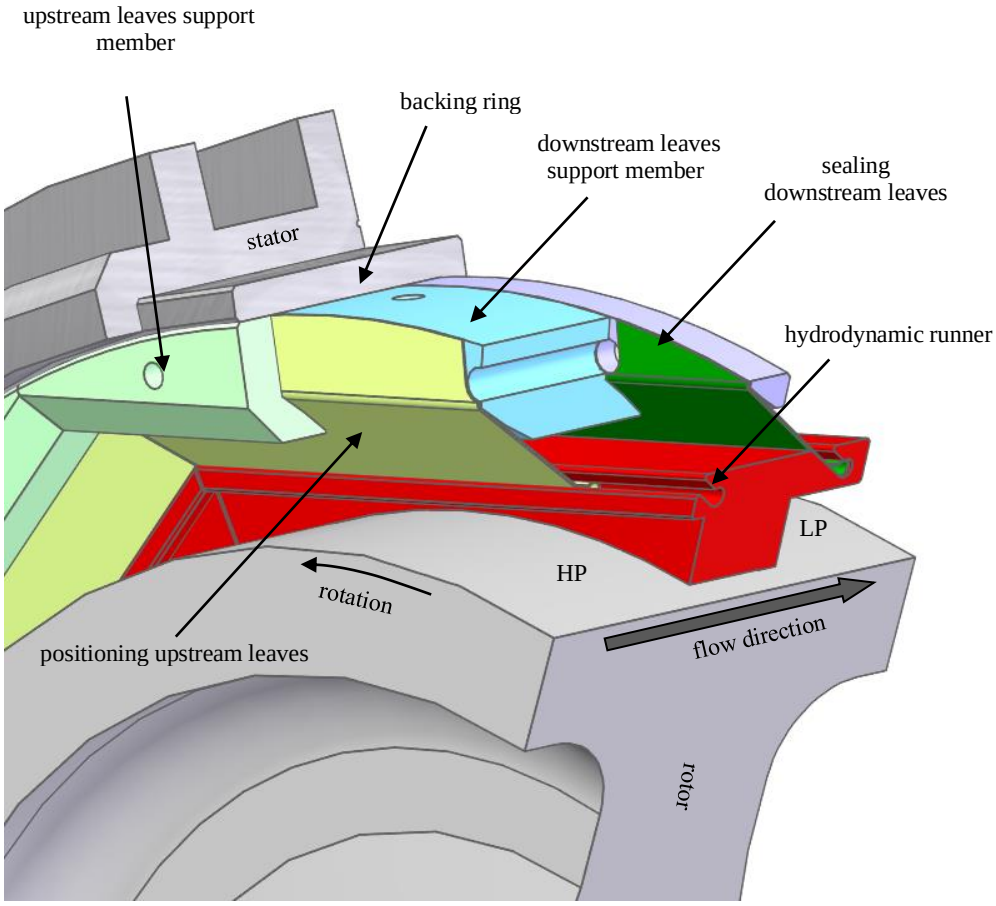

Figure 1.9. 3-D cut-out view of the Film Riding Pressure Actuated Leaf Seal.

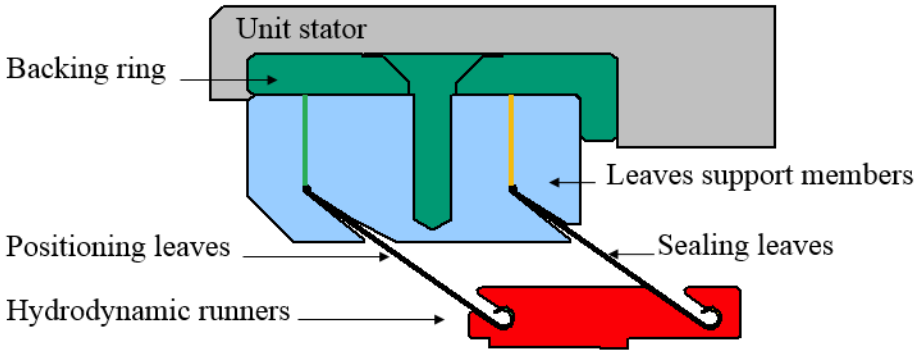

Figure 1.10. Cross section of the FRPALS.

The radial functionality of the seal is described by Grondahl and Dudley [2010] and is summarised hereinafter. In the cold condition, there is no pressure difference across the seal. The leaf elements are not in contact with the support and the seal clearance is large. When the unit starts operating, at the design pressure level, the leaves close towards the support elements and the sealing clearance is small, optimising the performance of the engine. At the steady-state operation of the engine, any change of clearance is accommodated by the seal as it film-rides and the existing pressurised thin film of air in the clearance keeps the runners separated from the rotor. During the shutdown process, as the rotor decelerates, the pressure drop decreases such that leaves retract from the support members, increasing the clearance and avoiding rub damage.

1.6 Thesis aims

The primary aim of this project is to test a FRPALS prototype in order to develop its technology readiness. The description of the FRPALS conceptual design and an analysis of the main parameters affecting the function of the seal, such as the forces acting in each component and the geometry of the clearance were presented in Gondahl and Dudley [2010]. Given this, and according to the description of the readiness levels of Figure 1.11, the new sealing technology has obtained TRL 2. It is currently at TRL 3 as active research and design is being carried out.

The next stage in the development of the FRPALS is the demonstration of the seal operability and the assessment of its leakage performance at both static and rotating conditions.

An evaluation of the rotordynamic performance of the seal is also a necessity for the validation of analytical, predictive design tools.

This aim is to be achieved by fulfilling the objectives specified in the following.

1. To design and build a high-speed rotating test rig to study the dynamic behaviour and characteristics of the FRPALS concept. The experimental facility will be capable of measuring pressure, leakage mass-flow rate and temperature. Additionally, a methodology to measure the rotordynamic coefficients from the literature has to be selected and the test rig specifically designed so that the chosen approach can be applied.

2. To validate the new experimental facility and the rotordynamic coefficients measurement methodology by testing a labyrinth seal, as this is a gas annular seal that is well established in the gas turbine industry.

3. To test a Rayleigh-step annular seal that reproduces the geometry of the FRPALS clearance in order to gain insight on the stability and leakage performance of the new compliant seal without the complexity that the moving parts add to the system.

4. To solve the steady-state Reynolds equation for gas lubrication in order to predict the pressure distribution along the FRPALS clearance. Predictions of pressure distribution will aid during the design process of the seal. Additionally, this is a stepping stone towards the solution of the transient form of the equation which will provide predictions of the rotordynamic coefficients of the seal.

5. To pressurise/depressurise the FRPALS prototype in static conditions in order to characterise the blow-down/opening process of the seal safely and assess whether the compliant seal film-rides or not. Perform rotating tests and confirm that the seal adapts to changes in clearance by generating an eccentricity between the rotor and the stator.

6. To measure the leakage passing through the FRPALS and compare it with the leakage mass flow rate of the labyrinth seal and the Rayleigh-step seal previously investigated.

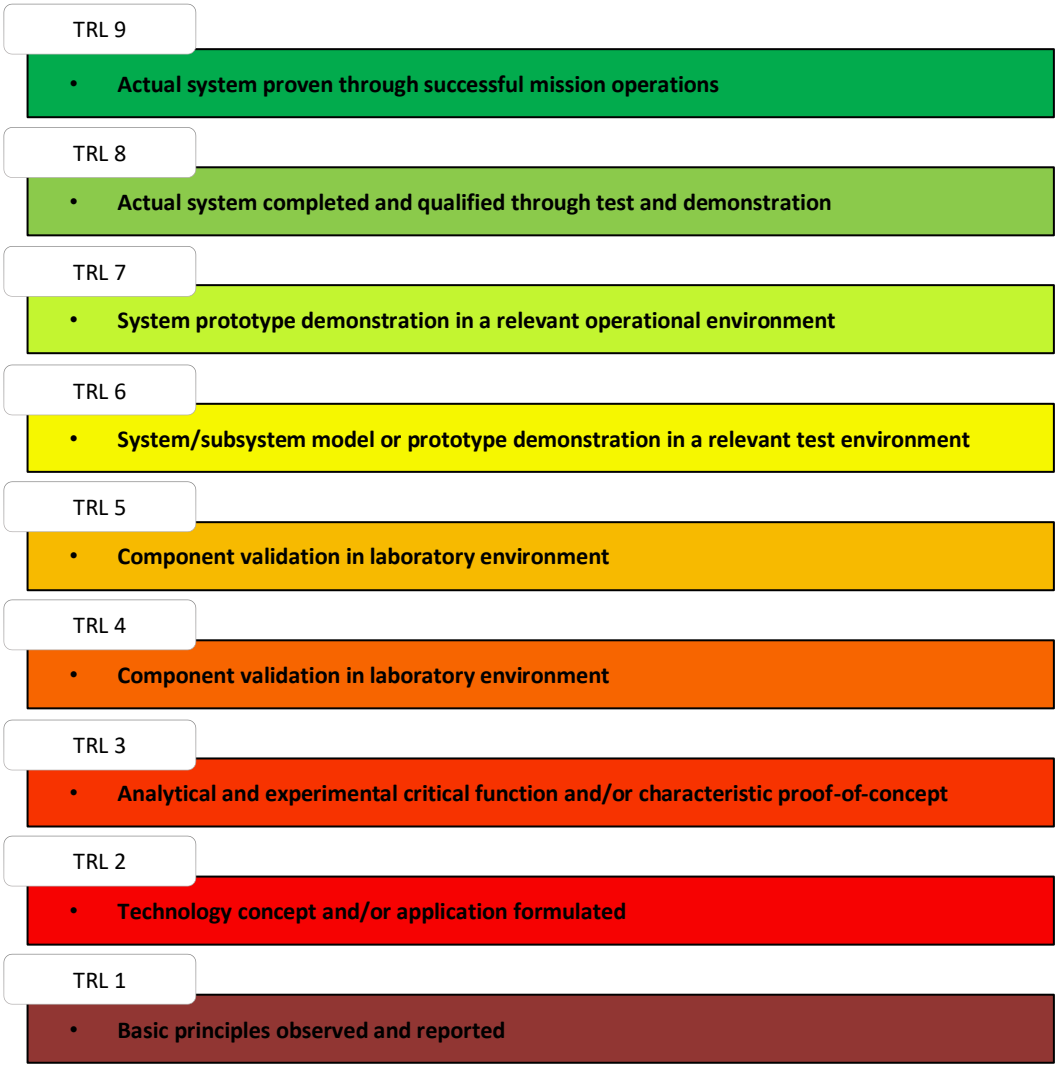

Figure 1.11. Technology readiness level.

1.7 Thesis outline

Chapter 1 of this thesis introduces the gas turbine technology and identifies the research paths followed in order to achieve efficiency improvements. A summary of the existing types of shaft seals used in turbomachinery is then provided and a new seal concept is explained. The aim and objectives of the author's research is also given.

Chapter 2 provides an overview of the labyrinth and brush seals which are the two most used shaft seals in turbomachinery. The most recent compliant seals designs together with the results from research carried out to understand their behaviour are also explained. The chapter ends with the conclusions extracted from the given literature review.

Chapter 3 describes the high-speed rotating facility designed to experimentally assess the behaviour of the FRPALS concept. The design of several existing rigs for seal research is

reviewed and the different sub-systems of the new rig are shown, detailing the design process for each one of them.

Chapter 4 shows the experimental methodology used to measure the rotordynamic coefficients of the seals under investigation and to determine their leakage performance from mass flow rate measurements. The instrumentation used is discussed and the data acquisition system is outlined.

Chapter 5 gives the characterisation of a short labyrinth seal. Its rotordynamic coefficients and leakage performance are discussed. This is done with the intention of validating the test rig of Chapter 3 and to have a benchmark for the air mass flow rate passing through the FRPALS. Additionally, a gap in the literature is filled, as no data for the rotordynamic coefficients of labyrinth seals with less than 5 cavities has been found.

Chapter 6 investigates the dynamic behaviour and leakage performance of a Rayleigh-step annular seal. Additionally, a solution of the Reynolds equation for gas lubrication is given to predict the pressure distribution in the clearance of the annular seal. The predicted pressure distribution is compared with pressure measurements and overall good agreement was proven.

Chapter 7 provides results data from measurements of the blow-down process of the FRPALS. The FRPALS is demonstrated to close towards the rotor when a pressure drop is applied, however it does not film ride, but touches the rotor instead.

Chapter 8 presents the conclusions of this thesis and recommendations for future work towards the development of the FRPALS.

1.8 Publications

Conference publications

1. Pedraza-Valle, E., Scobie, J. A, Sangan, C. M, Keogh, P. S, Bowsher, A, and Crudgington, P. F., 2019, “A New Rotating Test Facility for the Experimental Characterisation of Shaft Seals.” Proceedings of the 13th European Turbomachinery Conference. Paper No. ETC2019-105
2. Pedraza-Valle, E., Papageorgiou, G., Bowsher, A., Crudgington, P. F., Sangan, C. M., Keogh, P. S., and Scobie, J. A., 2019, “On the Development of a Pressure Actuated Leaf Seal for Turbomachinery Applications.” Proceedings of the ASME Turbo Expo 2019. ASME Paper GT2019-90991

Chapter 2: Literature Review

As explained in the previous chapter, the clearance between static and rotating parts must be controlled in order to maximise cycle efficiency and engine integrity, which in turns implies a reduction of fuel consumption and costly corrective maintenance.

A great deal of research has been conducted on the improvement of clearance control. This chapter provides with a review of the development of rotating seal technology for turbomachinery applications.

The two most used types of shaft seals; namely, labyrinth seals and brush seals, are described and their advantages and disadvantages are listed. Then, the new seal concepts investigated over the last three decades are described and the most important achievements in their development are presented.

2.1 Labyrinth seals

Gas labyrinth seals are widely used in turbomachinery as they represent a simple solution to stop the high-pressure air from flowing to lower pressure areas of the engine. Although an inexpensive, long life sealing technology that allows for shaft reverse rotation, labyrinth seals have numerous disadvantages including high leakage, long axial length and wear due to rubs with the rotor. Labyrinth seals also have a large impact on the stability of turbomachines, therefore, ever since their invention extensive research has been conducted to better understand and improve their performance.

The physical principles of labyrinth seal operation are illustrated in the sketch of Figure 2.1 and are based on the transformation of the pressure energy of the flow into kinetic energy, and the further dissipation of the latter into internal energy (Burcham and Keller [1978]). As the gas passes through the narrow restriction created at the tooth tip and discharges into the adjacent cavity, it expands and, consequently, accelerates creating a jet which is then stopped at the cavity downstream of the tooth. This sudden deceleration process is highly unsteady; part of the jet impinges on the wall of the cavity, rapidly changing its direction and generating turbulence that dissipates the kinetic energy of the flow.

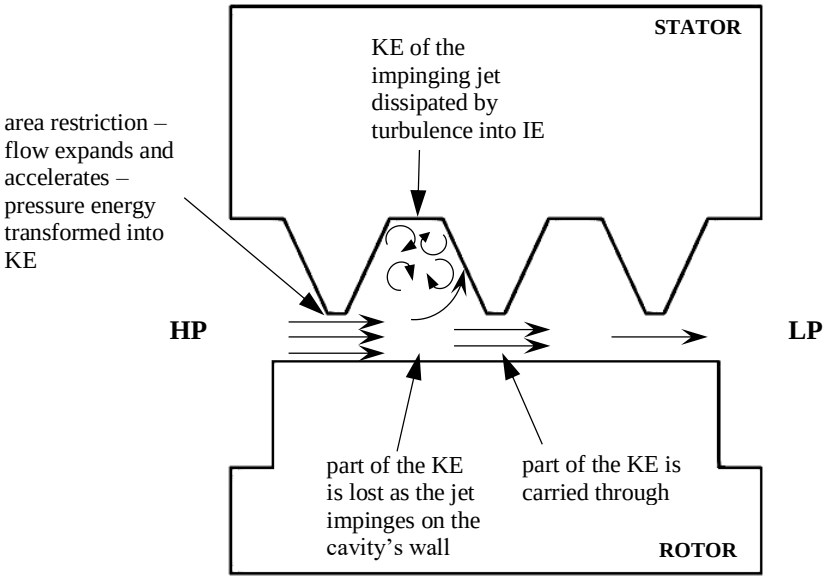

Figure 2.1: Schematic of the energy transformation processes occurring in a labyrinth seal.

The main design variables of labyrinth seals are the value of the radial clearance, the geometry of the teeth and cavities, and the number of restrictions. Aero-thermomechanical considerations are taken into account when choosing the geometry of the seal during design. For instance, thermal expansion of both stator and rotor reduces the clearance during operation and thin tooth tip reduces heat propagation towards the shaft (Chupp et al. [2006]). Figure 2.2 presents discharge coefficients obtained by Mahler [1972] for different sharp edge tooth geometry and illustrates how sensitive the performance of labyrinth seal is to tooth tip shape.

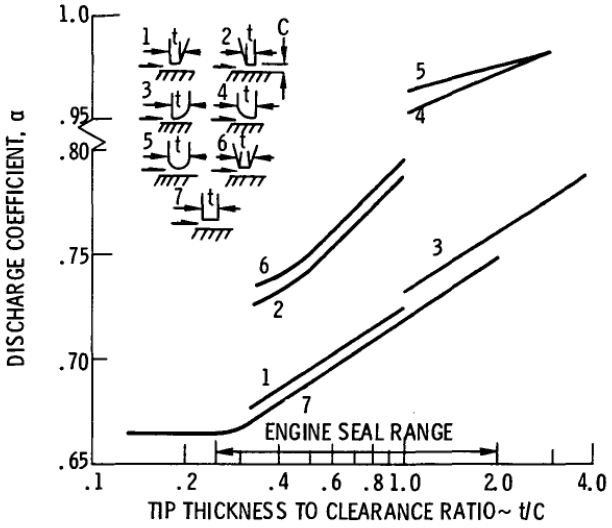

Figure 2.2: Effect of tooth tip geometry on discharge coefficient. From Mahler [1978].

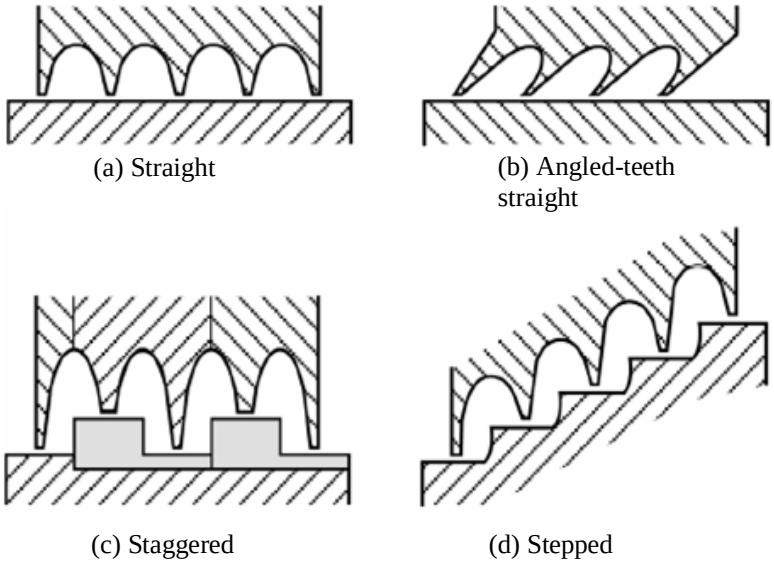

Figure 2.3: Different configurations of labyrinth seal. Adapted from Brucham and Keller [1978].

Figure 2.3 shows the four different configurations of labyrinth seals: straight with either squared or angled teeth, staggered, and stepped. Staggered and stepped seals have better leakage performance as they reduce the carry-through of the kinetic energy from one cavity to another, however they pose difficulties during manufacturing and assembly (Floyd [1986]). Depending on whether the teeth are either on the rotor or on the stator or both, labyrinth seals can be classified as tooth-on-rotor (TOR), tooth-on-stator (TOS) or interlocking (see Figure 2.4). Several studies have demonstrated the superior sealing performance of interlocking seals compared to see-through designs, Childs *et al.* [1988] and Wu *et al.* [2019]. Artur and Childs [2015] compared the mass flow rate of a TOR labyrinth seal and a TOS labyrinth seal; they concluded that the leakage of the TOR labyrinth was between 5 and 10% lower than that of the TOS labyrinth for rotational speeds of up to 20,200 rpm, an upstream pressure of 70 bar and pressure ratios from 0.4 to 0.6. However the geometry of the teeth and the number of cavities was different for both seals.

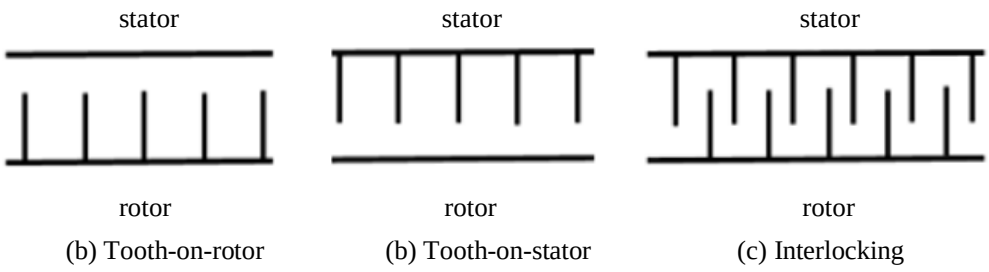

Figure 2.4: Classification of labyrinth seals according to the location of the teeth. From Gary *et al.* [2018].

The complex fluid dynamics of the labyrinth seals makes it difficult to analytically predict the pressure distribution, mass flow leakage and force coefficients. Additionally, the behaviour of the flow highly depends on the geometry of the teeth and the cavities. For these reasons, bulk-flow models that calculate the pressure and the swirling velocity of the flow are used. A bulk-flow model assumes that the flow properties are constant within each cavity but change from one cavity to another.

The first to develop a bulk-flow model for labyrinth seals was Iwatsubo [1980]. Childs and Scharrer [1986] used this model and reported good prediction of the leakage, however the agreement of the predicted and measured force coefficients did not match. More recently, Cangioli *et al*. [2019] presented a modified version of the model that predicts values of the rotordynamic coefficients in good agreement with the experiments. Nowadays computational fluid dynamics (CFD) codes are extensively used as a tool to investigate labyrinth seals.

2.2 Brush seals

Brush seals arose as the first alternative for labyrinth seals delivering gains in efficiency and stability. Ferguson [1988] reported that a brush seal installed in optimum conditions leaks ten times less than a labyrinth seal. Regarding the rotordynamic performance of brush seals, Conner and Childs [1993] showed that a four-stage brush seal has lower values of destabilising forces acting on the rotor compared to an eight-cavity labyrinth seal.

Brush seals need less axial length than a labyrinth seal for the same pressure drop and can be manufactured in segments for the ease of assembly within the turbine unit. Figure 2.5 depicts a conventional brush seal assembly which consists of a pack of fine wires or bristles (see Figure 2.6) welded on their outer diameter and stacked together in between two plates. The clearance of the back plate with respect to the rotor, often referred to as fence height, is a key design parameter. This has to be large enough to avoid contact with the rotor and, at the same time, small enough to support the bristles and stop them from bending axially under the effect of a pressure differential. Figure 2.7 illustrates this effect in an exaggerated manner. If the bristles are deflected axially, they separate from the rotor increasing the leakage. This represents a limit to the maximum pressure drop withstood by the seal. Crudgington [1998] stated that the maximum pressure differential that a brush seal can bear is 20 bar approximately.

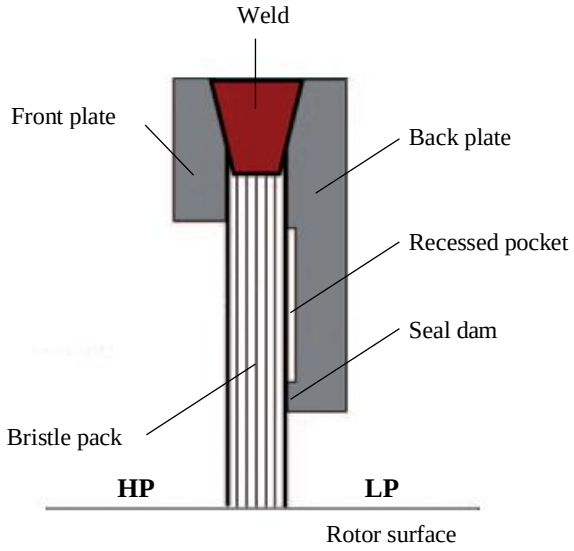

Figure 2.5: Schematic of the assembly of a brush seal. Adapted from Asla-zada *et al.* [2013].

The bore of the bristles is machined to mate the sealing shaft, normally with an interference interface. This interference will reach its optimum level after a break-in period through wear of the bristle tips. The pressure difference applied to the seal may have a blowdown effect on the bristles, i.e. the resultant pressure forces deflect the bristles towards the rotor. This effect further closes the seal clearance and reduces the leakage flow. However, as stated by Hendricks *et al.* [1993], enhanced contact between the bristles and the rotor due to blowdown effects results into excessive wear of the bristles and reduces sealing effectiveness.

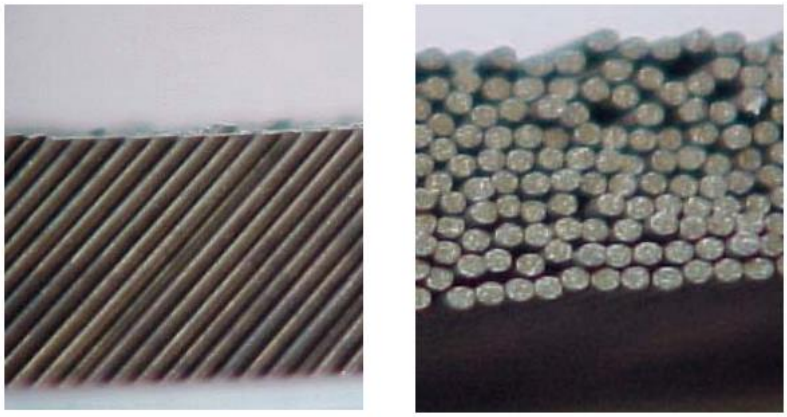

Figure 2.6: Typical brush seal bristle pack. From Crudgington and Bowsher [2002].

Crudgington and Bowsher [2003] investigated the blowdown effect on brush seals through changes in effective clearance and drag torque for varying pressure drops and installation clearances. They found reducing effective clearances for increasing pressure drops in clearance seals, demonstrating the existence of blowdown forces acting on the bristles.

Increasing torque measured in interference seals indicated that blowdown forces have an effect not only in clearance seals, but also for seals that are already in contact with the rotor.

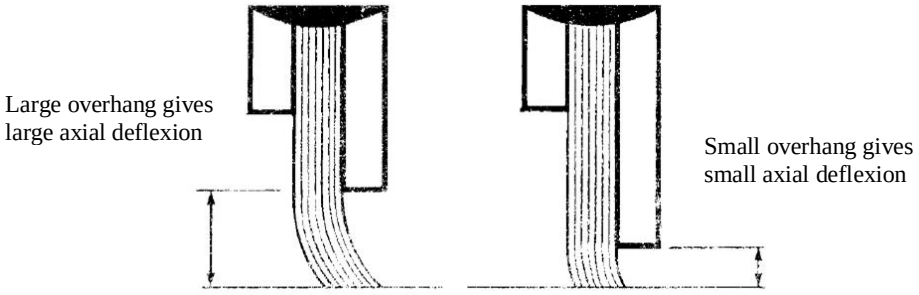

Figure 2.7: Effect of bristle overhang. Not to scale. Adapted from Ferguson [1988].

Brush seals are compliant seals, this is to say that they are able to adapt to rotor movements without damage; however large rotor eccentricities may deflect the bristles permanently, opening the clearance and decreasing the leakage performance of the seal. The bristles are assembled at an angle with respect to the direction of rotation so that they can accommodate rotor excursions without buckling. Because of the angled layup of the bristles, the rotor is only allowed to turn in one direction and reverse shaft rotation is likely to result in damage to the seal. This problem is particularly important in gas turbines used in power generation applications, where the rotor may wind-mill in the reverse direction under certain conditions. Solutions to prevent the rotor from wind-milling need to be designed, with the extra cost that this implies, if brush seals are to be used in gas turbines for power generation (Asla-zada *et al.* [2013]).

2.3 Leaf seals

Leaf seals are contacting, compliant shaft seals similar in general configuration and working principle to brush seals but with a main difference. Instead of an array of fine bristles, leaf seals use thin plates, known as leaves, stacked together around a ring and welded along their outer diameter (Jahn *et al.* [2008]). The leaves are sandwiched in between front and back cover plates, where the inner diameters are chosen to ensure a positive clearance between the plates and the rotor, taking into account difference in thermal growth, manufacturing run-outs and rotor growth under centrifugal stresses. Figure 2.8 shows a sketch of a typical leaf seal assembly.

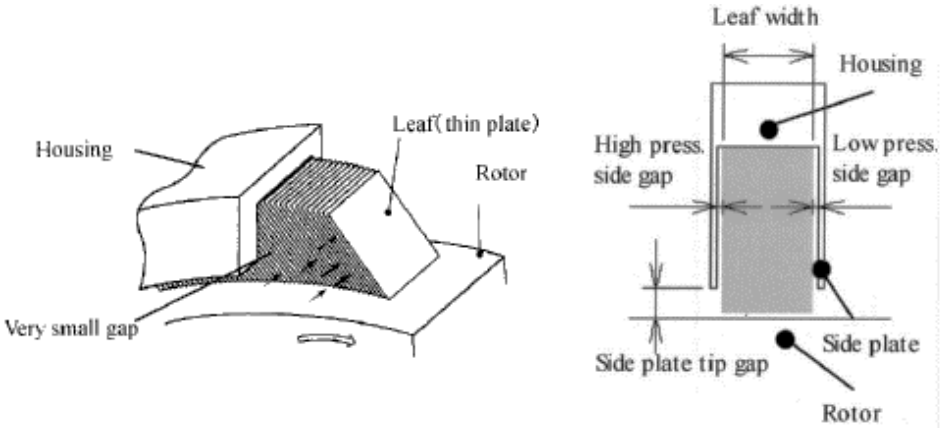

Figure 2.8: Assembly of the leaf seal investigated by Nakane *et al.* [2004].

Regarding leakage flow, Nakane *et al.* [2004] and Jahn *et al.* [2008] have reported leaf seals to have similar sealing performance to brush seals and to leak about a 30% less than labyrinth seals. Note that the reduction of leakage of brush seals with respect to labyrinth seals reported by Nakane *et al*. [2004] and that one given by Ferguson [1988] is significantly different. This difference is thought to be due to the brush seal technology being in a more mature phase of its development at the time that Nakane *et al.* [2004] conducted their research. One of the main features of leaf seals is their ability to withstand higher pressure drops than brush seals, as the axial stiffness of the leaves is larger than that of the bristles. Another advantage of leaf seals is the generation of hydrodynamic forces at the tip of the leaves. If the hydrodynamic force is larger than the sum of the stiffness of the leaves and the pressure forces pushing the leaves towards the rotor, the leaf tips will lift away from the rotor creating a positive clearance and, hence, preventing heating and wearing problems.

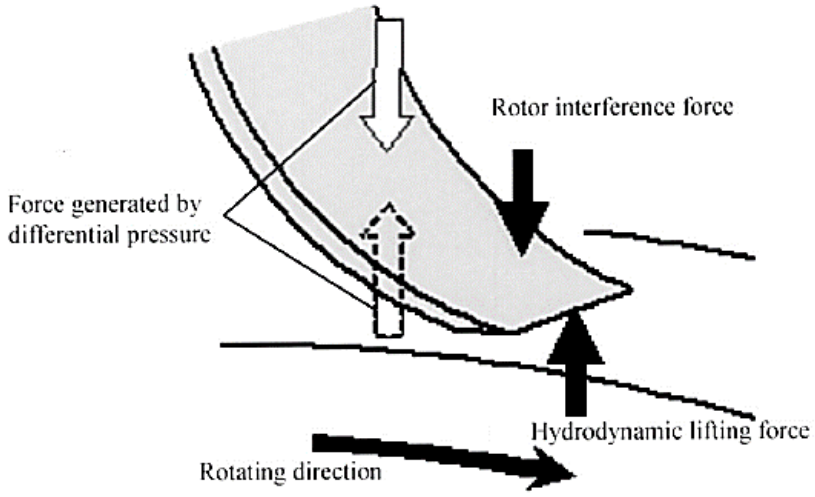

Figure 2.9: Balance of forces acting on a leaf plate. From Nakane *et al.* [2004].

Nakane *et al.* [2004] stated the importance of the seal stiffness for the determination of its lifting characteristics together with the levels of heating and wear. They stressed the fact that the overall stiffness of the seal differs from the sum of the mechanical stiffness of each isolated leaf plate as the interaction between the plates and the flow induced stiffness plays a role in the behaviour of the seal. There are three forces acting on the leaves as shown in Figure 2.9; namely the rotor reaction force, the hydrodynamic lifting force and the force generated by the applied pressure drop.

Nakane *et al.* [2004] confirmed the effect of the hydrodynamic force by measuring the discontinuity of electric current with an electrical contact check device that was in close circuit when the leaves touched the rotor and in open circuit when they lifted off. Indeed, zero voltage was measured at rotating speeds larger than 1,500 rpm. Jahn *et al.* (2013) gave more insight into the air-riding feature of leaf seals, by running CFD simulations of the flow in the passages between the rotor and the leaf tips for different passage maximum heights, passage height slopes and rotor tangential speeds. The pressure in the convergent channel of the illustration in Figure 2.10 varies in the direction of the flow as follows. First, the pressure decreases as the flow sees an increase in area. As the channel converges the pressure increases, which happens as the flow is actually experiencing a widening of effective area. This is the result of the low-pressure bubble at the maximum height region restricting the flow. At the part of the passage where the area is the smallest, there is a decrease in pressure attributed to the spillage of low-pressure flow from the downstream channel.

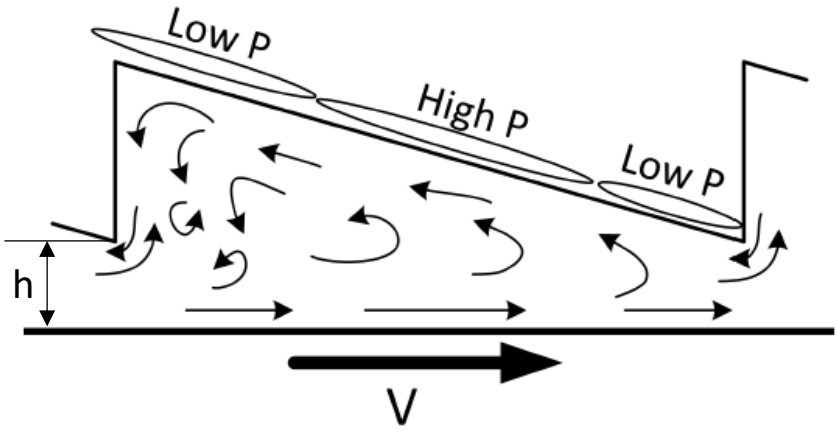

Figure 2.10: Flow field in the passage created between the rotor and the leaf tip. From Jahn *et al.* [2013].

This predicted pressure field was integrated and resolved in the directions perpendicular and parallel to the rotor in order to calculate the drag and the lift forces acting on the leaf tips,

respectively. The lift force was found to increase linearly with rotor velocity and to decrease proportionally to gap height as $1/(h)^3$.

In order to validate the predicted values of the lift and drag forces, the drag was used in a model to calculate the torque of the rotor which was then compared with experimental results. Good agreement between the model and the experiments was found at low rotor speeds, however discrepancies were identified at higher speeds.

The force generated by the differential pressure applied to the seal can either blow down or lift up the leaves. This is determined by the gap width that exists between the cover plates and the leaves on both upstream and downstream sides of the seal. Figure 2.11 from Nakane *et al.* [2004] shows the flow field and the pressure distribution across the width of the leaf depending on whether the high pressure side gap is equal, larger or smaller than the low pressure side gap.

Jahn *et al.* [2008] tested 52 coverplate combinations and measured mass flow leakage, torque loss and seal stiffness. They confirmed the finding Nakane *et al.* [2004] that the behaviour of LS is dependent upon the coverplate geometry as it changes the pressure forces acting on the leaves.

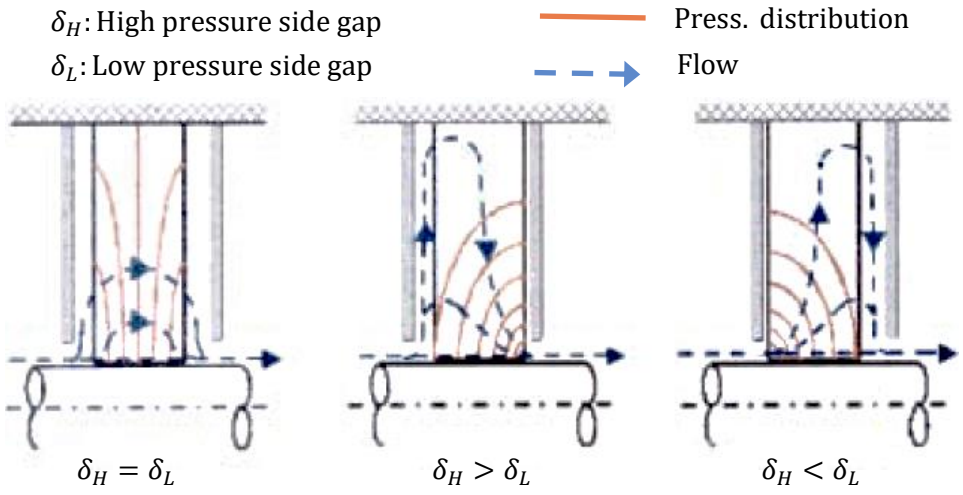

Figure 2.11: Pressure distribution depending on the relation between high pressure side and low pressure side gaps. From Nakane *et al*. [2004].

Nakane *et al.* [2004] showed that when keeping rotating speed and configuration the same the pressure forces exerted on the seal do not change when the applied pressure drop is changed. Therefore, and contrary to what happens with brush seals, no limits in pressure drop

exist due to risk of blow down effects, which is another advantage of leaf seals over brush seals.

Jahn *et al.* [2011] performed experiments to measure the stiffness of a prototype leaf seal at different pressure differentials and discovered that the stiffness of the tested seal was negative. Negative stiffness means that for a positive displacement of the rotor the reaction force of the seal is negative. Additionally, they developed a simple model for the stiffness, which is the sum of the mechanical stiffness and the stiffness related to the aerodynamic forces. They validated the model against one of the experimental cases and concluded that constants of the model change with the pressure drop.

Gillespie *et al.* [2016] developed a thermal model for the prediction of heat transfer at the rotor-seal interface to be used at design stages. They solved the energy equation assuming 1-dimensional flow and 1-dimensional conduction heat transfer with the aim of finding the 2-dimensional temperature distribution in the plane of the leaf. Large temperature gradients at the leaf tip were reported. The temperature of the leaf rapidly reduced to equalise the flow temperature along the length of the leaf.

Dimensional analysis of the heat transfer problem in leaf seals suggested that the heat generated by friction in the rotor-seal interface is proportional to the product of the temperature rise of the rotor with respect to the mainstream temperature and the square root of the mass flow rate. This result was confirmed by experiments carried out at the Oxford high speed Engine Seal Test Facility. The authors also claimed that the experiments showed a temperature increase of the rotor 30 °C lower than that found for a brush seal at the same testing conditions.

It is worth mentioning that Nakane et al [2004] tested a leaf seal at real engine conditions for over 1000 hour. They substituted a brush seal located in a section between the compressor and the turbine of a Mitsubishi-M501G gas turbine. Measurements of pressure and temperature at both the upstream and the downstream cavities of the seal showed similar performance of the new leaf seal in comparison to the substituted brush seal. Inspection after operation showed no lost, cracked or melted leaves. The tips of the leaves were slightly polished.

2.4 Hybrid brush seals

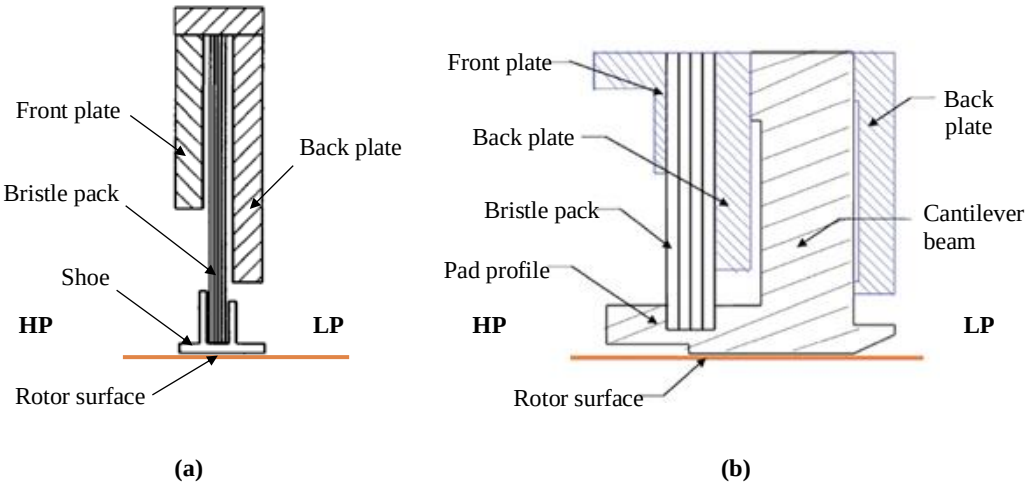

Figure 2.12: Schematic of the (a) Shoed Brush Seal and the (b) Hybrid Brush Seal assemblies. Adapted from Justak [2002] and San Andrés *et al.* [2009], respectively.

Justak [2002] patented the Shoed Brush Seal (SBS), which is a brush seal that has pads/shoes welded to the bristle tips. The second generation of shoed bush seals, known as Hybrid Brush Seals (HBSs), was created by Justak [2008]. The pads are now welded to radial spring-beams having higher axial stiffness than that of the brush bristles, stopping the shoes from rocking under the effect of the pressure drop and, hence, giving the seal better performance at high pressure differentials. The spring-beams also provide the seal with the radial compliance needed to accommodate to varying clearances. Figure 2.12 and Figure 2.13 show schematics of the assembly of both types of seal and photographs of the testing prototypes, respectively.

Justak and Crudgington [2006] listed several advantages for using padded brush seals instead of standard brush seals. Firstly, for the same sealing characteristics, the new generations of brush seal would not experience a change in performance due to bristle wear. Tight tolerances during manufacturing and assembly can be relaxed as the shoes can be designed to have a certain amount of interference with the shaft prior to rotation. The pads will then lift off during rotation under the effect of the hydrodynamic forces created by the air dragged by the rotor, creating a positive clearance between rotor and seal. Finally, reverse rotation of the rotor is allowed as the bristles are no longer in contact with the shaft.

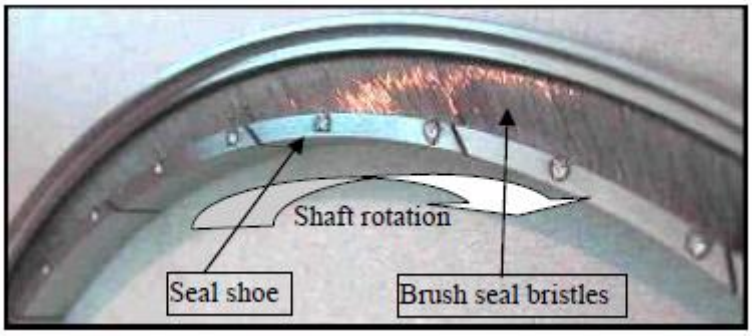

(a)

(b)

Figure 2.13: Photographs of (a) Shoed Brush Seal and (b) Hybrid Brush Seal. From Justak and Crudgington [2006].

The three different configurations of SBSs in Figure 2.14 were tested by Justak and Crudgington (2006); namely a narrow-shoe, single brush seal; a wide-shoe, dual brush seal; and a pressure-balanced, wide-shoe, dual brush seal. Results from a standard BS were used for comparison.

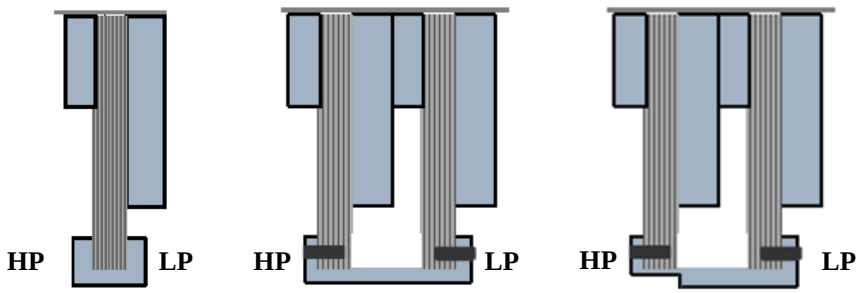

(a) **(b)** **(c)**

Figure 2.14: Schematic of the three configurations of SBS investigated by Justak and Crudgington [2006]: (a) narrow-shoe, single brush seal, (b) wide-shoe, dual brush seal and (c) pressure-balanced, wide-shoe, dual brush seal.

No hydrodynamic lifting was evident in the narrow-shoe, single brush seal. On the contrary, the temperature of the wide-shoe, dual brush seal stayed constant for increasing pressure drops, which indicates that the seal was not in contact with the rotor or, in other words, hydrodynamic lifting of the pads occurred. During offset tests, with a maximum offset of 508 μm, the temperatures slightly increased and the effective clearance increased by 38 μm. It was found that the standard brush seal operated with temperatures 20-30 °C higher than the shoed seal for concentric tests. This difference increased to 120 °C during offset tests.

Improvements in performance of the pressure-balanced design with respect to the wide–shoe, dual brush seal was found. The temperature decreased with increasing pressure drops, indicating that the hydrostatic forces of the clearance air film were enough to keep the pads separated from the rotor.

The success of the experiments performed with the SBSs encouraged further testing of a HBS design with a pad featuring the pressure-balancing step similar to the configuration in Figure 2.14(c). The authors concluded that the outlet air temperature for the reference brush seal exceeded 400 °C due to rotor contact, whereas no air temperature rise was detected across the HBS. During offset tests, the brush seal needed 30% more power with respect to concentric experiments. No extra power was needed for the HBS prototype when running eccentrically. Finally, after a ten-hour endurance test, the outer diameter of both seals was measured to account for the wear. The bore of the brush seal had increased by 63 μm, the bore of the HBS had not changed.

San Andrés *et al.* [2009] tested the leakage and power loss of the HBS configuration previously tested by Justak and Crudgington [2006] and shown in Figure 2.12(b), for pressure differentials ranging between 0 and 2 bar and low rotor surface speeds (11 m/s). Mass flow leakages 36% lower than a SBS were measured throughout the whole tested pressure range. The effective clearance did not stay constant for pressure ratios greater than the chocked flow pressure ratio for a constant area restriction, indicating that the clearance of the seal opened as the pressure drop increased and, hence, demonstrating the lifting effect of the hydrostatic forces acting on the seal shoes.

Additional evidence for the existence of this hydrostatic effect was gained through measurements of torque needed to turn the rotor. The torque needed to start rotating the shaft was significantly reduced from the case of zero pressure drop applied to the seal to a pressure drop of 0.7 bar.

2.5 Finger seals

Finger Seals are contacting compliant seals that use several precision-machined shim stock elements stacked together, normally referred to as sealing wafers or sealing laminates. Similar to the bristle pack of a BS, the stack of sealing wafers are clamped between forward and aft plates and assembled together by means of bolts or rivets. A spacer between the front cover plate and the upstream sealing element is used in order to avoid friction between both parts. Arora *et al.* [1999] defined the fingers as slender, curved, beams that support an elongated contact pad. The different sealing wafers are layered in a staggered way, so that the fingers of one layer covers the interstices between the fingers of the following layer, thus impeding the airflow. Figure 2.15 shows a sketch of an finger seal and depicts the main components of the assembly.

Arora *et al.* [1999] optimised the finger seal concept by testing 13 different configurations and published data for the baseline and final designs (see Figure 2.16). They first tested the baseline finger seal by applying a pressure drop across the seal at the same time that the speed of the rotor was ramped up and down three times consecutively. They observed that there was hysteresis in flow leakage. This hysteresis was attributed to the fact that the applied pressure causes the finger elements to react against the back plate. The fiction generated in between the fingers and the aft plate is greater than the restoring force of the fingers and, therefore, they do not deflect back down when the speed of the rotor decreases.

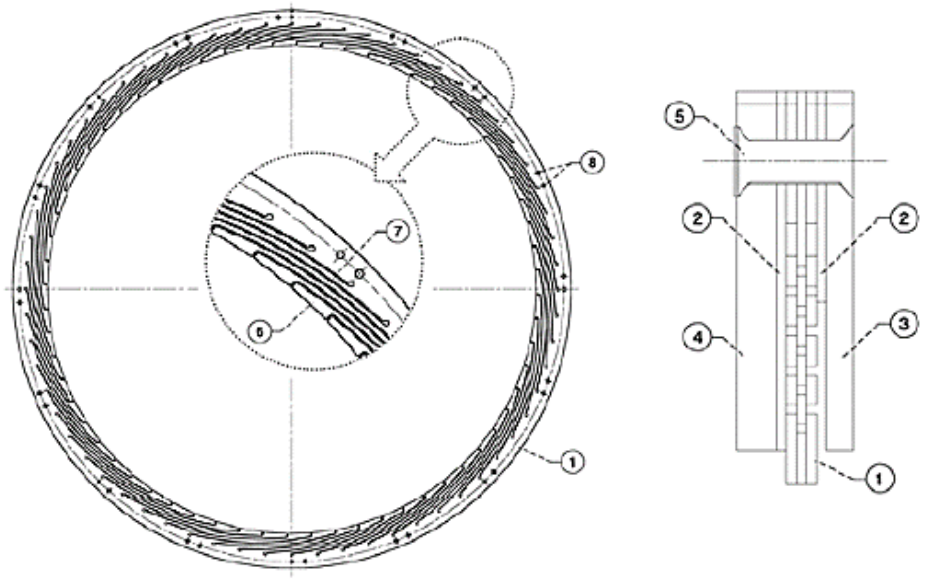

Figure 2.15: Finger seal assembly: 1 – finger element, 2 - spacer, 3 – forward cover plate, 4 – aft cover plate, 5 - rivet, 6 – finger contact pad, 7 – finger, 8 – indexing and rivet holes. From Proctor *et al.* [2002].

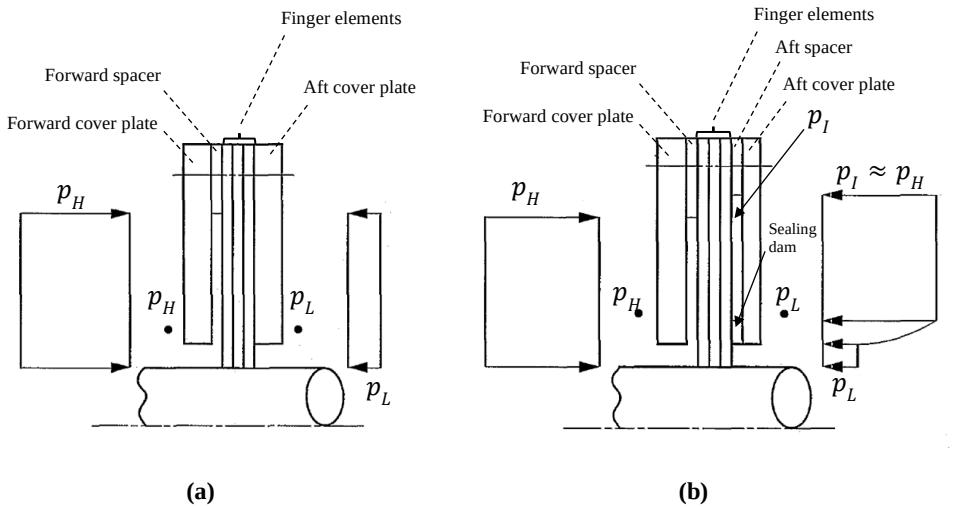

Figure 2.16: Comparison of the two finger seals presented by Arora *et al.* [1999]: (a) baseline seal and (b) pressure-balanced seal.

The problem of the leakage hysteresis was solved by reducing the area of contact between the aft plate and the downstream finger element. Figure 2.16 (b) shows this new configuration in which the aft cover plate is spaced from the finger element and a sealing dam is appended to the rear cover plate. In addition to a smaller area of friction with this configuration, the pressure between the downstream sealing element and the aft cover plate higher than the discharge pressure of the seal. The friction forces, which are proportional to both the pressure balance and the area of friction, decrease, allowing the fingers to deflect back to their initial position when the rotor speed decreases. The tests with the new pressure-balanced design showed the elimination of the hysteresis.

Run out tests were carried out with the objective of assessing the performance of the seal under transient conditions similar to those ones that occur in the engine, such as rapid acceleration and deceleration of the rotor and large rotor runouts. For a maximum rotor run out of 112 μm, the leakage and the wear of both the rotor and the seal were measured. The testing conditions were changed periodically from a rotor tangential speed of 288 m/s and pressure differentials as high as 5.5 bar to a rotor tangential speed of 237 m/s and a pressure differential of 2.0 bar.

In the same cyclic manner, an endurance test was performed with a brand new seal prototype for a total testing time of 120 hours, in this case with no eccentricity between the rotor and the stator. The wear of the rotor and the seal was checked after 60 hours and 120 hour of running time. Negligible wear of the rotor occurred in the second segment of the

endurance test, indicating that the interference between the rotor and the finger pad was approaching equilibrium.

The overall wear of the rotor during the run out test and the endurance test was 155 μm and 78 μm, respectively, and the authors claimed that this was an acceptable level of wear for use in a real engine. With respect to the leakage, the results obtained during static operation were similar to the values measured during both rotating tests. The authors reported a reduction of mass flow leakage raging between 20 and 70 percent to that of a see-through, four-knife labyrinth seal with 127 μm radial clearance.

Further testing was performed with the pressure-balanced seal by Proctor *et al.* [2002] at a maximum linear rotor speed of 366 m/s. The performance of the FS prototype was compared against a brush seal mounted with the same amount of interference with respect to the rotor for pressure drops of 0.7, 2.8 and 5.2 bar and temperatures of 700 and 922 K. No significant difference in power loss, mass flow leakage or wear was found between the two types of seals.

Arora [1998] patented the non-contacting finger seal of Figure 2.17. In this second version of the finger seal, a hydrodynamic pad was added to the fingers of both the upstream and downstream sealing layers, at the end of the fingers in contact with the rotor. The pad is designed so that the air, as it is moved by the rotor due to viscosity, generates a force that lifts the sealing element away from the rotor. The fingers are still in contact with the rotor at low rotational speeds. When the engine start up transient has been exceeded, the pads lift off and a positive clearance is created between the seal and the rotor. The decrease of torque loss due to friction and the reduction of seal wear would compensate for the increase of leakage due to a positive clearance.

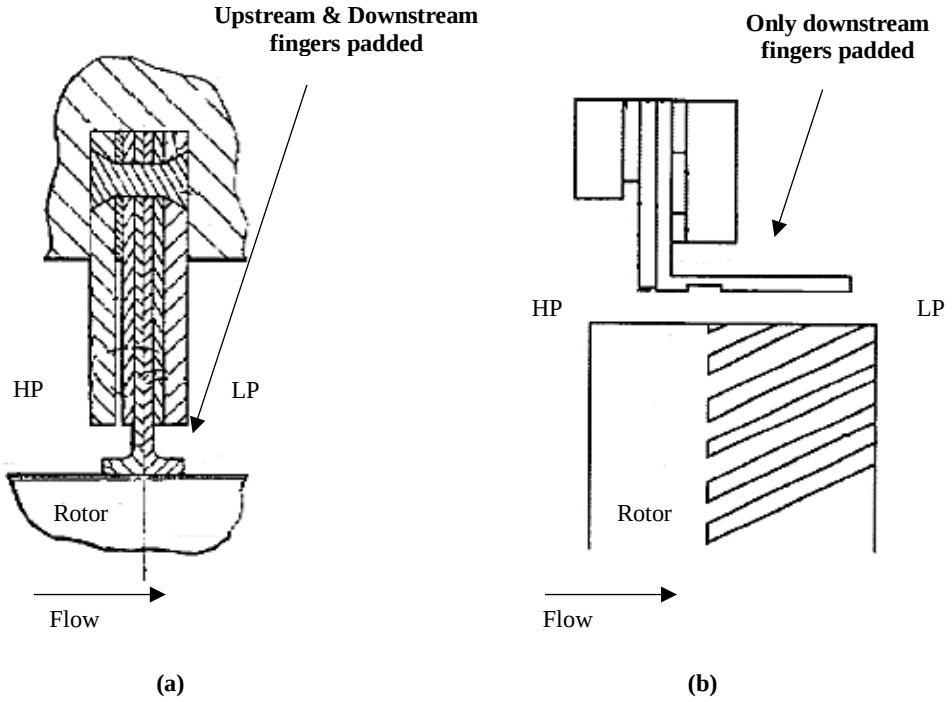

Figure 2.17: Comparison of two different non-contacting finger seal concepts (a) double-padded design by Arora [1998] and (b) single-padded design by Proctor and Steinetz [2004].

A second non-contacting finger seal patent, in which pads were only added to the downstream fingers was presented by Proctor and Steinetz [2004] and is shown in Figure 2.17 (b). As explained by the authors, the lifting forces on this pad would be negligible in comparison to the hydrostatic pressure field and, therefore, no benefit from the hydrodynamic effect was predicted.

Several numerical studies were performed to investigate the thermo-fluid characteristics of the non-contacting finger seal and the dynamic interaction between the rotor, the seal, and the film of fluid generated in between. Braun *et al*. [2003b] predicted the leakage of a finger seal with lift pads solving the Navier-Stokes equations in both 2D and 3D cases. The solution from the 2D case represents a lower limit for the leakage as this model does not have the secondary leakage path corresponding to interstices between fingers. On the other hand, the 3D model consisted of a pair of finger elements axially aligned, i.e. with the interstices between fingers of both upstream and downstream sealing elements not being staggered and, therefore, allowing the flow to leak through this secondary path. In turn, this implies that the solution from the 3D simulation sets an upper limit in the leakage flow prediction. These limiting cases are used for reference in further studies in which the geometry of the actual finger seal design with staggered interstices is modelled.

Braun *et al.* [2003b] performed CFD calculations on an angular segment of the finger seal design by Proctor and Steinetz [2004] featuring four high-pressure fingers and four low-

pressure, padded fingers staggered between each other (see Figure 2.18). For a rotor linear velocity of 216 m/s, it was reported that the effect of the rotation-induced pressure field was dominant at pressure drops smaller than 1.7 bar. Beyond this value, the effect of the hydrostatic pressure field dominates the hydrodynamic lift.

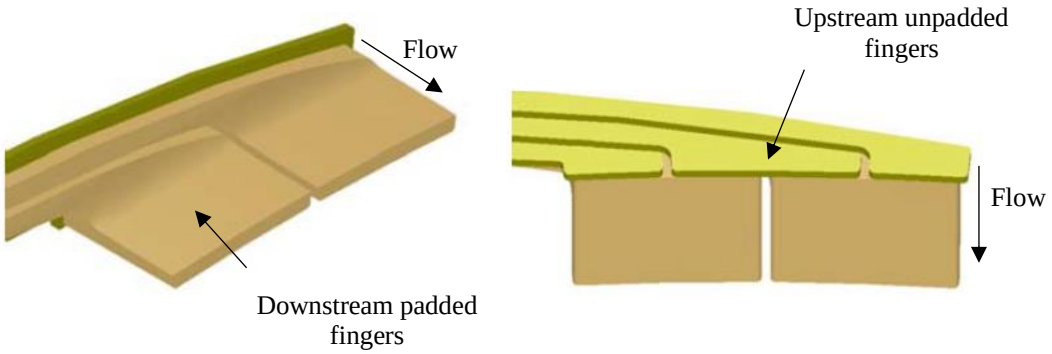

Figure 2.18: Modelled segment of the single-padded finger seal. From Braun *et al.* [2003b].

Additionally, Braun *et al.* [2003a] developed a one-degree-of-freedom dynamic model to estimate the dynamic response of the fingers under the movement of the rotor. The spring-mass-damper system, shown in Figure 2.19, models the fluid film by a linear spring and a viscous damper, and the finger beam by a linear spring. The fluid characteristics are calculated from the pressure results given by the CFD simulation coupled with a stress analysis tool that takes into account the movement of the finger.

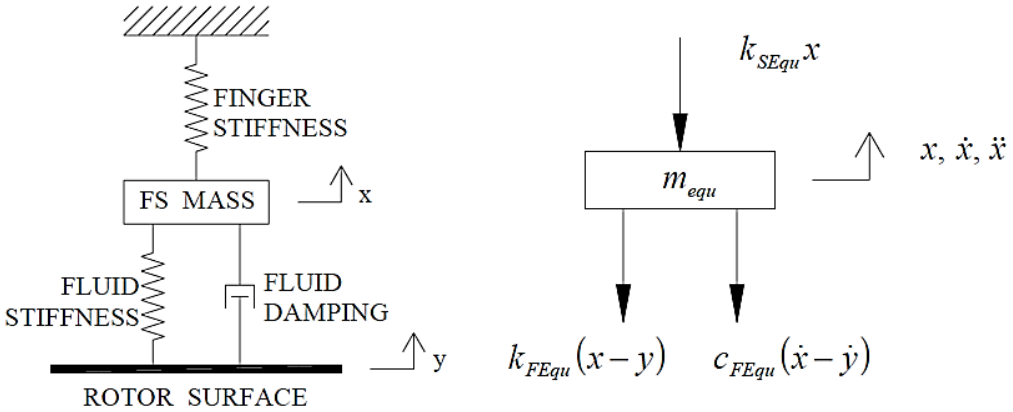

Figure 2.19: Dynamic model of the finger seal investigated by Braun *et al.* [2003a].

The main objective of this model was to find the relationship between the forced movement of the rotor (Y) and the reaction movement of the fingers (X). The results were expressed in terms of both phase lag and ratio of amplitudes (referred to by the authors as transmissibility = X/Y). The phase shift increased for low values of the fluid film (comparable to the stiffness

of the finger) and decreased for increasing values of the fluid damping. Regarding the transmissibility of the movement, the effect of the damping was negligible under a certain value. Combinations of small finger stiffness and high fluid stiffness yielded transmissibility values greater than one.

Braun *et al.* [2005] applied, to the same geometry and the same flow conditions of the study mentioned above, an upgraded dynamic model with two degrees-of-freedom, the motion of the rotor being the second degree of freedom. The friction between the back cover plate and the downstream seal layer is also introduced as a Coulomb effect that is proportional to the pressure drop applied to the seal and pushes the seal elements against the back plate. The main conclusion of this study was that a fine equilibrium has to be found between the Coulomb friction, the finger stiffness and the natural frequencies of both the rotor and the fingers, in order to have a finger seal design in which the fingers follow the movement of the rotor without delay. A good transmission of the movement of the rotor to the seal fingers is desired in other to prevent hysteresis in leakage flow.

Finally, Proctor and Delgado [2008] tested a prototype of the non-contacting FS design by Proctor and Steinetz [2004]; the seal featured padded fingers only in the downstream sealing wafer. Prior to installation in the testing rig, the measured clearance between the FS prototype and the rotating shaft at room temperature was 25.4 μm. Static and rotating tests were carried out during which the leakage performance of the seal was measured. During the static tests, it was realised that the rotor was not capable of spinning at certain pressure differentials, indicating contact between the rotor and the seal. Because of this, bind-up tests were done, in order to assess at which pressure differential the rotor was completely bound up by the seal. The rotor could free wheel up to 1.93 bar although the ease of turning had decreased at lower pressure drops. It was decided not to turn the rotor at pressure drops higher than 2.7 bar, in order to not damage the components. After this bind-up check, the dynamic tests were performed for a maximum pressure differential of 2.4 bar at a rotor tangential speed of 56 m/s and ambient temperature.

Hysteresis was found in the leakage measurements as the pressure drop was increased and decreased during the static test. This was again attributed to the friction forces stopping the fingers from springing back to their initial position. Contrary to the static test, this hysteresis was not present in neither the bind-up tests nor the dynamic tests, as in both cases there was rotation of the shaft which helped the seal settle at each tested pressure drop.

Leakage levels for the rotating test were found to be one third smaller than a straight four-tooth labyrinth seal and one half smaller than a brush seal at static conditions. The leakage and power loss of the non-contacting finger seal design were similar to the results obtained for the

contact finger seal version. According to the authors, the most important advantage of the non-contacting FS is the lack of wear found after 93 minutes of rotating testing indicating clearance operation of the seal for those conditions.

2.6 Positive-Installation-Gap Pressure-Actuated seals

All the seal designs described previously have a close clearance at the initial static conditions and, therefore, the risk of rubbing during engine start-up is high. It is only when the rotor starts rotating and achieves the critical speed at which the lift force is large enough to push the sealing elements away from the rotor that the seal works at its full performance. Once the rotor slows down, during engine shutdown, the risk of wear increases again.

The seals described in this section have a positive installation gap that closes towards the rotor as the pressure builds up in the system, thus, they are called pressure-actuated seals. Within this type of seals, two subgroups are found; those that have film-riding characteristics and those that do not.

2.6.1 Non-film-riding seals

Grondahl [2005] invented the PALS concept, which consists of bending leaves that close down to the rotor under the desired pressure level and keeps a larger clearance at starting/shut down conditions. A view of the PALS assembly is depicted in Figure 2.20. Support members are used as hard stops to prevent the leaves from deflecting too close to the rotor, which would cause high levels of wear and heat generation. The leaf thickness and material can be chosen such that the leaves deflect at the pressure loading required by each application.

Grondahl [2009] tested the PALS at static conditions. He proved the closing effect at the design pressure and the improved sealing effectiveness with respect to a four-tooth labyrinth seal. Figure 2.21 shows the PALS prototype under static testing at both non-deflected and closed positions. Bowsher *et al.* [2015] demonstrated the technology readiness of the PALS by performing tests in the Cross Manufacturing high speed rig. The seal showed its ability to tolerate radial offsets with small loss of performance. The seal kept operating consistently after an endurance test of 15 hours. Pasch and Stapp [2018] tested a new turbocompressor for supercritical carbon dioxide cycles featuring a PALS, thus demonstrating the performance of the adaptive seal in a relevant environment.

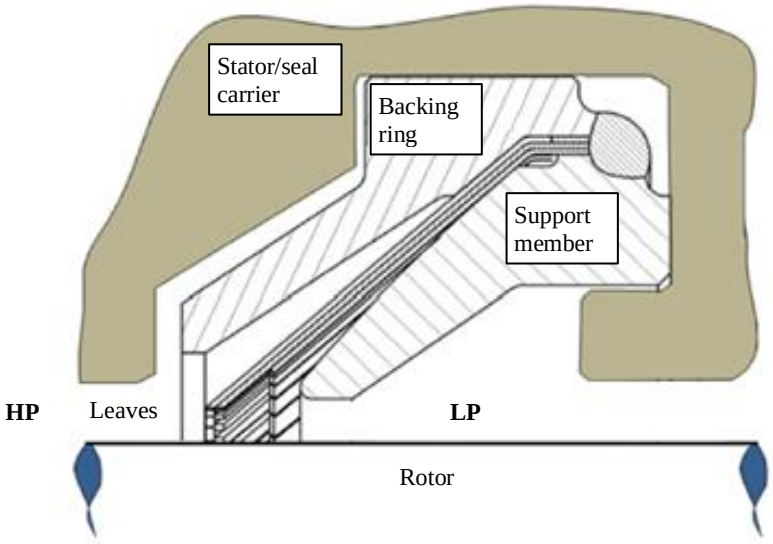

Figure 2.20: PALS section. From Bowsher et al. [2015].

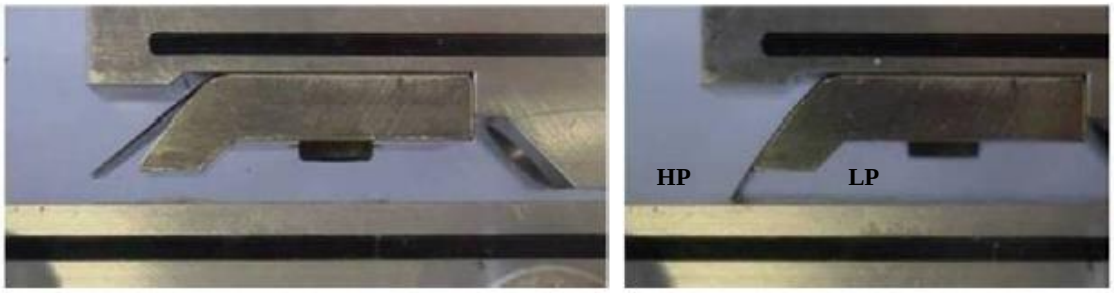

Figure 2.21: 2-D Pressure actuated leaf seal clearance change. From Grondahl [2005].

Herrmann *et al.* [2013] presented a flexible seal strip design which is similar to that of the PALS. A leaf element closes towards a support member when a pressure drop is created (see Figure 2.22). They also highlighted the need for support members to prevent the flexible strips from bending too much and touch the rotor. They performed CFD calculations on the three seals depicted in Figure 2.23; namely, a baseline staggered labyrinth seal and two different versions of a flexible seal combined with a labyrinth seal.

They concluded that the leakage of the baseline labyrinth seal was reduced, when using the first and second versions of the flexible seal by 14% and 40% respectively. They also proved that the radial deflexion of the strips was beneficial in terms of wear as the flexible fins showed almost no deformation after rub with the rotor when compared with the deformation of the fixed fins of the standard labyrinth seal.

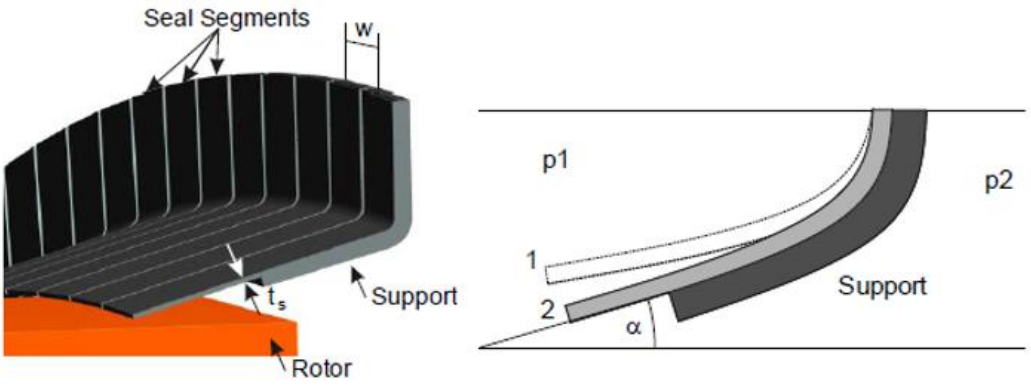

Figure 2.22: Segmented seal fins with support. From Herrmann *et al.* (2013).

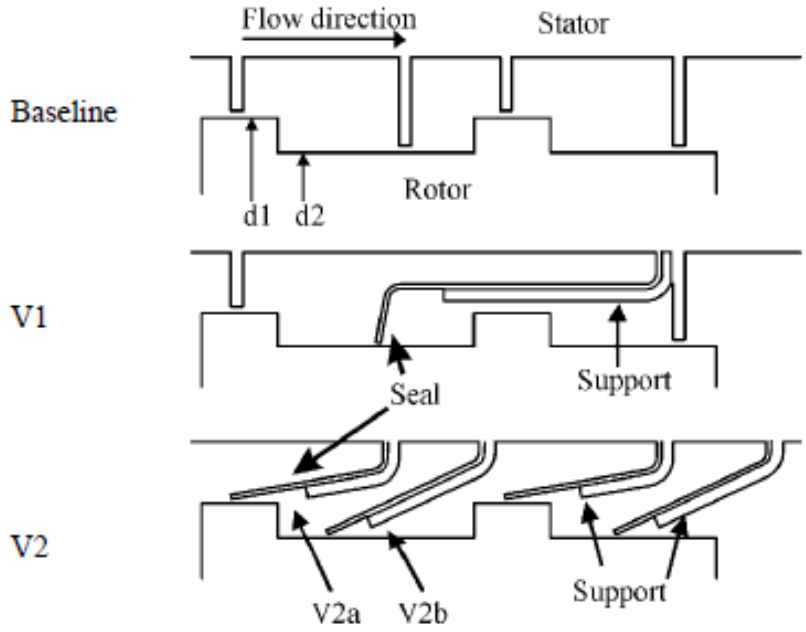

Figure 2.23: Investigated seals by Herrmann *et al.* (2013).

2.6.2 Film-riding seals

Justak and Doux [2009] presented the concept of a non-contacting, self-acting seal for control of the turbine blade tip clearance. This new concept is referred to as Compliant Outer Air Seal (COAS) and is similar in architecture to the HBS shown in Figure 2.14 (c). The segments are attached to the stationary part through flexible beams that allow radial movement of the sealing surface; this arrangement can be seen in Figure 2.24. One of the main differences between this novel seal and its precursor, the HBS, is that instead of a bristle pack, flexible metal walls are used upstream and downstream of the cantilevered pads in order to stop flow

leaking through the cantilever beams. Additionally, this new version of the seal is designed to have a positive installation clearance. Figure 2.25 shows a cross section of the assembly of the seal where the main components are the compliant segments that provide primary sealing in the rotor-seal interface and the secondary seals at both ends of the segments.

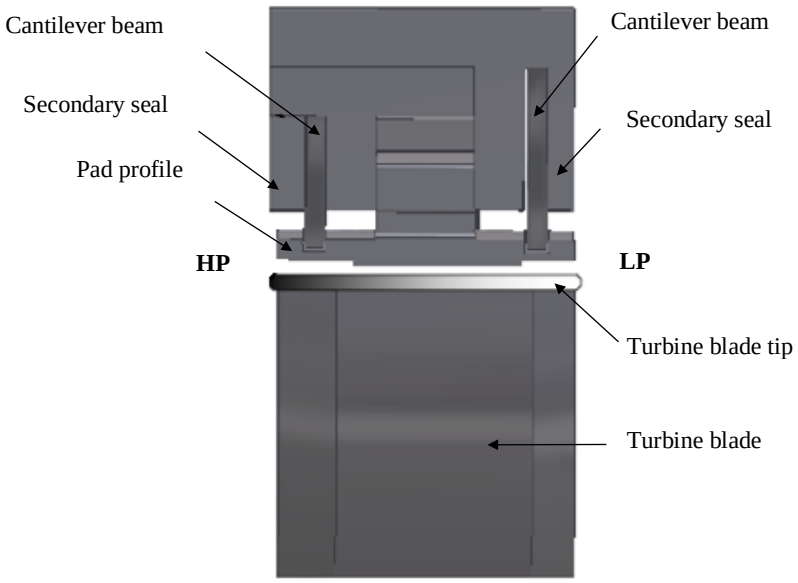

Figure 2.24: Cross section of the COAS investigated by Justak and Doux [2009] for turbine blade tip sealing applications.

CFD simulations of the clearance between the rotor and the seal confirmed the importance of the geometry of the segments on the pressure distribution and, therefore, for the balance of the forces controlling the position of the segments with respect to the rotor. Static experiments (no rotation) were carried out for maximum pressure differentials across the seal of 2.5 bar. The clearance decreased by 84 μm from the installation value when a pressure drop of 0.7 bar was applied.

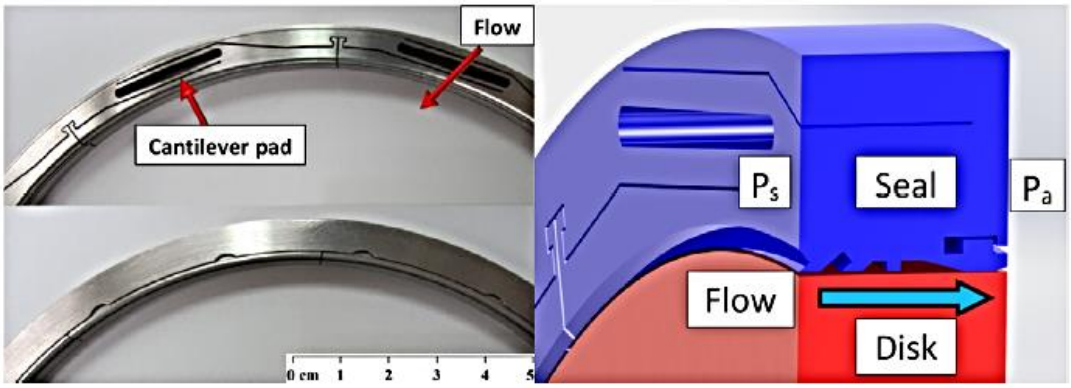

Figure 2.25: Front and back views of a Hydrostatic Advanced Low Leakage (HALO) seal and schematic view of the thru flow. From San Andrés and Anderson [2014].

San Andrés and Anderson [2014] tested a prototype of the self-acting seal described above for shaft sealing applications, referred to as the Hydrostatic Advanced Low Leakage (HALO) seal, and compared the results with a straight labyrinth seal with three teeth and an axial length of 8.40 mm. For a pressure drop range of 0-3 bar and a range of seal inlet gas temperatures of 303-573 K, they measured the leakage performance of the seals under investigation for both static and rotating conditions. The results showed how the flow factor corresponding to the HALO seal decreased as the pressure drop increased. This confirmed that the HALO seal self-acts and adapts its clearance as the applied pressure difference changes.

More recently Beerman *et al.* [2018] tested a HALO seal in order to assess the performance of the seal under changing conditions of inlet flow pre-swirl velocity, eccentricity between the rotor and the stator and rotor tangential speed. They concluded that the seal clearance is reduced by up to an 80% of the installation gap under the effect of the pressure drop across the seal. The gap then stabilised when further increasing the pressure difference. Hysteresis was found in the gap height when pressurising and depressurising for low values of the pressure drop, but not in the stable range of operation.

No changes in equivalent gap height were found for eccentricities lower than the installation clearance and no contact between the rotor and the stator was found, even at high pressure drops. However, eccentricities of the order of the installation gap caused permanent rotor-stator contact. No effects of rotational speed were found; this was attributed to the ability of the seal to accommodate the rotor growth due to centrifugal stresses. Finally, the leakage rate of the HALO seal was greater than that of a baseline labyrinth seal with a 450 μm radial clearance, which was justified as the HALO seal had a secondary air leakage path and the clearance of the labyrinth seal was small.

Messenger *et al.* [2015] presented the design of an aerostatic seal consisting of a pocket damper seal split in several segments, to allow for movement. Springs are used to link the segments together at the split locations to prevent the seal from touching the rotor when no pressure drop is applied to it. The segments, referred to as glands, float around the rotor and the clearance of the seal is determined by the equilibrium of the pressure forces, weight and friction forces acting on them. The cross section of a gland is shown in Figure 2.26, and it is similar to that of a labyrinth seal with three cavities. One of the main differences with respect to a labyrinth seal are that the cavities are not uniform in length; they are custom sized to tune the pressure forces. Additionally, the central cavity is connected to the upstream pressure level by a feed hole. This provides a means of regulating the pressure in the cavity and, hence, the clearance of the seal.

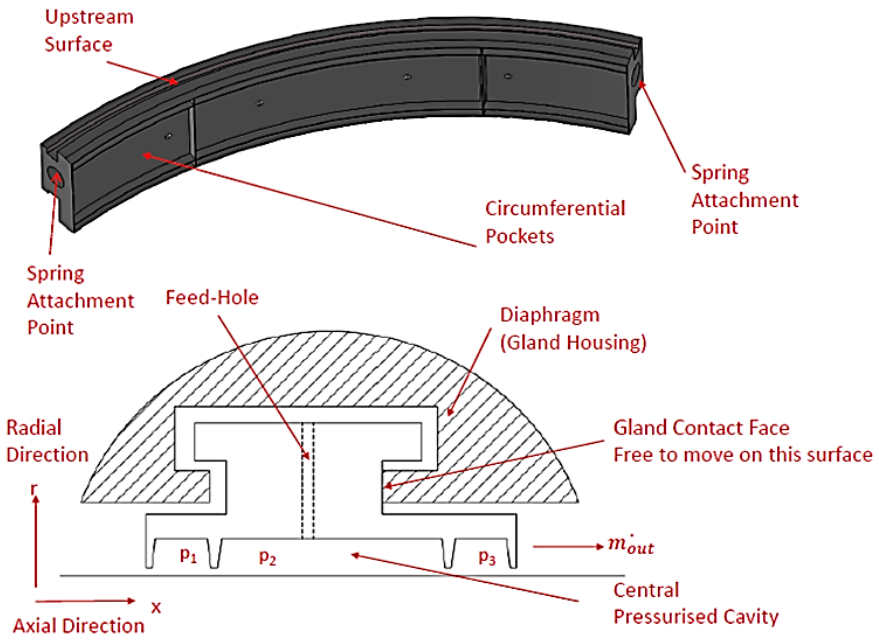

Figure 2.26: Key features of the segment and cross section of the aerostatic seal. From Messenger *et al.* [2015].

Experiments designed to accommodate one seal segment with no rotor rotation were performed by Messenger *et al.* [2016]. It was demonstrated that the seal has the ability to adapt its clearance under the effect of varying pressure drops. In addition, unlike retractable gland seals, the clearance increases not only when the pressure load is relieved, but also for increasing pressure drops. Tests with different levels of lubrication between the moving gland and the stationary wall highlighted the large effect that the friction forces have on the clearance of the seal.

Messenger *et al.* [2017] presented the experimental data of a complete aerostatic seal prototype, tested in a rotating rig. Tests at two levels of rotor eccentricity for rotational speeds of up to 1,500 rpm demonstrated the ability of the seal to follow fast rotor transients. Non-axisymmetric operation of the seal was indicated by the average clearance of each seal segment varying above and below the average rotor eccentricity. Mass flow rate data for the seal with the segments position locked and the feed holes blocked indicated potential for a 35% leakage reduction when compared to measurements from a labyrinth seal.

A final endurance experiment of five days was carried out in a steam rotating test facility by Messenger *et al.* [2019]. For a rotational speed of 8,760 rpm, an inlet pressure of 7.5 bar, and a steam temperature of 773 K, the relative position between the casing and the rotor was altered in order to reproduce the rotor excursions occurring in a full-scale turbine. The authors

concluded that for the increased levels of friction associated with the high steam temperatures, the seal segments moved to follow the rotor as expected from tests in an air environment.

The PALS concept evolved towards the second generation of pressure actuated seals. This second version was patented by Grondahl *et al.* [2011] under the name of the Film Riding Pressure Actuated Leaf Seal (FRPALS). A sectioned view of the FRPALS concept is shown in Figure 2.27. This seal features hydrodynamic runners at the tips of the leaves which ride over the thin film of fluid created between the rotor. The FRPALS profits from both the improved behaviour at transient conditions of the PALS and the adaptive capacity of compliant seals.

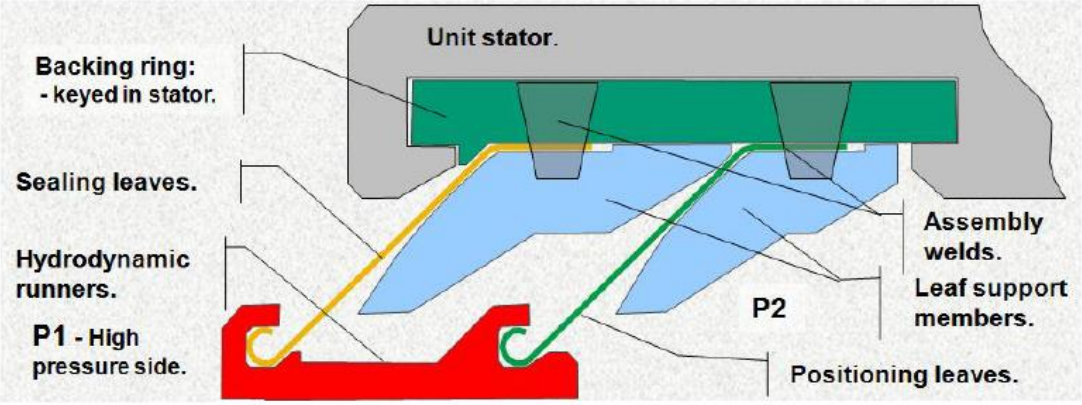

Figure 2.27. FRPALS section. From Grondahl and Dudley [2010].

Grondahl and Dudley [2010] presented a parametric study of the FRPALS. They described the results of the design process of the runner geometry needed to develop the desired hydrostatic forces that contribute to the overall forces acting on the seal elements and, therefore, that generate a balanced seal performance for rub avoidance. This design process resulted in the runner surface featuring a Rayleigh step that generates a force opposed to the pressure forces on the leaves. They also planned static and dynamic test campaigns needed to, firstly, validate the seal operation and, secondly, optimise it.

Kirk *et al.* [2016] presented the results of the first static FRPALS tests performed at Cross Manufacturing. They used a large scale, 2-dimensional, linear sealing segment fitted in test set up of Figure 2.28: a custom test rig designed with the ability of creating an eccentricity between the seal and the reference surface. The base plate acting as the rotor in the 2-D model was instrumented with four proximity probes and fourteen static pressure ports, in order to track the movement of the runner and the pressure distribution of the fluid thin film.

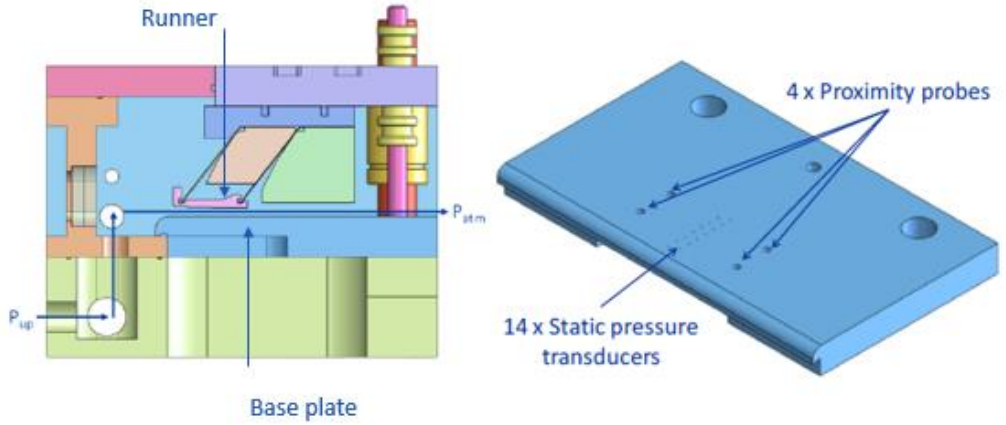

Figure 2.28. Cross section of the FRPALS static rig and close-up of the instrumented base plate under the runners. From Kirk *et al.* [2016].

The test showed stable operation of the seal even at the closure event of the leaves. The hysteresis of the leaves when depressurising the chamber was measured to be small. This can be seen in Figure 2.29 which shows the clearance change during both pressurising and depressurising processes. The pressure of the thin film between rotor and runner in the axial direction (flow direction) is shown in Figure 2.30. It was found to be the same as the upstream pressure level along the clearance region. At the Rayleigh step, where the clearance narrows, the pressure dropped and plateaued before reaching the film riding area. In the film riding surface, the pressure further decreased in a non-linear manner until reaching the imposed downstream pressure of atmospheric conditions.

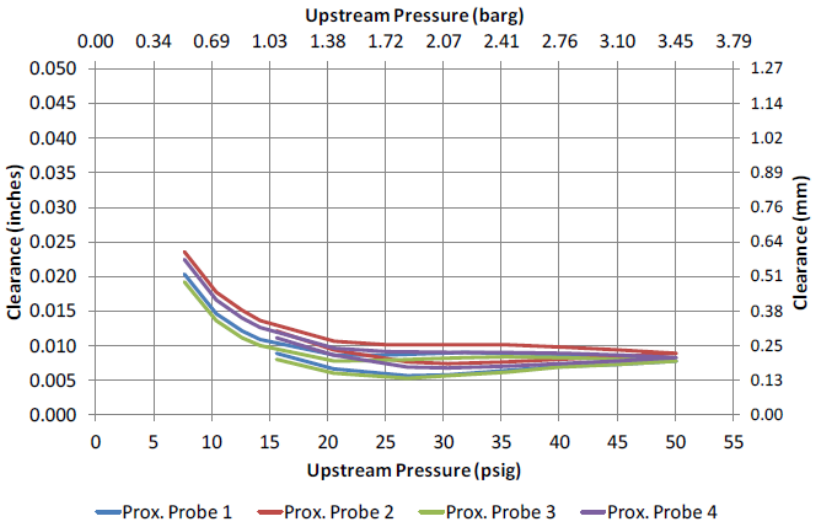

Figure 2.29. Runner clearance vs. upstream pressure. From Kirk *et al.* [2016].

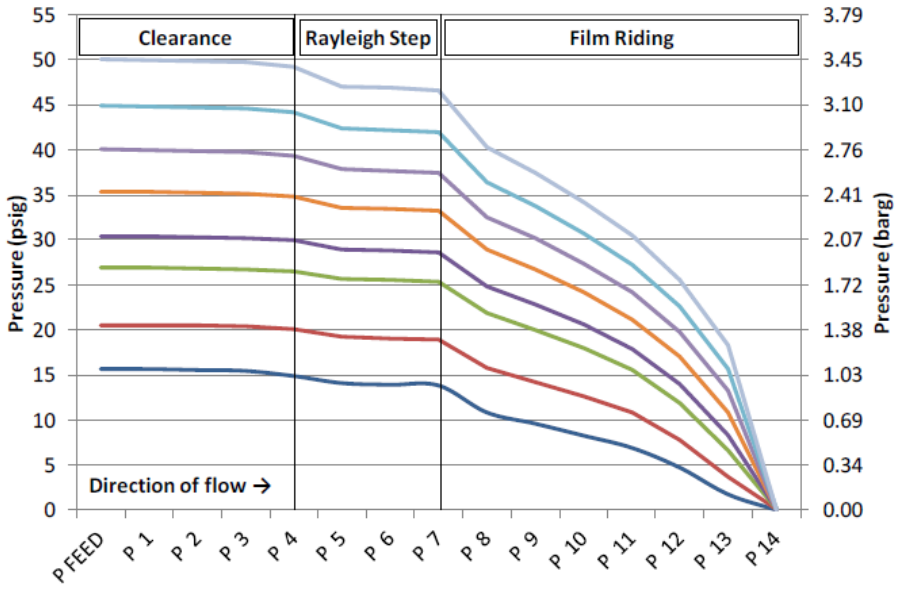

Figure 2.30. Pressure distribution across the runner for various upstream pressures. From Kirk *et al.* (2016).

2.7 Conclusions from literature review

The trend is to use designs with moveable parts that allow radial displacement of the sealing elements to accommodate to varying clearances. These new seal designs normally film ride or, in other words, exploit the leakage flow as a cushion between the rotor and the seal. The film-riding effect comes from the hydrostatic or hydrodynamic pressure fields created by the leakage flow as it passes through the clearance gap. These pressure forces counteract the spring-like forces of the flexible parts that push the sealing elements towards the rotor to close the leakage path.

Hydrostatic lift is preferred over hydrodynamic lift as the former is not dependant on rotation. Additionally, seals with an initial positive installation clearance have better performance at start-up; for instance, they experience zero breakaway torque and lack of initial wear.

For film-riding seals, whether they rely on either hydrostatic or hydrodynamic forces to keep the sealing elements away from the rotor, the fine balance of the forces acting on the sealing elements is crucial for the performance of the seal. The geometry of the seal pads plays a key role on this fine equilibrium of forces and, as such, is a powerful tool for the designer to tune in the behaviour of the adaptive elements. Geometric features such as steps or convergent/divergent channels are used to change the pressure distribution around the seals' pads. CFD is used to better understand the flow features associated with these geometries.

During the advancement of new sealing technologies, researchers use mass flow rate data from a see-through labyrinth seals as a benchmark for the leakage performance of the novel seal design.

Clear parallels have been found in the development of different adaptive seals; the successive steps are normally followed:

- **Stationary tests**: A first pressurisation of the seal is made in order to assess whether the seal touches the rotor or not. If needed, changes in the design are applied. This also allows the behaviour of the seal in the absence of hydrodynamic forces to be studied.
- **Short rotating tests with centred rotor**: Once it is determined that a positive clearance exists between the moving elements and the rotor for the whole range of pressure drops tested, rotation can be introduced.
- **Endurance rotating tests with simulated clearance changes**: The leakage performance and the clearance height are monitored for long periods of time to investigate the endurance performance of the seal. The clearance variations expected in a real engine are simulated to determine the adaptability of the seal. Once the test has finished, the seal and the rotor are inspected and wear marks are measured.

Table 2.1 shows the seals discussed in this literature review and provides their leakage performance relative to a reference seal (labyrinth seal or brush seal) together with the conditions at which they were tested and the chosen references from which the data has been extracted.

Table 2.1. Different sealing technologies

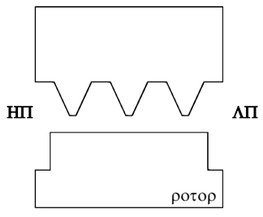	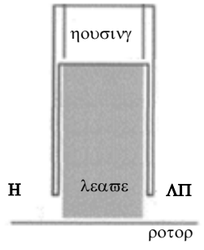	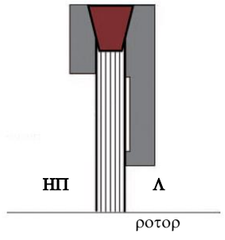	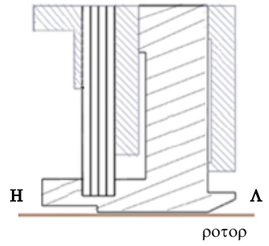	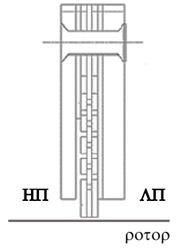	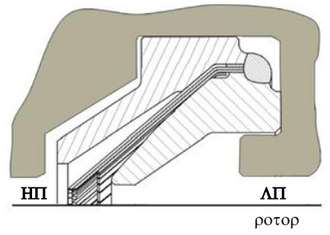
Labyrinth Seal	Leaf Seal	Brush Seal	Hybrid Brush Seal	Finger Seal	Pressure Actuated Leaf Seal
	Nakane *et al.* [2004] – concept & tests $\Delta p = 3\ bar$ $Rotor\ surface\ speed = 102\ m/s$ $T = T_{AMBIENT}$ $\dot{m}/\dot{m}_{REF\ LABY} = 0.3$	Ferguson [1988] – concept & tests $\Delta p = 12\ bar$ $Rotor\ surface\ speed = 300\ m/s$ $T = 923$ $\dot{m}/\dot{m}_{REF\ LABY} = 0.1$	San Andrés *et al.* [2009] – tests $\Delta p = 2\ bar$ $Rotor\ surface\ speed = 11\ m/s$ $T = T_{AMBIENT}$	Arora *et al.* [1999] – concept Proctor & Delgado [2004] - tests $\Delta p = 5.2\ bar$ $Rotor\ surface\ speed = 366\ m/s$ $T = 922\ K$ $\phi/\phi_{REF\ BRUSH} = 0.5$	Grondahl [2005] - concept Bowsher *et al.* [2015] - tests $\Delta p = 8.2\ bar$ $Rotor\ surface\ speed = 143\ m/s$ $T = T_{AMBIENT}$

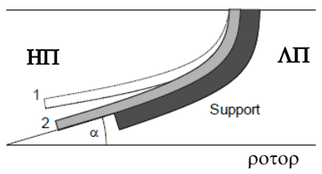	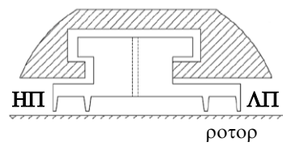	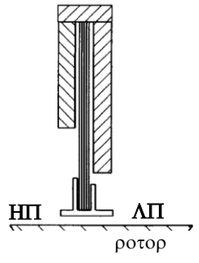	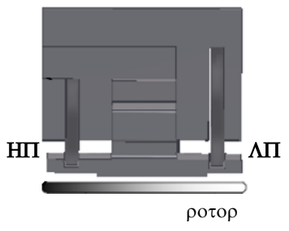	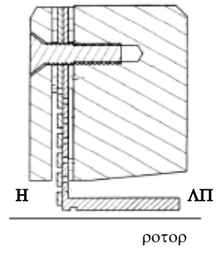	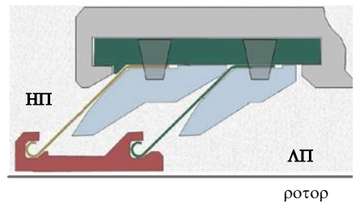
Flexible Strip Seal	Aerostatic Seal	Shoed Brush Seal	Hydrostatic Advanced Low Leakage Seal	Non-Contacting, Padded Finger Seal	Film-Riding Pressure-Actuated Leaf seal
Hermann *et al.* [2013] – concept and tests $\Delta p = 3\ bar$ $Rotor\ surface\ speed = 165\ m/s$ $T = T_{AMBIENT}$ $\frac{\Delta\dot{m}}{\dot{m}_{REF\ LABY}} = 0.43$	Messenger *et al.* [2015] - concept Messenger *et al.* [2019] – tests $\Delta p = 1.5\ bar$ $Rotor\ surface\ speed = 24\ m/s$ $T = 773\ K$	Justak & Crudgington [2006] –concept & tests $\Delta p = 3.5\ bar$ $T = T_{AMBIENT}$ $e/e_{REF\ BRUSH} = 1$	San Andrés & Anderson [2014] $\Delta p = 3\ bar$ $Rotor\ surface\ speed = 24\ m/s$ $T = T_{AMBIENT} - 573\ K$ $\phi/\phi_{REF\ LABY} = 0.3 - 0.5$	Proctor & Delgado [2008] – concept and tests $\Delta p = 5.7\ bar$ $Rotor\ surface\ speed = 56.5\ m/s$ $T = T_{AMBIENT} - 700K$ $\phi/\phi_{REF\ LABY} = 0.3$	Grondahl & Dudley [2010] - concept Kirk *et al.* [2016] – static tests $\Delta p = 3.5\ bar$ $Rotor\ surface\ speed = 0\ m/s$ $T = T_{AMBIENT}$

Chapter 3: Design of a Test Facility for Turbomachinery Seal Research

The need for high performance, long life seals has been introduced in Chapter 1 as the motivation of this research. Additionally, the significant efforts that have been made since the 1980's towards the development of new shaft sealing technologies has been summarised in Chapter 2. After a new seal design is conceived it must then undergo a rigorous validation process. This technology development is necessary to prove the correct operation of the concept under the severe conditions to which it will be subjected in the target application. Performing this process in a real engine is expensive and, therefore, the technology readiness of new seals is advanced in facilities capable of simulating some of the operating conditions of real machines, such as pressure, speed, temperature and size.

This chapter describes the design of a new research facility which experimentally investigates different seals for turbomachinery environments. The new facility is a high speed, rotational rig conceived to prove the operation of the FRPALS at engine-like conditions. The rig has also been designed to accommodate various seal concepts; this versatility allows for the comparison of performance of new and existing sealing technologies.

As the main feature of the FRPALS is to maintain a close clearance between rotor and stator during steady state engine operation, the rig must be able to reproduce the misalignments of the rotor relative to its centre found in gas turbines. The rig is designed such that the mass flow rate of air passing through the seal under investigation is collected and measured.

The rig is also designed to experimentally measure the rotordynamic coefficients of the seal. The rotordynamic coefficients are necessary to implement modelling tools used in early design stages, and also to understand the seal behaviour and hence to optimise it.

In the following sections, existing rotor-stator test rigs are reviewed and the concept of the new rig is presented, together with the dimensions and parameters that were specified by Cross Manufacturing and that represent the inception of the rig design. The design of the major subassemblies of the rig is then explained. Appendix B shows several photographs of the testing facility and the overall dimensions of the assembly.

3.1 Existing test rigs for rotor-stator seals

A summary of the key capabilities of the facilities found in the literature for shaft seals research is presented in this section. The maximum supply pressure to the testing seal and the ability of the rig to generate a back pressure is discussed, and whether they are high temperature rigs or if they work at ambient temperature levels. The diameter of the rotor and the maximum rotational speed are also stated together with the resulting rotor surface speed and the ability of the rigs to generate pre-swirl or not. Finally, the arrangement of the testing seal is depicted, i.e. whether there is a double seal arrangement or a single seal configuration, and their ability to simulate radial offsets is analysed. A sketch of their cross section is shown, if available.

The search has been limited to test rigs for gas turbine applications. The existing test facilities have been divided into two different groups according to the criterion of being capable of measuring rotordynamic coefficients or not.

3.1.1 Test rigs for the characterisation of shaft seals

Nakane *et al.* [2004] tested a leaf seal mounted in a double seal rotating rig (see Figure 3.1). The air at room temperature is supplied radially between the testing seal and a baseline, small gap labyrinth seal. The inlet air mass flow and the mass flow through the lab seal are measured; the leaf seal leakage is the difference between the two. The 350 mm diameter rotor is spun up to a maximum of 5,000 rpm by a motor fitted with a gearbox, resulting in an outer diameter tangential speed of 92 m/s. The pressure differences applied to the seal ranged from 0 to 4 bar.

The applied torque to the rotor was also recorded as a measurement of the seal power loss, due to both windage and friction between the leaves and the rotor. The authors used an electrical circuit to determine at which operating conditions the leaves lift-off the rotor, and tested different seal configurations to investigate the effect of the gap between the cover plates and the leaves. The stiffness of the leaves was also measured by pushing the seal against the rotor and measuring both the displacement of the movement and the applied force.

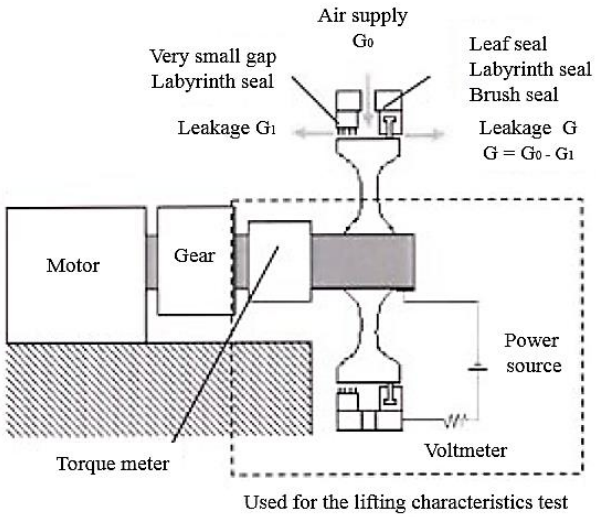

Figure 3.1: Cross section of the seal rotating test device used by Nakane *et al.* [2004].

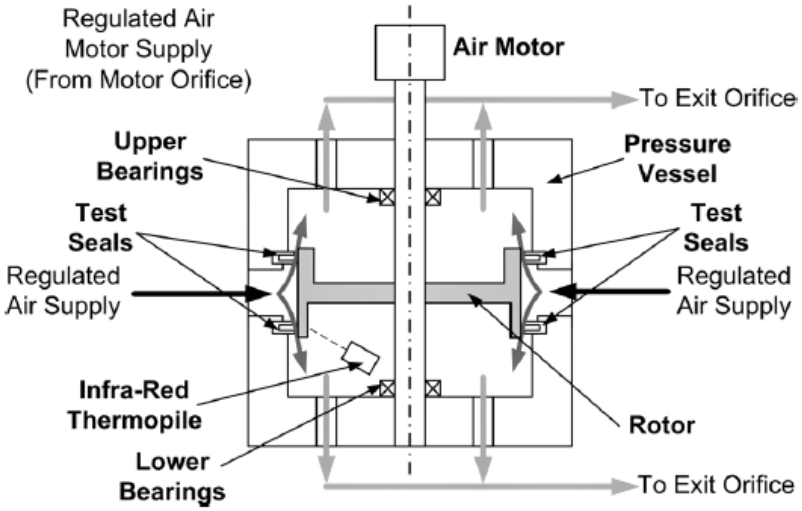

Figure 3.2: Schematic diagram of the Oxford Engine Seal Test Facility. Pekris *et al.* [2015].

The Oxford Engine Seal Test Facility, represented in Figure 3.2, has been used for the characterisation of brush and leaf seals. In this rig, two identical seals are symmetrically fitted to the rotor outer surface and the air is introduced radially between both seals via a buffer vessel at ambient temperature. The rig was designed to create engine representative pressure differences across the seals of 11.5 bar. Jahn *et al.* [2008] used a low speed version of the rig with rotational speeds ranging between 0.3 and 13 RPM.

In the upgraded configuration of the rig used by Pekris *et al.* [2015], the maximum rotation speed was 7,000 rpm. Given the rotor diameter of 300 mm, the maximum rotor peripheral speed is 110m/s. It is possible to move the casing radially and axially relative to the fixed rotor

in order to reproduce the eccentricities that the seal may experience in service. The range of these offsets is ±2.5 mm at speeds of 8 mm/s for both directions, which gives a frequency of the movement of 1.6 Hz.

Proctor *et al.* [2002] conducted tests in the NASA High Temperature, High Speed Turbine Seal Test Rig (see Figure 3.3). This turbine test rig consists of a 215.9 mm diameter rotor around which a single finger seal is located. The seal is axially fed with air at temperatures of up to 922 K from an upstream pressurised plenum. The maximum pressure drop across the seal is 5.2 bar and the maximum rotational speed is 32,000 rpm (365 m/s of maximum tangential speed at the rotor outer diameter). Measurements of mass flow rate at different pressures, temperatures, and rotational speeds were taken. Endurance and wear tests were also performed, in which the wear mark left on the rotor by the seal was measured and the loss of material in the seal was tracked.

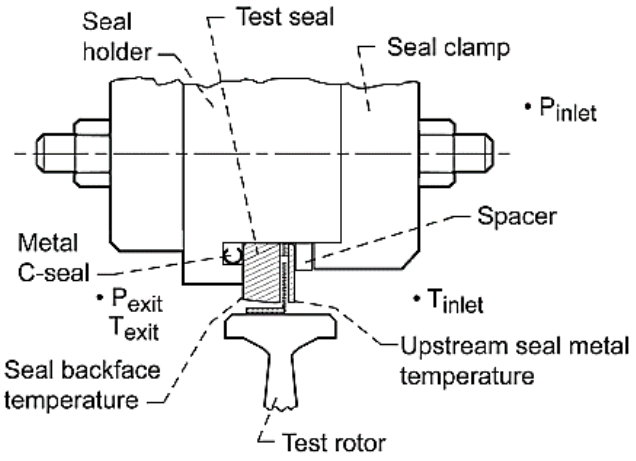

Figure 3.3: Schematic of the NASA High Temperature, High Speed Turbine Seal Test Rig test section. Proctor *et al.* [2002].

Beermann *et al.* [2015] presented the design of a new high-speed rotating test rig for adaptive seals at the Karlsruhe Institute for Technology. The rig, shown in Figure 3.4, hosts a single seal and has an air supply system that introduces the flow both radially and tangentially at a temperature of 330 K. This allows the inlet tangential velocity of the flow to be varied so that pre-swirl can be studied. A maximum pressure of 9 bar can be supplied to the upstream side of the testing seal, while the downstream side can be subjected to a maximum back pressure of 4 bar. The tangential speed of the rotor outer surface is 280 m/s, which for a rotor diameter of 290 mm yields a maximum rotating speed of 9,200 rpm. The casing can be traversed ±3 mm radially at 6 mm/s (1 Hz) and ±10 mm axially at 175 mm/s (8.75 Hz), in order to simulate rotor/stator movements due to temperature changes. Beermann *et al.* [2018] used this rig to experimentally investigate a HALO seal. They measured the leakage and rotor-

to-seal gap under different pressure drops, rotational speeds, static eccentricities and pre-swirl levels.

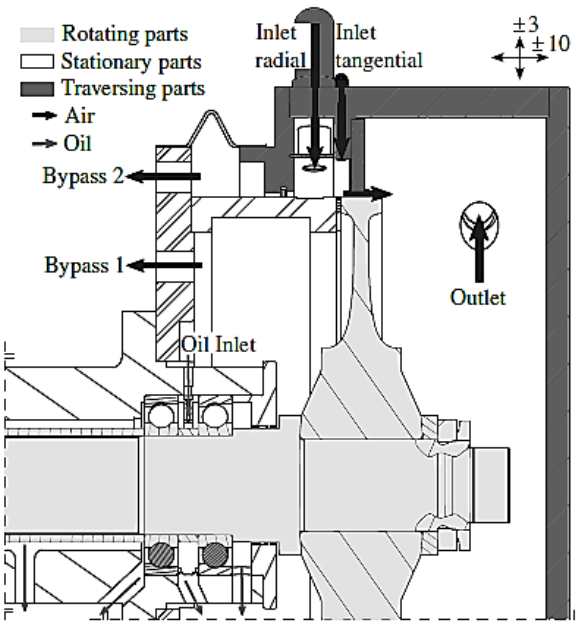

Figure 3.4: Karlsruhe rig test section. Beermann *et al.* [2015].

Intensive testing programmes have been carried out at Cross Manufacturing in order to develop the state-of-the-art of the brush seal technology; this has been achieved by means of two single-seal arrangement testing facilities. The first rig was presented by Flower [1990] and is known as the cold rig as the air is supplied at ambient temperature. It features a 130 mm diameter rotor that can rotate at speeds of up to 21,000 rpm (143 m/s tangential speed). Crudgington [2001] described the second rig, or so-called hot rig, which is able to rise the inlet air temperature up to 893 K. The rotor has a diameter of 190 mm and can rotate at a maximum speed of 38,500 rpm (380 m/s surface speed). Both rigs use the same air delivery system, which is able to supply flow to the test section from 1 to 20 bar. The bristle blow down phenomenon or the effect of fence height in brush seals has been investigated by means of mass flow rate measurements at different pressure drops and rotating speeds.

Deo [2012] at GE Global Research used the dual seal arrangement test rig shown in Figure 3.5 to investigate the behaviour of compliant plate seals. High pressure, room temperature air is supplied to the test section through a swirl plate that can adjust the inlet swirl conditions to the testing seal. The maximum pressure to the upstream cavity is 35 bar and the leakage air is discharged to a downstream chamber, where the pressure is regulated to balance the axial thrust on the bearings. The rotor has a diameter of 80 mm and can rotate in forward and reverse direction at maximum rotating speed of 10,000 rpm (68 m/s surface speed). Slow and fast (1/rev) radial transients can be reproduced by moving the stator housing.

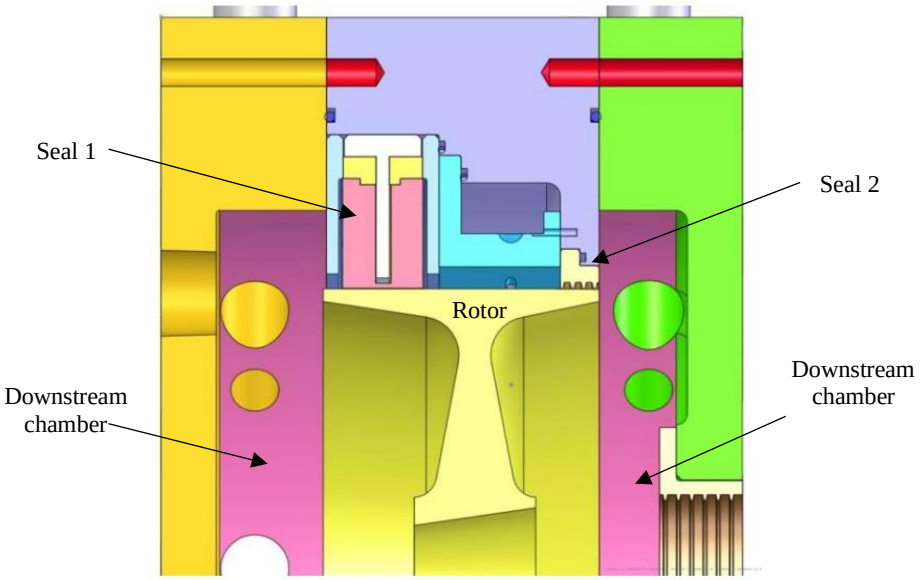

Figure 3.5: Cross section of the GE Research Subscale rig. Deo [2012].

3.1.2 Test rigs measuring rotordynamic coefficients

There are two test rigs at the Technical University of Munich for the investigation of the rotordynamic behaviour of shaft seals. Gaszner *et al.* [2013] tested a combined brush-labyrinth seal using both rigs, which have a double seal configuration and work at ambient temperature. The air is supplied to the test section both radially and tangentially. The main difference between the two rigs is the way the rotordynamic coefficients are measured.

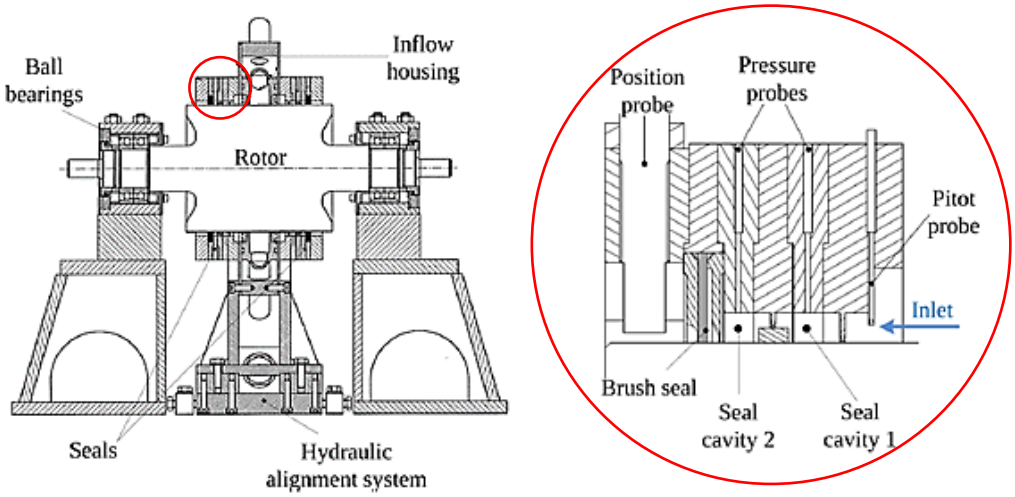

Figure 3.6: Cross section of the non-whirl seal rig at TU Munich. Gaszner *et al.* [2013].

The first rig is shown in Figure 3.6 and is referred to as the non-whirl rig, as the rotor is rigidly mounted on ball bearings. A maximum rotor tangential speed of 113 m/s can be

achieved with the 180 mm diameter rotor spinning at a rotational speed of 12,000 rpm. Static offsets are imposed between the rotor and the stator by changing the position of the seal housing with the hydraulic system shown in Figure 3.6. The force coefficients are calculated by integrating the pressure distribution measured along the circumference of the seal at the cavities between seal restrictions. This method only provides local values of the stiffness coefficients, i.e. force coefficients due to pressure changes in the seal cavities, but not due to the effects of the bristles.

Figure 3.7 shows the so-called whirl rig. The rotor is supported by journal bearings that allow for elastic deformation of the shaft and, hence, for whirl to occur. The amount of rotor whirl is controlled by regulating the distance between bearings. A magnetic actuator actively excites the rotor and the changes in current needed to adjust the motion of the rotor are measured to quantify the applied force. This force together with measurements of rotor displacement yield the rotordynamic coefficients of the seal. For safety reasons, this rig is operated at a maximum rotating speed of 1,400 rpm and a maximum inlet pressure of 4 bar.

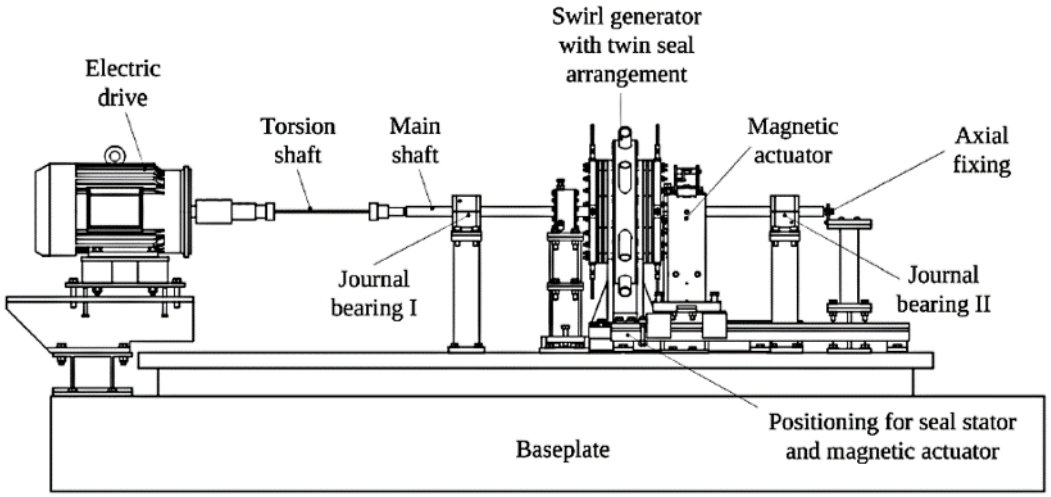

Figure 3.7: Cross section of the whirl seal rig at TU Munich. Gaszner *et al.* [2013].

The cross section of the rig used by San Andrés *et al.* [2009] at Texas A&M University to test hybrid brush seals is shown in Figure 3.8. It featured a single seal arrangement, to which the air was supplied axially from a plenum at pressures ranging from 1 to 3 bar and ambient temperature. The bore diameter of the seals tested in this rig was 167.1 mm and the maximum rotational speed was 1,300 rpm, which translates to a maximum tangential speed of 11 m/s. The overhanging rotor was driven directly by a DC motor and its free end is connected to an electromagnetic shaker used to measure the rotordynamic coefficients of the seal.

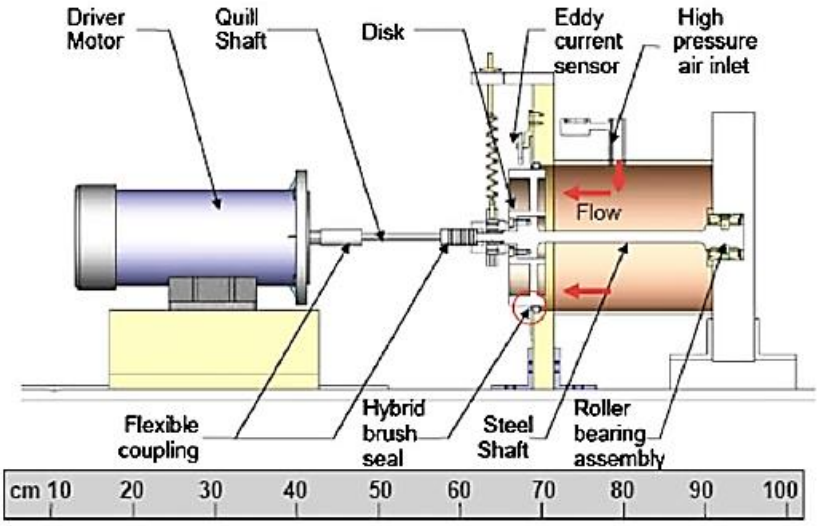

Figure 3.8: Cross section of the hybrid brush seal rig used by San Andrés *et al.* [2009].

Also at Texas A&M University, Childs and Hale [1994] presented a rig with which to investigate hydrostatic bearings. It was further modified to also accommodate turbomachinery seals by Dawson *et al.* [2002]. The rig comprises of a 114.3 mm rotor driven by an electric motor and supported by two pedestals, in between which the test seals are located in a back-to-back configuration. The top speed of the rig is 29,800 rpm, which yields a maximum rotor surface speed is 178.3 m/s. The maximum supply pressure is 137.9 bar and pressures different than atmospheric can be applied to the downstream side of the testing seals.

Two hydraulic shakers, orthogonally attached to the stator by means of stingers, move the stator relative to the rotor. Additionally, a static load is applied parallel to the direction of motion of one of these shakers. The force of the excitation introduced by the shakers is measured with load cells mounted in line with the shaker stingers. Both the acceleration and displacement of the stator are also measured to calculate the rotordynamic coefficients. Three sets of pre-stressed cables are arranged by pairs from each side of the casing in order to restrict the pitch of the casing and, therefore, to assure axial alignment between rotor and stator. The applied load and the stiffening cable arrangement can be seen in Figure 3.9 and Figure 3.10, respectively.

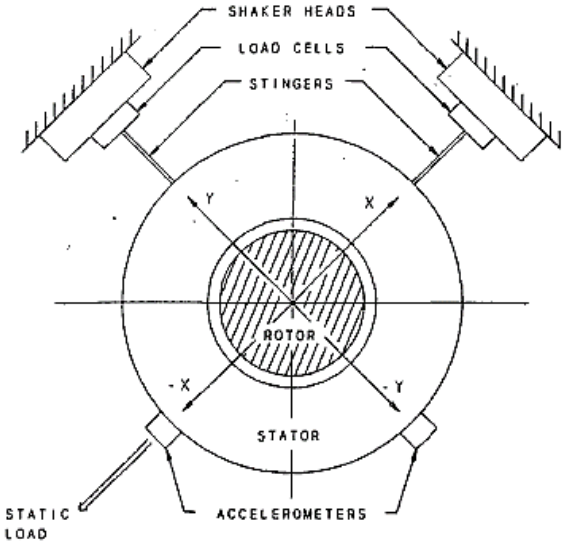

Figure 3.9: Applied loads to the bearing casing. From Childs and Hale [1994].

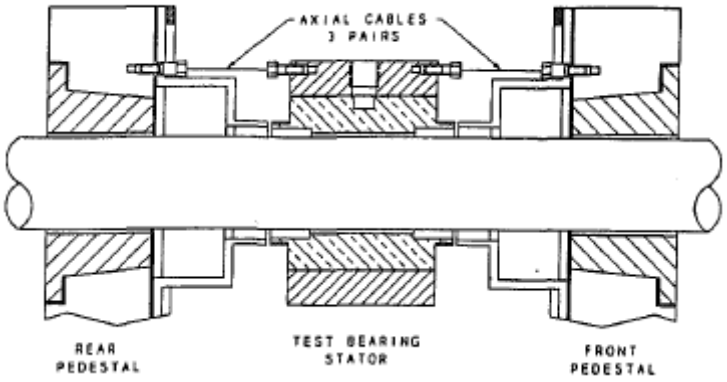

Figure 3.10: Side view of a test bearing showing axial-tensioning cables. From Childs and Hale [1994].

Vannini *et al.* [2011] presented the development of the rig shown in Figure 3.11. It features a double seal arrangement and was designed for the characterisation of internal seals of centrifugal compressors. The 220 mm rotor is able to rotate up to a maximum speed of 15,000 rpm, resulting in a rotor surface speed of 173 m/s. The working fluid is nitrogen and can be supplied upstream of the test section with varying pre-swirl levels at a maximum pressure of 350 bar. The downstream pressure can also be regulated to reach a maximum pressure drop of 210 bar. Active magnetic bearings are used to excite the rotor and, hence, measure the rotordynamic coefficients of the test seal. The maximum force and frequency at which the rotor can be shaken are 5,000 N and 350 Hz, respectively.

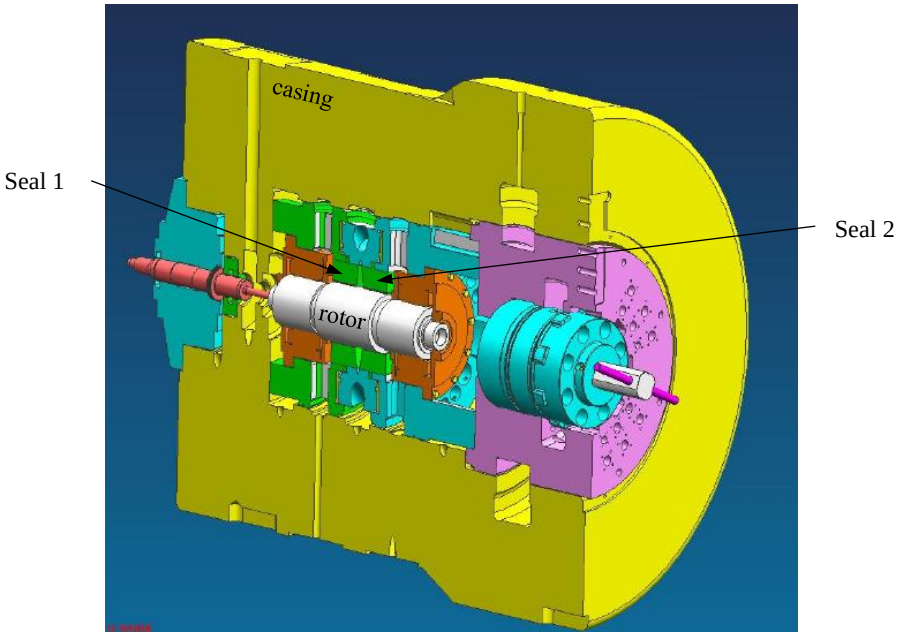

Figure 3.11: Cross section of the high-pressure rig presented by Vannini *et al.* [2011].

The review of existing test rigs for rotor-to-stator seals has been done with the intention of taking inspiration to design the new test facility described in this chapter. In the following, the conclusions drawn from this review are presented together with Table 3.1, which is a summary table that includes the key capabilities of the rigs discussed.

In general, single-seal arrangement rigs work at lower pressure drops than rigs with double-seal configuration. This is because, in single-seal facilities, the pressure drop acts directly on the rotor and, therefore, the resultant axial force has to be withstood by the bearings, imposing a trade-off between the applied pressure drop and the rotational speed. In rigs with two identical seals the pressure is symmetric; however, when two different designs are installed an imbalance of axial forces acting on the shaft may arise. This imbalance has to be either corrected, by adjusting the backpressure on the low-pressure side, or absorbed by the bearings.

A single-seal configuration has been preferred, despite the fact that the pressure drop level has to be compromised as the rigs with two test seals are more complex and expensive to manufacture. For instance, test facilities featuring a double-seal arrangement measure the mass flow rate of air passing through the seals upstream of the prototypes, i.e. the mass flow meter needs to have a range twice as large as in the case of a single-seal test rig. This may increase the cost of the design. Additionally, if the two test seals are different, a calibration of the secondary seal has to be performed before carrying out the final test, which adds complexity to the experiments and uncertainty to the results.

The rigs that have been designed to measure the rotordynamic coefficients of the test seals can be subdivided into two groups: those that move the rotor relative to the stator (as what happens in a real engine), and those that keep the rotor fixed and move the casing around it.

The rigs of the first group, even if more intuitive in first instance as they are similar to the real engine scenario, have a more complex architecture as it is difficult and dangerous to perform a vibration test to a rotating element. For instance, the rig at the Technical University of Munich has a flexible whirling rotor and the distance between bearings is tuned to change the whirling frequency. In the case of the rig at Texas A&M University by San Andrés *et al.* [2009], the rotor is also flexible and is excited by means of a shaker attached to one of the bearing units. In both cases, both the pressure and the rotational speed are limited for safety reasons. An exception to this is the rig by Vannini *et al.* [2011] which is able to rotate at 15,000 rpm and has a maximum upstream pressure of 350 bar. This is possible thanks to the use of magnetic bearings, however this solution is very expensive.

For these reasons, a configuration similar to the rig by Childs and Hale [1994] in which the casing is supported by pre-tensioned cables and shaken around the rotor has been chosen. Section 3.1.3 explains why vibrating the stationary seal components relative to a fixed rotor will allow meaningful rotordynamic coefficients to be measured, when in real turbomachinery sealing systems it is the rotor that is vibrating relative to fixed static components.

Regarding fluid pre-swirl, it is known that fluid rotation has a critical impact on the stability of gas seals. For instance, several studies have shown that labyrinth seals with an inlet tangential velocity close to the rotational speed of the test generate destabilising forces (Picardo and Childs [2005], Vannini *et al.* [2014]). Some of the rigs discussed in this section have the ability to adjust the inlet tangential velocity of the air to study the effect of this parameter. This is normally done by installing inlet guide vanes upstream of the testing seal or by using customised air supply systems with tangential and radial feeding holes. The test facility presented in this chapter has been designed so that the air enters the test section axially. Therefore, no effect of the inlet pre-swirl will be studied.

3.1.3 Rotordynamics of the FRPALS - preliminary considerations

This subsection aims to justify why a test facility that shakes the stator instead of the rotor is suitable for measuring the stiffness and damping coefficients of a seal with moving elements like the FRPALS. The method presented in Chapter 4 to measure the rotordynamic coefficients of a gas seal consists of performing a vibration test on the seal by shaking the casing to which it is attached. For rigid annular seals, such as labyrinth seals, the measurement of the stator

(seal) motion in the two degrees of freedom in the plane of shaking suffices to work backwards the equations of motion and calculate the constants of the model (i.e., the rotordynamic coefficients). Unlike an annular seal, the FRPALS has moving elements and these add degrees of freedom to the system. Therefore, measurements of displacement of the runners is needed in order to determine the full behaviour of the seal. The test rig described in this chapter is able to measure the radial displacement of the segments of the seal while being shaken by using the eddy current transducer arrangement shown in Chapter 7 (Figure 7.10 and Figure 7.11). Thus, full characterisation of the FRPALS should be possible.

Figure 3.12 depicts the degrees of freedom of a system comprised of the FRPALS mounted on the stator and surrounding the rotor with the runners being allowed to move only in the radial direction (r_i). In the following, a description of the complete system is given, and a schematic representation is shown in Figure 3.13.

Each one of the eight segments in which the seal is divided up into has a pad (runner) with a mass M_p. The runners are attached to the stator by the leaves, which are modelled as a spring of stiffness K_p. The interface between the runners and the rotor is the thin film of fluid. The forces in the fluid film are modelled by means of its equivalent stiffness and damping coefficients, K_f and C_f, respectively.

The stator has a mass M_s and is linked to the absolute frame of reference by two springs of stiffness K_s, located at two orthogonal directions X and Y. The coordinates of the centre of the stator in this reference are X_s and Y_s.

In the same manner, the rotor has a mass M_r and is attached to the absolute frame of reference by two springs of stiffness K_r, located at two orthogonal directions X and Y. The coordinates of the centre of the rotor in this reference are X_r and Y_r.

Note that both the rotor and the stator are supported by two springs. If the equations of motion of the system are to be solved, this allows the real-engine case to be modelled by exciting the rotor and keeping the stator fixed ($k_R \sim 0;\ \ k_S \to \infty$), or to model the test-rig case, by keeping the rotor fixed and exciting the stator ($k_R \to \infty;\ \ k_S \sim 0$).

This is done because, at first instance, one may think that performing the vibration test to such seal by shaking the stator may yield values of the rotordynamic coefficients different to the case in which the rotor moves relative to the casing.

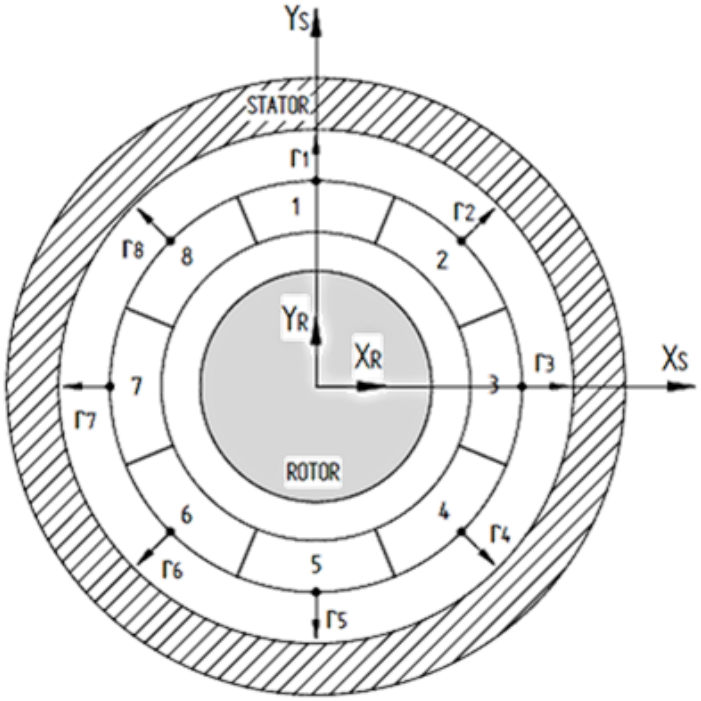

Figure 3.12. Degrees of freedom of the stator-FRPALS system when the runners of the seal are assumed to move only in the radial direction.

In order to shed light on this, let the zoomed-in part of system shown in Figure 3.13 (b) be further simplified to the diagrams of Figure 3.14, and assume movement only in the vertical direction. The problem has now been reduced to a two-degrees-of-freedom system, which is easier to visualise. The dynamics of the systems represented in Figure 3.14 (b) and Figure 3.14 (c) will be different, i.e. the natural frequencies and the amplitudes of the degrees of freedom will differ from one case to another. However, the constants of the system; namely the stiffness of the leaves (K_p), and the stiffness and damping of the fluid film (K_f and C_f) are the same. Therefore, if the measured displacements, forces and accelerations are consistent with the excited component of the system, being it either the rotor or the stator, the results from the experiments will be the coefficients corresponding to the fluid thin film in the seal clearance.

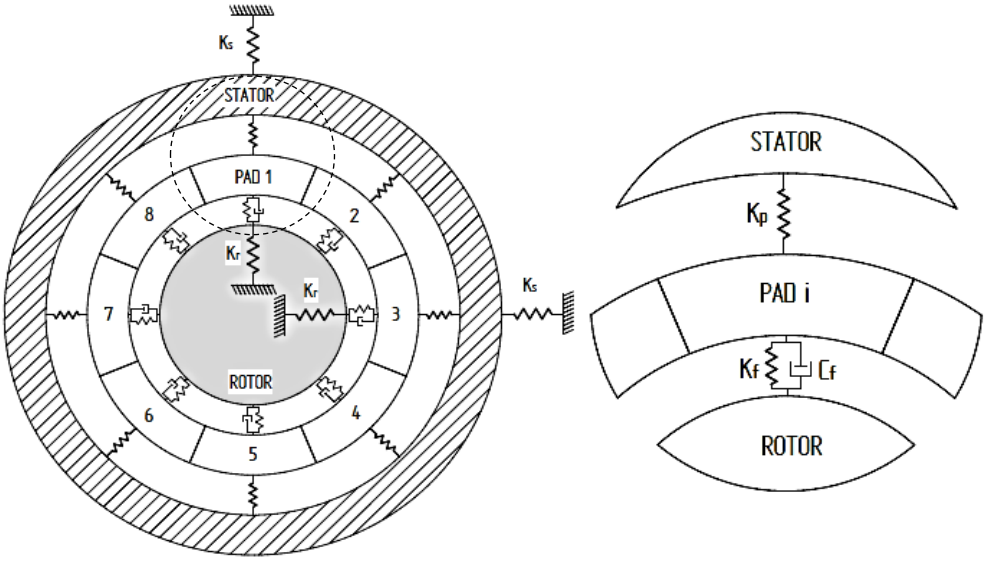

(a) **(b)**

Figure 3.13. (a) Schematic of the vibration model of the FRPALS and the film of fluid film created in the clearance between the rotor and the stator. (b) Close-up view of one of the runners of the FRPALS.

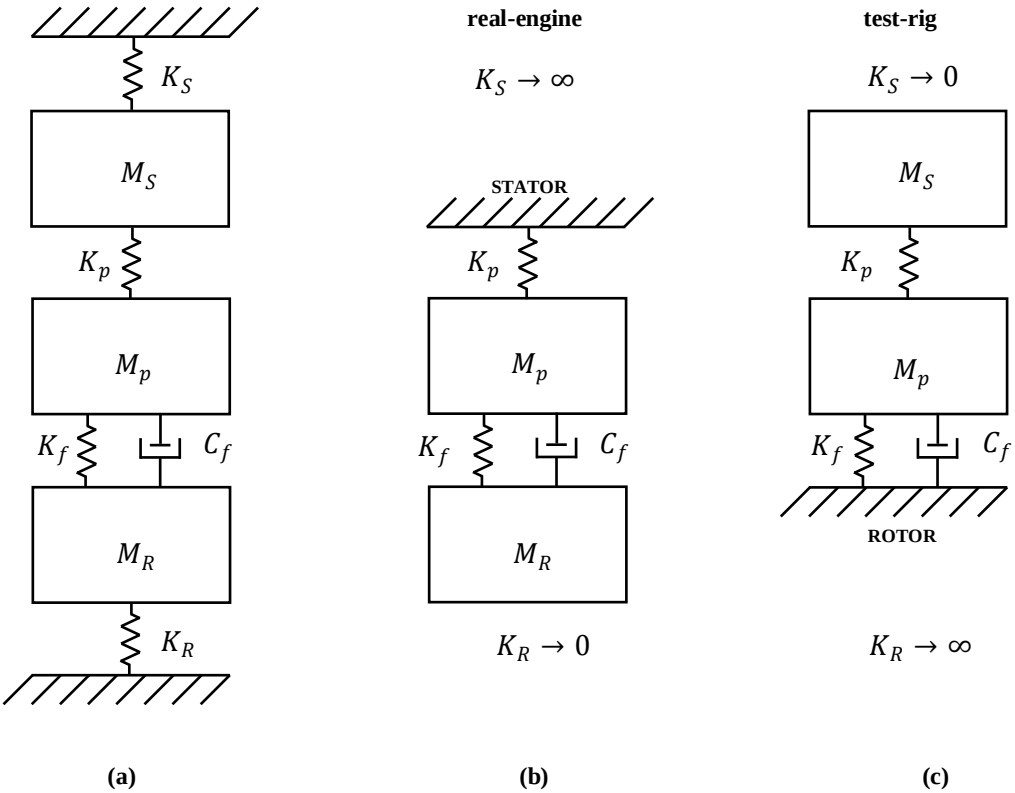

(a) **(b)** **(c)**

Figure 3.14. Simplified vibration model of the system composed by the stator, one segments of the FRPALS and the rotor. (a) General case, (b) rotor shaken – stator fixed, and (c) rotor fixed – stator shaken.

Table 3.1. Summary of existing rotor-stator seal rigs.

No.	Test rig	Pressure drop [bar]	Temperature [K]	Rotational speed [rpm]	Diameter [mm]	Surface speed [m/s]	Pre-swirl [Yes/No]	Configuration [Single/Double	Rotordynamic Coeff [Yes/No]
1	**MHI** Nakane *et al.*[2004]	4	Ambient	5000	350	92	No	Double	No
2	**University of Oxford** Pekris *et al.* [2015]	11.5	Ambient	7000	300	110	No	Double	No
3	**NASA Glenn Research Centre** Proctor *et al.* [2002]	5.2	922	32000	215.9	365	No	Single	No
4	**Karsruhe University** Beermann *et al.* [2015]	4	Ambient	9200	290	280	Yes	Single	No
5	**Cross Manufacturing – Cold rig** Fowler [1990]	20	Ambient	21000	130	143	No	Single	No
6	**Cross Manufacturing – Hot rig** Crudgington [2001]	20	893	38500	190	380	No	Single	No
7	**GE Global Research** Deo [2012]	35 (upstream	Ambient	10000	80	68	Yes	Double	No
8	**TU Munich – Non-whirl rig** Gaszner *at al.* [2013]	-	Ambient	12000	180	113	yes	Double	Yes moves rotor
9	**TU Munich – Whirl rig** Gaszner *at al.* [2013]	4	Ambient	1400	-	-	yes	Double	Yes moves rotor
10	**Texas A&M – Single seal rig** San Andrés *et al.* [2009]	3	Ambient	1300	167	11	No	Single	Yes moves rotor
11	**Texas A&M – Double seal rig** Childs and Hale [1994]	70	Ambient	29800	114.3	178.3	Yes	Double	Yes moves stator
12	**GE Italy** Vannini *et al.* [2011]	210	Ambient	15000	220	173	Yes	Double	Yes moves rotor
13	**University of Bath** This thesis	3.5	Ambient	15000	254	199.5	No	Single	Yes moves stator

3.2 Conceptual design of the rig

The considerations given in the previous section regarding the rig architecture and the rotational and tangential rotor speeds required by Cross Manufacturing constitute the origin of the design of the new test facility. Table 3.2 summarises the key parameters of the rig.

Table 3.2: Design parameters of the new test facility.

Max rotational speed	15,000 rpm
Max rotor peripheral speed	200 m/s
Resulting rotor diameter	254 mm

The conceptual design of the new test facility is represented in cross-section in Figure 3.15. Additionally, Figure 3.16 shows a close-up view of the test section. The rig features a 254 mm diameter rotor capable of rotating at a maximum speed of 15,000 rpm. An electric motor drives the shaft through a belt and pulley system. The bearing block keeps the rotor fixed. A translatable casing holds the test seal around the rotor. An electromagnetic shaker is used to move the casing, allowing the misalignments between the rotor and stator found in gas turbine engines to be modelled and the rotordynamic coefficients of the seal under investigation to be measured. Eddy current transducers are used to track the relative position between the rotor and the stator.

High pressure air is supplied to the test section from the University's compressed air facilities. The pressure drop across the seal and, hence, the mass flow rate are controlled by a valve and a pressure regulator upstream of the rig. Both the pressure drop and the leakage flow rate are measured by pressure transducers and a thermal mass flow meter, respectively.

In Sections 3.3 to 3.7 the design of the main subassemblies of the rig is described. The final general assembly and a summary of the features of the test facility is shown in Section 3.8.

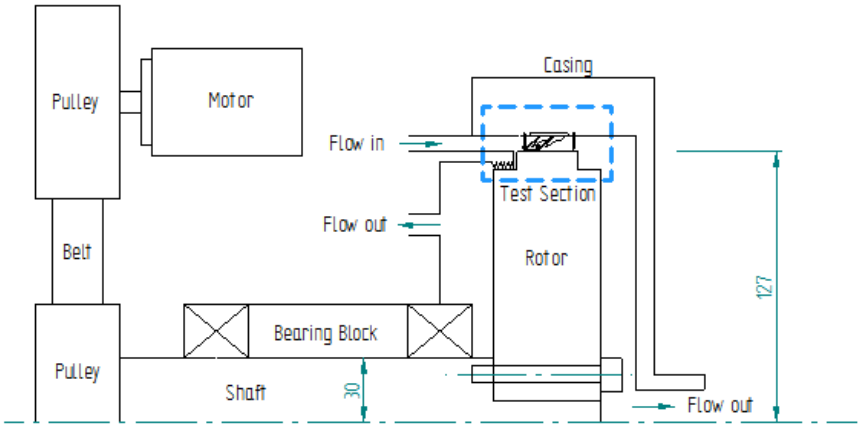

Figure 3.15. Cross section of the conceptual rig design. Scobie *et al.* [2015].

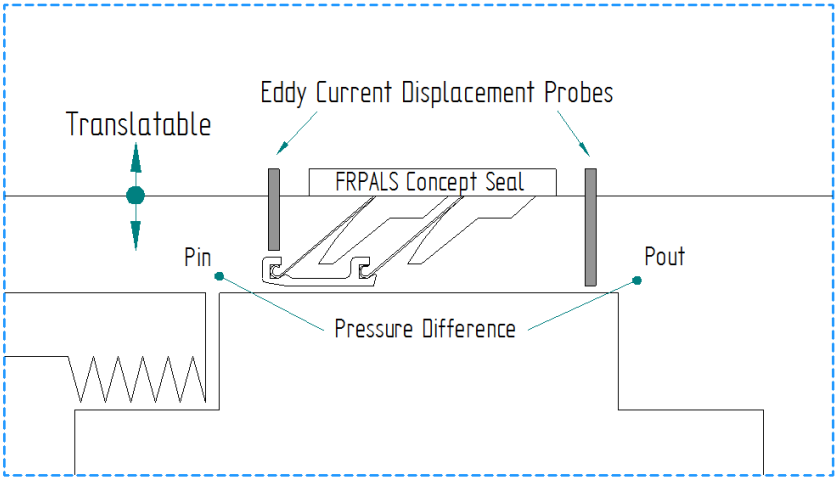

Figure 3.16. Close-up view of the rig test section. Scobie *et al.* [2015].

3.3 Test section

Figure 3.17 depicts the cross section of the test section. The testing seal is mounted on the casing, encompassing the rotor and has been represented in Figure 3.17 as a crossed box to indicate that the casing can accommodate different types of seals. Figure 3.18 shows the three different seals that have been fitted in the casing as part of this research, highlighting the versatility of the rig.

The components of the test section have been colour coded in Figure 3.17 to indicate the function of the rig. The stationary parts are shaded in blue, red is used for the rotor and the spindle, and the components that are shaken are shaded in grey and depicted as translatable.

In Figure 3.17, the paths followed by the flow as it passes through the test section are also labelled. The high-pressure air is supplied to the upstream region of the test section and from there it can flow through three different seals; namely the testing seal, the contact seal and the secondary labyrinth seal. The air through both the secondary labyrinth seal and the contact seal is discharged directly to the atmosphere, whilst the air through the testing seal is collected and directed towards a mass flow meter in order to quantify its leakage performance.

The parts that form the test section are described hereinafter and the materials of which they are made from are shown in Figure 3.19. Following subsections give the justification for the choice of material for each component of the test section and explain the design of the parts.

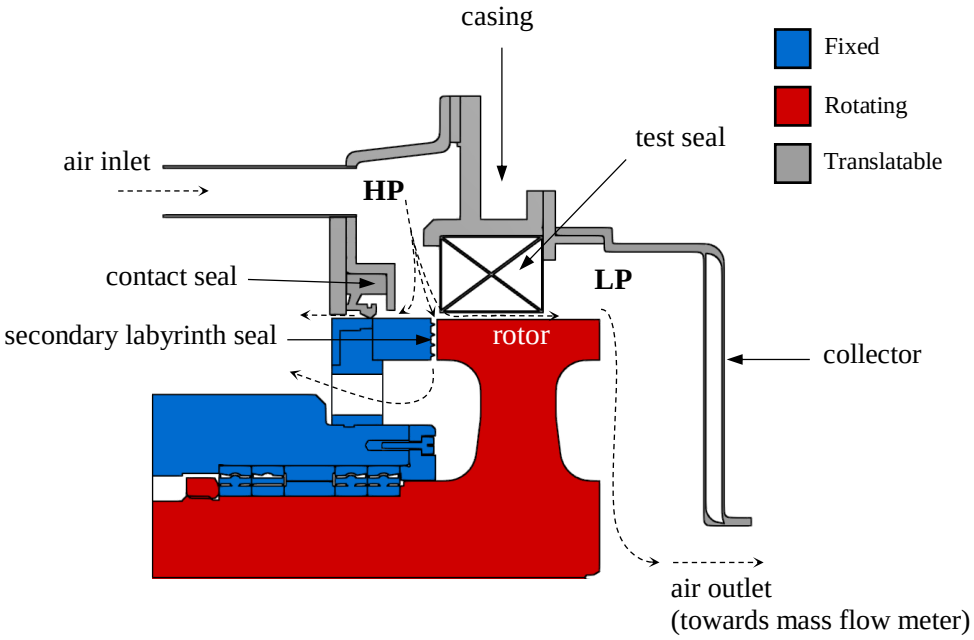

Figure 3.17: Flow paths in the test section of the FRPALS rig.

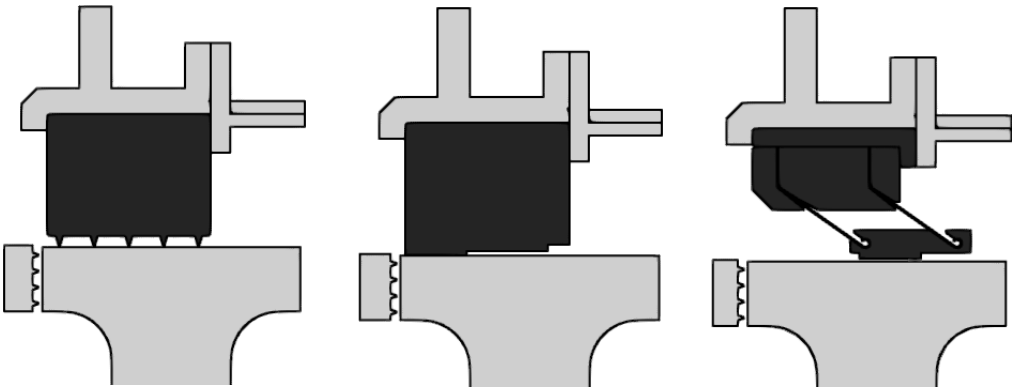

(a) **(b)** **(c)**

Figure 3.18: Close-up view of the test section for three different seals installed: (a) four-tooth labyrinth seal, (b) annular seal and (c) FRPALS.

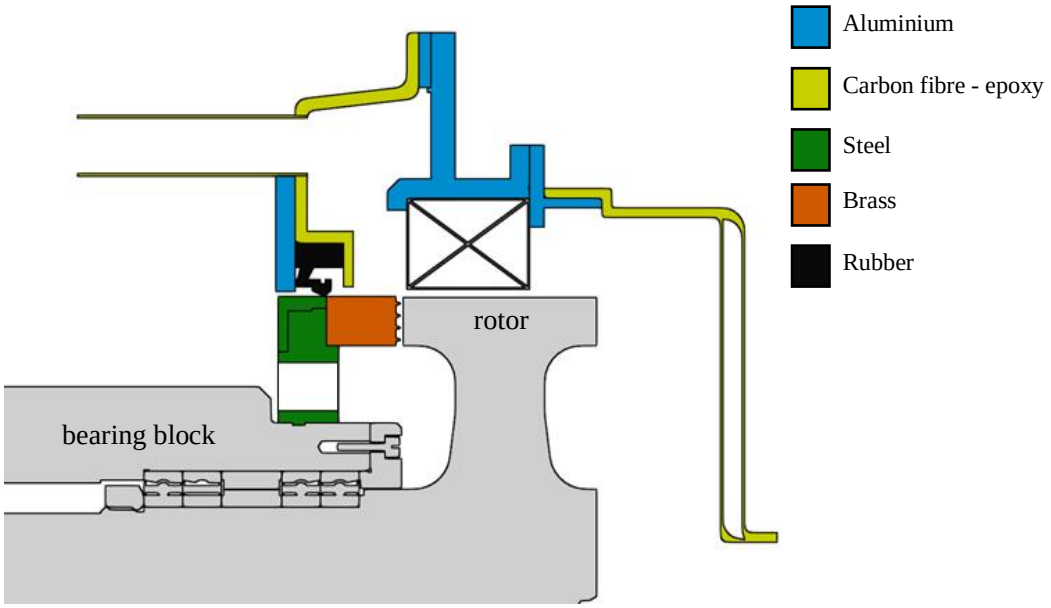

Figure 3.19: Close-up view of the test section, colour coded for materials.

3.3.1 Secondary labyrinth seal

The secondary labyrinth seal is used to limit flow leakage from the upstream cavity at the axial face of the rotor and also to reduce the axial thrust acting on the rotor, which is required to maximise the life of the bearings.

This labyrinth seal is designed as a split collar, wrapping around the front part of the bearing block. Figure 3.20 shows an exploded view of this subassembly and Figure 3.21 represents the two secondary seals assembled in the rig. A groove 5 mm wide and 1 mm deep was machined in the bearing block to be used as the reference for positioning the seal with respect to the rotor surface. As indicated in Figure 3.19, the part positioned on the bearing block is made from mild steel. Several holes are machined in this part in order to allow the leakage air of the seal to vent out to the atmosphere. The holes used to clamp the two halves of the split collar together are topped with a cover in order to provide a homogeneous surface for the contact seal to sit on.

The part containing the teeth and cavities that form the labyrinth seal is machined from brass. This material is softer that the rotor and, therefore, it will wear away in case of contact between the rotor and the seal. After assembly, the maximum clearance for this secondary labyrinth seal is 0.08 mm.

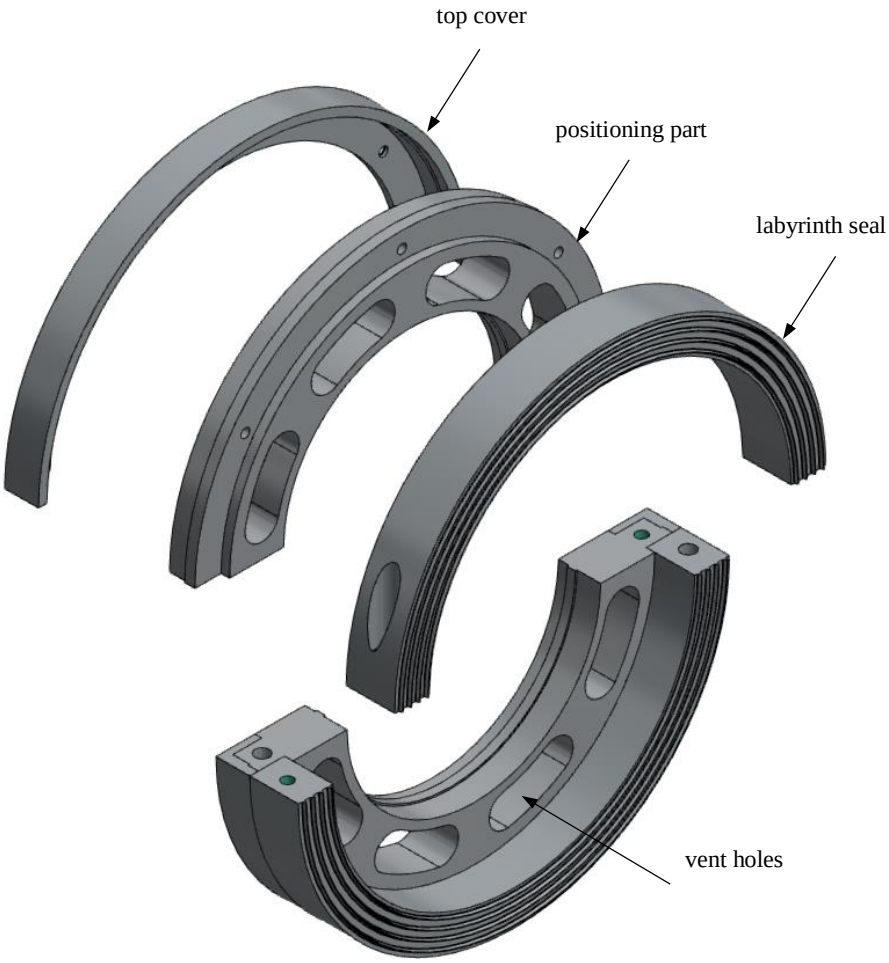

Figure 3.20: Exploded view of the secondary labyrinth seal subassembly.

3.3.2 Contact seal

The contact seal consists of a flexible rubber lip that is clamped to the translatable casing and sits on the outer dimeter of the top cover of the secondary labyrinth seal. The flexibility of the rubber allows the casing to be translated. The rubber seal was ordered to have a custom inner diameter of 255 mm and can hold a maximum pressure drop of 4 bar.

The recess made on the upstream cover of the casing to host the contact seal was dimensioned as per the indications of the seal manufacturer, likewise the size of the flange and the bolts used to clamp the seal in position.

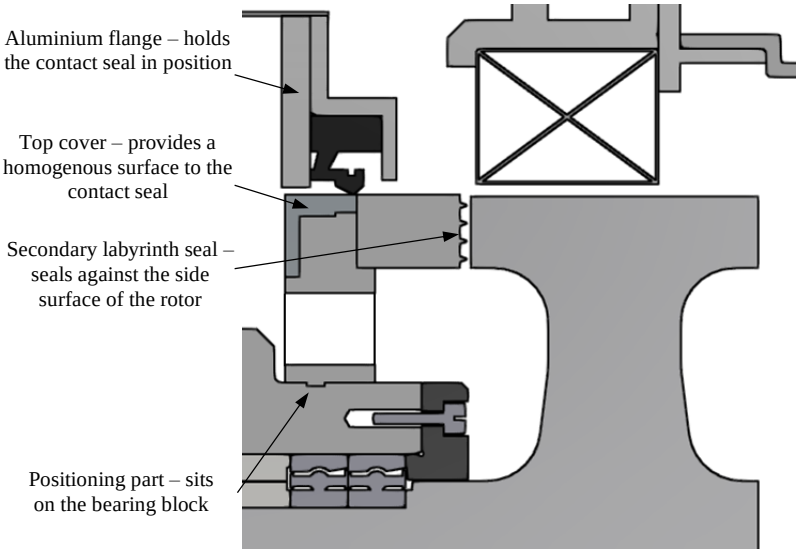

Figure 3.21: Close-up view of the secondary labyrinth seal and the contact seal as mounted in the rig.

3.3.3 Casing

The design of the casing is driven by the requirement of low weight, which is imposed by the maximum force of the shaker and the maximum acceleration of the experiment. Given these limiting parameters, in Appendix A, Newton's second law yields a maximum value of the mass of the casing equal to 18.5 kg. Because of this requirement, it was decided to make the casing out of composite material and aluminium as indicated in Figure 3.19. The final mass of the casing, including the testing seal and the bolts and nuts used to assemble the flanges together, was 15.3 kg. Taking into account the drive rod, the load cell, and the plate used to attach the drive rod to the shaker, the total mass of the shaker's payload is 17.8 kg, which is still smaller than the maximum calculated.

Figure 3.22 shows an exploded isometric view of the casing. The central part is made out of aluminium as this hosts the test seal. On both sides of this middle component, there are two covers manufactured from carbon fibre and epoxy resin that form both the upstream and downstream cavities of the test section. The attachment between these two covers and the central part is made through flanges. Aluminium rings are bonded to the composite components in order to have an aluminium-to-aluminium interface that enables the fitting of an O-ring seal in the flange coupling.

The front view and cross section of the upstream cover is shown in Figure 3.23. This part of the casing features fourteen holes, in which the air supply pipes are inserted and bonded. It also contains a recess, in which the rubber contact seal fits, and tapped steel bushes used to bolt on an aluminium flange that keeps the contact seal in place. Several pressure taps are included on the cover that were used during the commissioning of the rig to check that the

flow is axisymmetric at the upstream region of the test seal. Finally, the cross section shows a crosspiece that was added for structural reinforcement, as a pressure of 3.5 bar has to been withstood by the upstream casing. The hollow space between the outer wall of this component and the crosspiece is filled in with foam during the layup process of the composite material layers.

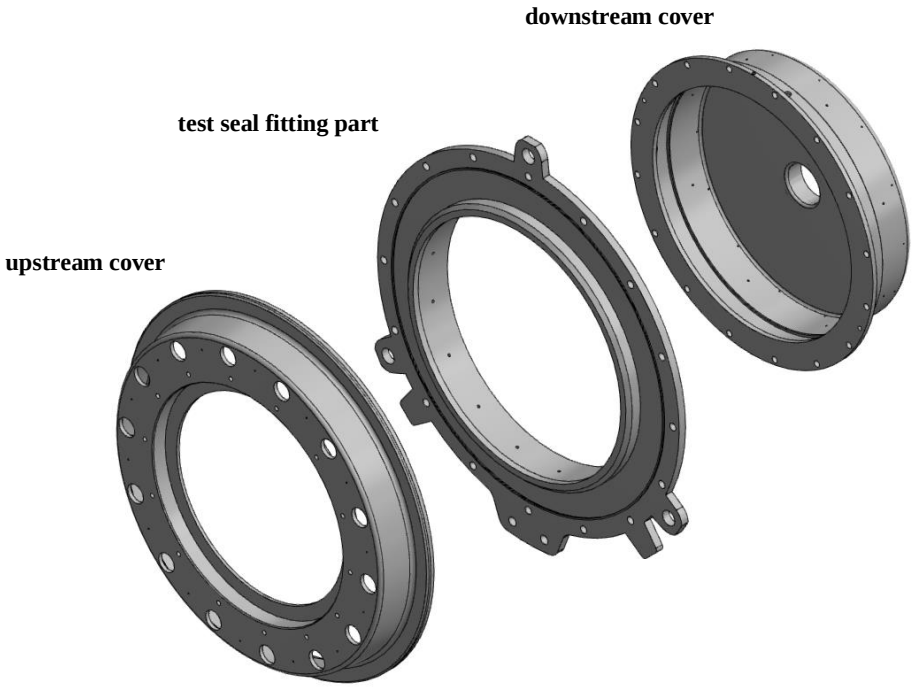

Figure 3.22: Isometric view of the three parts that form the casing.

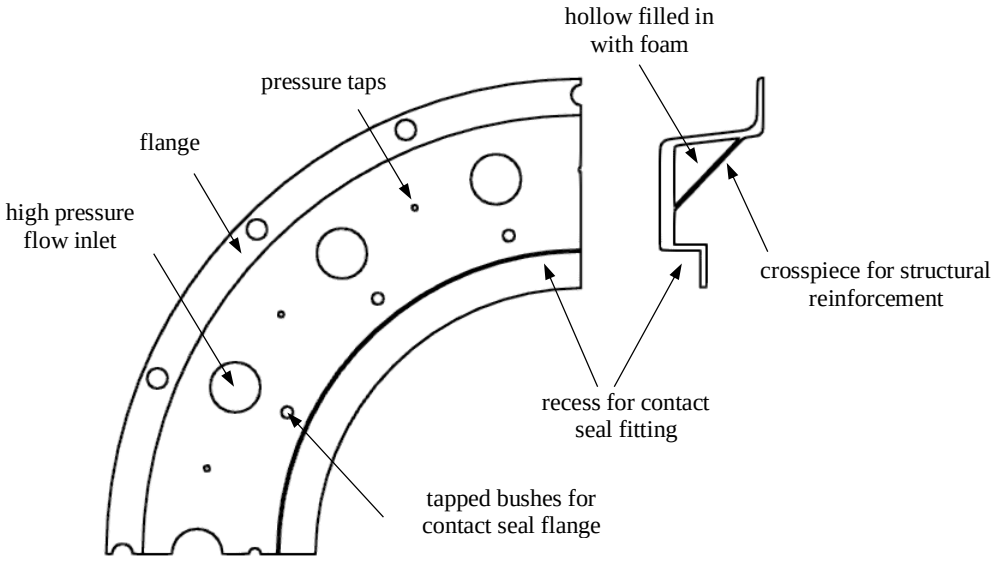

Figure 3.23: Front view and cross section of the upstream cover of the casing.

Figure 3.24 shows the cross section of the downstream cover of the casing. This cover is used as a collector of the test seal leakage air. It does not have to bear any pressure load as the air is allowed to fully expand to atmospheric pressure level. For this reason, the bonding surface between the aluminium flange and the composite part can be done horizontally, which simplifies the manufacturing of the composite component. Additionally, the walls can be thinner than the upstream cover, which helps to reduce the overall weight of the translatable subassembly. A sandwich arrangement with honeycomb panel is used to further reduce the mass of this part.

The moulds for the composite material parts are made out of aluminium. The final dimensions of the moulds were calculated taking into account a resin curing temperature of 150 °C and the thermal growth rate of the 6082 aluminium equal to $\alpha = 23.1 \cdot 10^{-6} \frac{m}{m\,K}$.

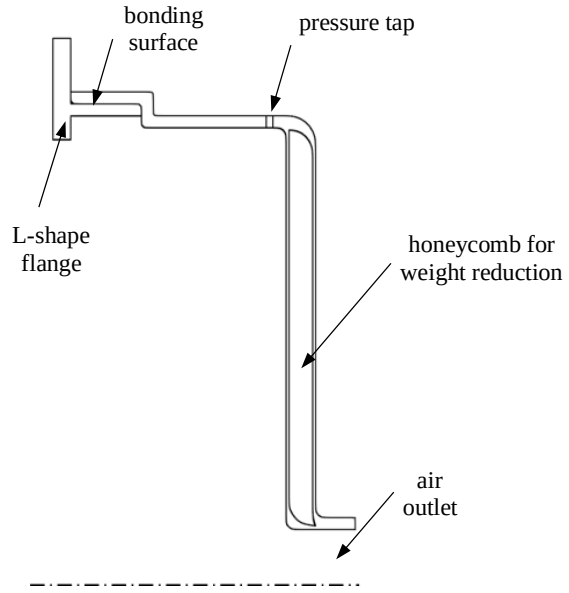

Figure 3.24: Cross section of the downstream cover of the casing.

The front view and the cross section of the testing seal housing can be seen in Figure 3.25. This part includes the connection for the shaker rod located at the bottom. Three protruding lobes distributed 120 degrees apart from each other and located at the outer rim are used to attach the casing to the supporting cables. The upstream flange features a step that assures correct positioning between the mating parts. In the downstream flange two dowel pins are used for the same purpose. Radial clearance holes are drilled on the bore of the casing to bolt the testing seal to the housing. This enhances the transmission of the shaker movement to the seal and prevents the deformation of the casing from changing the measured frequency response function of the system. Two blocks are located in the bottom half of the testing seal

housing that are used to support the translatable subassembly and stopping it from dropping under its own weight when the shaker is not engaged.

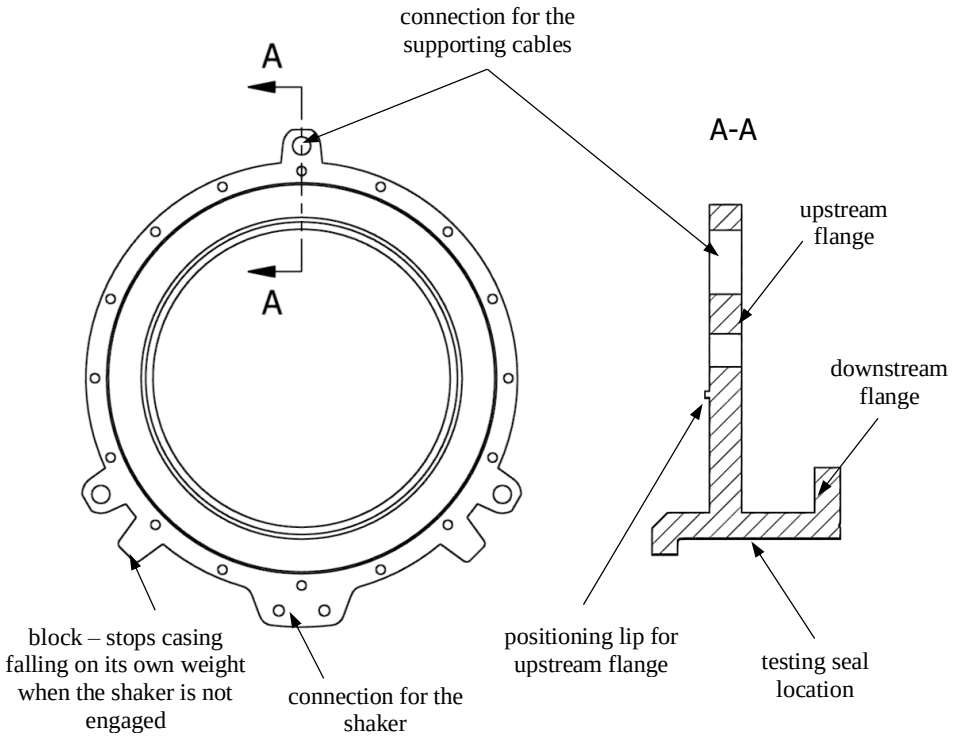

Figure 3.25: Front view and cross section of the testing seal fitting part of the casing.

3.4 Rotor and bearing housing

Several types of fittings between the rotor and the shaft, such as a tapered fit or keyway fit, were considered, since they give the rig versatility in easily being able to change the rotor and study different geometries. However, given that the rotor has to rotate at speeds of up to 15,000 rpm the fitting has to withstand large stresses, for this reason it was decided that the rotor and the shaft were to be manufactured from one piece.

In order to design the rotor and select the material, preliminary analytical stress calculations were applied to a solid annular disc. A detailed FEA analysis was then carried out for the same geometry and the results were checked with the analytical model (see Figure 3.26). Once the FEA model was trusted the rotor geometry was upgraded to a conical profile finished in a crown ring. Figure 3.27 depicts the three geometries considered and modelled by means of FEA.

Figure 3.28 shows the radial displacement at the rotor outer surface (i.e. the growth) given by the FEA calculations. Looking at the results of the predicted growth along the span of the disc for the three configurations shown in Figure 3.27, it can be seen that a constant-thickness

geometry yields the most uniform deformation along the rotor outer surface. However, even if not as uniform as the annular disc, the second version of the conical disc was chosen as this geometry has the advantages of reducing the weight and inertia of the rotor, thus relieving the load applied to the bearings. Additionally, according to Vullo and Vivio [2013], the tapered shape also has the advantage of providing a more uniform tangential stress distribution than the constant thickness disc.

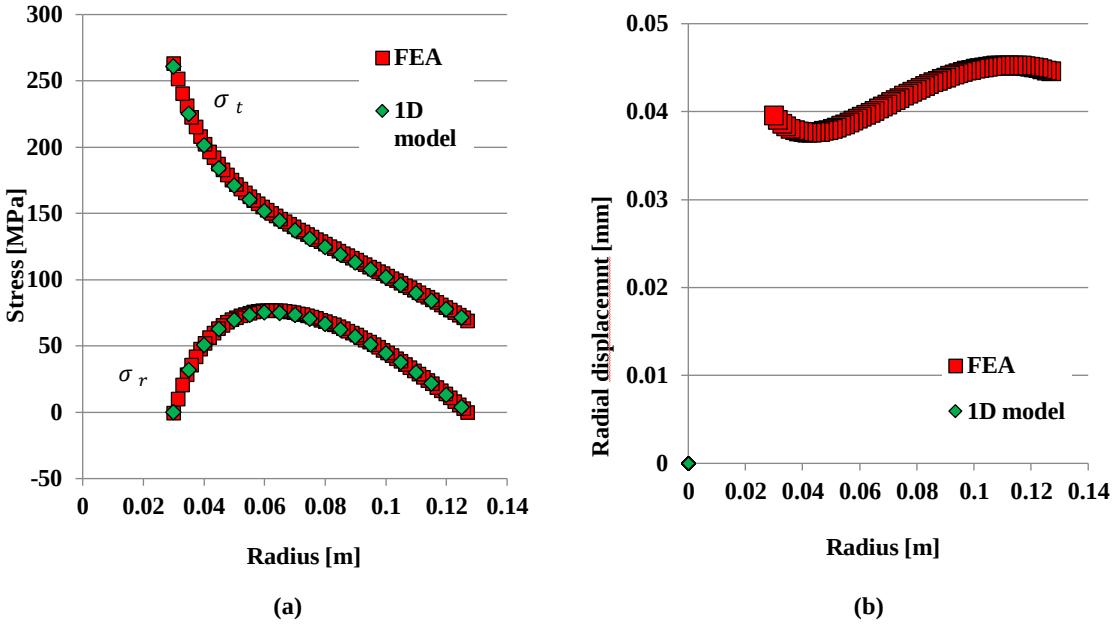

Figure 3.26. (a) Stress-distribution σ_r, σ_t and (b) radial displacement u_r in an annular, constant thickness steel disc from analytical model and FEA calculations.

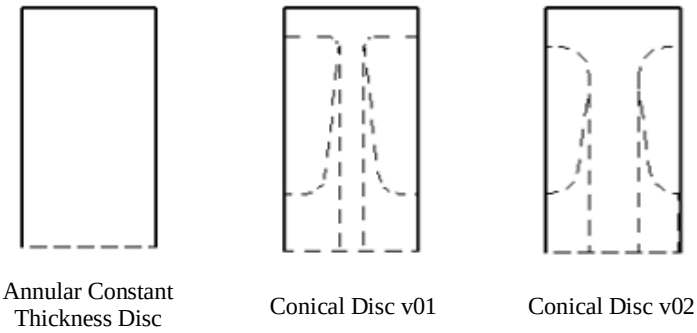

Figure 3.27. Different considered rotor geometries in the FEA model.

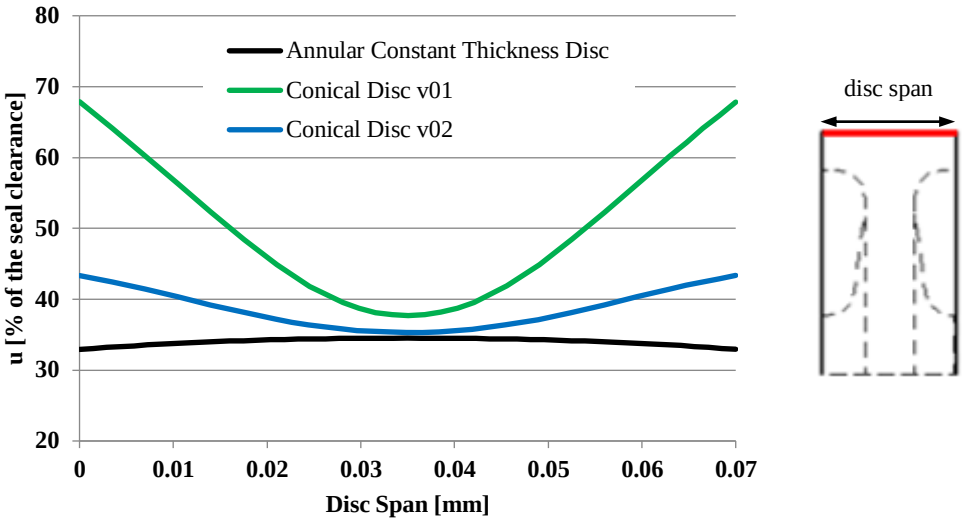

Figure 3.28. Radial displacement of the rotor outer surface relative to the seal clearance (0.127 mm), from FEA analysis.

Once the rotor and bearing unit were mounted on the bedplate, the growth at the mid-span point of the rotor was measured for a set of rotational speed up to 14,600 rpm. The measured growth is plotted in Figure 3.29 together with that predicted by the elastic theory. Both measured and predicted values match well and are within the measurement error of +/- 6 microns of the eddy current probe sensor used to perform the experiment (Appendix C). The results are plotted against $\Omega^2 r^2$, as the growth is linear with the square of the peripheral rotor speed.

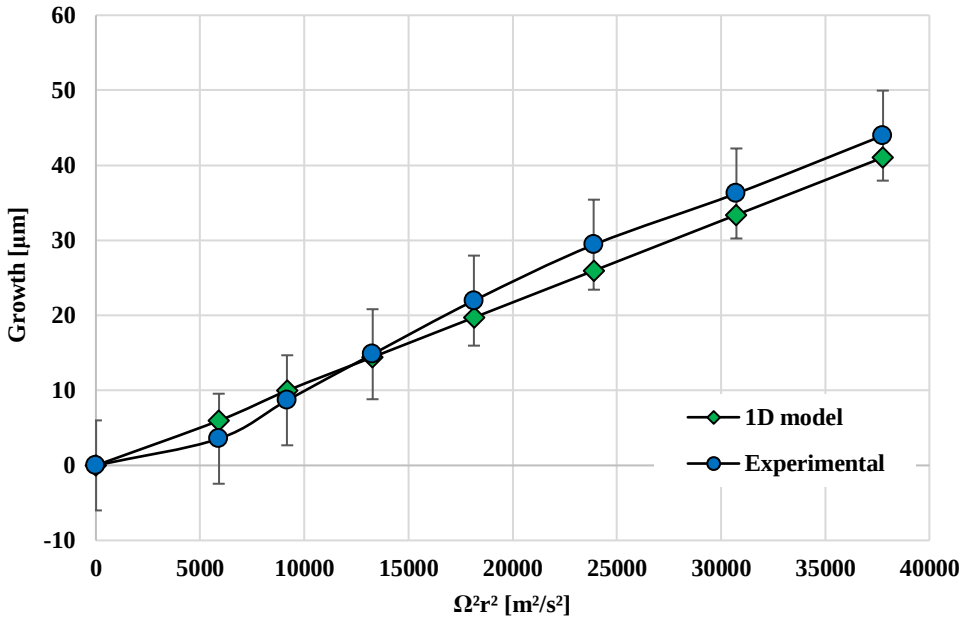

Figure 3.29: Measured and predicted growth of the rotor as a function of the square of the rotor surface velocity.

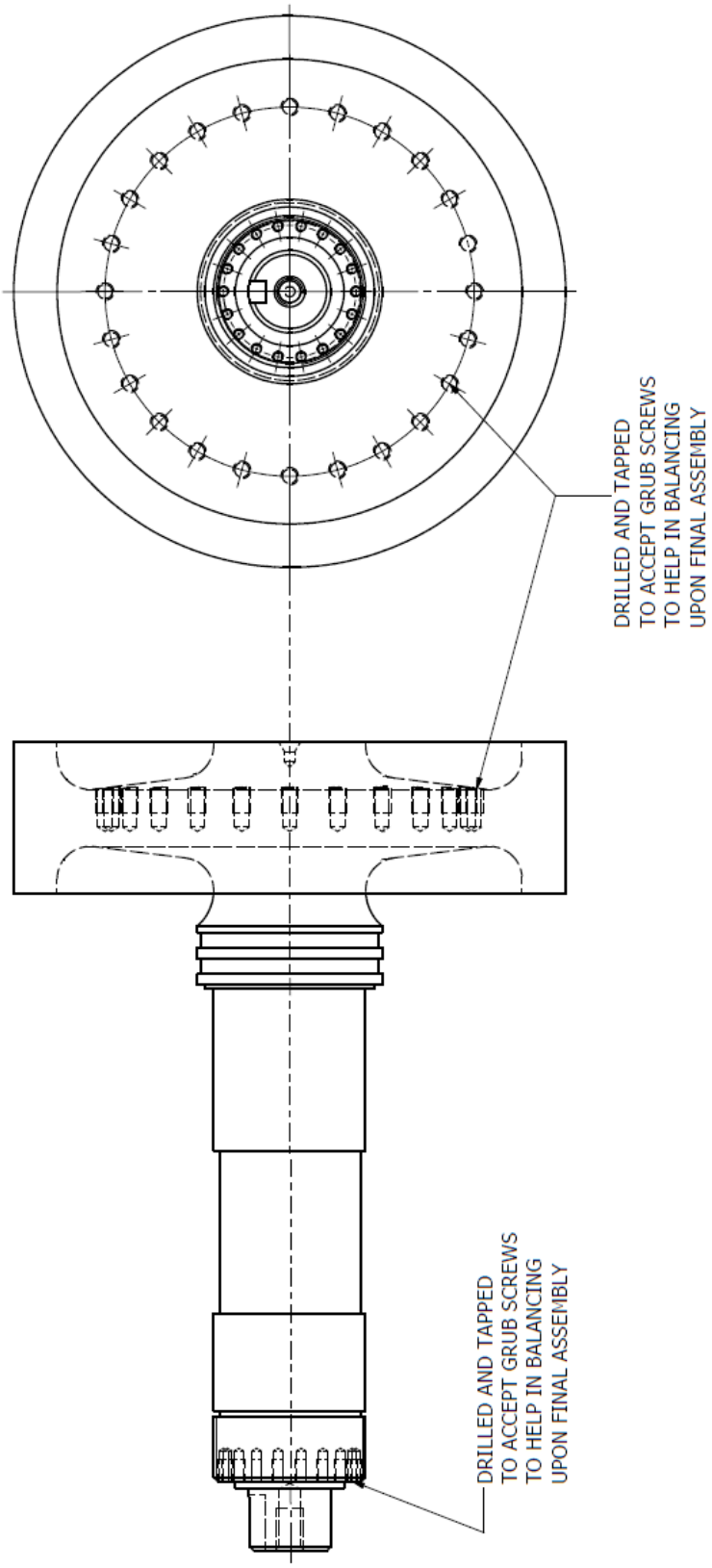

Figure 3.30. Front and side views of the spindle.

The material chosen is high strength, case hardening EN-40B nitriding steel which is heat treated at T condition (hardened and tempered). The yield strength of this material is 680 MPa, which is above the maximum estimated stresses in the rotor (180 MPa). In other words, the estimated safety factor for the rotor stress is 3.7. In order to increase the resistance of the disc to rotating stresses, the material was forged in such a way that the grain direction corresponded to the radial direction of the disc.

Once the rotor is manufactured and prior to finish-machining, a nitride coating is applied to both the shaft and the rotor outer surfaces. The shaft hardness after the coating will be the same as the bearing units, such that the spindle is not deformed by the bearings. On the rotor side, the coating also increases the hardness of the test surface up to values between 62-65 HRC (Rockwell C hardness), protecting the rotor from possible rubbing contacts with the FRPALS runners.

In order to balance the rotor upon final assembly, circumferentially distributed tapped holes are drilled at both ends of the spindle to accommodate grub screws. The rotor assembly is required to be dynamically balanced at grade G2.5 of ISO1940-1:2003. The final geometry of the rotor, including the balancing drills, is presented in Figure 3.30.

The shaft is mounted on a bearing block designed to keep it axially and radially fixed whilst it rotates at its design speed of 15,000 rpm and is subjected to a maximum axial force of 2,646 N, due to the force created by the pressure difference across the axial faces of the rotor. The total indicated runout (TIR) of the rotor outer surface had also to be specified; the radial TIR is 0.01 mm and the axial TIR is 0.1mm.

The design of the bearing block was decided to be outsourced because of the high speed and precision requirements. Additionally, the machining of the spindle and rotor, manufactured from a single forging, was also outsourced as the external grinder available in the University's workshop was not big enough to finish-machine a rotor of 254 mm diameter. Table 3.3 summarises the specifications given to the sub-contractor:

Table 3.3: Specifications of the spindle.

Rotor Diameter	254 mm
Rotor Axial Length	80 mm
Maximum Rotational Speed	15000 rpm
Radial TIR	0.005 mm
Axial TIR	0.01 mm
Maximum Axial Load	2646 N
Life (@ max. speed & max. axial load)	1000 hours

The solution given by the outsourcing company was a bearing housing that consists of five bearing units sealed and greased lubricated for life. Figure 3.31 shows the final configuration of the bearings as mounted on their housing and a description of the bearing units is given in the following.

The rear bearing is in charge of absorbing the reaction force of the belt; it consists of a super-precision cylindrical roller bearing. This type of bearings is designed to take high to extreme radial loads, while running at very high speeds and at a very accurate radial run out.

The bearings at the front are a quad set of super-precision angular contact ball bearings. The preload inside these bearings is the same for all of them. Two are pushed up against another two to ensure a constant reaction force greater than that exerted by the application so that they are completely, or as near as possible, to rigid; i.e. the TIR of the rotor is minimised. Angular contact ball bearings are designed to take medium to high axial loads and low to medium radial loads while running at very high speeds and at very accurate radial and axial run outs.

A pulley is mounted at the end of the spindle opposite to the rotor. There is also a toothed end cap used to measure the speed of the rotor. Both parts are described more extensively in subsequent sections. An exploded view of the rotor assembly is shown in Figure 3.32.

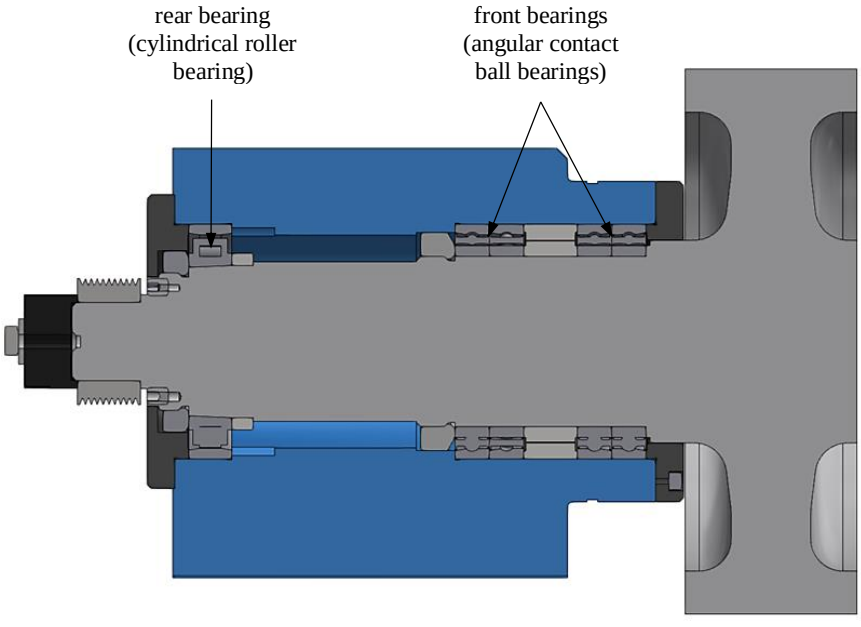

Figure 3.31. Arrangement of bearing elements within the bearing housing.

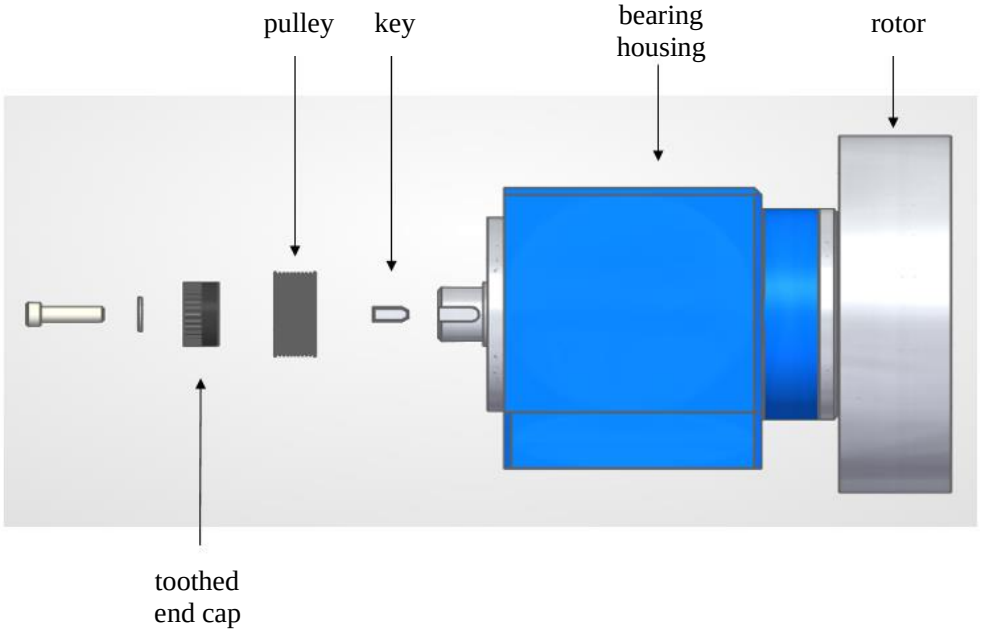

Figure 3.32. Rotor assembly.

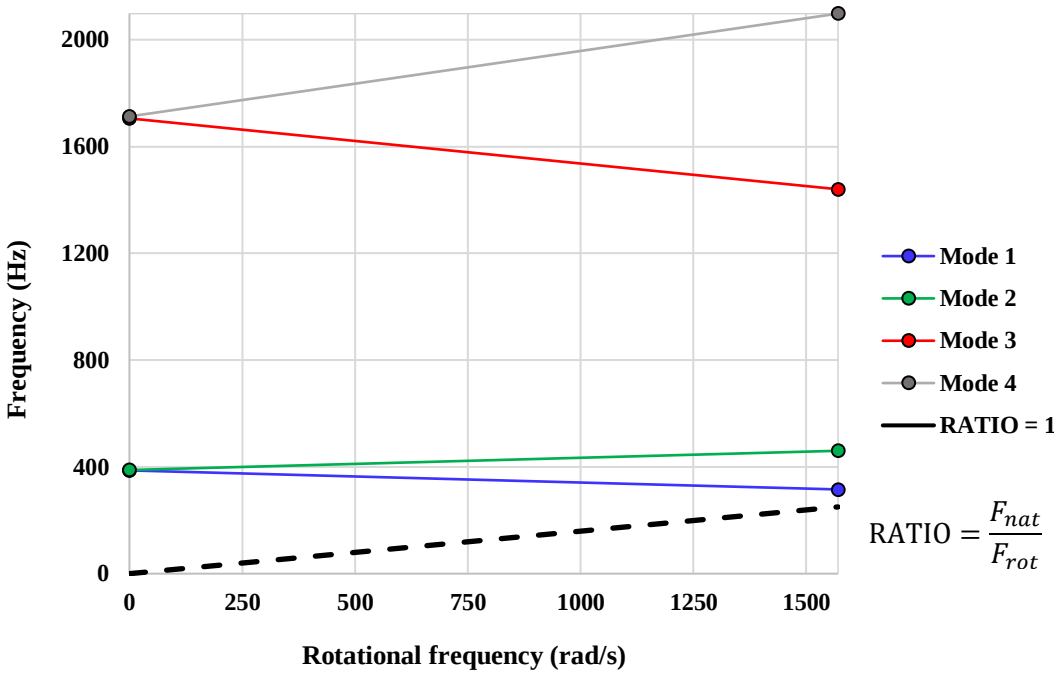

Figure 3.33. Campbell diagram of the rotor-bearing system.

Once the outsourcing company offered the final solution a stability analysis was performed to predict the rotordynamic behaviour of the spindle within the bearing block. For the rotordynamic analysis in Ansys, the stiffness of the bearing units was needed. The stiffness of the four front ball bearings is equal to 0.6 MN/m and the one of the rear roller bearing is 0.855

MN/m. With these values for the bearing stiffness, provided by the sub-contractor, and a rotational speed ranging from 0 to 15,000 rpm, the software gives the natural frequencies of the system at each rotational speed. These results are shown in the Campbell diagram in Figure 3.33. This diagram shows the modes of vibration of the rotor and the natural frequency of each mode is greater than the rotational frequency for all rotational speeds. This implies that the system will not have auto-excitation. In other words, the rotor will not introduce spurious vibrations into the whole seal-rotor system when measuring the rotordynamic coefficients of the test seal by means of a vibration test.

The TIR in both the radial and axial direction was measured with a digital DTI probe once the spindle and bearing block were manufactured, assembled together and balanced. Figure 3.34 shows these measurements for a complete turn of the rotor and proves that the actual values of the TIR fall within the specified target values at the design stage shown in Table 3.3.

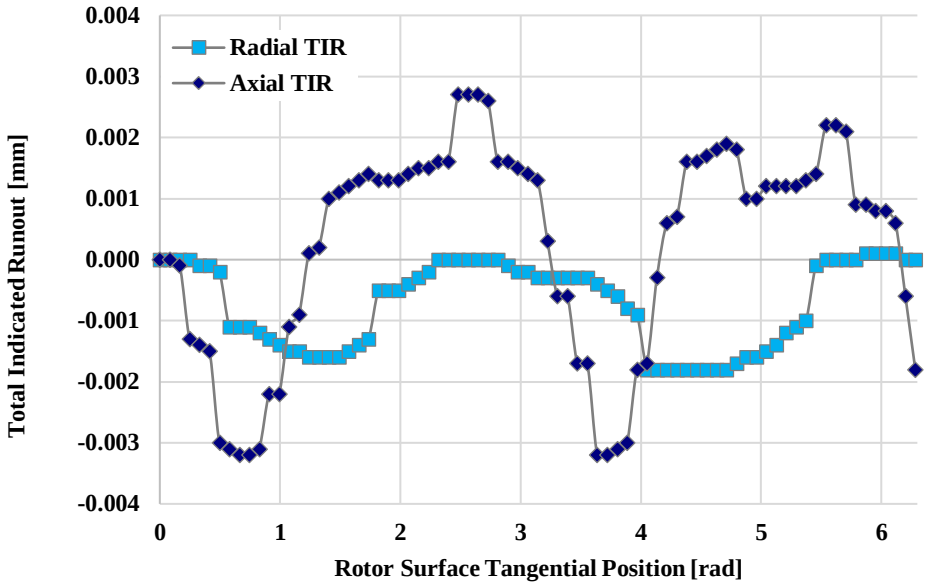

Figure 3.34: Measured radial and axial TIR of the disc after assembly.

3.5 Drivetrain subassembly

The rotor is powered by a 15 kW electric motor via a belt and pulley system (see Figure 3.35). The electric motor is fitted with a break resistor which is able to slow the system to rest in 18 seconds from the nominal speed of 15,000 rpm in case of emergency. The power needed to overcome the windage of the rotor is calculated in Appendix A and is equal to 332 W. The power required to overcome the friction in the bearings was estimated by the manufacturing company of the spindle bearing block to be 4.5 kW.

The maximum rotational speed of the electric motor is 5,000 rpm; therefore, a pulley ratio of 3:1 is required to rotate the disc up to 15,000 rpm. A poly-V configuration with ten ribs is chosen as the most suitable belt type (Figure 3.36) in order to increase the surface friction and make sure that the belt does not slip with respect to the pulleys.

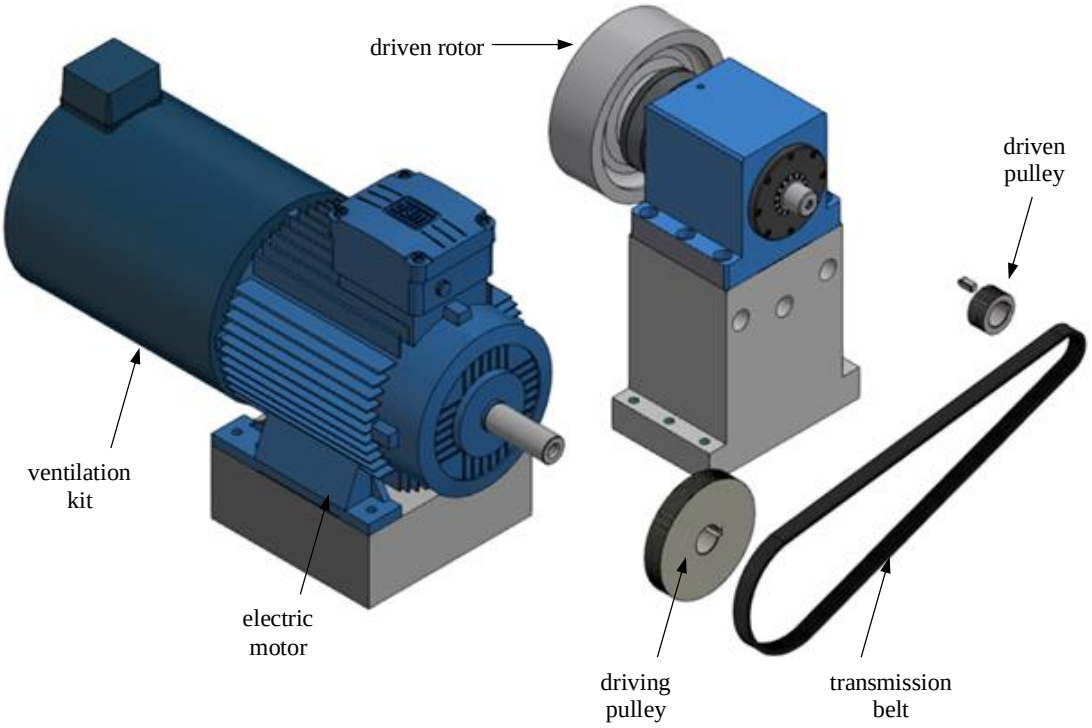

Figure 3.35. Drivetrain of the FRPALS rig.

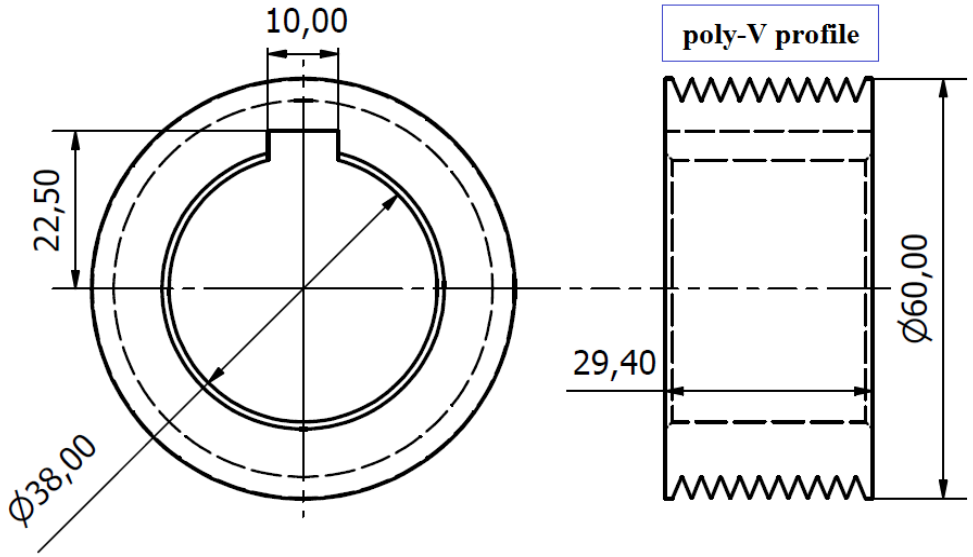

Figure 3.36. Front and side view of the poly-V pulley.

3.6 Leakage flow subassembly

The air flow is provided to the testing facility by the laboratory compressed air supply via a two-inch pipe system. The pipework features a Norgren pressure regulator and a Kinetrol pneumatic gate valve to set up the inlet conditions to the seal. Finally, a pressure relief valve with a maximum working pressure of 5 bar is placed between the pressure regulator and the inlet of the rig as a backup means to ensure that the pressure of the air supplied to the rig is never higher than the design value.

The air path through the rig can be tracked in Figure 3.37. The two-inch pipe supplies the air to a settling plenum, which splits the flow into fourteen inlet pipes. These inlet pipes are evenly distributed around the seal circumference in order to assure axisymmetric inlet pressure to the seal. The high-pressure air in the casing can follow the three paths explained in Section 3.3. The leakage air of the secondary labyrinth seal and the contact seal is expelled to the atmosphere. On the contrary the leakage air that passes through the testing seal is collected by the downstream composite casing cover and directed to the mass flow meter by the three-inch downstream pipe. After the mass flow meter, the air is also discharged to the test cell. The design of the rig air system is explained in the following paragraphs.

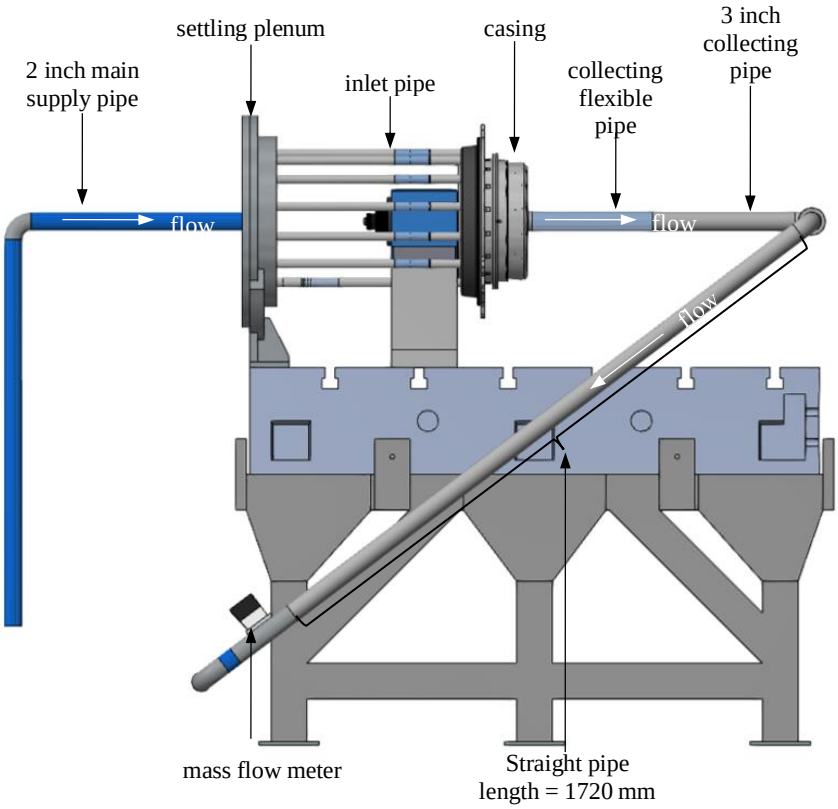

Figure 3.37: Air system of the rig.

The estimation of the mass flow rate passing through the seal is shown in the following. This estimation is important as the velocity of the flow at the different parts of the rig air system is derived from it. Additionally, the size of the mass flow meter was chosen based on this estimation.

The equation for the mass flow rate, for an ideal compressible gas is:

$$\dot{m} = \rho v A = \frac{A\, p_t}{\sqrt{T_t}} \sqrt{\frac{\gamma}{R}} M \left(1 + \frac{\gamma - 1}{2} M^2\right)^{-\frac{\gamma+1}{2(\gamma-1)}} \quad 3.1$$

The area of the flow has been calculated using the target effective clearance of the FRPALS design of 0.127 mm. A Mach number equal to unity (choked conditions) has been used as this represents the maximum flow rate condition. Assuming zero velocity at the region immediately upstream of the seal, the total pressure in this region corresponds to the maximum design static pressure of the rig (p_t = 4.5 bar). Likewise, the total temperature has been assumed to be an average value of the ambient air temperature (T_t = 293 K). Finally, the two constants R = 287 J/kg K and γ = 1.4 are the ideal gas constant and the heat capacity ratio, respectively. With these values for the parameters of Eq. 3.1, an estimated mass flow rate of $\dot{m}$ = 0.1 kg/s is found. Nevertheless, a value of 0.2 kg/s has been selected in order to have a margin in the mass flow meter.

3.6.1 Settling plenum

The plenum is comprised of two parts clamped together by means of a flange. This configuration was chosen in order for the walls forming the chamber to be as parallel as possible, thus, avoiding the flow to accelerate more in some regions than in others on its way out of the plenum. Figure 3.38 shows the front and exploded, cross section two parts constituting the plenum. Both walls have a flatness tolerance of 0.05 mm and the parallelism tolerance of the mating faces with respect to their datum surface is also 0.05 mm. The fact that a tolerance different than zero has been used implies that in reality the walls of the chamber are not perfectly parallel. Therefore, the air will be subjected to a certain amount of squeeze resulting in the discharge velocity to the upstream cavity of the casing not having an axisymmetric distribution along the circumference of the seal. This may be regarded as a problem, however the rig has been designed so that the air velocity at this point in the rig is small or, in other words, so that the difference between the total and the static pressure is negligible.

The dimensions of a metric standard flange DIN 2501 rated for 6 bar and a nominal pipe diameter of 400 mm were used as a first sensible rule of thumb to design the plenum. This should give an over-engineered flange as the pipe diameter is 380 mm and the maximum pressure to be withstood by the plenum is 5 bar. Once a design was obtained, an FEA simulation was performed. Figure 3.39 shows contours of the stresses obtained for the quarter of the assembly simulated for an applied internal pressure of 6 bar. The maximum value of stress is five times smaller than the yield strength of the material and is located at the holes used to fit the pipes. An expected area of concentration of stresses is the corner of the perpendicular walls. This corner was designed to have a radius of 5 mm in order to reduce the level of stress. According to the FEA simulation the stress values in this area are acceptable.

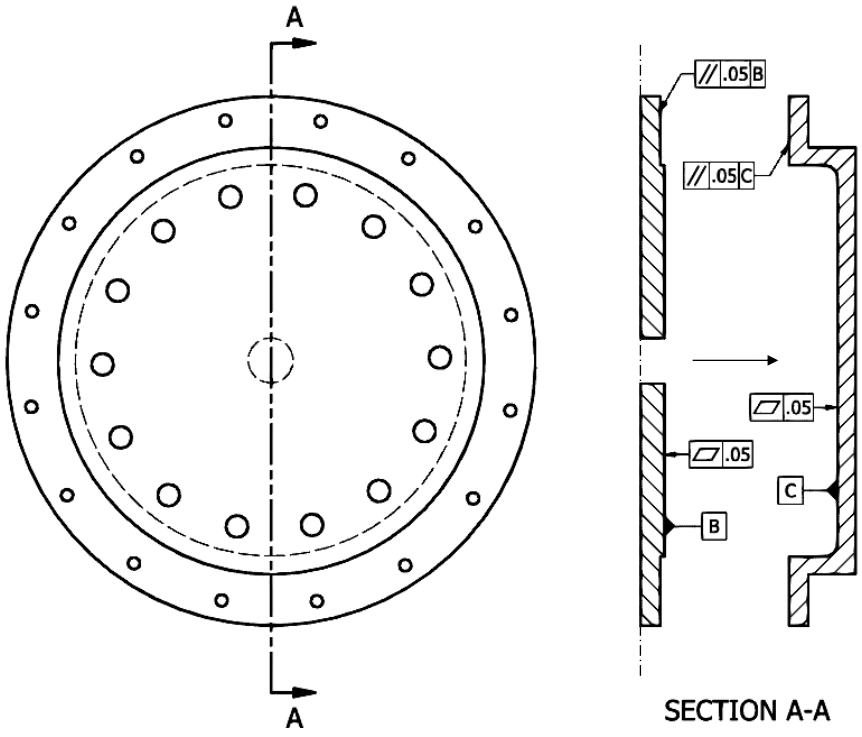

Figure 3.38: Front view and cross section of the exploded plenum assembly. Flatness and parallelism tolerances.

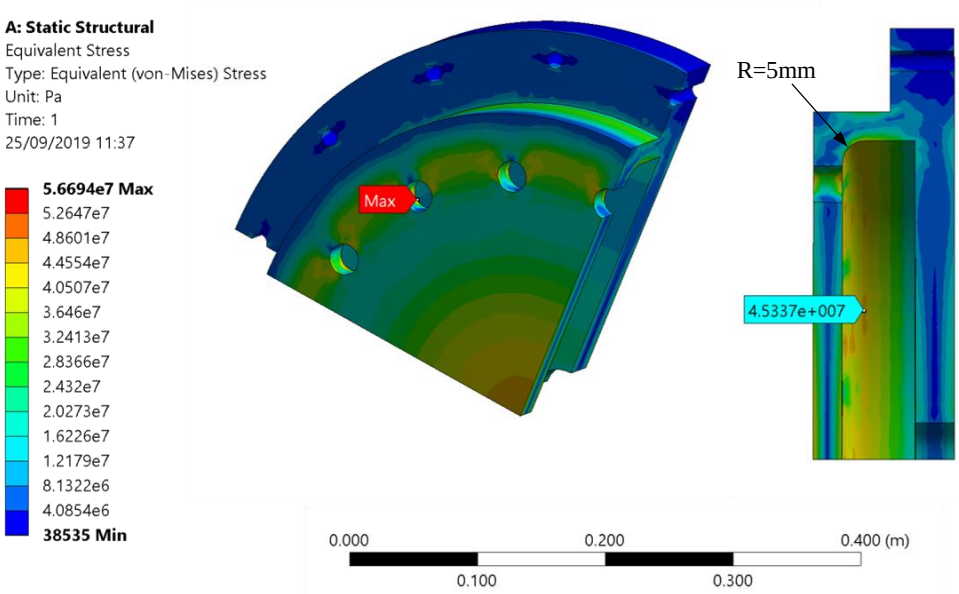

Figure 3.39. Stress contours of the inlet plenum for an applied pressure of 6 bar.

3.6.2 Inlet pipes

The number and the diameter of the inlet pipes was decided using the aforementioned criterion of minimising the velocity of the flow at the outlet of the pipes, i.e., at the upstream region of the testing seal. Additionally, rig assembly considerations were taken into account as the pipes have to avoid the drivetrain belt and pass through the metal block that raises the bearing unit from the bedplate level. Fourteen pipes along the test section outer diameter could be fit without interfering with the belt. Once the number of pipes was decided, the diameter of the pipes was chosen by calculating the velocity of the air. The total flow area was calculated for values of pipe inner diameter ranging between 10 and 25 mm, The calculated area for each pipe diameter value was then used with Eq. 3.1 together with the chosen mass flow rate of 0.2 kg/s. Table 3.4 is a snapshot of the spreadsheet, where values of the air velocity, Mach number and dynamic pressure can be seen. A value of 19 mm was chosen.

Table 3.4: Calculation of the speed of the air for 14 inlet pipes and different values of the pipe inner diameter

p [Pa]	450000	N inlets	14		
R [J/kg/K]	287	D [mm]	V [m/s]	M [-]	$^1/_2\,\rho v^2$ [mbar]
T [K]	293	10	34.0	0.099	30.9
ρ [kg/m^3]	5.35	11	28.1	0.082	21.1
$\dot{m}$ [kg/s]	0.2	12	23.6	0.069	14.9
		13	20.1	0.059	10.8
		14	17.3	0.051	8.0
		15	15.1	0.044	6.1
		16	13.3	0.039	4.7

17	11.8	0.034	3.7
18	10.5	0.031	2.9
19	9.4	0.027	2.4
20	8.5	0.025	1.9
21	7.7	0.022	1.6
22	7.0	0.020	1.3
23	6.4	0.019	1.1
24	5.9	0.017	0.9
25	5.4	0.016	0.8

During the commissioning of the rig, measurements of static pressure in each supply pipe were taken at the upstream cavity. The results, shown in Figure 3.40, indicate axisymmetric static pressure into the test section. A maximum difference of 0.2% of the mean pressure was measured across all circumferential positions. This difference is approximately three times the estimated value of the dynamic head of the flow (2.4 mbar) given in Table 3.4.

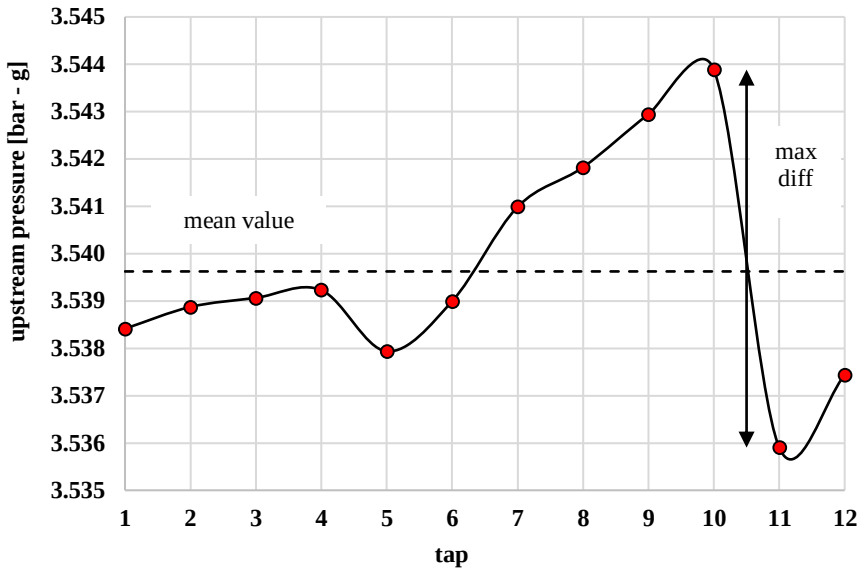

Figure 3.40: Measured tangential distribution of the static pressure in the upstream region of the testing seal.

Because the casing is required to be translatable, the inlet pipes must have a certain level of flexibility. To fulfil this requirement the inlet pipes are split in two parts. One part is made out of aluminium and is rigidly fixed to the plenum, the second part is made out of composite material and is bonded to the upstream cover of the casing. A piece of flexible pipe forms the link between both rigid parts and jubilee clips are used to seal the joints. A close-up photograph of this assembly is shown in Figure 3.41.

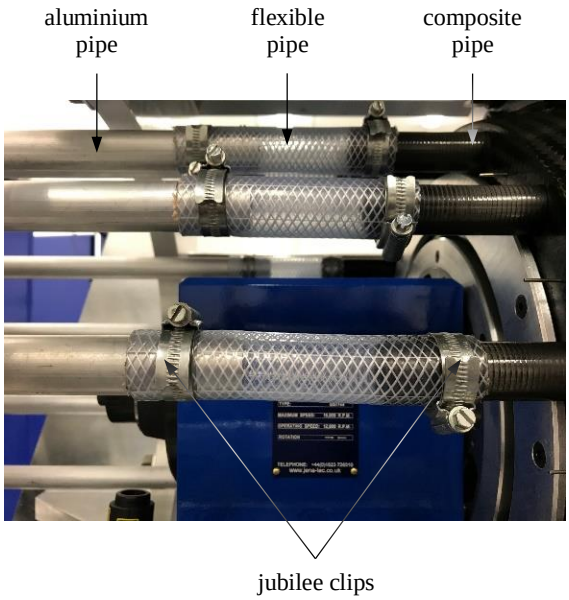

Figure 3.41: Detail of the flexible pipes

3.6.3 Leakage flow collecting system

The downstream cover of the casing, the design of which has been explained in Section 3.3.3, collects the leakage air downstream of the testing seal. A layer of honeycomb mesh is bonded at the outlet of the collector, where the air is directed towards the three-inch pipe, in order to straighten the flow. This helps to remove the tangential component of the flow velocity (swirl) introduced by the rotation of the rotor. A means of cancelling the swirl of the flow is needed as swirl is detrimental for the accuracy of the mass flow meter readings and viscous dissipation might not be enough to completely eliminate it. Figure 3.42 shows the flow straighteners glued to the downstream collector.

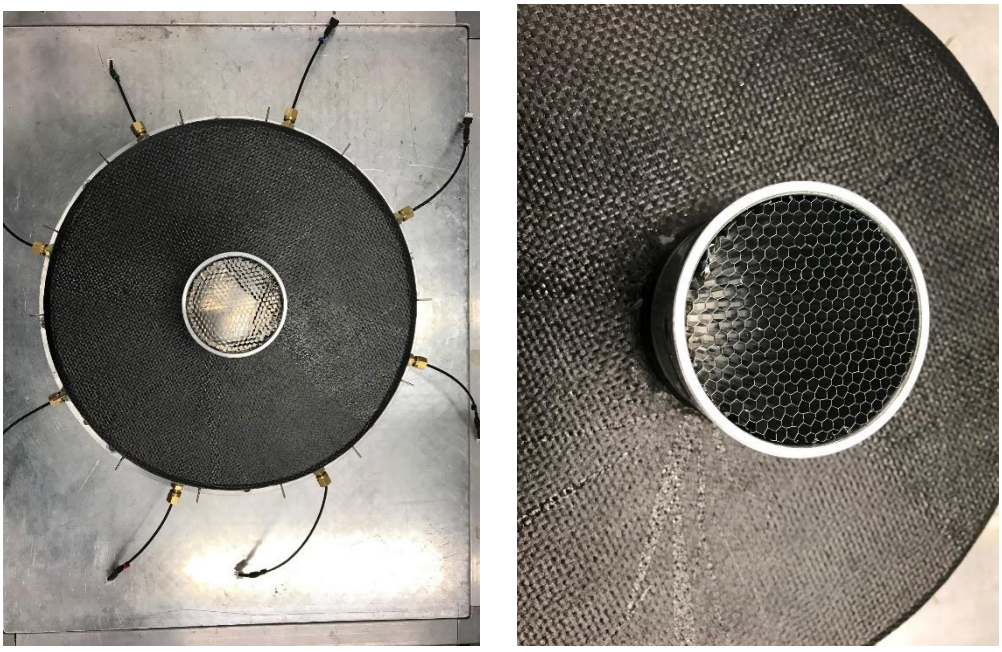

Figure 3.42: Photograph of the downstream cover and detail of the honeycomb mesh bonded at the outlet.

Similar to the flexible pipe solution on the inlet pipes, a flexible pipe is used downstream of the leakage flow collector to allow the casing to be shaken. Aside from the flow straighteners used to get rid of the flow tangential velocity, the flow needs further conditioning on its way to the mass flow meter. In these regards, the manufacturer of the instrument provides guidelines that have to be followed if accurate measurements are to be taken. Depending on the number of 90 degree bends that the flow undergoes upstream of the meter, a minimum length of straight pipe is needed between the last bend and the inlet of the instrument. In this case, the 80mm diameter outlet pipe features two elbows located in two different planes, which translates into a recommended straight pipe length equal or greater than 20 times the diameter of the pipe, i.e. 1600 mm, prior of the mass flow meter. This feature of the leakage flow subassembly of the rig is depicted in Figure 3.37.

After the mass flow meter, the air is discharged to atmosphere. A similar straight pipe length requirement has to be fulfilled downstream of the meter. Once again, following the guidelines of the manufacturer the downstream straight length is 320 mm

3.7 Vibration test subassembly

The inertia, stiffness and damping coefficients of the FRAPLS are to be experimentally measured using the methodology introduced in Section 4.3. For this a vibration test is needed, which consists of applying a controlled excitation to the casing and measuring the response in terms of displacement and acceleration. Additionally, the operation of the seal has to be

simulated under non-uniform clearance conditions similar to those occurring in a real engine due to rotor manufacturing runout, non-uniform stator wall thickness at the assembly flanges, discreet thermal gradients, or transient rotor misalignments.

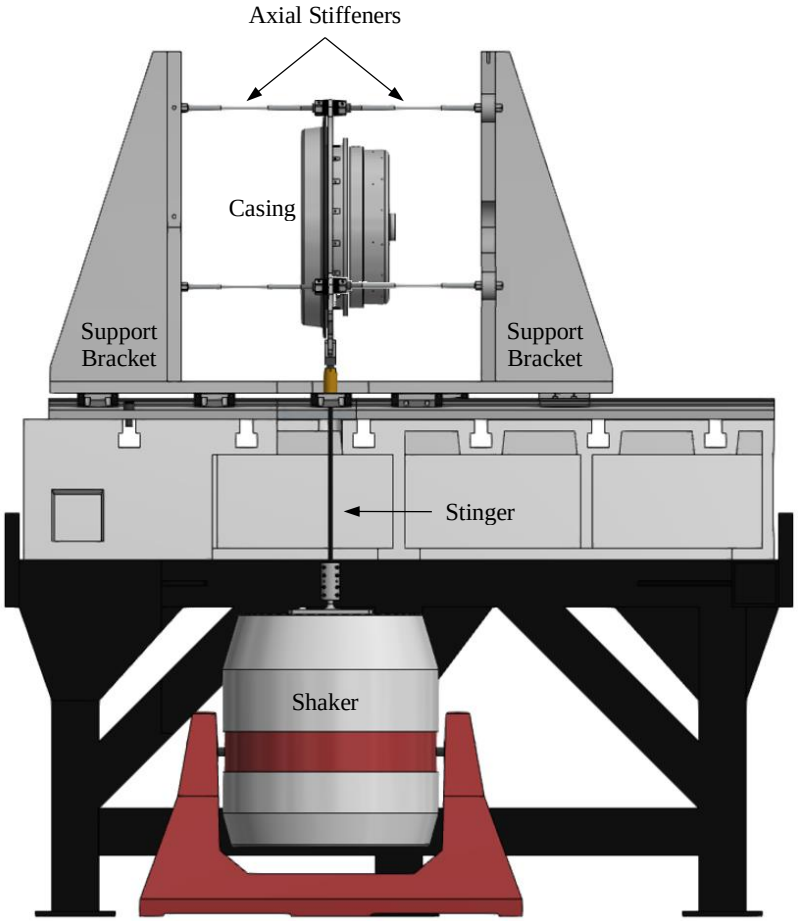

Figure 3.43. Vibration test subassembly.

The vibration test subassembly is depicted in Figure 3.43 and is composed of an electromagnetic shaker attached to the casing by a stinger. The casing is intended to move only within the plane containing the radial direction of the system, therefore it is mounted on three pairs of axial stiffeners, similar to those used by Childs and Hale [1994], that restrict the pitch of the casing. Two brackets are used at both sides of the casing in order to give support to the axial stiffeners.

3.7.1 Shaker stinger

A V-721 Bruel & Kjaer shaker able to supply a maximum force of 3000 N at a maximum acceleration of 66.3 g is utilised. The usable frequency range of this shaker is from 10 to 4000 Hz. The shaker is fixed to the ground and the casing is softly supported by the cables. According to Ewins [1984], this is the ideal mounting arrangement for an exciter. However,

in this case, the distance between the top surface of the shaker and the test structure is rather long and, therefore, care must be taken in order to stop the stinger from introducing spurious effects on the measured response of the system.

Previous research has been conducted in order to understand the effect that the stinger has on the modal test results and to find suitable stinger designs that decouple the behaviour of the shaker from that of its payload. In general terms, low bending stiffness and high axial stiffness are desirable, which is normally achieved by using long drive rods. However, stingers that are too long may result in axial resonance that contaminates the measured frequency response functions (Cloutier et al. [2009]). Harris and Bush [2015] summarised these generic rules into four quantitative criteria for the selection of an exciter drive rod. These four guidelines are the avoidance of fatigue-induced failure, buckling, axial resonance and transverse resonance. The length of the stinger was fixed by the distance between the shaker and the casing, and the selected material was steel; therefore, the only free parameter to be used as the design variable was the diameter of the rod. Appendix A shows the application of the four criteria mentioned previously for a final value of the rod diameter of 10 mm.

Figure 3.44 shows the drive rod and how it is assembled to the casing and the shaker. A left-hand threaded rod is bolted to the top plate of the shaker. The bottom end of the stinger is right-hand threaded. Both threaded rods are clamped together with a split coupling. If this coupling is fully fastened the stinger is locked. When the bolts are loosened, the height of the casing can be adjusted by rotating the coupling.

The top end of the stinger is bolted to the load cell. A fork attached to the casing is bolted to the other end of the load cell. Lock-nuts are used against the load cell to prevent the attachment from loosening under the effect of the vibrations.

3.7.2 Axial stiffeners

The axial stiffeners had the requirements of being flexible and having an adjustable means of attachment with the support brackets and the casing. Crimped stainless steel cables were the chosen solution as they provide the flexibility needed for the casing to be shaken and the threaded ends allow to control the position of the casing.

The cables were specified to have a tension load limit of 300 kg and a length of 360 mm. Two extra cables were purchased in order to perform tensile strength and fatigue tests on them. The calculation of the maximum load born by the cables and the results from these tests are presented in Appendix A. The cables were able to withstand a tensile load of 3,000 N with no plastic deformation. Likewise, the fatigue test proved the suitability of the cables for this

application; no change in length was observed after 3,000 cycle at the rated load. After these tests, the breaking load was checked. The cables yielded at 12,000 N and completely broke at 17,500 N.

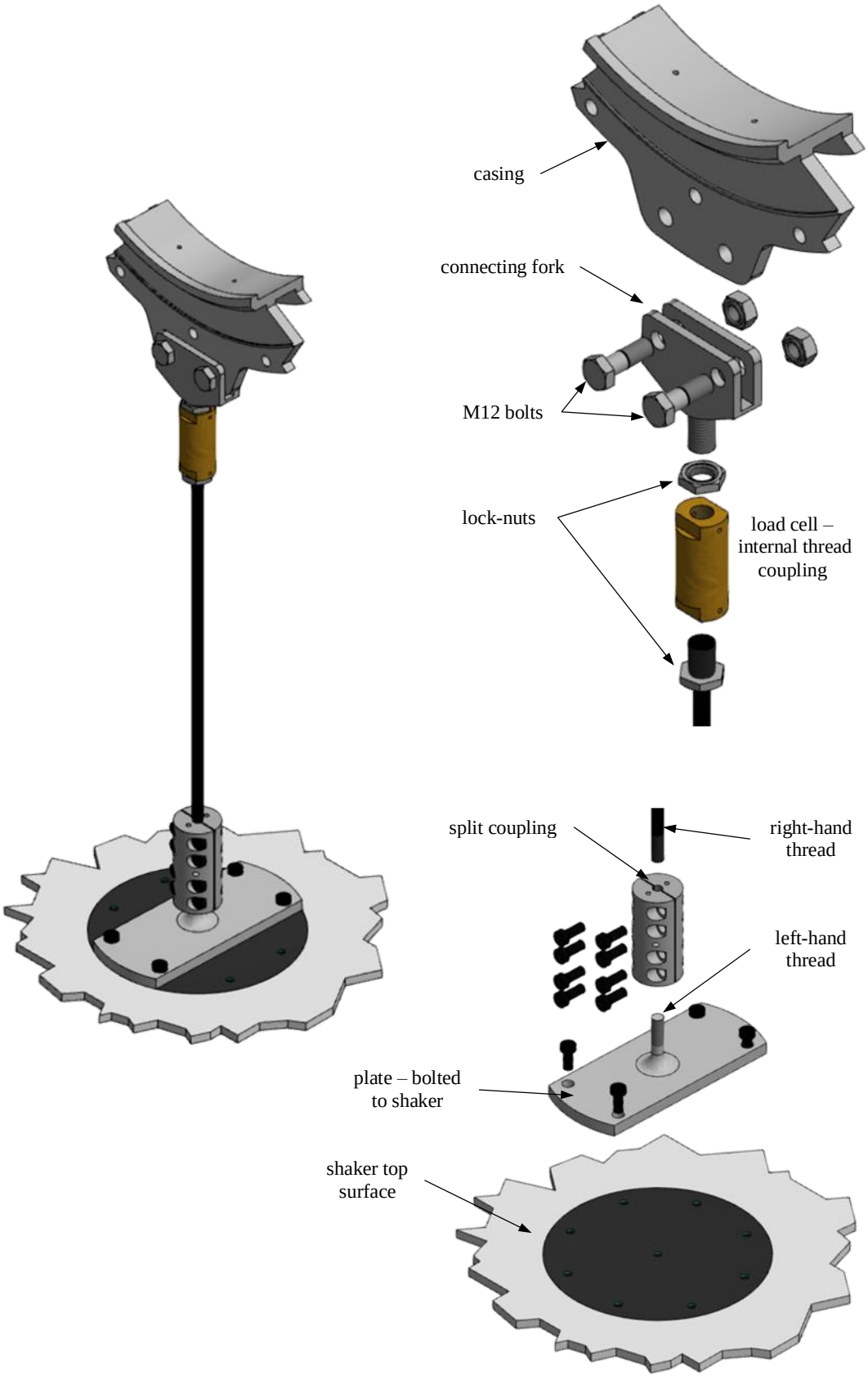

Figure 3.44: Isometric view of the rod connecting the shaker and the casing.

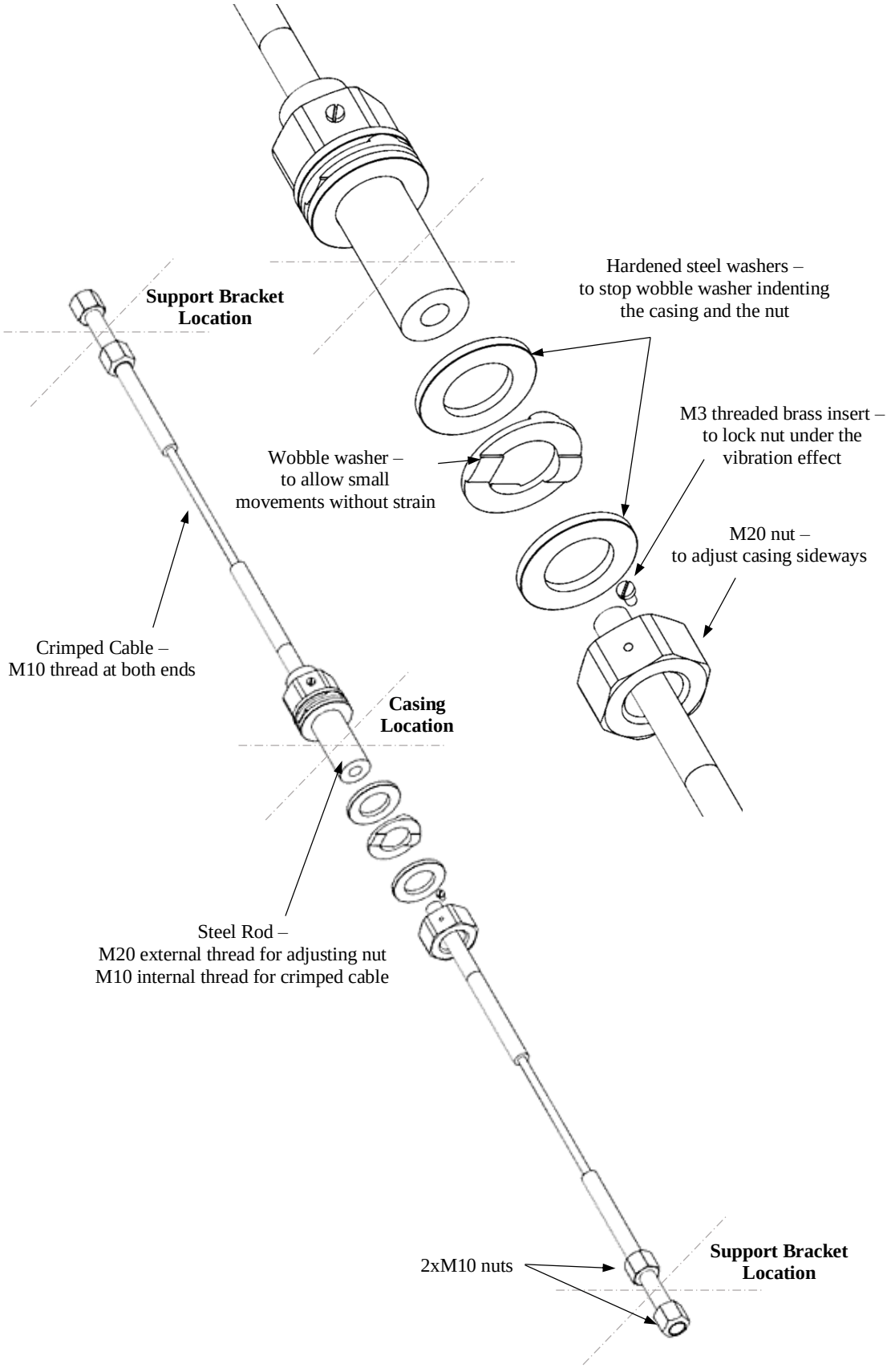

Figure 3.45: Axial stiffeners as assembled in the rig.

Figure 3.45 shows a pair of axial stiffeners and how they are assembled to the casing. A steel stud is internally threaded to fit the end of the crimped cables, ensuring good alignment of the cables. The steel stud is inserted on the lobe features of the casing (shown in Figure 3.25) and the external thread on the stud allows a nut on each side of the lobes to fix the casing in position. A brass insert is bolted to the positioning nuts through the stud in order to lock the nuts and prevent them from vibrating as the system is excited by the shaker.

3.7.3 Positioning ring

A positioning element encompasses the casing. It consists of a ring instrumented with four proximity probes used to track the position of the casing with respect to the absolute frame of reference. It also acts as a safety device which prevents the casing from moving further than desired. This is achieved by changing the clearance between the ring and the casing by adjusting locating screws. The screws also allow for a static eccentricity to be applied to the casing. Figure 3.46 shows an isometric view of the positioning ring where the squirrel-cage like design can be seen. Additionally, the positioning rig is shown in Figure 3.47 as assembled in the rig.

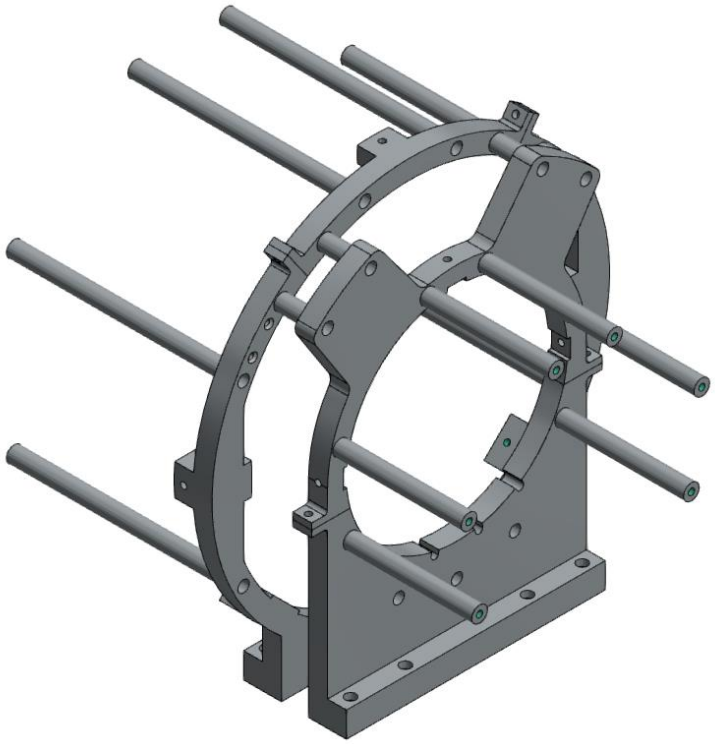

Figure 3.46: Isometric view of the positioning ring.

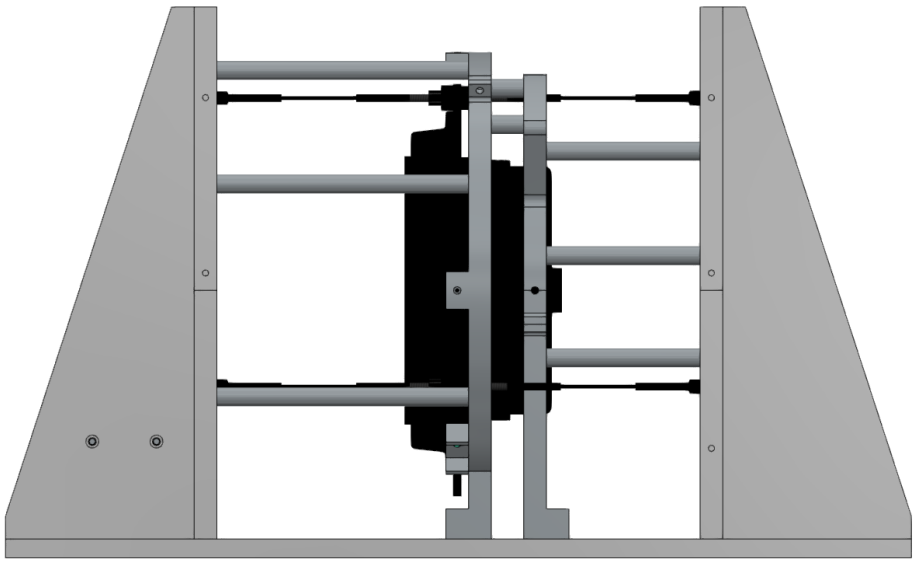

Figure 3.47: Positioning ring mounted around the casing

3.8 Rig design overview

After describing each subsystem composing the new test facility, the final general assembly of the rig together with a summary of its main characteristics is given in this section. Figure 3.48 shows a CAD representation of the new test facility; Figure 3.49 shows a cross-section view of the test section. The test section and the electric motor are located on top of a cast iron bedplate. A frame raises the bedplate from floor level and allows an electromagnetic shaker to be arranged underneath the test section. Compressed air at ambient temperature is supplied to a radial diffuser through a 50 mm diameter pipe. Once diffused, the air is split into 14 pipes, each of 19 mm diameter, before emerging into a small cavity, immediately upstream of the test section. A maximum pressure ratio of 3.5 bar across the test seal can be achieved in the rig.

The test seal is mounted in a casing that surrounds the rotor, containing the pressurised air in an annular test section; the leakage flow emerges into a collection system downstream of the seal. This collection system directs the leakage air towards an 80 mm pipe to which the mass flow meter is connected. Once the mass flow rate is measured the air is discharged to the atmosphere. If required, tests can be performed without the downstream collector in order to obtain access to the seal.

An electromagnetic shaker is used to perform a vibration test from which the rotordynamic coefficients of the testing seal are measured. Contrary to the real engine scenario, where the rotor translates relative to the seal, the test facility has been designed so that the casing is

shaken around the fixed rotor. Three pairs of pre-tensioned cables support the casing, allowing for the stator assembly to be shaken and preventing out-of-plane movement between the seal and the rotor. A drive rod connects the casing to the shaker.

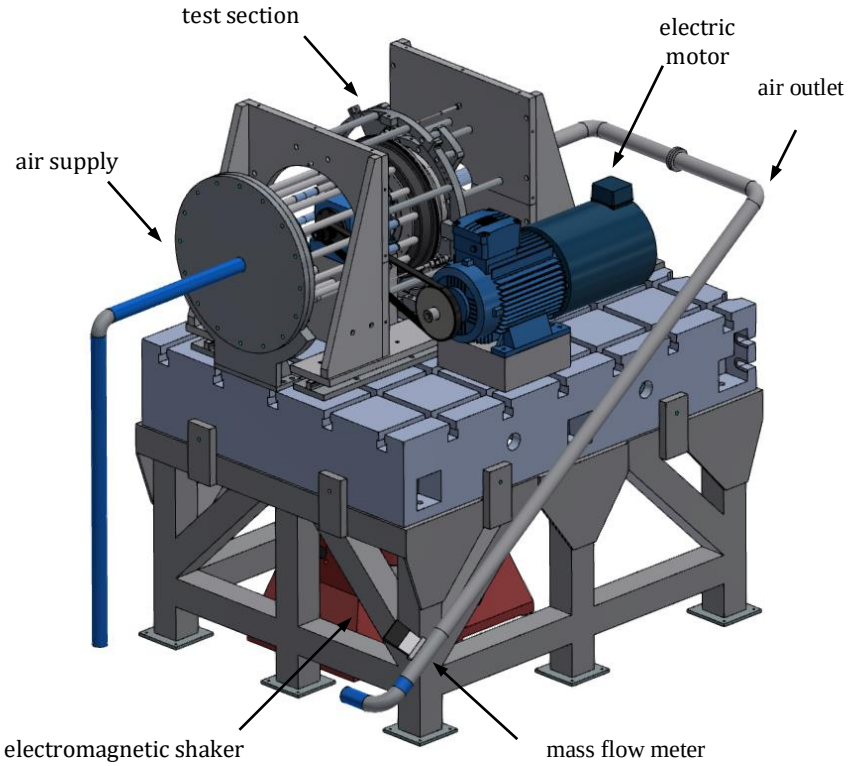

Figure 3.48. General assembly of the FRPALS rig.

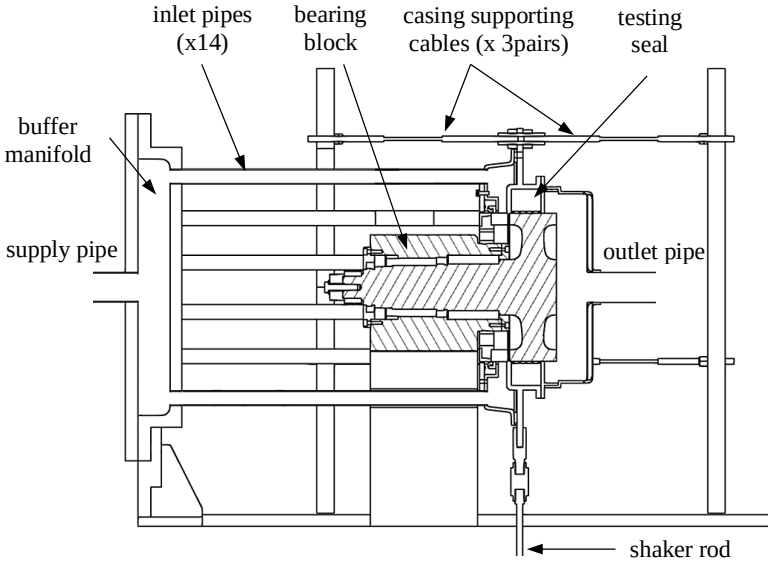

Figure 3.49: Cross section view of the test section

The electromagnetic shaker is capable of exciting the stator in the vertical plane, with a maximum force of 3000 N and a maximum frequency of 4000 Hz. The magnitude of the force applied to the seal is measured by a load cell, installed in line with the drive rod. Additionally, the acceleration of the casing and the relative position between the casing and the rotor are measured by an accelerometer and an eddy current probe, respectively, in both the direction of shaking and the lateral plane. Two horizontal stiffeners are mounted in the lateral plane, restricting the movement of the casing in this direction. The reaction force of the casing against these stiffeners is measured with a further load cell, installed in line with the stiffeners.

The rotor features a shaft and rotor disc, machined as one piece from forged EN40B nitrided, case-hardened steel. The shaft is rigidly supported by grease lubricated bearings and the rotor disc, with a diameter of 254 mm and an axial length of 80 mm, overhangs the bearing block in a cantilever arrangement. A 15 kW variable-speed AC motor drives the shaft through a 3:1 ratio pulley system, up to a maximum rotational speed of 15,000 rpm; the maximum rotor surface velocity is 200 m/s.

Chapter 4: Experimental methodology

This chapter introduces the rotordynamics problem in turbomachinery and the linear model used to represent the measured seal reaction forces. The methodology used to calculate the rotordynamic coefficients from measurements is then explained together with the steps to debug the parameter identification process. Additionally, the instrumentation used to measure the leakage performance of the seals tested is described and the concepts of flow coefficient and effective clearance are explained. A description of the data acquisition system is also given.

4.1 Turbomachinery rotordynamics

Since the advent of the gas turbine, the size and rotational speed of these machines have steadily grown in order to meet the ever-increasing demands for power output and efficiency. The rotational energy of such machinery is high and, hence, even small dynamic perturbations of the system may result in significant vibration problems. Additionally, the rotors of modern gas turbines are made relatively flexible, often operate above the flexural critical speeds. For these reasons, the study of the rotordynamic behaviour is of paramount importance during the design of turbomachines.

In the early stages of gas turbine development, only vibrations due to the structural aspect of the rotor were taken into account. However, designers soon realised that the dynamic behaviour of high performance turbomachinery is a result of the interaction of all the forces acting on the system. For instance, hydrodynamic bearings play an essential role in the stability of rotors. The thin film of oil that separates the rotor and stator absorbs the load of the rotor and changes its critical speeds. In the same way, the fluid-structure-interaction forces due to gas seals for steam and gas turbines, and non-symmetric clearances in turbine stages have a great impact on the stability of turbomachinery rotors. To give an idea of the complexity of the rotor dynamics problem, Table 4.1, from Matsushita *et al.* [2017], summarises the vibration phenomena occurring in a modern compressor and their causes.

One of the objectives of this thesis is to measure the rotordynamic coefficients of shaft seals for gas turbines. This is motivated by the fact that the experimental rotordynamic coefficients are needed to validate the mathematical models developed to predict the stability of gas seals. Once validated, the predicted rotordynamic coefficients are used as an input to models that simulate the rotor system as a whole. This is with the final goal of predicting the behaviour of the entire machine.

Table 4.1: Vibration phenomena in a modern compressor. From Matsushita *et al.* [2017].

FORCED VIBRATION	
PHENOMENA	CAUSES
Unbalance vibration	residual unbalance, thermal unbalance
Resonance	critical speed, blade resonance, foundation resonance, torsional resonance
Flow induced vibration	rotating stall, blade passing frequency
FREE VIBRATION (UNSTABLE)	
PHENOMENA	CAUSES
Oil-whip	sliding bearing, hydrodynamic bearing
Flow induced instability	gas seals, hydrodynamic bearings
Internal friction whirl	shrink-fit

4.2 Rotordynamic coefficients of gas seals

The gas that flows through the clearance of a seal exerts a force on the rotor that has an effect on the stability of the rotor system. This force arises due to changes in the pressure of the fluid film between the rotor and the seal. Direct measurement of the seal reaction force is rather complicated and, therefore, the linear model of Eq. 4.1 is used to represent it. The terms K_{ij}, C_{ij} and M_{ij} of Eq. 4.1 are the so-called rotordynamic coefficients. Note that in Eq. 4.1 the force due to the seal fluid film has been decomposed in the two directions of and orthonormal coordinate system attached to the rotor frame of reference. Figure 4.1 illustrates how the seal reaction force is modelled by a spring-damper system in a simplified one-dimensional case. Figure 4.2 is the upgraded two-dimensional version of Figure 4.1.

$$-\begin{bmatrix} f_{fluid_x} \\ f_{fluid_y} \end{bmatrix} = \begin{bmatrix} K_{xx} & K_{xy} \\ K_{yx} & K_{yy} \end{bmatrix} \begin{bmatrix} \delta x \\ \delta y \end{bmatrix} + \begin{bmatrix} C_{xx} & C_{xy} \\ C_{yx} & C_{yy} \end{bmatrix} \begin{bmatrix} \dot{\delta} x \\ \dot{\delta} y \end{bmatrix} + \begin{bmatrix} M_{xx} & M_{xy} \\ M_{yx} & M_{yy} \end{bmatrix} \begin{bmatrix} \ddot{\delta} x \\ \ddot{\delta} y \end{bmatrix} \quad \textbf{4.1}$$

Contrary to liquid journal bearings and liquid seals, annular gas seals and labyrinth gas seals have axisymmetric behaviour when small motion about a centred position is assumed (Childs [1993], San Andrés *et al.* [2010]). This allows the model of Eq. 4.1 to be further simplified:

$$-\begin{bmatrix} f_{fluid_x} \\ f_{fluid_y} \end{bmatrix} = \begin{bmatrix} K & k \\ -k & K \end{bmatrix} \begin{bmatrix} \delta x \\ \delta y \end{bmatrix} + \begin{bmatrix} C & c \\ -c & C \end{bmatrix} \begin{bmatrix} \dot{\delta} x \\ \dot{\delta} y \end{bmatrix} + \begin{bmatrix} M & 0 \\ 0 & M \end{bmatrix} \begin{bmatrix} \ddot{\delta} x \\ \ddot{\delta} y \end{bmatrix} \quad \textbf{4.2}$$

where *K* and *C* represent the direct stiffness and damping respectively, and *k* and *c* are the cross-coupled stiffness and damping coefficients, respectively. The second order coefficient M is referred to as added mass. It will be shown that this coefficient is zero for annular gas seals, however is left in the methodology for the sake of completeness.

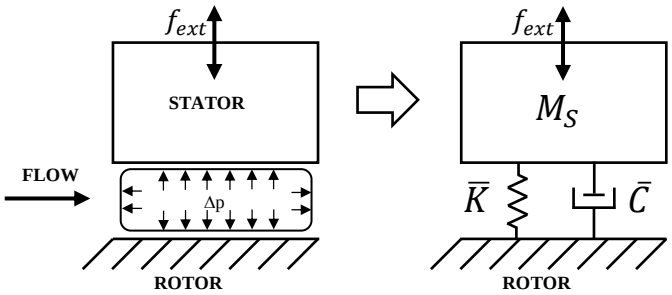

Figure 4.1: Model of the seal reaction forces as a spring-damper system. The frame of reference is fixed to the rotor.

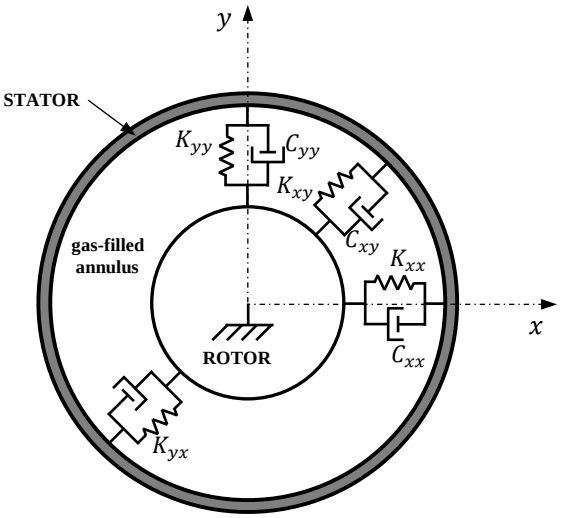

Figure 4.2: Dynamic model of a gas seal with a centred rotor.

To understand the physical meaning of the rotordynamic coefficients, consider the whirling rotor of Figure 4.3, with rotational speed, ω, a precession with a forward orbit of amplitude, *A*, and whirling speed, Ω. Rotor instabilities occur when the rotor precessional speed is equal to the rotational speed, i.e. ω = Ω. The seal forces in Eq. 4.2, reacting on the rotor and projected in the radial and tangential directions, are expressed by:

$$\begin{aligned} \boldsymbol{f_r} &= -(\boldsymbol{K} + \boldsymbol{\Omega} \cdot \boldsymbol{c}) \cdot \boldsymbol{A} \\ \boldsymbol{f_\theta} &= (\boldsymbol{k} - \boldsymbol{\Omega} \cdot \boldsymbol{C}) \cdot \boldsymbol{A} \end{aligned} \qquad \textbf{4.3}$$

Positive values of f_r and f_θ are destabilising for the rotor (moving it away from the seal centre), whereas negative values of these forces have a stabilising effect. Radial forces are typically small in labyrinth seals (Childs and Vance [1997]). The tangential component of the

seal reaction force has a greater impact on the stability of the seal. From Eq. 4.3, in order to have a stable system, i.e. negative values of the tangential force, the factor ($\Omega \cdot C - k$) has to be maximised; this is achieved by increasing the value of C or reducing k.

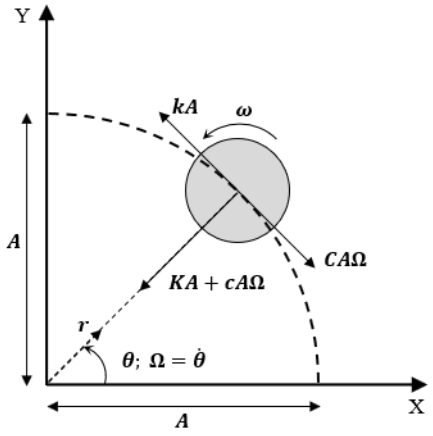

Figure 4.3: Schematic of the seal reaction forces on a whirling rotor. Adapted from Arthur and Childs [2015].

The expression of the tangential force in Eq 4.3 can be manipulated to give:

$$-\frac{f_\theta}{A} = C \cdot \Omega - k = C\left(1 - \frac{k}{C \cdot \Omega}\right)\Omega = C_{eff} \cdot \Omega \qquad 4.4$$

were C_{eff} is the effective damping. This is a parameter that combines the effect of both the cross-coupled stiffness and the direct damping, which are the rotordynamic coefficients that contribute to the tangential reaction force of the seal. For this reason, and according to Childs and Vance [1997], the effective damping is the best parameter to compare the stability of different annular gas seals at a given rotational speed.

4.3 Rotordynamic coefficients measurement methodology

The method developed by Rouvas and Childs [1993] is used. Newton's second law applied to the stator with a fixed rotor to yield:

$$\sum \vec{f} = \vec{f}_{fluid} + \vec{f}_{ext} = M_{stator} \cdot \vec{a} \qquad 4.5$$

where $\vec{f}_{ext}$ is the external force applied with the shaker, M_{stator} is the mass of the stator and $\vec{a}$ is the measured acceleration of the stator. For the sake of completeness, the linear model of Eq 4.1 for the forces generated by the fluid film between the rotor and the seal (f_{fluid_x}, f_{fluid_y}) is used. The combination of Eq. 4.1 with Eq. 4.5 gives the following expression:

$$\begin{bmatrix} f_{ext_x} - M_{stator} \cdot a_x \\ f_{ext_y} - M_{stator} \cdot a_y \end{bmatrix} = \begin{bmatrix} K_{xx} & K_{xy} \\ K_{yx} & K_{yy} \end{bmatrix} \begin{bmatrix} \delta x \\ \delta y \end{bmatrix} + \begin{bmatrix} C_{xx} & C_{xy} \\ C_{yx} & C_{yy} \end{bmatrix} \begin{bmatrix} \dot{\delta x} \\ \dot{\delta y} \end{bmatrix} + \begin{bmatrix} M_{xx} & M_{xy} \\ M_{yx} & M_{yy} \end{bmatrix} \begin{bmatrix} \ddot{\delta x} \\ \ddot{\delta y} \end{bmatrix} \quad \textbf{4.6}$$

Assuming that the force applied with a shaker and the displacement components of the stator are sinusoidal functions as depicted in 4.7:

$$f_{ext} = A \cdot cos\omega t;\ \delta x = B \cdot cos\omega t \quad \textbf{4.7}$$

Transformation of Eq. 4.6 to the frequency domain results in:

$$\begin{bmatrix} F_{ext_x} - M_{stator} \cdot A_x \\ F_{ext_y} - M_{stator} \cdot A_y \end{bmatrix} = \begin{bmatrix} H_{xx} & H_{xy} \\ H_{yx} & H_{yy} \end{bmatrix} \begin{bmatrix} X \\ Y \end{bmatrix} \quad \textbf{4.8}$$

where F and A are the Fourier transforms of the applied force and the measured acceleration of the stator, respectively. In the same manner, X and Y are the direct Fourier transforms of the casing displacement measured in the time domain.

To completely determine the four components of H_{ij}, two separate excitations must be applied to the seal, to yield independent sets of Eq. 4.8. This is done by sequentially exciting the seal in the X and Y directions individually, while ensuring the external force in the other direction equal to zero. The two separate applied excitations yield the system of equations depicted in Eq. 4.9:

$$\begin{bmatrix} {F^x}_{ext_x} - M_{stator} \cdot {A^x}_x & {F^y}_{ext_x} - M_{stator} \cdot {A^y}_x \\ {F^x}_{ext_y} - M_{stator} \cdot {A^x}_y & {F^y}_{ext_y} - M_{stator} \cdot {A^y}_y \end{bmatrix} = \begin{bmatrix} H_{xx} & H_{xy} \\ H_{yx} & H_{yy} \end{bmatrix} \begin{bmatrix} X^x & X^y \\ Y^x & Y^y \end{bmatrix} \quad \textbf{4.9}$$

The superscripts in Eq. 4.9 refer to the direction in which the excitation is applied. However, as explained in Section 4.2, the behaviour of gas seals is axisymmetric for small movements of the rotor from its centre. Therefore, in this case it is assumed that $H_{yy} = H_{xx}; H_{yx} = -H_{xy}$, which reduces the four H_{ij} unknowns of Eq. 4.9 into only two. For this reason, only one excitation is needed to calculate the rotordynamic coefficients of the seal.

H is obtained by solving Eq. 4.9:

$$H = A \cdot B^{-1} \quad \textbf{4.10}$$

were A is the left hand side matrix of Eq. 4.9 ($A_{ij} = F^j_{ext_i} - M_{stator} \cdot A^j_i$) and B is the displacement matrix in Eq. 4.9.

Finally, each term of the matrix H_{ij}, is a function of the frequency and of the rotordynamic coefficients:

$$\boldsymbol{H_{ij} = K_{ij} + j\omega C_{ij} - \omega^2 M_{ij}} \quad \textbf{4.11}$$

If the real part of the complex stiffness, $Re(H_{ij})$, is fitted with a second order polynomial, the zero-frequency intercept corresponds to the stiffness coefficient of the seal and the second order coefficient to the added mass of the seal. The damping is determined by the first order coefficient (slope) of a linear curve fit passing through the origin of the imaginary part of the complex stiffness, $Im(H_{ij})$. The maximum likelihood estimation method has been used to calculate the fit coefficients of both the real and imaginary parts of the complex stiffness; see Davison [2003] and Silvey [2017] for a detailed explanation of this technique.

Note that, in contrast to what happens in a real engine, in the experiment the absolute frame of reference is fixed to the rotor and the stator moves relative to it. This is depicted in Figure 4.2, which is a schematic representation of Eq. 4.6. This may seem odd when the purpose of this experiment is to measure the effect a gas seal has on the dynamic behaviour of the mating rotor, i.e. the rotordynamic coefficients of the seal. However, as mentioned before, these coefficients represent the forces that the leakage air exerts on the rotor and, therefore, these are the only forces that are going to be measured, no matter whether they react on the rotor or on the stator. Indeed, because of the nature of this experiment, in which the rotor is kept fixed for the ease of operation, the seal reaction forces are measured as they react on the stator.

The vibration test records the response of the casing. This response includes not only the reaction forces of the seal, but also the dynamics of the mechanical parts to which the casing is attached; namely, the axial stiffeners, the flexible inlet pipes, and the contact seal. The effect of all these components has to be decoupled from the overall response of the casing. This is done by running two different experiments. Firstly, a test is performed without air passing through the seal and without rotation of the rotor. This test is referred to as ‘baseline’ test and accounts for the response of the casing system without the effects of the seal forces. In the second test a pressure drop is applied across the testing seal and the rotor is spun to measure the overall response of the casing. The results from the baseline test are subtracted from the results of the second run in order to obtain the response of the stator due to the seal reaction forces only.

The methodology explained in this section has been derived under some assumptions:

- The stiffness and damping of the system are independent of the excitation frequency.
- Second order effects of the displacement, velocity and acceleration of the rotor are neglected in the model of the seal reaction forces.
- The behaviour of gas seals is axisymmetric for small motions around the centre of the seal.

4.3.1 Rotordynamic coefficients instrumentation

Figure 4.4 and Figure 4.5 show the instrumentation arrangement used to measure the rotordynamic coefficients using the methodology explained previously. The magnitude of the force applied to the seal with the shaker is measured by a load cell, installed in line with the drive rod. Additionally, the acceleration of the casing and the relative position between the casing and the rotor are measured by an accelerometer and an eddy current probe, respectively, in both the direction of shaking and the lateral plane. Two horizontal stiffeners are mounted in the lateral plane, restricting the movement of the casing in this direction. The reaction force of the casing against these stiffeners is measured with a further load cell, installed in line with the stiffeners.

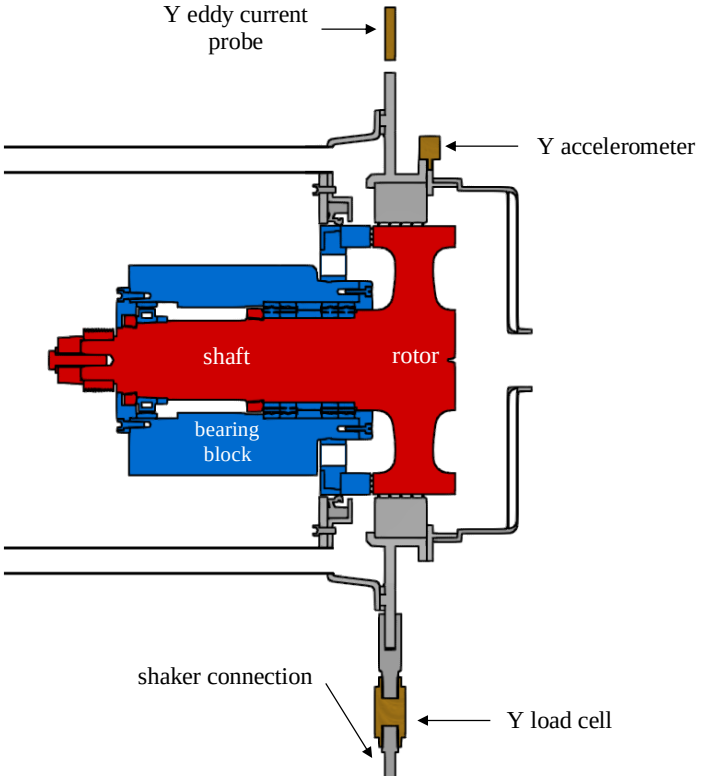

Figure 4.4: Close-up view of the test section: details of instrumentation for rotordynamic coefficients.

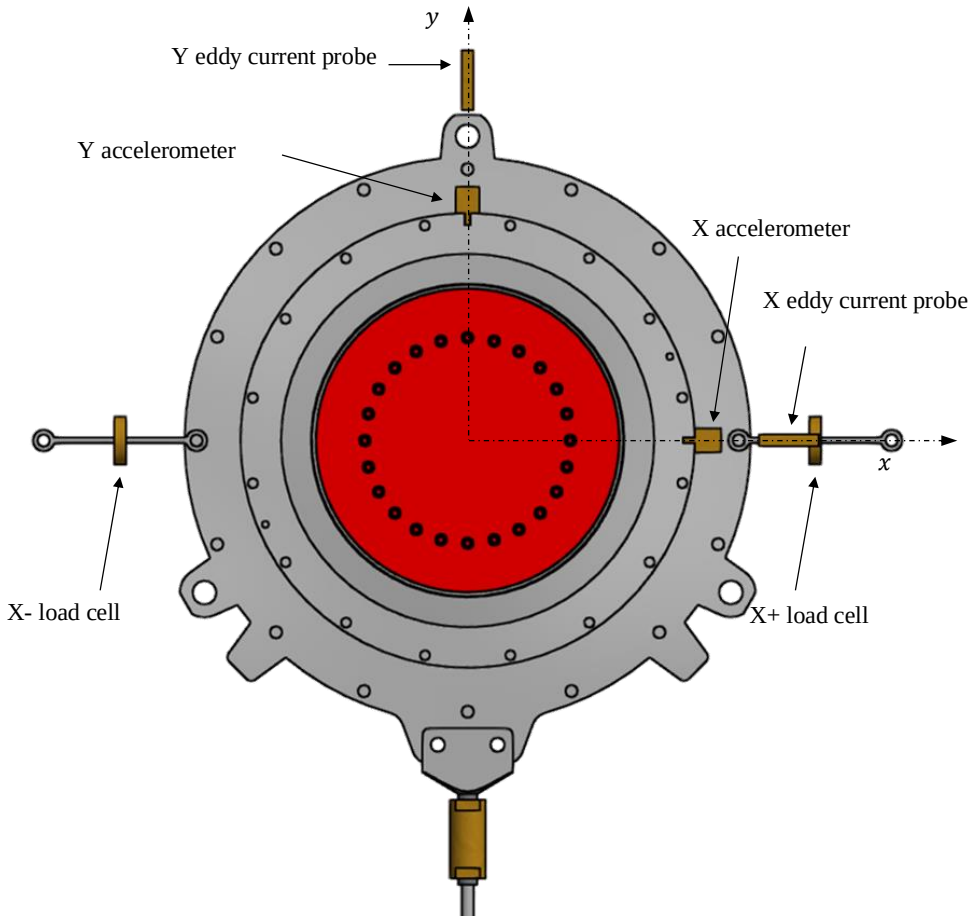

Figure 4.5: Front view of the test section: plane of casing movement (x-y) and instrumentation used to measure the rotordynamic coefficients of the testing seal.

4.3.2 Methodology debugging

A Simulink model that simulates the mass-spring-damping system in Figure 4.1 is used to apply the parameter identification methodology explained above to a known system and confirm that the results given by the methodology are as expected. The block diagram of the modelled system is represented in Figure 4.6, where the mass, stiffness and damping constants are highlighted. The input force, and the output acceleration and displacement given by the model are saved as Matlab variables. They are then fed into the post-processing routine in order to calculate back the constants of the simulated system.

The input force of the simulation is a chirp waveform which frequency changes linearly with time between 10 Hz and 160 Hz. The waveform is followed by a zero level continuous signal (no excitation) that allows residual vibration of the system to be damped out without being forced to stop.

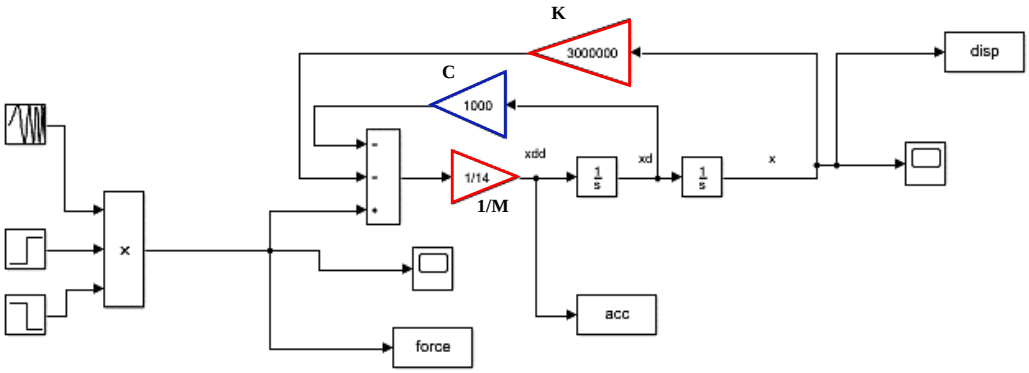

Figure 4.6: Block diagram of the second-order system used to validate the parameter identification methodology.

$$\boldsymbol{f_{ext} = K \cdot x + C \cdot \dot{x} + M_{stator} \cdot \ddot{x}} \qquad \textbf{4.12}$$

Eq. 4.12 governs the movement of this one-dimensional system. The identification parameter problem can be tackled from two different points of view. One way is to assume that the mass is known and equal to 14 kg. With this approach, the resulting added-mass must be equal to zero. In other words, the real part of the complex stiffness is a horizontal line; this is shown in Figure 4.7. An alternative way of identifying the parameters of the system is assuming that the mass is zero. This cancels the acceleration term in Eq. 4.12 and the effect of the mass manifests now as a result in the form of added-mass. In this case, the second order term of the polynomial fit of the real part of the complex stiffness is equal to 14 kg, as shown in Figure 4.8. This highlights the importance of the stator mass term in the dynamic equation of the system and it will be further discussed in the next step of the debugging process.

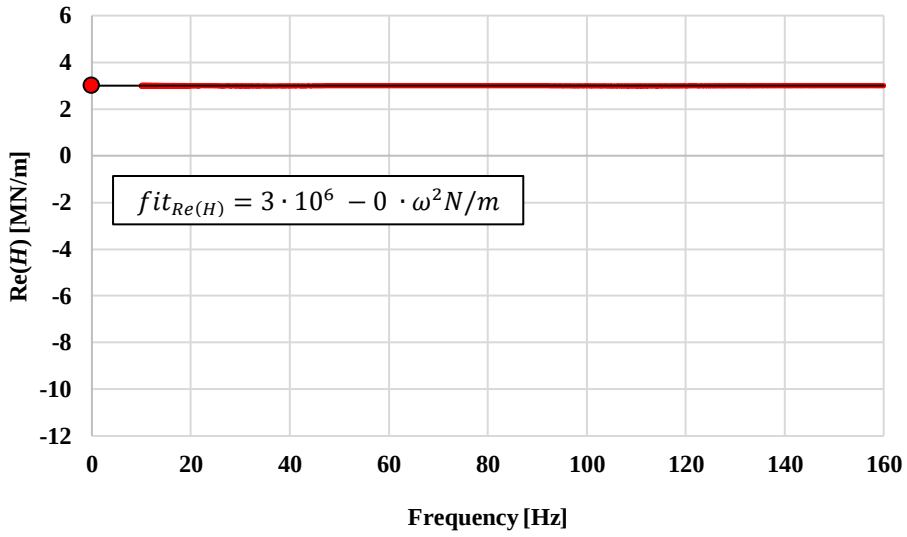

Figure 4.7: Real part of the direct complex stiffness when calculated using a stator mass equal to 14 kg.

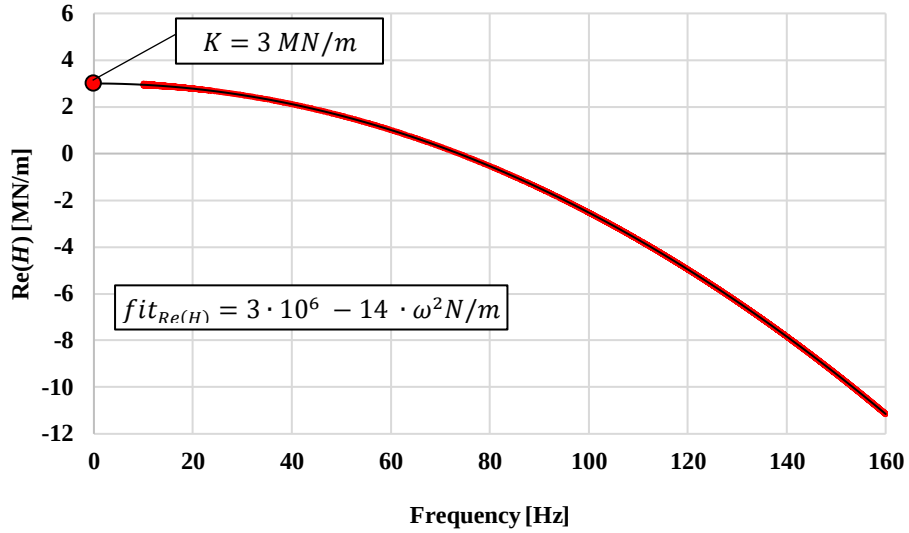

Figure 4.8: Real part of the direct complex stiffness when calculated using a zero stator mass.

The zero intercept of the real part of the frequency response function in both cases is equal to 3 MN/m which is the value of the displacement gain (stiffness) in the Simulink model. Likewise, the imaginary part of the frequency response function remains unchanged for both cases and its slope is equal to 1000 Ns/m, which corresponds to the value of the velocity gain (damping) in the model; this is shown in Figure 4.9.

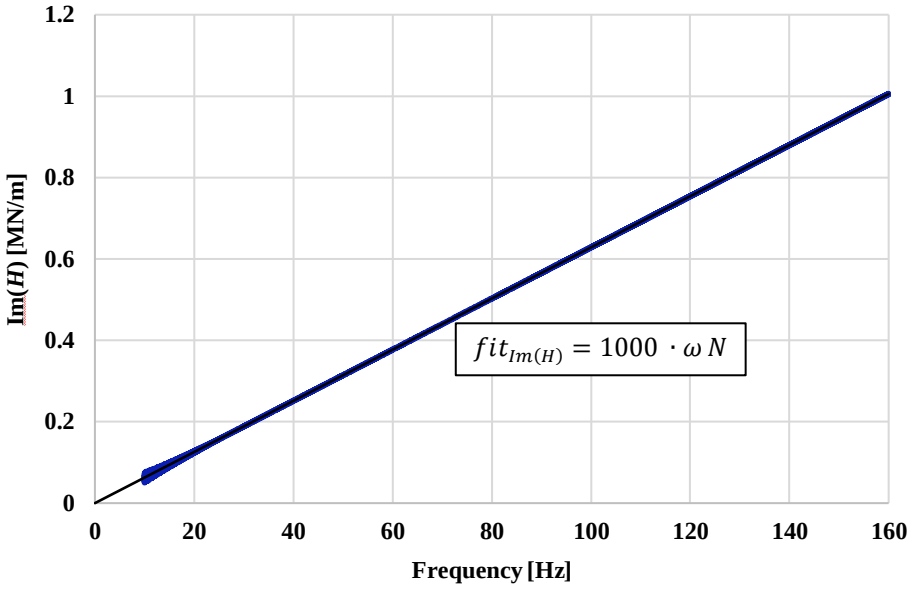

Figure 4.9: Imaginary part of the direct complex stiffness.

Once the post-processing routine was validated with the synthetic data, the following step was to examine the behaviour of the real seal system. The casing assembly was broken down into different levels of complexity and different vibration tests were performed to understand

the contribution of each component of the assembly to the final results. A first vibration test was performed in which only the casing hanging from the cables and attached to the inlet pipes is shaken. The impedances (complex stiffnesses) of this set-up against frequency are shown in Figure 4.10, Figure 4.12, and Figure 4.14. In general terms, it can be seen that the frequency response functions do not perfectly match the trends dictated by the linear model, which is expected when dealing with a real system. The largest mismatch occurs at the high frequency range.

The fit of the real part of the direct complex stiffness, shown in Figure 4.10, gives a stiffness of the system equal to 0.4 MN/m. A value of the second order term coefficient of 0.802 kg is obtained, whereas a value of zero was expected. This non-zero value of the added-mass coefficient gives the real part of the complex stiffness the apparent frequency dependency shown in Figure 4.10. As stated before, the mass of the stator is an important input to the parameter identification procedure and small errors in this input are reflected in the form of an added-mass. This complex stiffness has been computed with a stator mass equal to 9.45 kg, which corresponds to the weight of all the components that have been shaken in the test. The difference between the weighed mass and the predicted one may be due to the fact that it is difficult to assess what is the proportion of the support cables that is actually 'seen' by the system and what is the effect of the flexible hoses that are attached to the casing.

If the added-mass of 0.802 kg is summed with the stator mass and the parameter identification routine is run again with this new mass ($M_s = 10.258\ kg$), the new resultant added-mass is negligible ($M_{added} = 0.03\ kg$). Consequently, the real part of the direct complex stiffness is horizontal, i.e. it does not depend on the frequency, as shown in Figure 4.10. The other two impedances only marginally change when adjusting the value of the stator mass in the routine. The difference is so small that only the final results computed with the new mass ($M_s = 10.258\ kg$) are shown in Figure 4.12 and Figure 4.14.

It was anticipated that the resulting added mass was negligible for the tests shown in this section. This term is different than zero only when the shaken payload has moving parts attached to it, adding degrees of freedom to the system, as what happens with some seal designs. For instance, the FRPALS is expected to yield a non-zero added-mass coefficient. Therefore, this term has been left in the equation during the debugging process for the sake of completeness.

The real part of the cross-coupled complex stiffness is shown in Figure 4.12. This impedance of the system is frequency independent between 10 to 90 Hz. In this same frequency range, the value of the cross-coupled stiffness is zero, which means that as the casing is forced to move in the vertical direction no movement is recorded in the horizontal direction.

This is expected in a well aligned system in which all the movement occurs in the direction of the applied force. However, perfect alignment is impossible and, at frequencies higher than 90 Hz, the real part of the complex cross-coupled stiffness differs from zero.

Figure 4.14 shows the imaginary part of the direct complex stiffness. According to Eq. 4.11, the slope of this curve is equivalent to the damping of the system. A linear fit passing through the origin gives a damping value of 242 Ns/m.

Next, the contact, rubber seal is installed and a new vibration test is performed. The results are plotted in Figure 4.11, Figure 4.13 and Figure 4.15, together with the results from the test without rubber seal for reference. Figure 4.13 shows no significant changes in the real part of the cross-coupled complex stiffness between both tests. In contrast, the direct stiffness has increased by a factor of two, as indicated by the difference between the ordinate in the origin of the polynomial fits of both tests, highlighted in Figure 4.11 by a red and a grey circle.

The direct damping of the system with rubber seal is five times the value of the damping when the seal was not installed; this can be seen in the difference in slope of the linear fits shown in Figure 4.15. Additionally, as the high frequency data deviates from the linear model more than the low frequency results, it was decided to fit only the data between 0 and 50 Hz in order to have a more accurate estimation of the damping of the system. The low frequency range fit, shown in Figure 4.15 in red, yields a value of the damping of the rig with the rubber seal installed almost 2.5 times greater than the fit including the data of the whole tested frequency range. Overall, it can be said that the signal noise influence on the real and the imaginary parts of the direct complex stiffness has significantly increased.

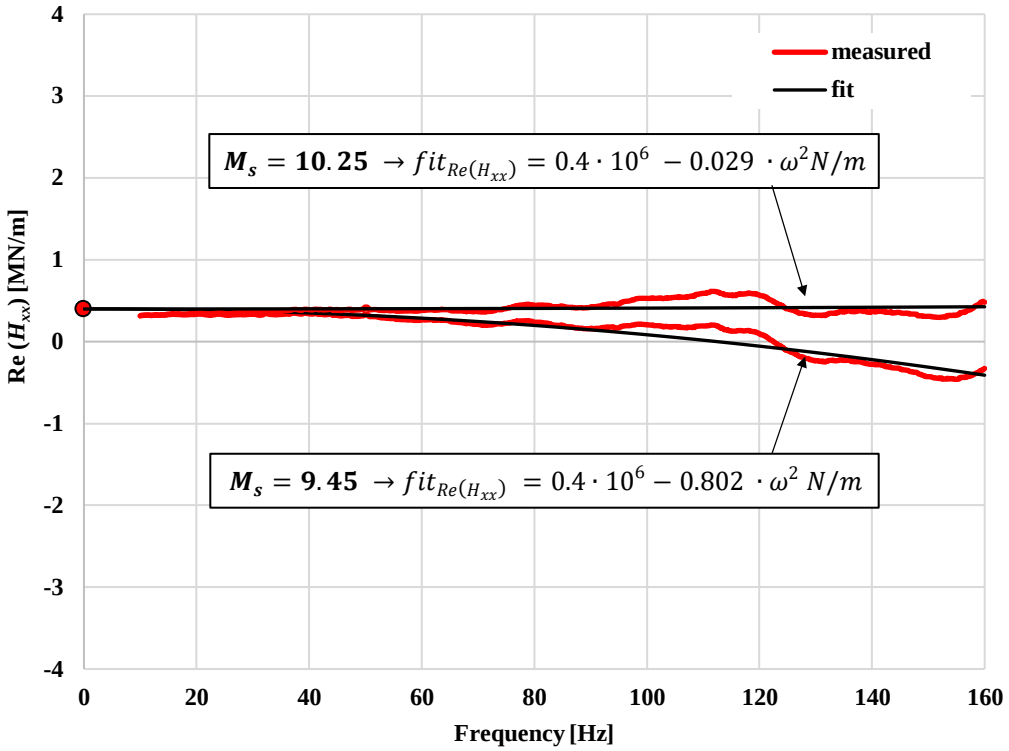

Figure 4.10: Real part of the direct complex stiffness for the test in which only the casing is shaken (without the rubber seal installed).

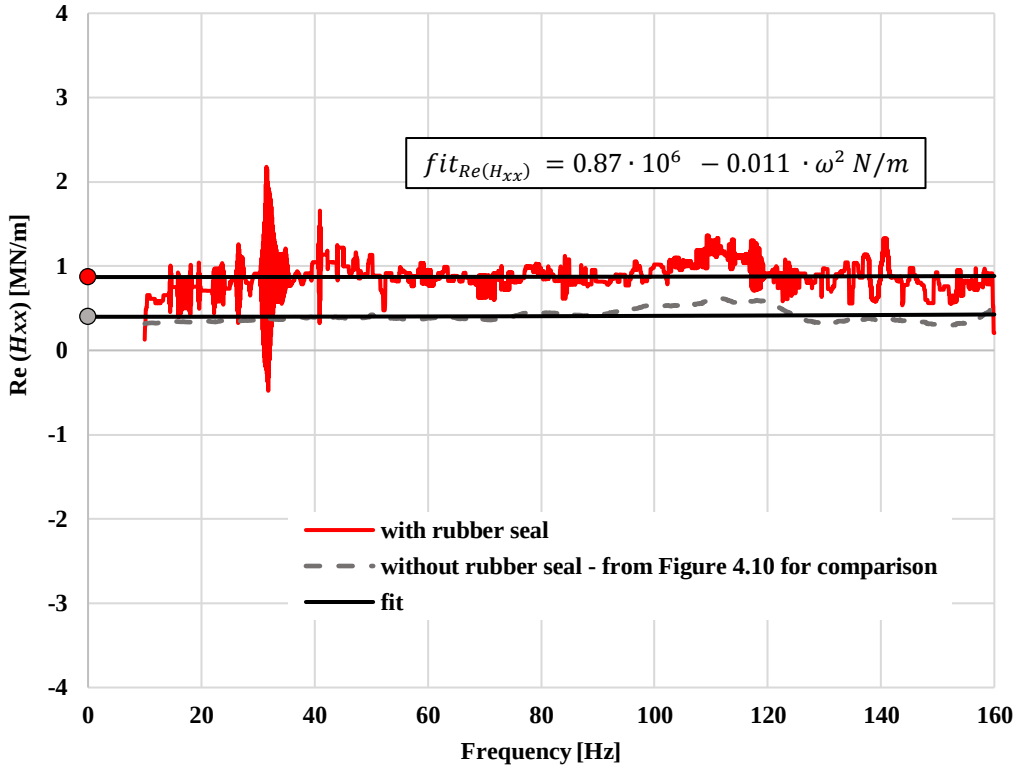

Figure 4.11: Real part of the direct complex stiffness for the test with the rubber seal installed.

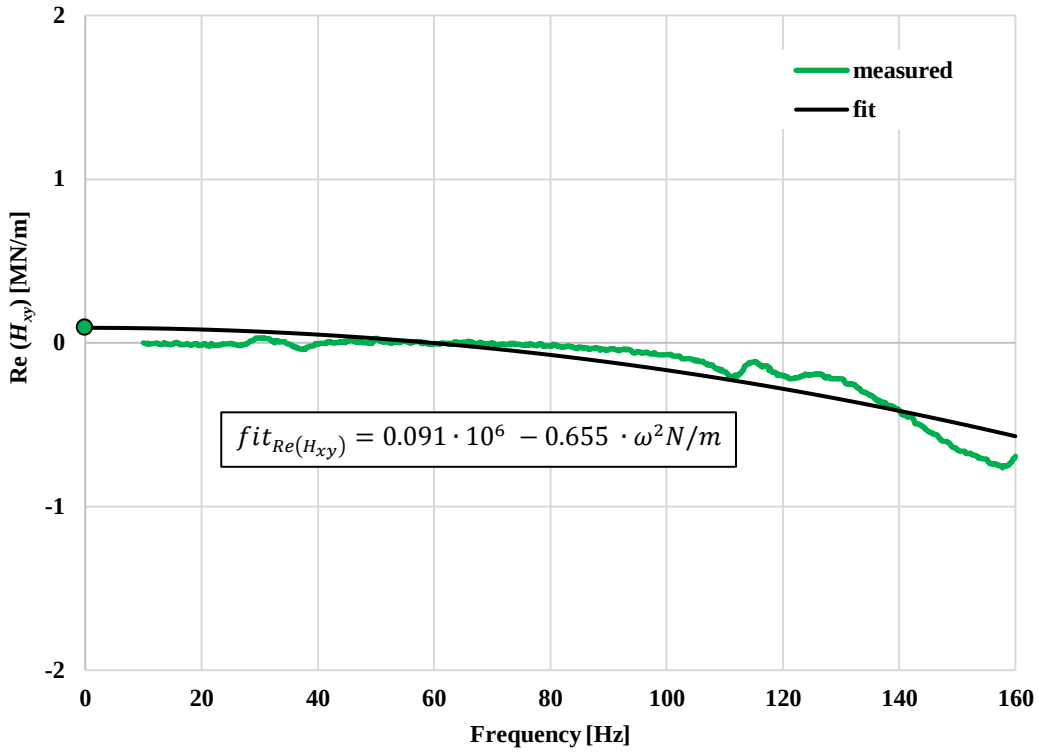

Figure 4.12: Real part of the cross-coupled complex stiffness for the test in which only the casing is shaken (without the rubber seal installed).

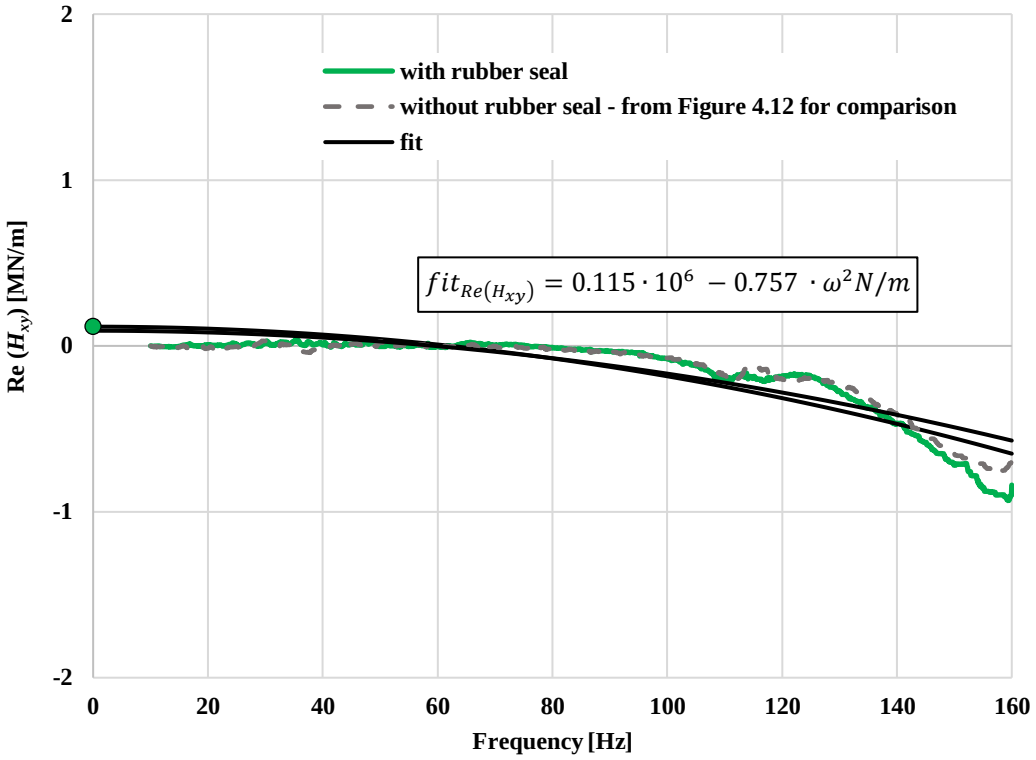

Figure 4.13: Real part of the cross-coupled complex stiffness for the test with the rubber seal installed.

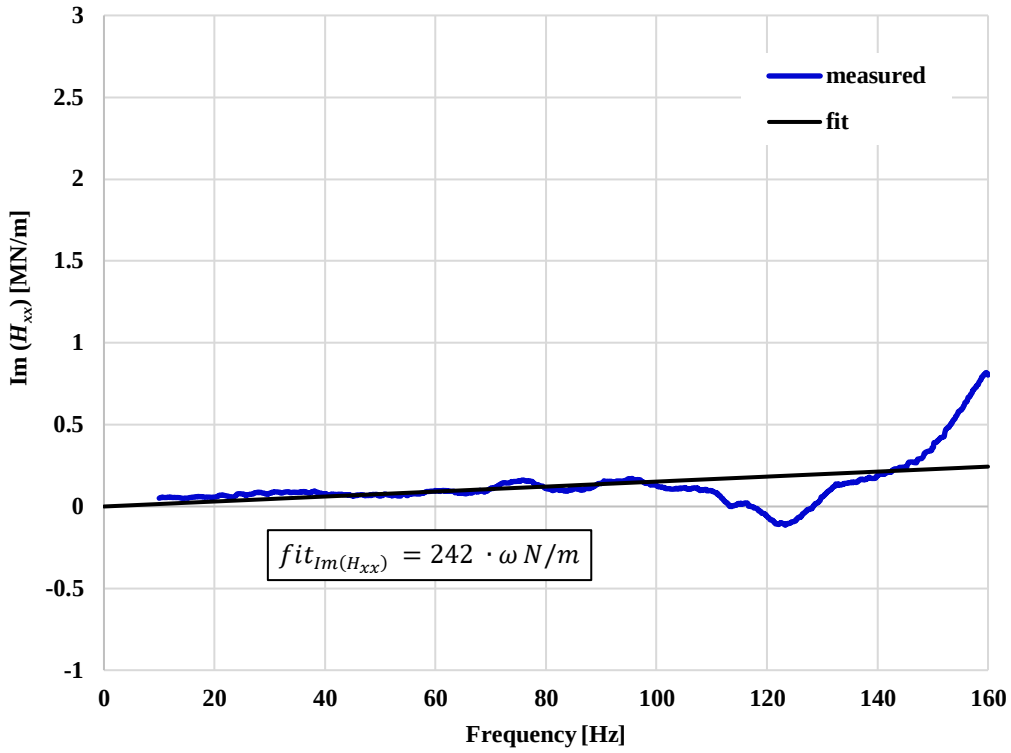

Figure 4.14: Imaginary part of the direct complex stiffness for the test in which only the casing is shaken (without the rubber seal installed).

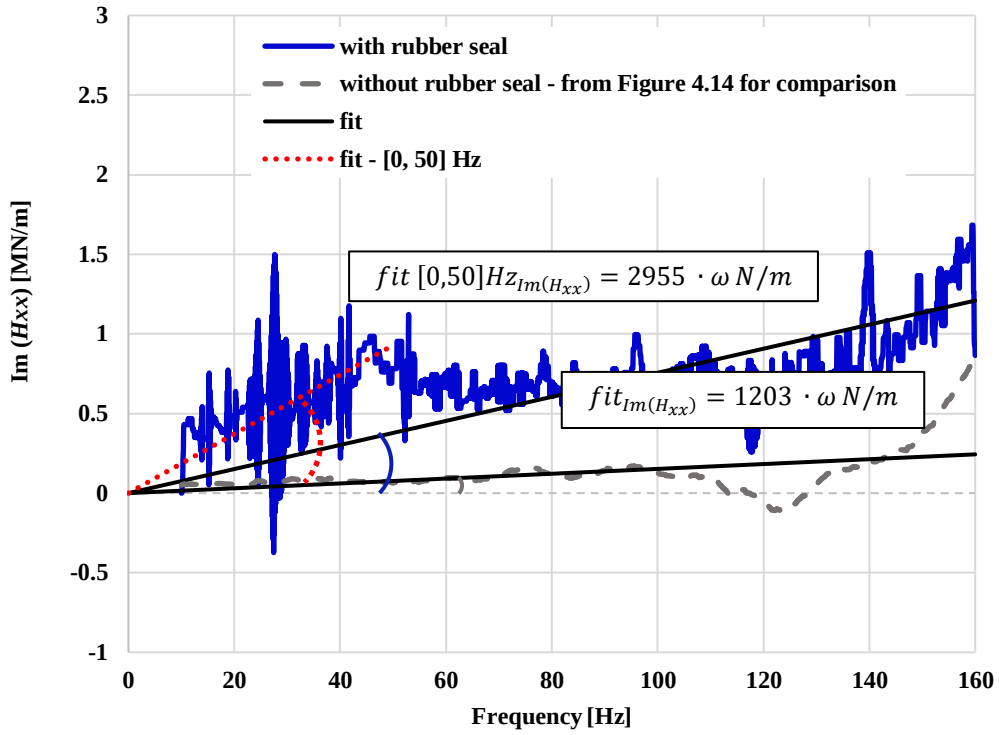

Figure 4.15: Imaginary part of the direct complex stiffness for the test with the rubber seal installed.

The frequency response functions shown above are the result of exciting the seal housing with the shaker. The type of dynamic excitation chosen is a sinusoidal waveform in which the frequency varies linearly with time, i.e. a chirp signal. As summarised by Tiwari et al. [2004], other researchers have used pseudo random binary sequences or Schroeder-phased sinusoidal signals. These signals are claimed to give better results as they yield a peak factor of the force given by the shaker ($F_{max} - F_{min}$) greater than the sine sweep. However, the linear sine sweep excitation is used in this research as it allows to excite all the frequencies of interest with the advantage of being a more controllable and intuitive approach.

For a constant input signal, the amplitude of the force given by the shaker decreases as the frequency increases. Therefore the amplitude of the demand signal has to be adjusted so that the output is large enough. If this is not done, the response of the system at high frequencies is hidden in noise (a low signal-noise ratio). Several trial-and-error iterations were made to find a shaker input signal that provided good results. Figure 4.16 shows three examples of amplitude vs. frequency profile tested.

Also, in the low frequency range, large shaker inputs imply large output forces which translates into displacements that are greater than the seal clearance; for safety reasons this is undesirable.

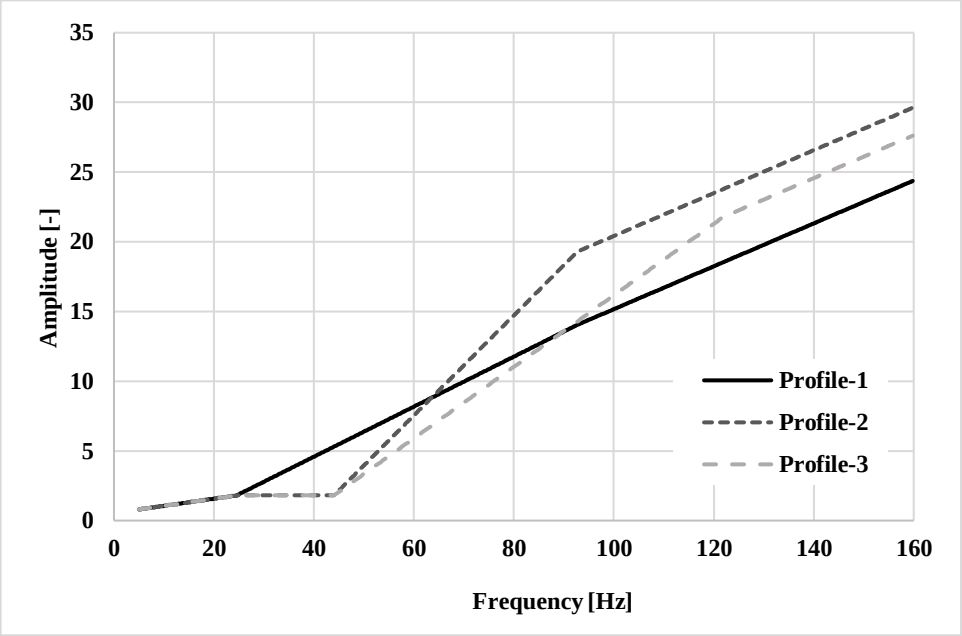

Figure 4.16: Amplitude of three different shaker input signals.

4.4 Mass flow rate, effective clearance, flow coefficient and discharge coefficient

- **Leakage mass flow rate**: Downstream of the seal, the air is collected in a single exit pipe and a mass flow meter measures the leakage of the seal. A Bronkhorst thermal mass flow meter is used for this purpose. The meter has a range of 0.004 – 0.35 kg/s with an accuracy, at calibration conditions, equal to +/- 1% of the full scale. This translates into an accuracy of +/- 3.5% of the reading for a typical test with a mass flow rate of 0.1 kg/s. This is an acceptable level of accuracy for the nature of this test, given that any deviation of the flow temperature from the calibration one will have a greater impact on the reading than the accuracy of the meter itself. The calibration given by the manufacturer is used.
- **Pressure drop**: Two Druck differential pressure transducers located upstream and downstream the seal are used to measure the pressure difference across the seal. The pressure transducers have a range of 5 bar-g and an accuracy of +/- 0.04% of the full scale.
- **Temperature**: K-type thermocouples are used to measure the temperature upstream and downstream of the testing seal. The standard calibration of a K-type thermocouple is used, thus the temperature readings have an uncertainty of +/- 0.5 K.

Results of leakage mass flow rate are typically plotted as a function of the applied pressure drop across the seal or the pressure ratio. However, the leakage flow rate of seals of different sizes that are tested at different conditions cannot be directly compared. Eq. 4.13 is an expression for the mass flow rate air that passes isentropically through an annular orifice of inner diameter *D* and clearance *c*. Eq. 4.13 shows the dependency of this parameter with the testing pressure, temperature and geometry of the seal.

$$\dot{m}_{ideal} = \rho v A = \frac{\pi D c p_u Q}{\sqrt{T_u}} \tag{4.13}$$

$$Q = \begin{cases} \sqrt{\dfrac{2\gamma}{R(\gamma-1)}\left(\left(\dfrac{p_u}{p_d}\right)^{\frac{-2}{\gamma}} - \left(\dfrac{p_u}{p_d}\right)^{-\left(\frac{\gamma+1}{\gamma}\right)}\right)} & for \left(\dfrac{p_u}{p_d}\right) < \left(\dfrac{2}{\gamma+1}\right)^{-\left(\frac{\gamma}{\gamma-1}\right)} \\ \sqrt{\dfrac{\gamma}{R}\left(\dfrac{2}{\gamma+1}\right)^{\frac{\gamma+1}{\gamma-1}}} & for \left(\dfrac{p_u}{p_d}\right) > \left(\dfrac{2}{\gamma+1}\right)^{-\left(\frac{\gamma}{\gamma-1}\right)} \end{cases} \tag{4.14}$$

To overcome this problem, several parameters that gather the information of both the mass flow rate and the testing conditions have been derived from the expression of the mass flow

rate equation. These parameters are the flow coefficient (ϕ), the effective clearance (e) and the discharge coefficient (c_D). These expressions are defined in Eq. 4.15, Eq. 4.16 and Eq. 4.17, respectively:

$$\boldsymbol{\phi = \frac{\dot{m}_{measured}\sqrt{T_u}}{\pi p_u D}} \quad \textbf{4.15}$$

$$\boldsymbol{e = \frac{\dot{m}_{measured}\sqrt{T_u}}{\pi p_u D Q}} \quad \textbf{4.16}$$

$$\boldsymbol{c_D = \frac{\dot{m}_{measured}\sqrt{T_u}}{\pi p_u D c Q}} \quad \textbf{4.17}$$

The effective clearance is defined as the clearance of an annular restriction of the same diameter as the tested seal required to pass the measured leakage isentropically. The discharge coefficient is the ratio between the real (measured) and the ideal mass flow rate. It has the advantage of being a non-dimensional parameter, but requires as an input the real clearance of the seal under the operating conditions, i.e. taking into account the growth of the rotor due to rotation and/or thermal expansion, which can be difficult to measure.

4.5 Rotational speed

- **Rotor speed**: The end of the rotating spindle where the pulley is located is instrumented with a toothed cap which together with an optical sensor, determines the rotational speed of the rotor. The optical sensor generates a pulse in the output signal per revolution; this pulse is read by a signal conditioning card that transforms the frequency of the pulses into a calibrated voltage.
- **Motor speed:** The motor is fitted with an encoder that outputs a TTL signal (0-5 V) that is read directly by a counter data acquisition module. The encoder signal has 1024 pulses per revolution.

4.6 Data acquisition system

A National Instruments device with an analogue to digital converter of 16 bits is used to acquire the data. The signals used to measure the rotordynamic coefficients (load cells, accelerometers and eddy current probes) are acquired simultaneously so that they have the same time reference. The input signals are amplified as needed and filtered with analogue filters before being converted to digital to avoid aliasing problems. The cut-off frequency of

the filters was chosen to be 1250 Hz. This is five times the maximum rotating frequency (250 Hz), which is the maximum frequency expected phenomenon to be recorded. The sampling frequency is 8,192 (2^{13}) Hz, over six times greater than the cut-off frequency of the filters, thus fulfilling the Nyquist criterion ($f_{sampling} > 2 \cdot f_{max}$).

Noise problems were found when the inverter powering the motor is switched on. This digital switching noise has a high frequency, therefore, the low-pass filters described above helped in reducing it. Additionally, care was taken to earth the testing facility to the same ground level.

Chapter 5: Characterisation of a short labyrinth seal

This chapter presents the rotordynamic coefficients and leakage performance of a labyrinth seal measured using the test facility described in Chapter 3 and the experimental methodology given in Chapter 4. The objective of investigating a labyrinth seal is to validate both the performance of the rig and the chosen parameter identification procedure. Additionally, the understanding of the behaviour of short labyrinth seals with less than five cavities is established, filling a gap in the literature. The mass flow leakage data will be used as a benchmark for comparison with other type of seals.

A review on the published experimental work on labyrinth seals is given. The geometry and dimensions of the tested seal prototype are then described and the results and their uncertainty are discussed.

5.1 Rotordynamic coefficients of labyrinth seals

Labyrinth seals are known to create instabilities in compressors and turbines. These instabilities arise due to the tangential velocity of the air within the seal, which can be generated by two mechanisms. On the one hand, as the rotor spins it drags the gas due to viscous interaction in the direction of rotation. On the other hand, the fluid may have a level of swirl prior to entering the seal. This pre-swirl level can be positive (in the direction of rotation) or negative. Several studies have been carried out in order to determine the rotordynamic behaviour of labyrinth seals.

Childs [1993] summarised the research into labyrinth seals to date. He stressed the fact that the rotordynamic behaviour of gas seals is not ruled by a single variable but it depends on a host of different parameters (Reynolds number, surface roughness coefficient, inlet tangential velocity ratio, pressure drop, clearance ratio, length ratio and number of cavities). As a result, it is difficult to standardise the results of experiments carried out at different conditions with seals of varying geometry. In an effort to extract some general trends from the reviewed work, the author concluded that, for seals with five or more cavities, the direct stiffness coefficient is negative and becomes increasingly negative as the number of cavities or running speed increases. The cross-coupled stiffness was shown to increase with the number of cavities, the inlet tangential velocity and the density of the air within the seal. Finally, the direct damping coefficient is small in comparison, however plays an important role in the stability of the seals, counteracting the destabilising effect of the cross coupled stiffness.

Peletti & Childs [1991] tested different configurations of seven-cavity tooth-on-rotor (TOR) and a tooth-on-stator (TOS) short labyrinth seals (L/D = 1/6) at rotor surface speeds of up to 127 m/s, upstream pressures of 17.3 bar and pressure ratios (P_d/P_u) ranging between 0.4 and 0.67. They found that the direct stiffness of the tested seals did not change significantly when the pressure drop, the rotational speed or the pre-swirl were varied. For the zero pre-swirl case, the cross-coupled stiffness is negative and decreases (becomes more negative) with increasing rotational speed, whilst no trend could be deduced for changes in pressure ratio.

Picardo and Childs [2005] investigated a labyrinth seal with 19 cavities and an L/D ratio of 3/4 at an upstream pressure of 70 bar and rotor surface speeds up to 243 m/s. The direct stiffness was found to be negative and increased in magnitude with increasing rotational speed. The cross-coupled stiffness was reported to be negative for zero pre-swirl and the minimum value of rotational velocity, and to change sign as the inlet tangential velocity or the rotational speed increased. The direct damping remained unchanged for varying pre-swirl levels and increased with increasing rotational speed. Changes in pressure ratio did seem to not affect any of the rotordynamic coefficients.

Three pre-swirl rings were used to perform tests at different levels of air inlet tangential velocity. At the minimum rotational speed tested, the maximum pre-swirl ratio was greater than one, which in turns translates into the air inlet tangential velocity being larger than the rotor tangential velocity. The effective damping was reported to decrease with increasing values of the pre-swirl ratio and to become negative (unstable seal behaviour) for values of the pre-swirl ratio greater than one. This highlights the importance of the relative level of pre-swirl of the entering air to the seal with respect to the rotor tangential velocity.

Vannini *et al.* [2014] tested a TOS labyrinth seal with 13 cavities at an upstream pressure of 72 bar with a pressure drop of 22 bar and two levels of inlet tangential velocity, one positive and one negative. They reported negative direct stiffness becoming more negative with increasing rotational speed. Positive direct damping increasing with rotational speed was measured. The effect of the pre-swirl was found to be small for both the direct stiffness and damping coefficients. The cross-coupled stiffness was not significantly affected by changes in the rotational speed, whereas it was negative (stabilising) for negative pre-swirl and positive (destabilising) for positive pre-swirl.

5.2 Labyrinth seal geometry and test conditions

The data presented in this chapter are the experimental results of a four-cavity, see-through, teeth-on-stator labyrinth seal. Figure 5.1 and Table 5.1 show the geometry and dimensions of the seal under investigation, respectively.

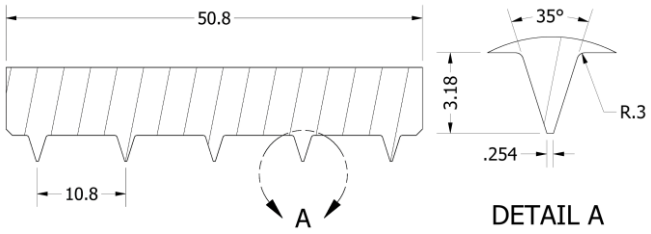

Figure 5.1: Schematic of the labyrinth seal under investigation.

Table 5.1. Labyrinth seal dimensions.

Seal Diameter	254.75 mm
Seal Clearance	0.375 mm
No. of Cavities	4
Length/Diameter (*L/D*)	1/5
Cavity Width	10.8 mm
Cavity Height	3.18 mm
Tooth Thickness	0.25 mm

For the pressure drops of 2.0, 2.4, 2.9 and 3.3 bar, the rotordynamic coefficients of the labyrinth seal were measured at each of the rotational speeds depicted in Table 5.2. For this set of experimental conditions, the rotational Reynolds number (Re_ϕ) ranges between $3 \cdot 10^5$ and $7 \cdot 10^5$. It is worth mentioning that the inlet velocity of the air is axial and, therefore, the effect of the inlet tangential swirl in the stability of the seals under study is not investigated in this research.

Table 5.2. Tested rotational speeds.

rotational speed [rpm]										
900	**2100**	**3400**	**4700**	**6100**	**7600**	**8800**	**10100**	**12100**	**13400**	**14600**

5.3 Frequency response functions – an example

The methodology introduced in Chapter 4 to calculate the frequency response functions and the rotordynamic coefficients of gas seals is exemplified in this section for one of the test cases given above – 2.9 bar pressure drop and 14,600 rpm rotational speed.

Figure 5.2 shows the frequency response functions of the labyrinth seal for data collected at 14,600 rpm and 2.9 bar pressure difference. The three plots in each of the figures show the process followed to obtain the final rotordynamic coefficients. The dark line corresponds to the frequency response function of the casing assembly shaken between 10 and 160 Hz with flow and rotation. The light curve is the frequency response function of the casing with no flow and no rotation (baseline test). Finally, by subtracting to the complex stiffness obtained with flow and rotation the one of the baseline test, the complex stiffness corresponding to the thin film of air created in between the rotor and the labyrinth is obtained. This final value is fitted with Eq. 4.11 as explained in Section 4.3.

The frequency response functions have been computed with a stator mass of 16.26 kg. The baseline test and the test with flow and rotation needed an adjustment of the mass of 0.1 kg and 0.6 kg, respectively. (The mass correction process was explained in Chapter 4 and is illustrated in Figure 4.7 and Figure 4.8) The difference of mass between the two types of tests is thought to be due to the pressurised air contributing to the weight of the whole system. In Figure 5.2, the real part of the direct complex stiffness is shown as computed using the mass correction. The second order coefficient of the fit of the frequency response function corresponding to the fluid film alone is nearly zero; this is indicated by the horizontal line in Figure 5.2 (a).

The real part of the cross-coupled complex stiffness, shown in Figure 5.2 (b), is frequency independent for frequencies ranging between 10 and 90 Hz. For frequencies above 90 Hz the curve is not flat. One may think that this is due to an added-mass effect of the film of air generated by the labyrinth seal, however gas labyrinth seals are known to have zero added-mass as the density of the air is relatively low. Therefore, this frequency dependency could be due to the dynamics of the rig itself and any misalignment of the shaker, as it was already pointed out in Chapter 4.

The imaginary part of the direct complex stiffness is shown in Figure 5.2 (c). A linear fit of this impedance corresponding to the thin fluid film has also been plotted, with the zero-order coefficient forced to be zero. The slope of this curve is equal to the damping of the seal.

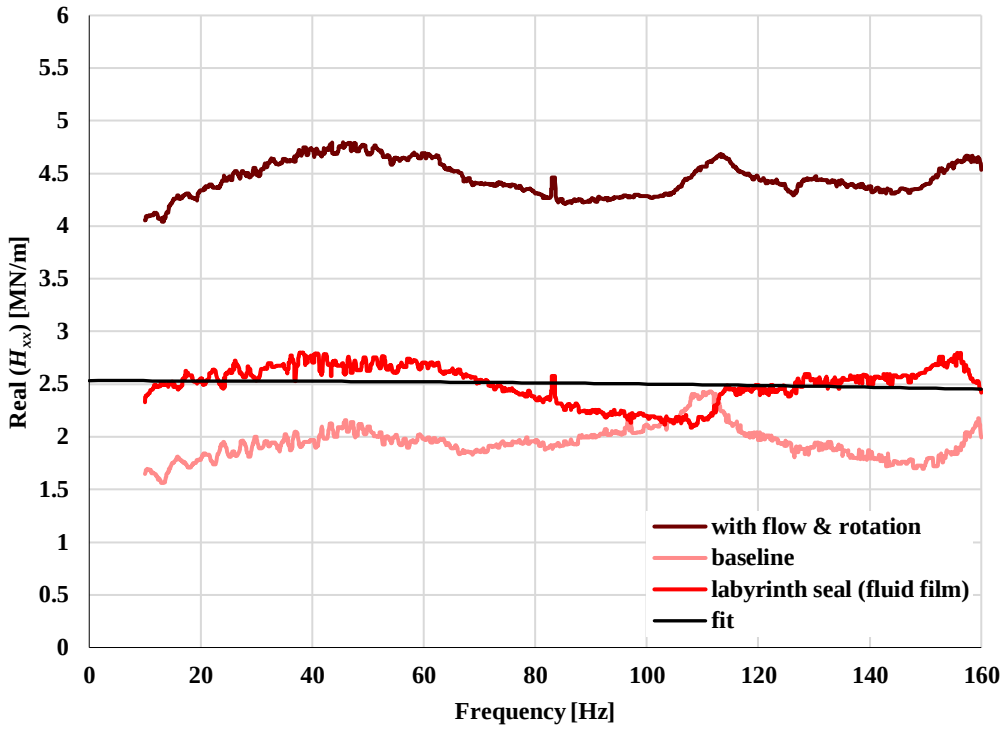
Real (H_{xx}) [MN/m]
Frequency [Hz]
with flow & rotation
baseline
labyrinth seal (fluid film)
fit

(a)

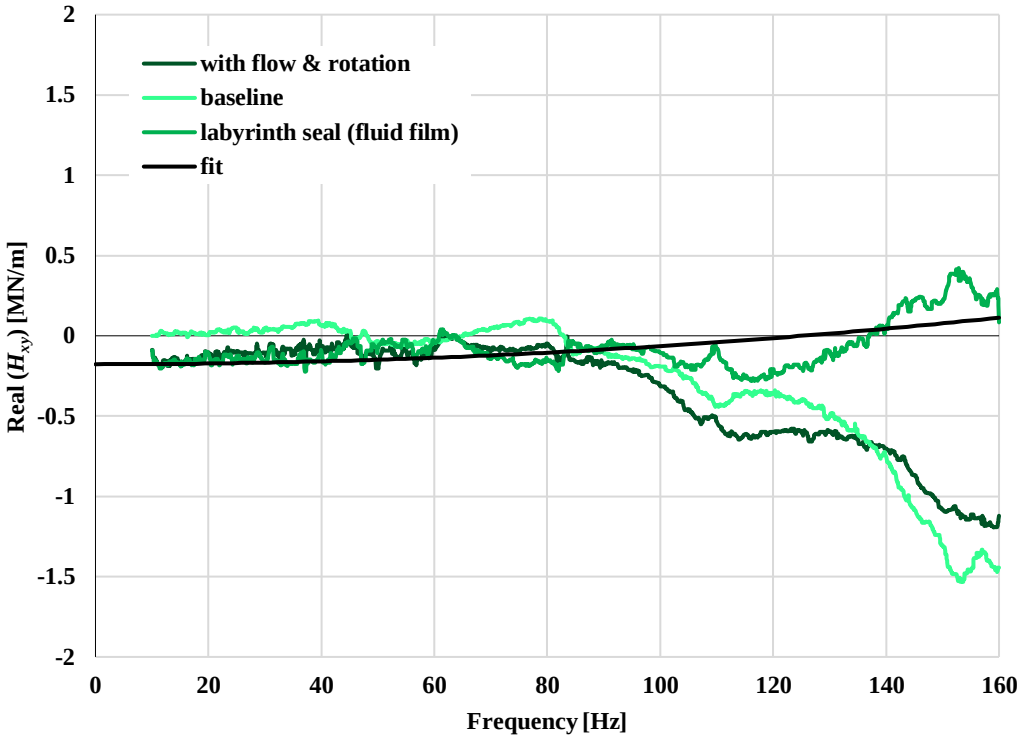
Real (H_{xy}) [MN/m]
Frequency [Hz]
with flow & rotation
baseline
labyrinth seal (fluid film)
fit

(b)

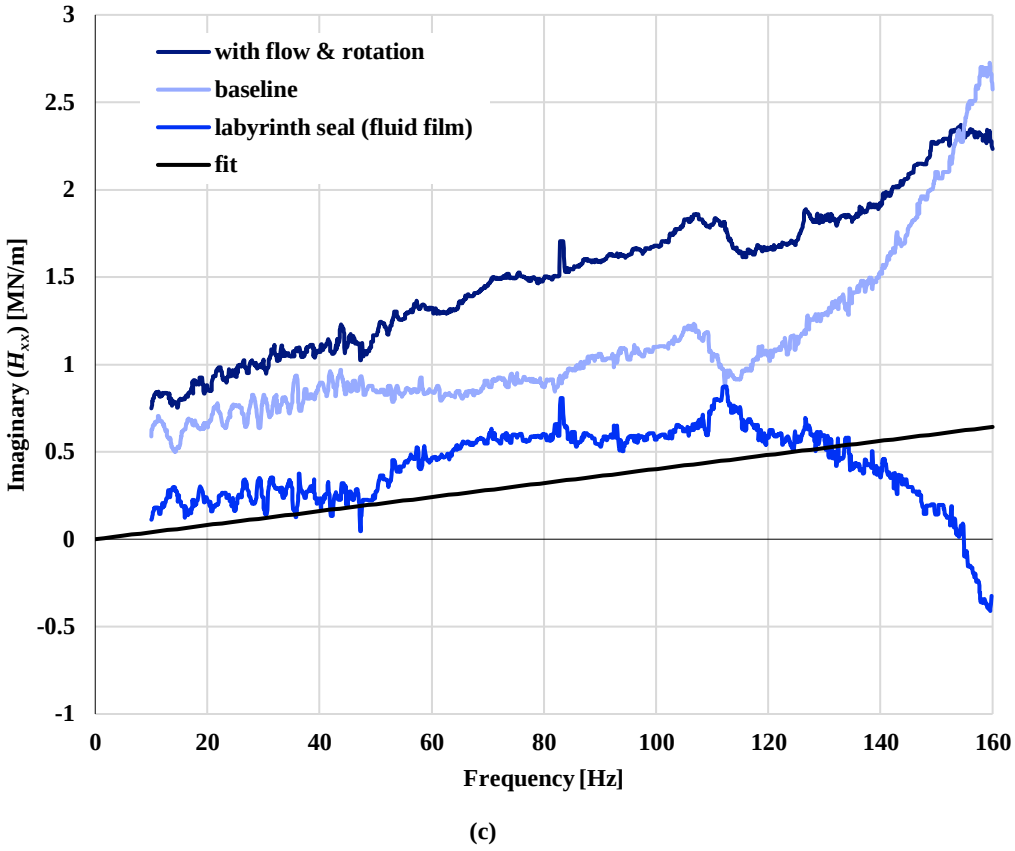

(c)

Figure 5.2. (a) Real part of the direct complex stiffness *Re(H_{xx})*, (b) real part of the cross-coupled complex stiffness *Re(H_{xy})* and (c) imaginary part of the direct complex stiffness *Im(H_{xx})* against frequency for the baseline test, the test with flow and rotation and the resulting fluid film. First order curve fit of the resulting fluid film. Tests made at a rotational speed of 14,600 rpm and a pressure difference of 2.9 bar.

5.4 Uncertainty

Before presenting the final rotordynamic results, the method used to calculate the uncertainty is shown. Six repetitions of both the baseline test and the test with flow and rotation are made for each point of the test matrix. The standard deviation of the six repetitions is calculated as per Eq. 5.1:

$$s_x = \sqrt{\frac{\sum_{i=1}^{N}(x_i^2 - \bar{x}^2)}{N-1}} \; ; \; \bar{x} = \frac{\sum_{i=1}^{N} x_i}{N} \qquad 5.1$$

Finally, the standard deviation of the complex stiffness corresponding only to the film of air is calculated combining the values obtained for both tests as indicated in Eq. 5.2:

$$s_{fluidfilm} = \sqrt{s_{total}^2 + s_{bl}^2} \qquad 5.2$$

Figure 5.3 and Figure 5.4 show, respectively, the real and imaginary parts of the complex stiffnesses of the fluid film discussed in the previous section together with their standard deviation. Note that the imaginary part of the cross-coupled complex stiffness has been included here for the sake of completeness. The upper and lower limits of the shaded area are calculated by adding and subtracting, respectively, one standard deviation to the mean value. In other words, it can be said, that the 68.2% of the measurements lie within the plotted range of two standard deviations. The standard deviation represents the uncertainty of the frequency response functions of the seal. Note that the uncertainty of the dynamic stiffness changes with frequency.

As the rotordynamic coefficients are not the result of direct measurements but are estimated parameters after transforming the measurements into the frequency domain and further fitting of these with a theoretical model, their uncertainty cannot be directly calculated from the measurements. Instead, the confidence intervals of the fit parameters given by the maximum likelihood estimation technique are used (see Davison [2003]).

Table 5.3 shows the values of the upper and lower limits of the rotordynamic coefficients uncertainty calculated with the method mentioned previously for the example case (ω = 14,000 rpm and Δp = 2.9 bar) for which the frequency response functions have been discussed at the beginning of this section. The values are given in absolute terms and in percentage relative to the rotordynamic coefficients.

From the values in Table 5.3 it can be seen that the cross-coupled damping, c, has the largest uncertainty. This is because the cross-coupled damping coefficient has a small value that is the result of subtracting one large quantity from another. On the contrary, the error of c is the sum of the error from the two measurements used to calculate the final value of this rotordynamic coefficient. This happens for all four rotordynamic coefficients, but the case of the cross-coupled damping is highlighted as it is the most affected one by this drawback of the technique.

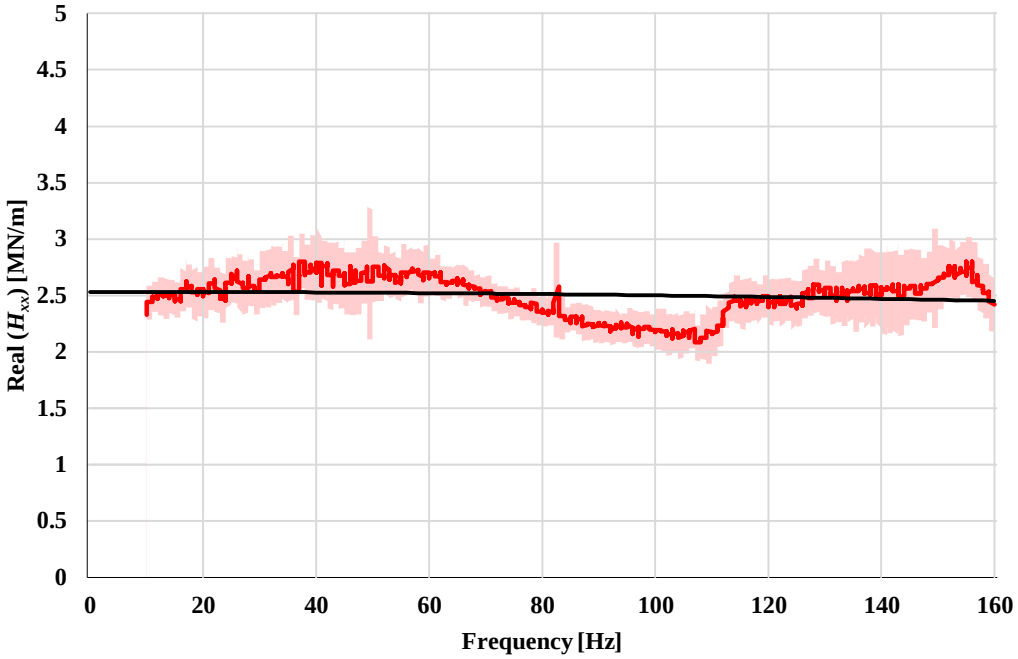

(a)

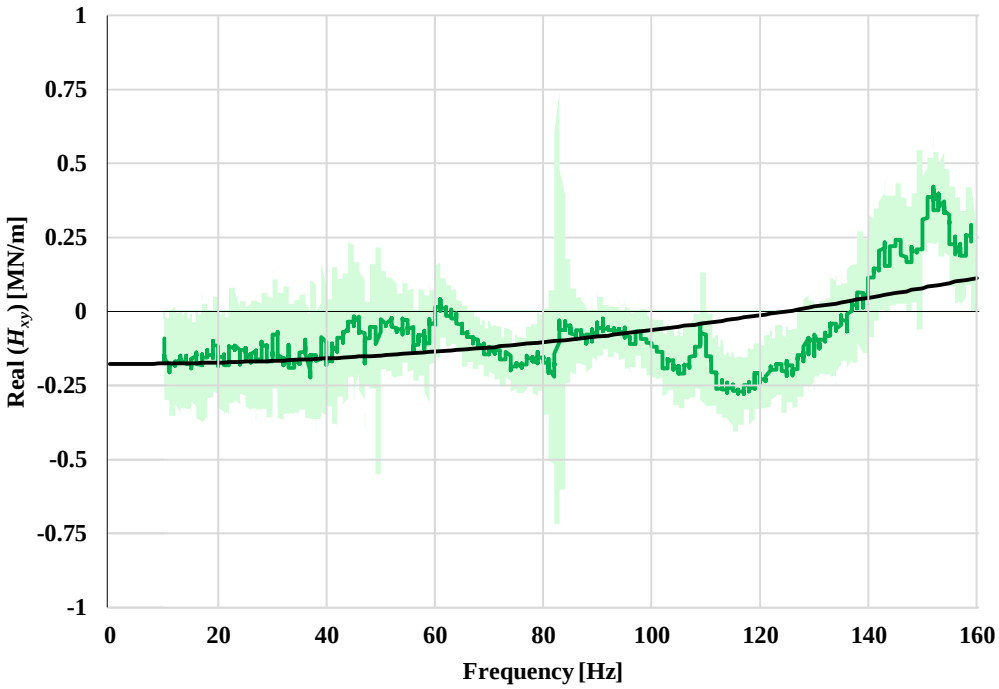

(b)

Figure 5.3. Real part of the (a) direct complex stiffness *Re(H_{xx})* and (b) cross-coupled complex stiffness *Re(H_{xy})* of the fluid film against frequency. The shaded area corresponds to one standard deviation above and below the mean value of the six test repetitions. Tests made at a rotational speed of 14,600 rpm and a pressure difference of 2.9 bar.

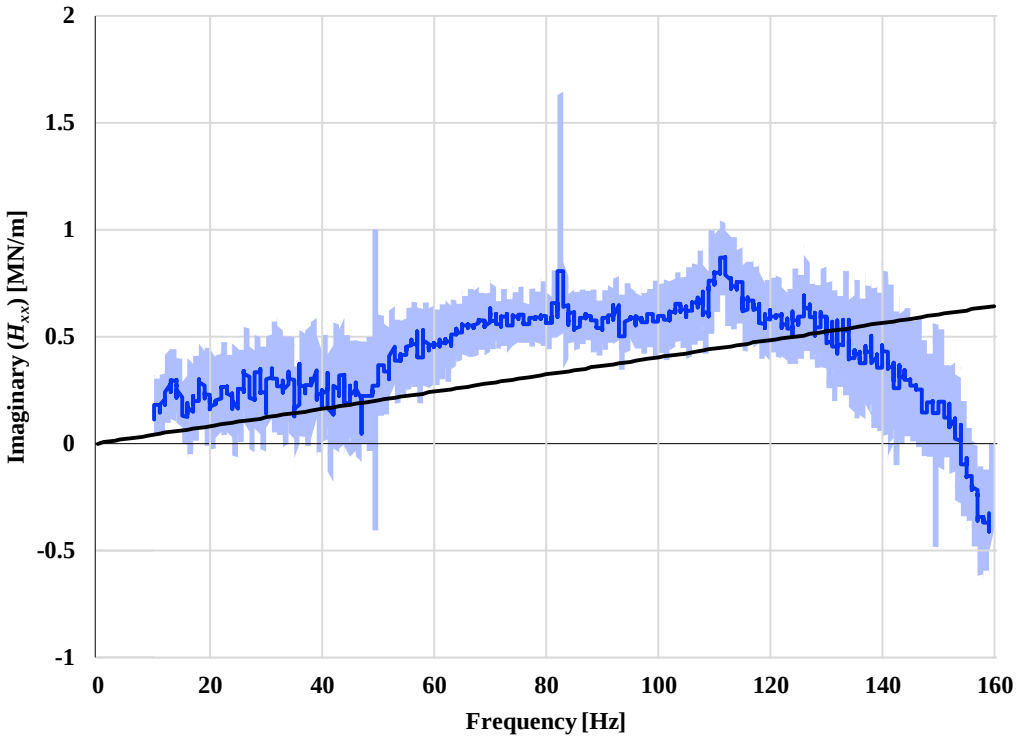

(a)

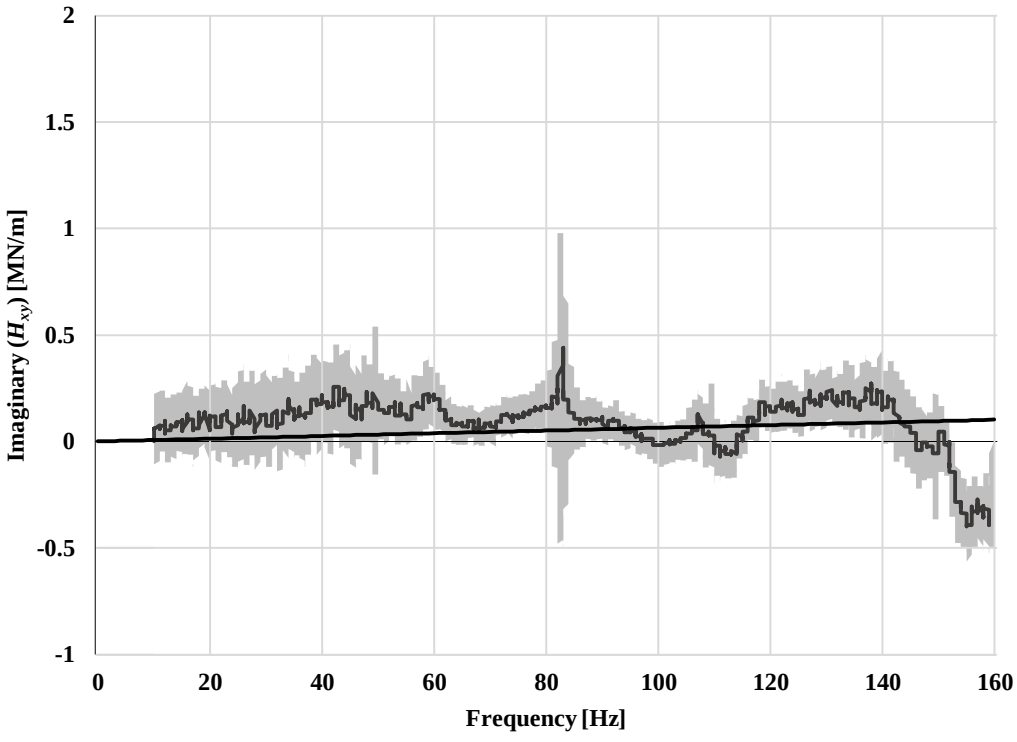

(b)

Figure 5.4. Imaginary part of the (a) direct complex stiffness *Im(H_{xx})* and (b) cross-coupled complex stiffness *Im(H_{xy})* of the fluid film against frequency. The shaded area corresponds to one standard deviation above and below the mean value of the six test repetitions. Tests made at a rotational speed of 14,600 rpm and a pressure difference of 2.9 bar.

Table 5.3. Values of the rotordynamic coefficients and their 95 % confidence uncertainty interval expressed in both absolute values and percentage variation. (ω = 14,600 rpm and Δp = 2.9 bar).

Figure 5.3 (a)	**K**	$2532.2\ \frac{kN}{m}$	$\pm\ 15.8\ \frac{kN}{m}$	$(\pm\ 0.6\ \%)$
Figure 5.3 (b)	**k**	$-177.4\ \frac{kN}{m}$	$\pm\ 10.1\ \frac{kN}{m}$	$(\pm\ 5.7\ \%)$
Figure 5.4 (a)	**C**	$639.0\ \frac{Ns}{m}$	$\pm\ 26.0\ \frac{Ns}{m}$	$(\pm\ 4.1\ \%)$
Figure 5.4 (b)	**c**	$101.4\ \frac{Ns}{m}$	$\pm\ 12.7\ \frac{Ns}{m}$	$(\pm\ 12.5\ \%)$

The cross-coupled damping contributes to the radial force acting on a whirling rotor with precession amplitude A and rotational speed Ω, as shown in Figure 4.3. The expression for the radial force is:

$$\boldsymbol{f_r = -(K + \Omega \cdot c) \cdot A} \qquad \textbf{5.3}$$

Using the values of Table 5.3 in Eq. 5.3, the contribution of the cross-coupled damping to the radial force is calculated to be only 6 percent of the direct stiffness (see Eq. 5.4). Additionally, and according to Childs [1993], the radial component of the force acting on the rotor has an impact on the stability of the latter that is not as large as the tangential component. For these two reasons, and due to the fact that the uncertainty is large, the cross-coupled damping is not discussed further.

$$\boldsymbol{\Omega \cdot c = 14{,}600 \cdot \frac{2\pi}{60} \cdot 101.4 = 155 \frac{kN}{m}}$$
$$\boldsymbol{K = 2532.2 \frac{kN}{m}} \qquad \textbf{5.4}$$

A sensitivity analysis was performed to determine the effect of averaging different number of test repetitions. Table 5.4 shows, for the real and imaginary parts of the direct complex stiffness and the real part of the cross-coupled complex stiffness, the variation of the uncertainty of the coefficients of the fit (K, C and k, respectively) and the variation of the standard deviation of the fit when calculated using the experimental data from 6, 12, 18, 24, 30 or 36 repetitions. The experiments for this sensitivity analysis were carried out at a rotational speed of 8,800 rpm and a pressure drop of 2.9 bar.

The reason for averaging the repetitions is to reduce the level of noise under the assumption that the noise is random and, therefore, it tends to zero as the number of averaged samples tends to infinity. It is expected that both the uncertainty of the coefficients and the standard deviation of the fit decreases as the number of averaged repetitions increases. This is the case

for both the real and imaginary parts of the direct complex stiffness. However, for the number of repetitions investigated, this decrease is marginal compared with the extra time needed to record more data sets. For this reason it is decided to use six repetitions for the test points of this experimental campaign.

Table 5.4. Uncertainty of the coefficients of the fit and standard deviation of the fit when fitting the average of different number of test repetitions. Tests performed at ω = 8,800 rpm and Δp = 2.9 bar.

	No. reps	**6**	**12**	**18**	**24**	**30**	**36**
$\boldsymbol{Re(H_{xx})}$	$\pm unc\ \boldsymbol{K}$ [%]	0.59	0.58	0.57	0.56	0.55	0.54
	$\sigma_{fit}\ [\frac{MN}{m}]$	2.01	1.96	1.94	1.90	1.86	1.85
$\boldsymbol{Re(H_{xy})}$	$\pm unc\ \boldsymbol{k}$ [%]	4.45	4.32	4.55	4.88	5.42	5.84
	$\sigma_{fit}\ [\frac{MN}{m}]$	0.92	0.87	0.89	0.91	0.96	1.01
$\boldsymbol{Im(H_{xx})}$	$\pm unc\ \boldsymbol{C}$ [%]	1.45	1.44	1.41	1.40	1.38	1.37
	$\sigma_{fit}\ [\frac{MN}{m}]$	1.74	1.74	1.71	1.70	1.67	1.67

5.5 Rotordynamic coefficients

In this section the rotordynamic coefficients of the labyrinth seal described in Section 5.2 are provided. The experimental conditions presented here are the ones depicted in Table 5.2. Results are plotted as a function of rotational speed.

Figure 5.5 to Figure 5.7 show the stiffness and damping coefficients of the seal for three different tests, all performed at a pressure drop across the seal of 2.9 bar. These tests were performed in three different days in order to check the repeatability of the results. It can be seen that for the direct stiffness and direct damping, the results from Test1 and Test 3 collapse on top of each other, whereas the results from Test 2 differ in magnitude.

As both the pressure drop and the rotational speed of the rotor are controllable variables and were checked to be within the uncertainty limits for all the tests, the temperature of the air at the upstream cavity of the test section was measured in order to determine the effect this parameter had on the results. Figure 5.8 shows the upstream temperature as measured at each shaft speed. Similar to the direct rotordynamic coefficients, the temperature for Test 1 and Test 3 are close to each other (with a maximum difference of 1.8 °C at 900 rpm). On the contrary, the temperature of Test 2 is, on average, four degrees apart from the temperature of the other two tests. The rotordynamic coefficients are inversely proportional to temperature, thus, for Test 2 where the temperature is the lowest the stiffness and damping are the greatest.

Regarding the trend with rotational speed, the results from the three tests show good repeatability. The direct stiffness (Figure 5.5) does not significantly change with rotational speed, whereas the cross-coupled stiffness (Figure 5.6) and the direct damping (Figure 5.7) decrease as rotational speed increases. Note that the results of Test 2 at a rotational speed of 2,100 rpm are off the trend and have an uncertainty significantly larger than the rest of the results. Due to these reasons, it is thought that something went wrong during the vibration tests and, therefore, this data point has been considered as an outlier.

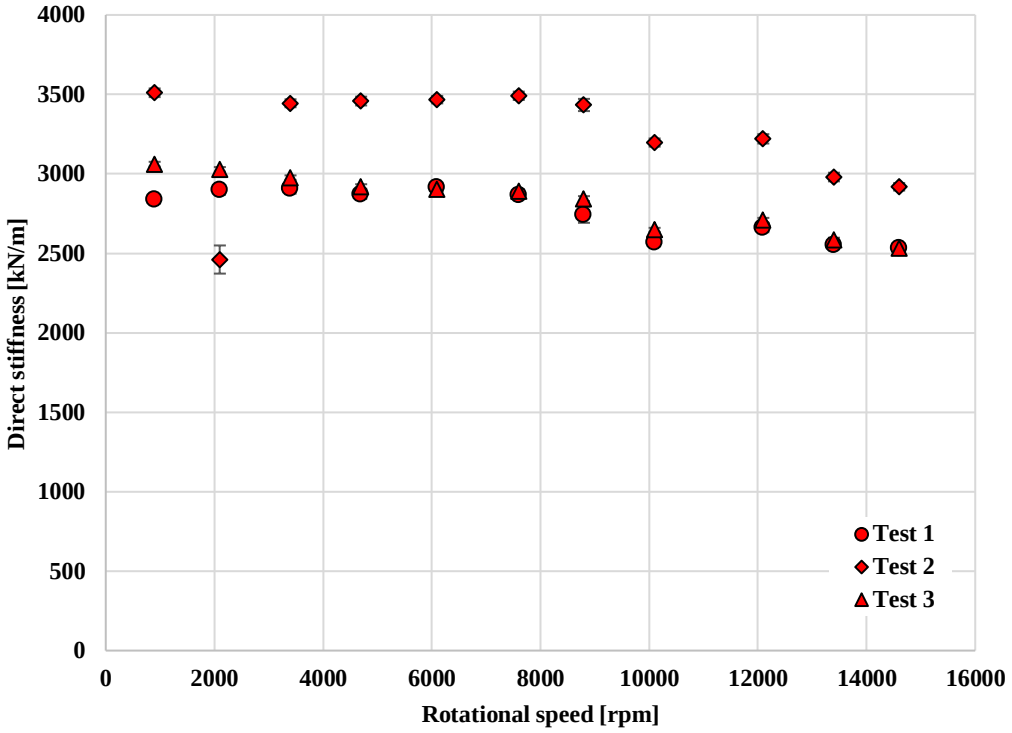

Figure 5.5. Comparison of the direct stiffness of a four-cavity labyrinth seal tested at a pressure drop of 2.9 bar in three different days.

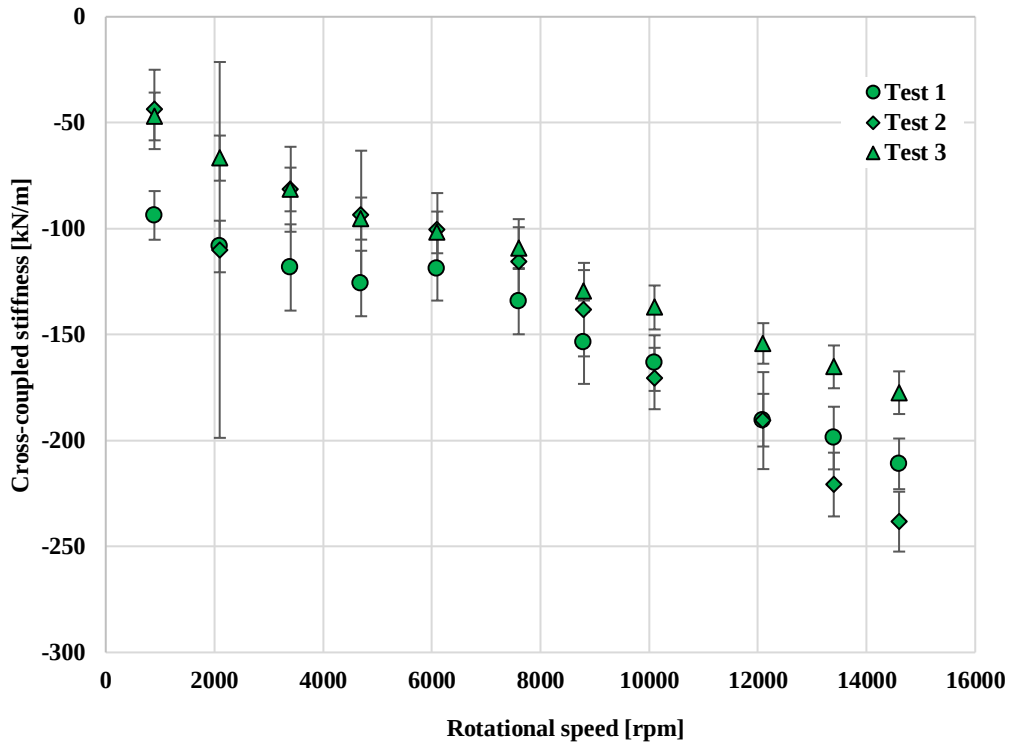

Figure 5.6. Comparison of the cross-coupled stiffness of a four-cavity labyrinth seal tested at a pressure drop of 2.9 bar in three different days.

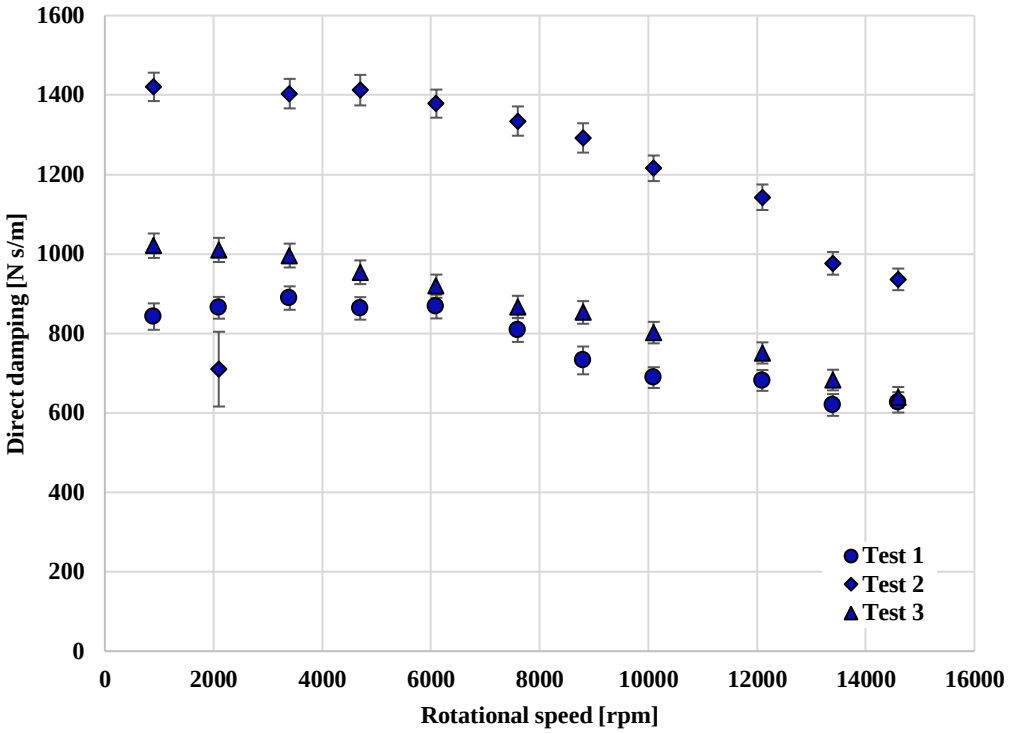

Figure 5.7. Comparison of the direct damping of a four-cavity labyrinth seal tested at a pressure drop of 2.9 bar in three different days.

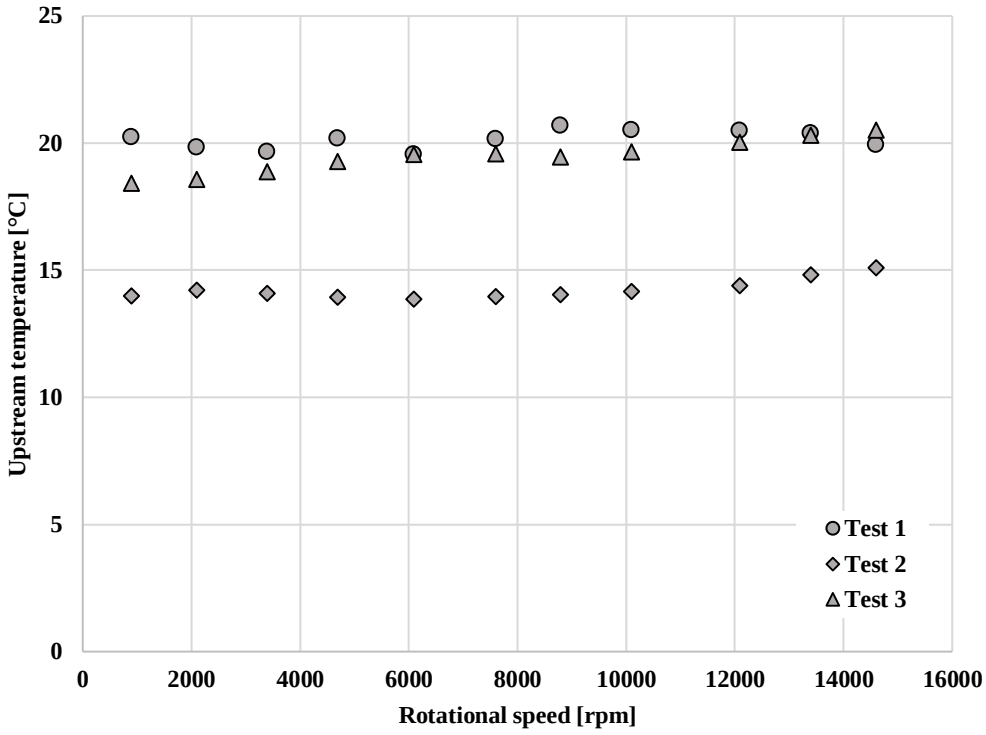

Figure 5.8. Air temperature upstream of a four-cavity labyrinth seal tested at a pressure drop of 2.9 bar in three different days.

After this repeatability check, the rotordynamic coefficients at the four pressure drops given in Section 5.2 are measured. Figure 5.9 to Figure 5.11 show the results for these tests and Figure 5.12 depicts the temperature of the air at the upstream cavity to the seal.

Both the direct stiffness and damping increase with increasing pressure drop. This is expected as a larger pressure drop, for a constant discharge pressure, translates into a greater density of the fluid forming the clearance film and, therefore, higher forces are needed to displace the seal by the same amount.

However, as a temperature dependency was discovered during the repeatability tests explained before, the upstream temperature was also investigated in order to see any effect of this variable on the rotordynamic results. Indeed, the temperature decreased as the pressure drop increased, which is thought to have an effect on both the direct stiffness and damping. The difference in temperature for the 2.4 and the 2.9 bar pressure drop tests is almost zero, which is reflected in the coefficients results. Between the 2.9 and 3.3 bar pressure drop tests the temperature experiences the greatest change and so the direct rotordynamic coefficients do.

Figure 5.9 shows that the direct stiffness is positive and slightly decreases with rotational speed. However, this trend might also be affected by the increase in temperature experienced during the test as shown in Figure 5.12. A steeper decrease in direct damping with shaft speed was measured, as presented in Figure 5.11.

No trend with pressure drop can be inferred for the cross-coupled stiffness (Figure 5.10). Additionally, this rotordynamic coefficient is negative and decreases (becomes more negative) with rotational speed. The behaviour of the cross-coupled stiffness with both pressure drop and rotor speed is similar to Peletti & Childs [1991] for a labyrinth seal with seven cavities, which is the most comparable geometry found in the literature.

For the sign convention adopted in Section 4.2, negative values of the cross-coupled stiffness and positive values of the direct damping yield stabilising tangential forces. Therefore, the stabilising effect of the negative cross-coupled stiffness increases, whereas, the stabilising effect of the direct damping decreases with shaft speed. From this, no conclusion can be deduced about the trend of the tangential force due to the air passing through the seal. However, it was demonstrated in Section 4.2 that the effective damping groups the effect of both the cross-coupled stiffness and the direct damping in a single parameter. The effective damping is used here to assess the stability behaviour of the labyrinth seal. It can be seen in Figure 5.13 that the effective damping increases with increasing pressure drop, but it decreases as rotational speed increases.

Note that the direct stiffness of the labyrinth seal is of the order of $10^6 N/m$, whereas the cross-coupled stiffness and the direct damping are one order of magnitude and three orders of magnitude smaller, respectively. The relative order of magnitude between the three rotordynamic coefficients is consistent for the labyrinth seals found in the literature, regardless of the pressure level at which they are tested or of their geometry. It is worth mentioning that the results for the test at 2 bar pressure drop and 3,400 rpm rotational speed were found to be an outlier.

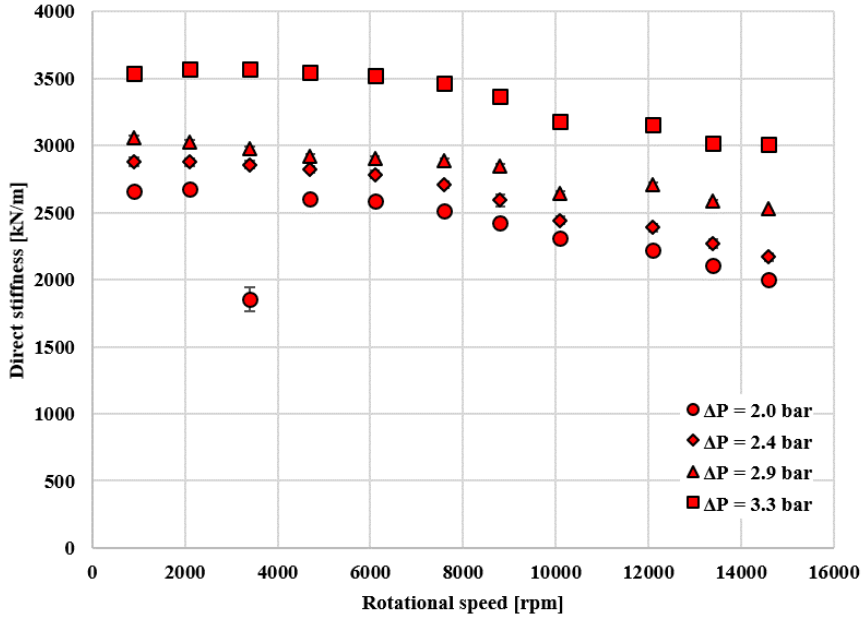

Figure 5.9. Comparison of the direct stiffness of a four-cavity labyrinth seal tested at four different pressure drop values.

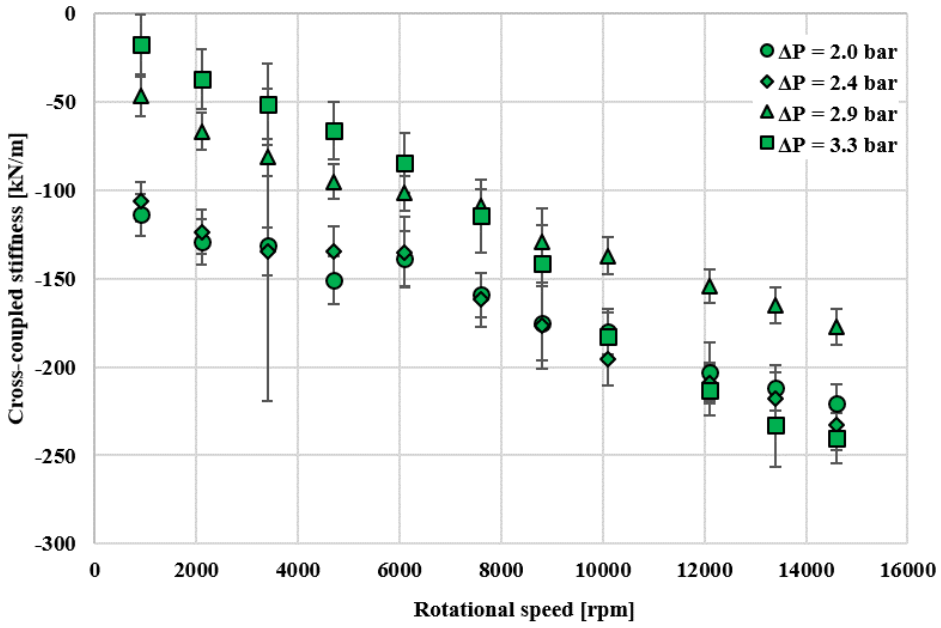

Figure 5.10. Comparison of the cross-coupled stiffness of a four-cavity labyrinth seal tested at four different pressure drop values.

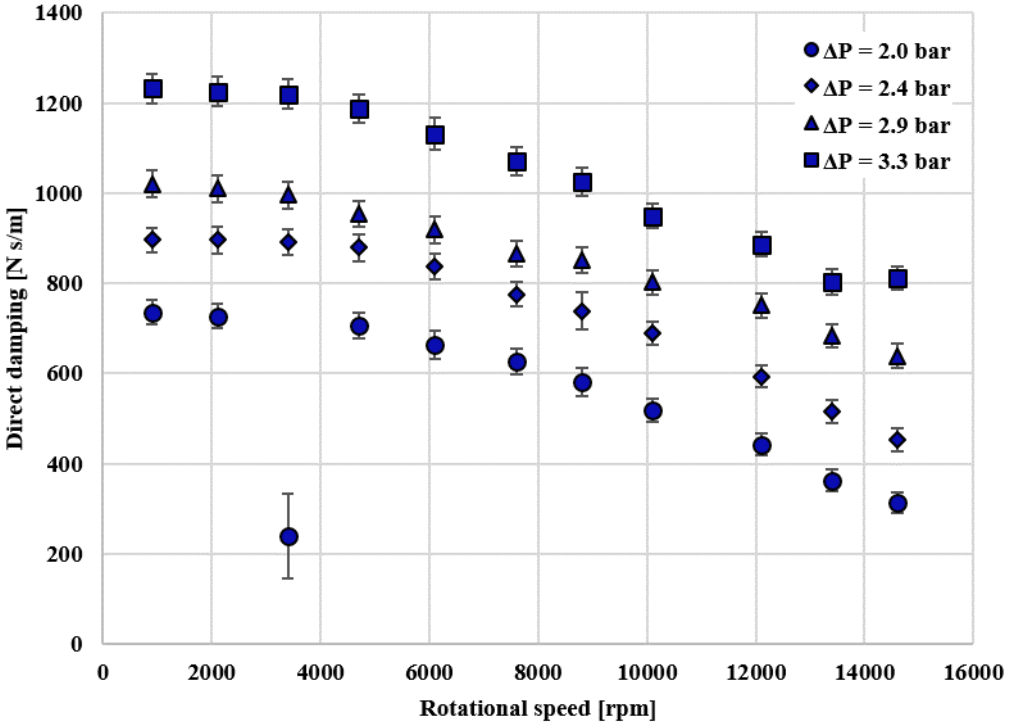

Figure 5.11. Comparison of the direct damping of a four-cavity labyrinth seal tested at four different pressure drop values.

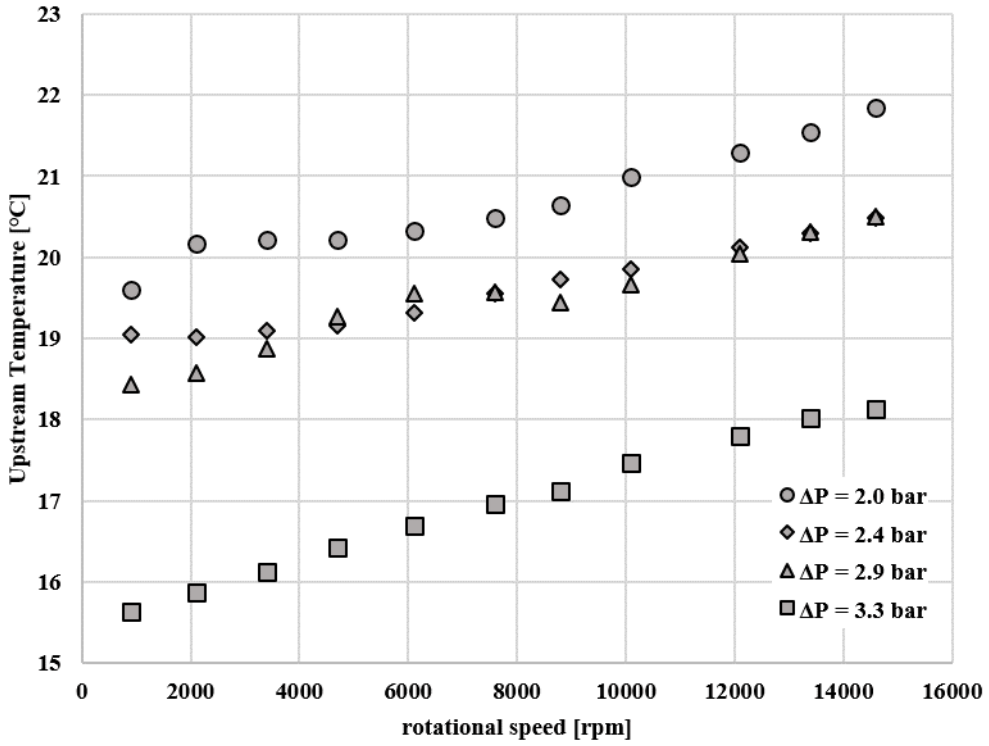

Figure 5.12. Air temperature upstream of a four-cavity labyrinth seal tested at four different pressure drop values.

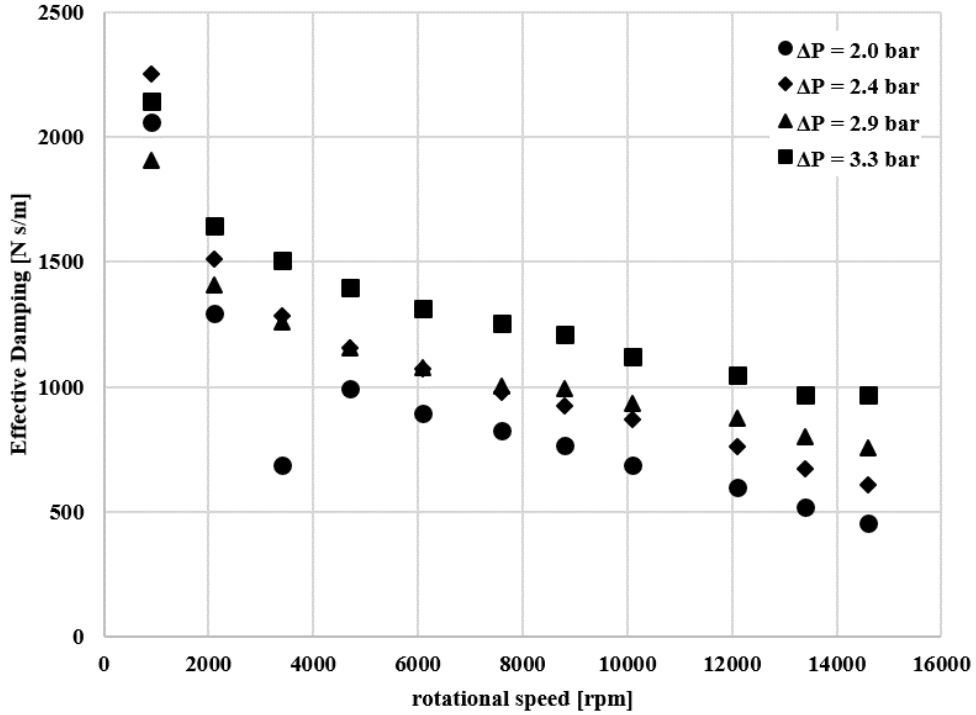

Figure 5.13. Comparison of the effective damping of a four-cavity labyrinth seal tested at four different pressure drop values.

Finally, a group of tests for the four pressure drops discussed above and three rotational speeds (900, 7600 and 13400 rpm) was performed, all in the same day. This was done with the intention of ensuring the temperature variation between days was minimised and double check the trends with pressure drop.

The temperature, shown in Figure 5.17, changed less than one degree between the four pressure drops at each tested speed and yet both the direct stiffness and direct damping were found to increase as pressure drop increased (see Figure 5.14 and Figure 5.16). This confirms the effect of the pressure drop on the rotordynamic coefficients. However, the magnitude of the changes are smaller than that shown in Figure 5.9 and Figure 5.11, thus, indicating that the temperature still has an effect on the results.

Figure 5.15 shows that the cross-coupled stiffness increases (becomes less negative) with increasing pressure drop, which implies that the greater the pressure drop the more unstable the seal is. This is in contrast with the results shown in Figure 5.10, where the effect of the pressure did not have an apparent trend.

It is thought that the temperature has an effect on the results as the rig is manufactured from metal (aluminium and steel, mainly). Variations in temperature imply changes in size of the rig components due to expansion/contraction effects. These changes in size, even if within the

order of the micrometre, may have a large impact on the stiffness as this is the ratio of a force over a displacement.

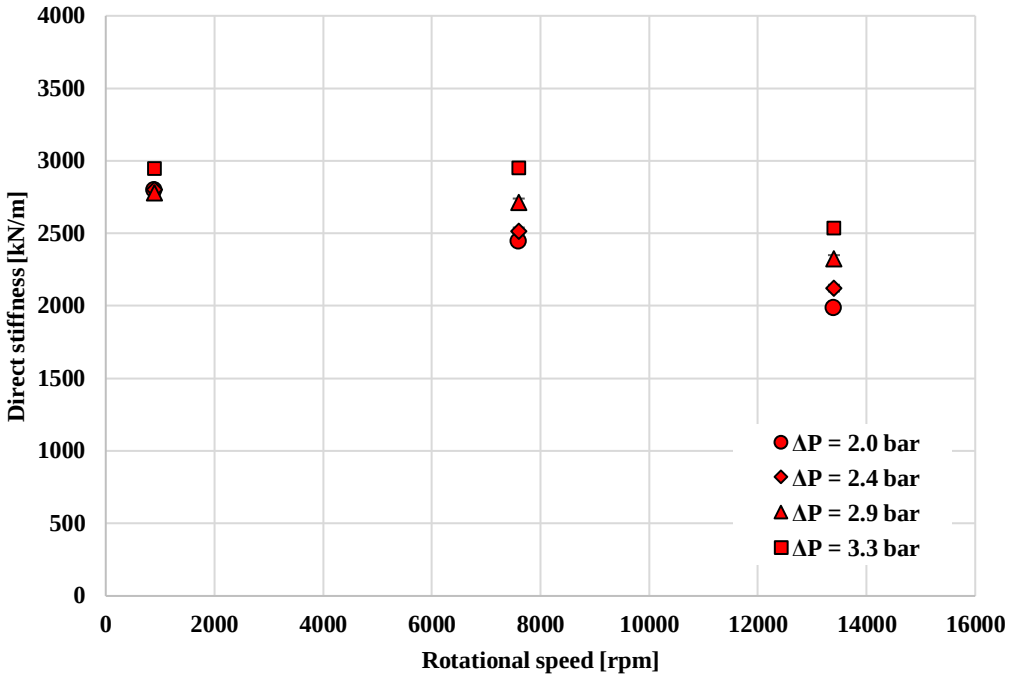

Figure 5.14. Comparison of the direct stiffness of a four-cavity labyrinth seal tested at four different pressure drop values and three rotational speeds on the same day (to minimise ambient temperature effect).

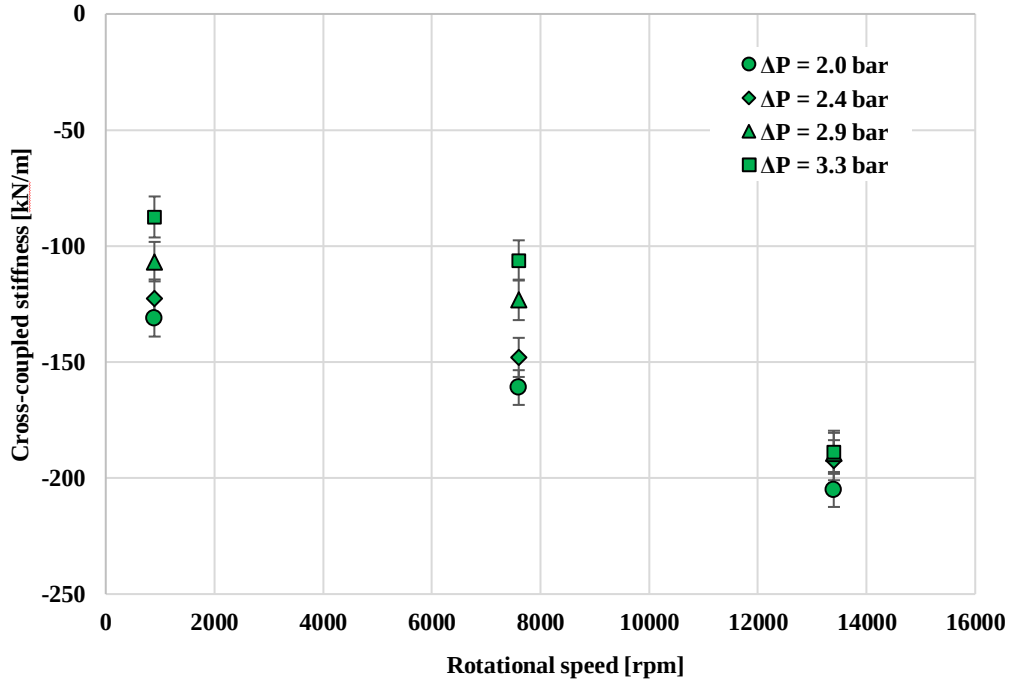

Figure 5.15. Comparison of the direct stiffness of a four-cavity labyrinth seal tested at four different pressure drop values and three rotational speeds on the same day (to minimise ambient temperature effect).

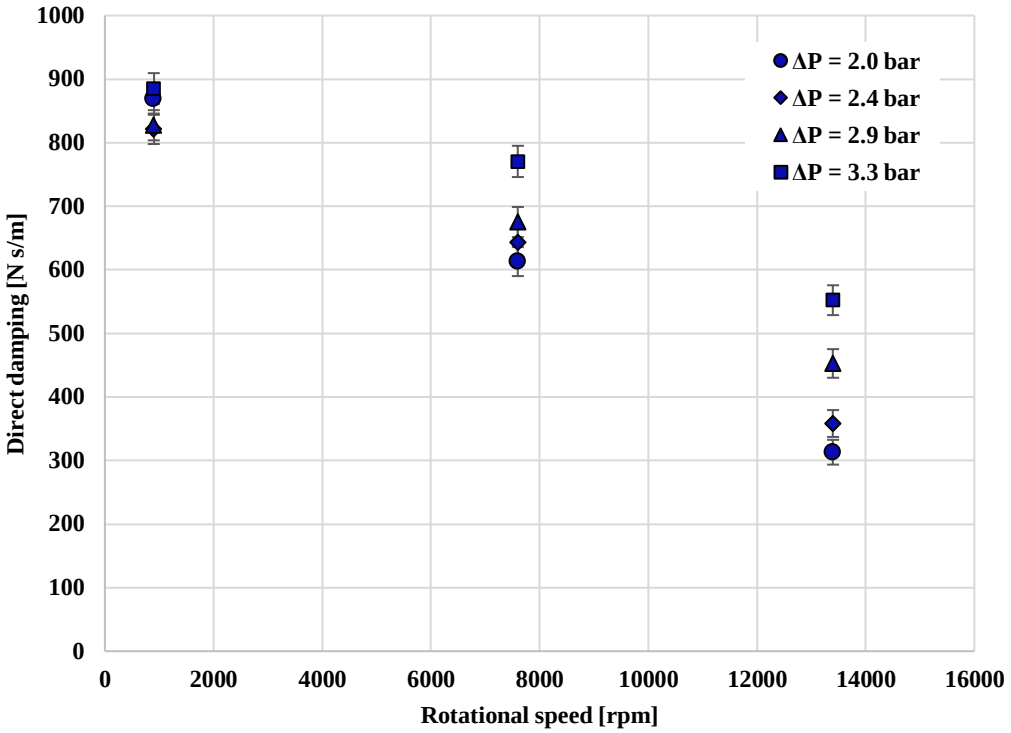

Figure 5.16. Comparison of the direct damping of a four-cavity labyrinth seal tested at four different pressure drop values and three rotational speeds on the same day (to minimise ambient temperature effect).

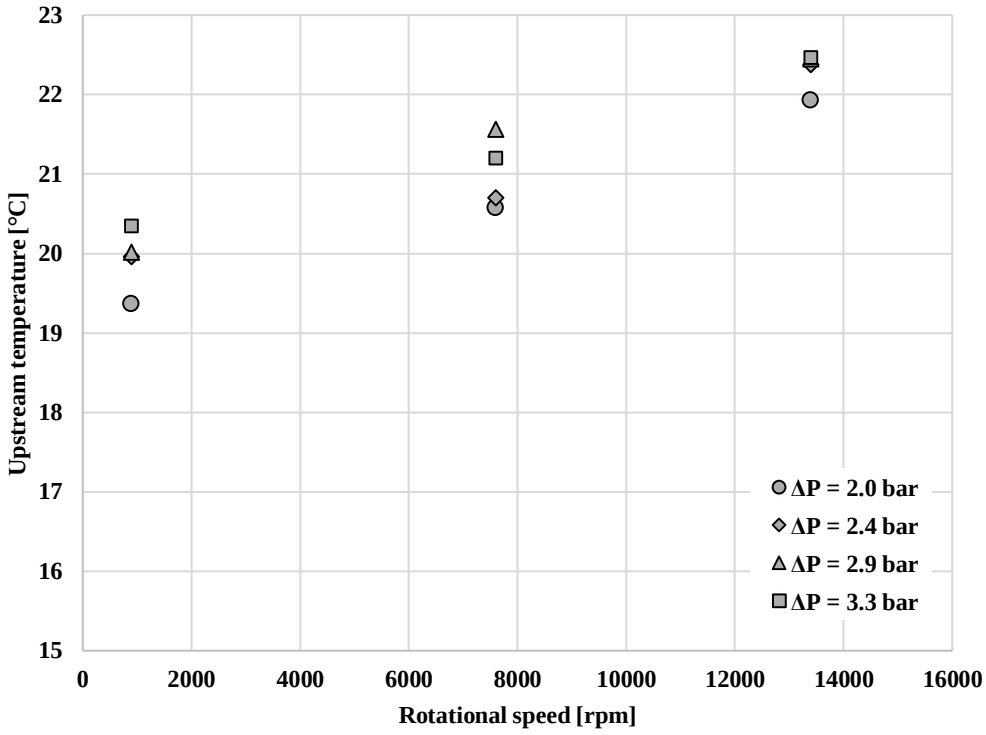

Figure 5.17. Air temperature upstream a four-cavity labyrinth seal tested at four different pressure drop values and three rotational speeds.

5.6 Leakage performance

The leakage mass flow rate of the labyrinth seal at three rotational speeds is plotted against pressure difference in Figure 5.18. The variation of leakage with pressure drop is linear, as indicated by the ideal mass flow rate equation (Eq. 4.13) shown in Section 4.4. The data shows that the leakage mass flow rate is independent of rotational speed across the range tested, which is in agreement with the findings of el-Gamal *et al*. [1996] for see-through labyrinth seals with a small number of cavities. As predicted by ideal mass flow rate expression, the data is linear with upstream pressure (even though the mass flow measurements are presented against pressure drop, the variation of downstream pressure is negligible and it can be said that pressure drop is effectively upstream pressure).

The effective clearance and the discharge coefficient corresponding to the measured mass flow rate is shown in Figure 5.19 and Figure 5.20. These two parameters were calculated using the equations given in Section 4.4 and are shown to reach an asymptotic value at choked conditions. This asymptotic value of the discharge coefficient is 0.4, which is in line with the values presented by Wittig *et al.* [1987] for the experimental discharge coefficient of a labyrinth seal with five cavities and clearances ranging from 0.5 mm to 2.5 mm.

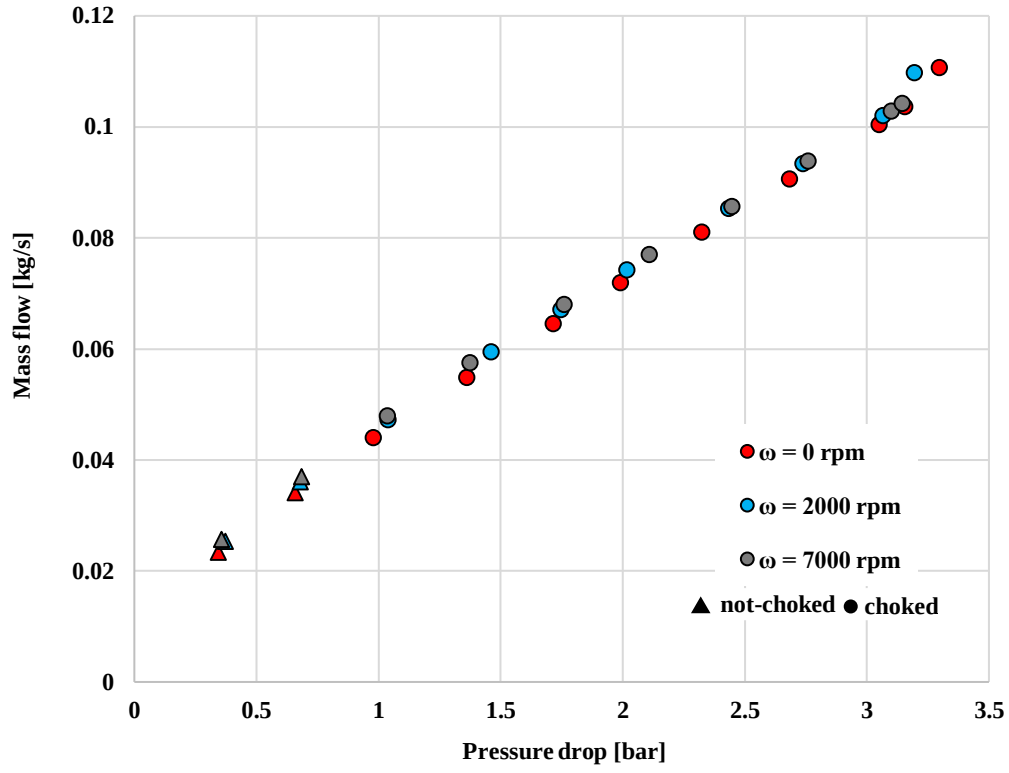

Figure 5.18. Variation of mass flow rate with pressure difference for three rotational speeds.

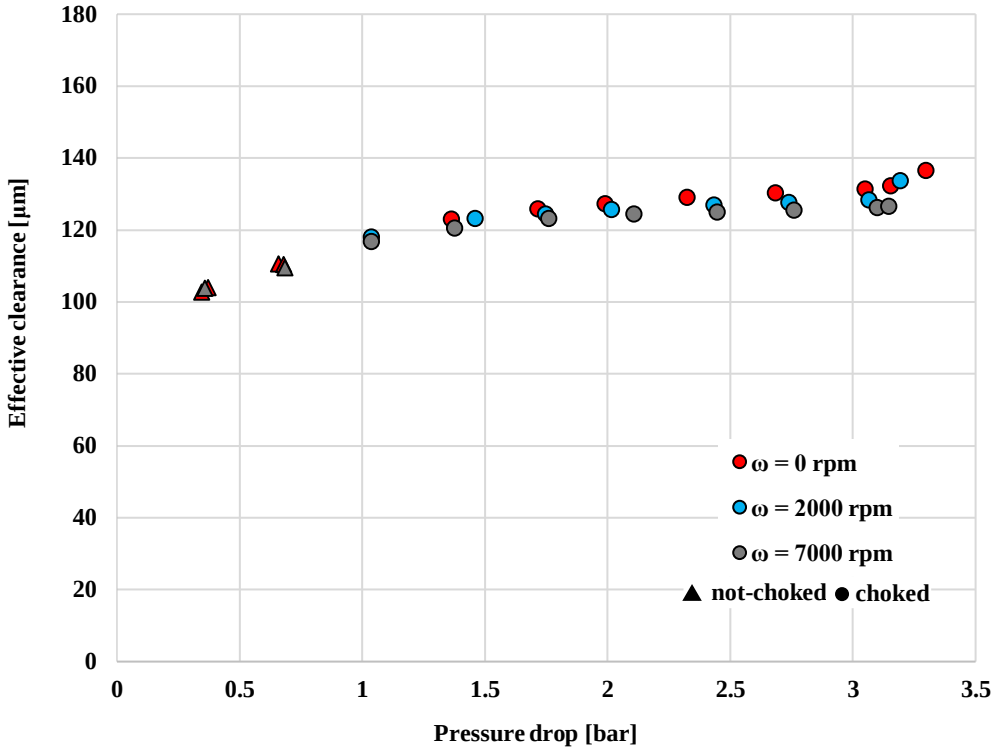

Figure 5.19. Variation of effective clearance with pressure difference for three rotational speeds.

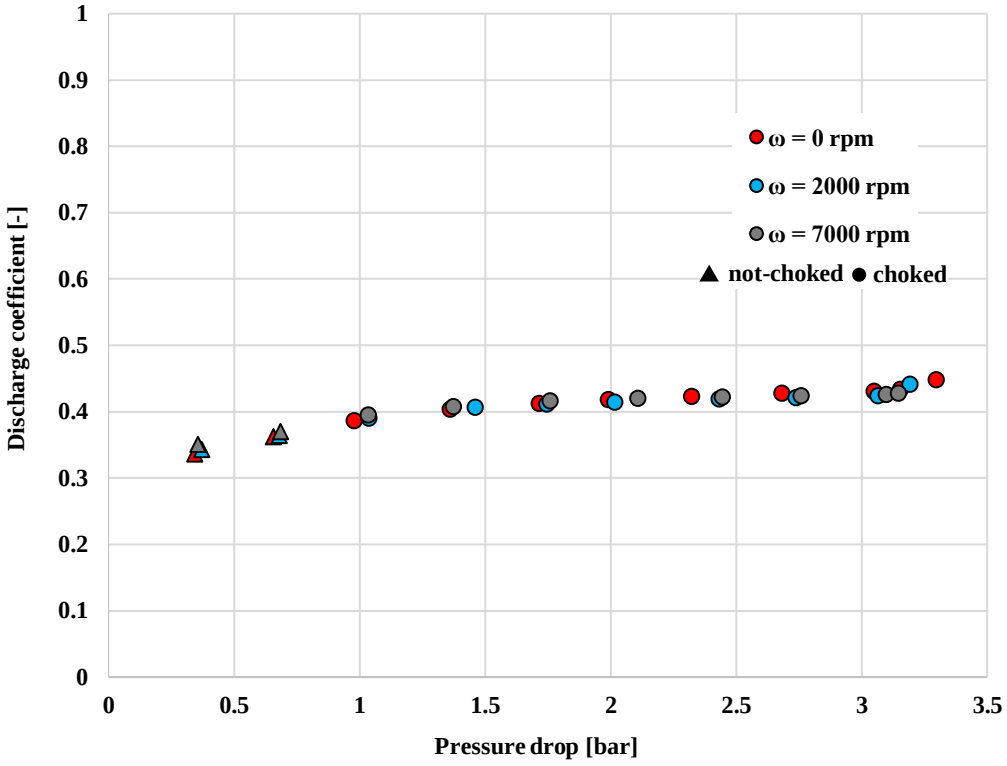

Figure 5.20. Variation of discharge coefficient with pressure difference for three rotational speeds.

5.7 Summary

This chapter presented the rotordynamic coefficients and the leakage performance of a short labyrinth seal with four cavities measured in a high-speed rotating test facility. Before discussing the results, a review of the existing literature on experimental rotordynamic coefficients of labyrinth seals was given. It was found that the majority of the studies investigated the behaviour of long labyrinth seals with a large number of cavities (13 or more). Hence, the results presented in this chapter fill this gap in the literature.

The frequency response functions of the seal clearance thin film of air were discussed and the process to calculate them from the combination of two different vibration tests (baseline test and test with flow and rotation) was explained. The real part of the direct complex stiffness is frequency independent, i.e. the resulting added-mass is zero, which is expected for a gas seal with no moving parts. The real part of the cross-coupled complex stiffness is also frequency independent for a frequency range between 10 and 90 Hz. However, at the high frequency end, the function changes with frequency, which is thought to be due to misalignments in the vibration test set-up.

Six repetitions of the vibration test were performed at each condition tested and the measurements from these were averaged to calculate the rotordynamic coefficients of the seal. By averaging multiple tests, the uncertainty of the rotordynamic coefficients is reduced, although only marginally. It was also demonstrated that the effect of the cross-coupled damping on the stability of the seal is negligible.

The results of the rotordynamic coefficients were shown to be affected by the ambient temperature. Tests performed at the same conditions of pressure drop and rotational speed, but on different days, showed an inverse variation of the rotordynamic coefficients with the measured temperature upstream of the seal; i.e. both the direct stiffness and damping increased as the temperature decreased. However, there was no control over the temperature and changes in this variable were purely due to day-to-day variation.

The direct and cross-coupled stiffness and the direct damping of the labyrinth seal were measured at pressure drops of 2.0, 2.4, 2.9 and 3.3 bar for rotational speeds ranging between 900 and 14,600 rpm. The results showed that the three rotordynamic coefficients increase with increasing pressure drops, although this trend is not as obvious for the cross-coupled stiffness. The direct stiffness is positive and it slightly decreases with increasing rotational speed. The cross-coupled stiffness is negative and it decreases as the rotational speed increase, likewise the direct damping. Plots of the effective damping indicated that increments in pressure drop stabilise the behaviour of the seal, whereas increasing rotational speed has the opposite effect.

The leakage performance of the labyrinth seal was determined from mass flow rate measurements. The mass flow rate does not vary with rotational speed within the range of speeds tested and behaves linearly with pressure drop for values at which the flow is choked, thus in agreement with the theory. A discharge coefficient of 0.4 was calculated for the seal, which is similar to that found by Wittig *et al.* [1987].

Chapter 6: Characterisation of an annular Rayleigh-step seal

An annular seal featuring a Ryleigh step is studied in this chapter. The clearance profile of this seal is the same as that of the FRPALS prototype to be investigated during this research. This is done with the intention of gaining a better understanding of the behaviour of a seal with such geometry, but without the complexity of the FRPALS moving parts.

The ability to model the clearance film under all dynamic conditions would support the design process of a future FRPALS. The integral of the pressure distribution over the seal runner surface results in the forces/moments, which are key components to balance for reliable performance of the FRPALS. Within the scope of this project, a solution of the steady state Reynolds equation for gas lubrication is presented with experimental validation.

6.1 Annular Rayleigh-step seal geometry

The annular seal under investigation consists of a solid ring turned in the lathe as a single part and Figure 6.1 shows its geometry. The seal features a Rayleigh step 15.24 mm long and 0.134 mm high, which is located at 15.24 mm downstream of the seal leading edge. The minimum clearance of the seal is 0.165 mm, yielding a clearance ratio of $c/R = 1.29 \cdot 10^{-3}$.

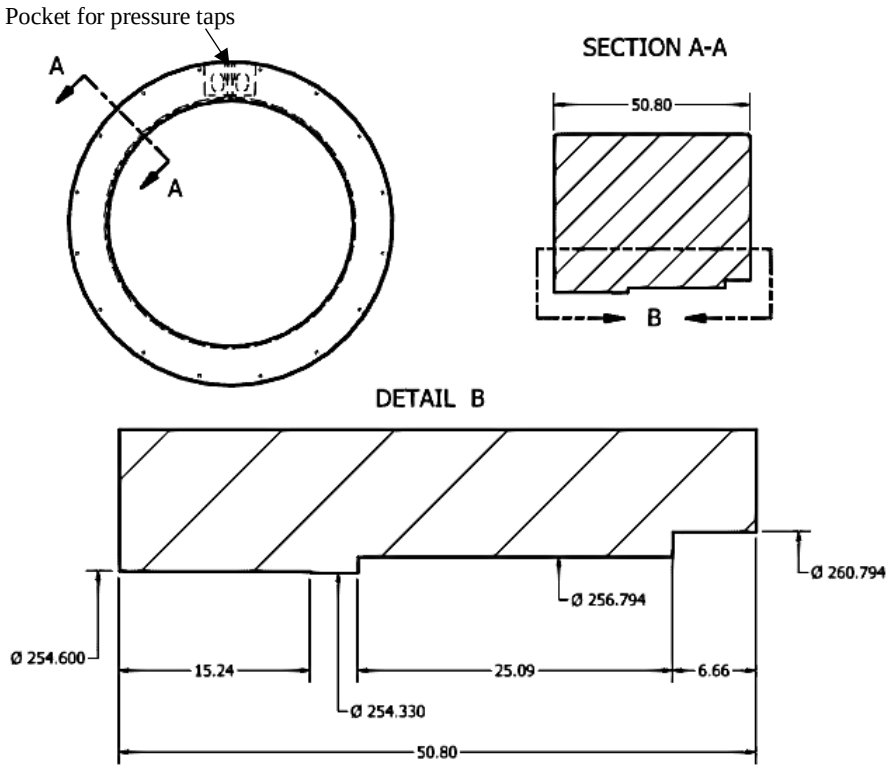

Figure 6.1: Geometry of the Rayleigh-step annular seal under investigation.

Several pressure taps were incorporated in the seal at one circumferential location and distributed along the axial direction in order to measure the pressure distribution of the clearance film. The location of the pressure taps was chosen so that the measurements were taken in the regions were the pressure changes are the greatest; namely where the geometry varies abruptly, i.e. where the Rayleigh step is located. Figure 6.2 shows an isometric view of a 3D cut away of the seal showing the milled recess needed to install the pressure taps and the top view of the pressure taps arrangement.

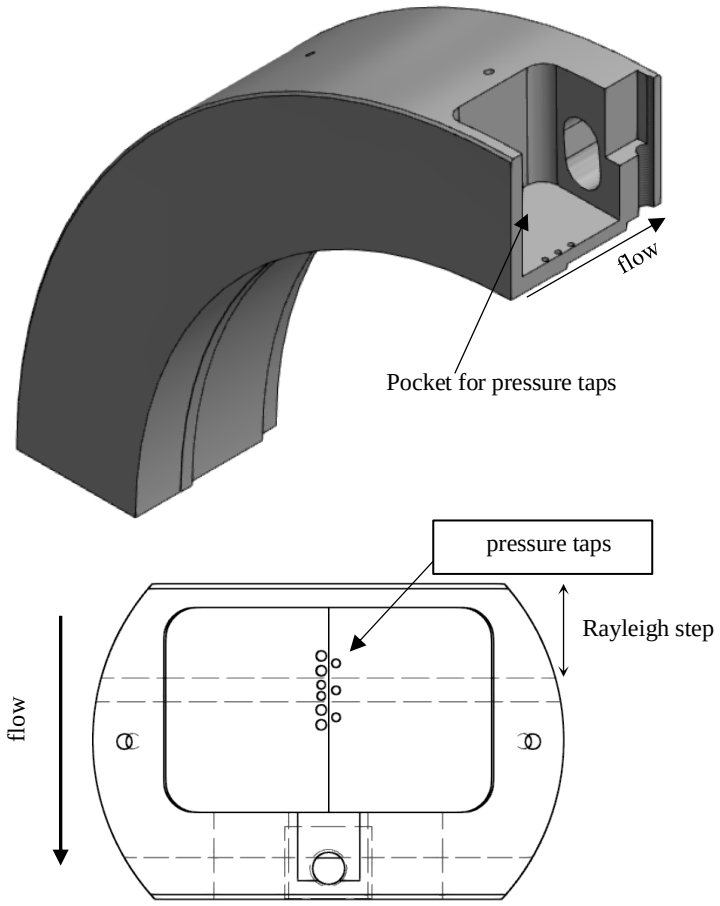

Figure 6.2: Isometric-quarter section view of the Rayleigh step annular seal showing the pocket machined to install the pressure taps and a detail of the top view of the pocket featuring nine pressure taps along the axial direction.

6.2 Rotordynamic coefficients

Figure 6.3 to Figure 6.5 show the rotordynamic coefficients of the Rayleigh-step annular seal. The measurements have been performed at the same experimental conditions as the labyrinth seal in Chapter 5 and are given in Section 5.2.

The direct stiffness is presented in Figure 6.3. It is shown to be virtually independent of the rotational speed and increases with pressure drop across the seal. Contrary to the behaviour of the labyrinth seal, no effect of inlet temperature is identified in this case, which may be interpreted as the impact of the pressure drop being large enough to outweigh any temperature influence. The direct stiffness of the Rayleigh-step annular seal is 1.6 times as large as the labyrinth seal. For instance, at a pressure drop of 2.0 bar, the direct stiffness is 4 MN/m for the Rayleigh-step annular seal and 2.5 MN/m for the labyrinth seal. The difference in direct stiffness from both seals may be attributed to the fact that the Rayleigh-step annular seal clearance has a large, flat region in which the high pressure air effectively transmits the movement between the stator and the rotor, whereas in the labyrinth seal the pressure of the air decreases from the first restriction. This may also be the reason for the clear increase in direct stiffness with increasing pressure drop mentioned above.

The cross-coupled stiffness is shown in Figure 6.4. This rotordynamic coefficient is positive, which translates into a destabilising behaviour of the seal, according to the sign convention of Figure 4.3. Additionally, the cross-coupled stiffness is larger in magnitude than the cross-coupled stiffness of the labyrinth seal. None of these two results are surprising as this seal has a long region of tight clearance where high pressure air is contained before it is expanded along the Rayleigh step. Under system perturbations, this high pressure air acting on a relatively large area would have an effect not only in the direction of the perturbation but also in the direction orthogonal to this. Similar to the direct stiffness, the cross-coupled stiffness does not show a strong dependency with rotational speed. No trend can be identified with varying pressure drop.

Unlike the direct stiffness, the direct damping shows a stronger dependency with temperature. When comparing Figure 6.5 and Figure 6.6, it can be seen that the direct damping is largest when the temperature is the lowest, i.e. at 2.9 bar pressure drop. It is also clear that the direct damping at this pressure drop follows the trend of the temperature with rotational speed. These two results confirm the inverse proportionality between the direct damping and temperature observed in the rotordynamic coefficients of the labyrinth seal. The change in damping due to changes in pressure drop is not as obvious for the other three values of the pressure drop tested. This is thought to be due to the pressure drop and the temperature having opposite effects. In other words, the damping would be expected to increase with larger values of the pressure drop; but the temperature increases, causing the direct damping to decrease and overriding the effect of the pressure drop.

As explained in Chapter 4 by means of Eq. 4.4, the effective damping is the parameter used to compare the stability of different annular gas seals. Figure 6.7 shows together the effective

damping of the labyrinth seal and the Rayleigh-step annular seal measured at a pressure drop of 2.9 bar. The short labyrinth seal is shown to be superior to the Rayleigh-step annular seal from a stability standpoint at low rotational speed. This is due to the destabilising effect of the positive cross-coupled stiffness values measured for the Rayleigh-step annular seal. The difference in effective damping between both types of seals reduces with increasing shaft speed and is marginal beyond 12,000 rpm. Only one pressure drop is presented here for the sake of clarity as the same trend is observed for the other three cases.

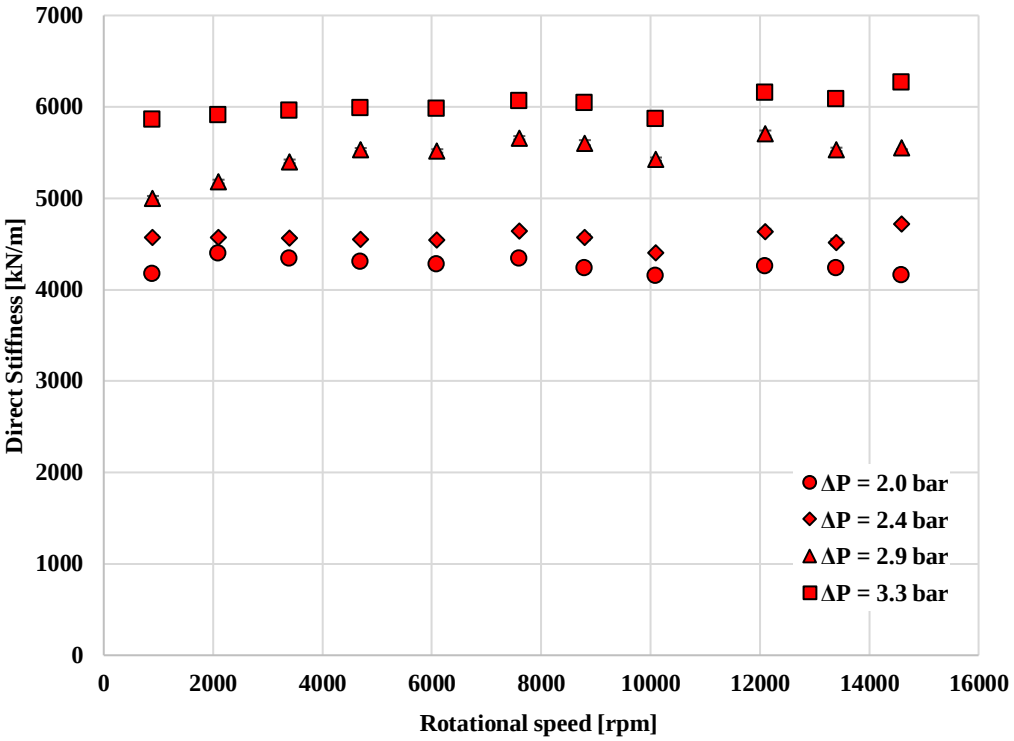

Figure 6.3. Comparison of the direct stiffness of a Rayleigh-step annular seal tested at four different pressure drop values.

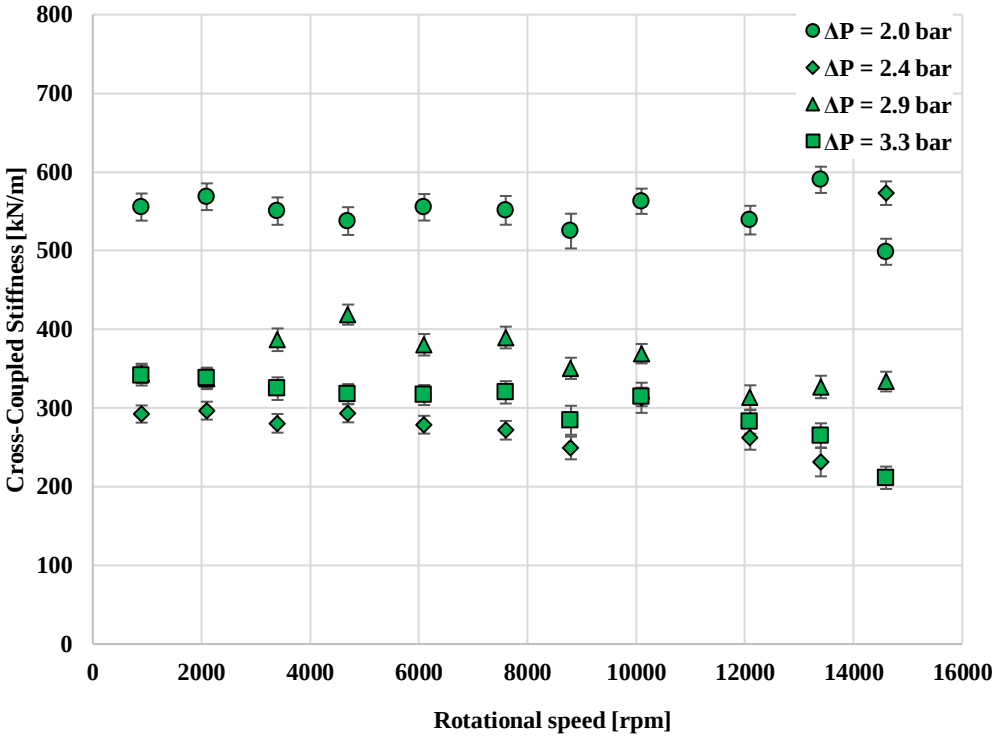

Figure 6.4. Comparison of the cross-coupled stiffness of a Rayleigh-step annular seal tested at four different pressure drop values.

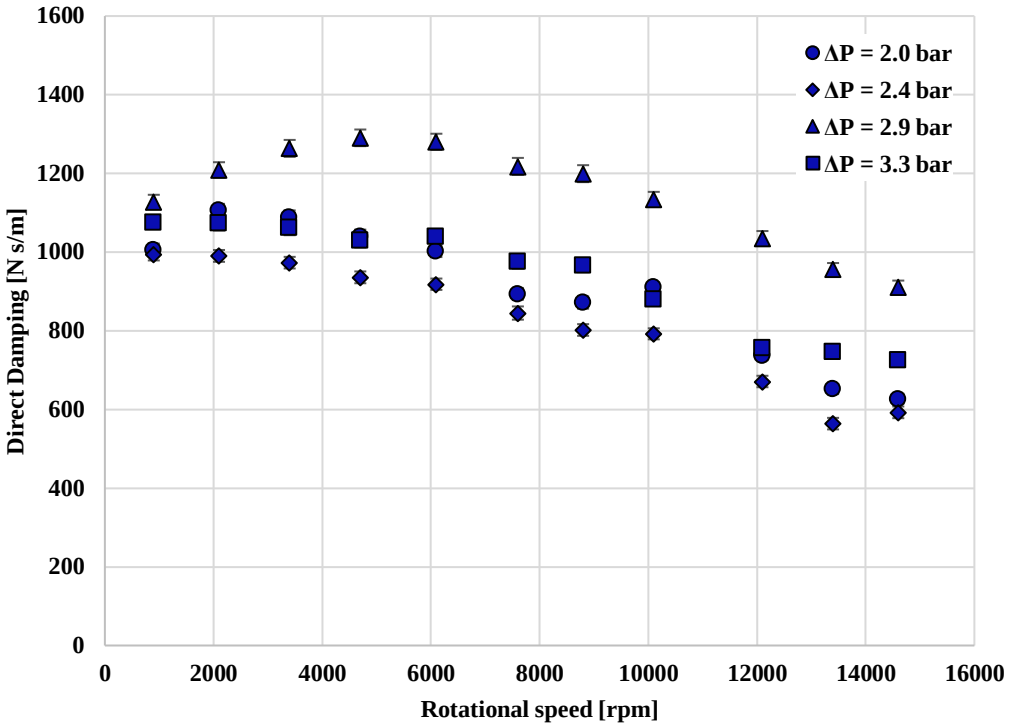

Figure 6.5. Comparison of the direct damping of a Rayleigh-step annular seal tested at four different pressure drop values.

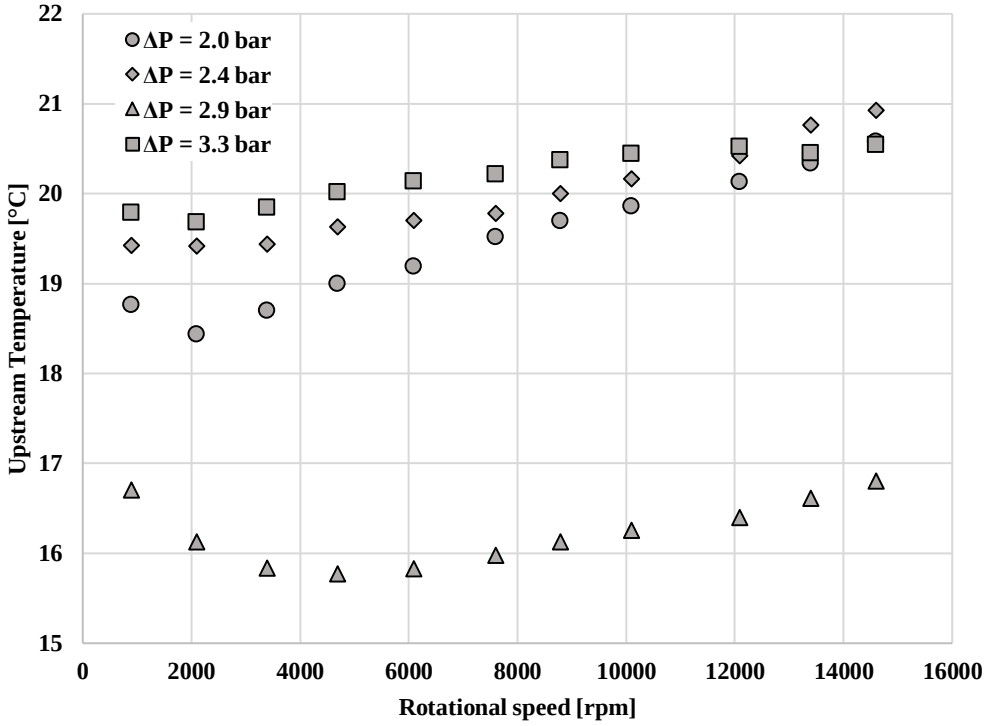

Figure 6.6. Temperature of the air upstream of a Rayleigh-step annular seal tested at four different pressure drop values.

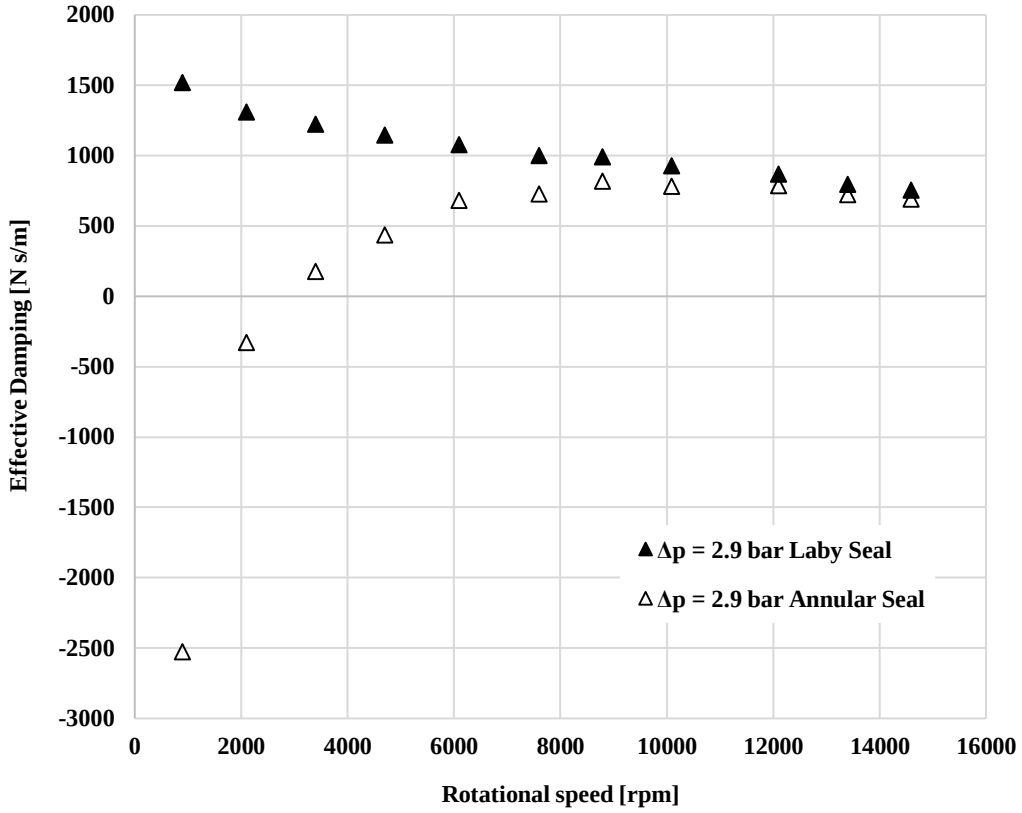

Figure 6.7. Comparison between the effective damping of the short labyrinth seal from Chapter 5 and the Rayleigh-step annular seal tested at a pressure drop of 2.9 bar.

6.3 Leakage performance

The leakage mass flow rate of the annular seal at four rotational speeds is plotted against pressure difference in Figure 6.8. The data shows the leakage mass flow rate decreases as the rotational speed increases. This effect of the rotational speed is directly translated into the effective clearance, as shown in Figure 6.9, and is thought to be caused by the narrowing of the clearance due to the growth of the rotor. In order to confirm this hypothesis, the difference in effective clearance between the tests with a rotational speed greater than zero and the static case was calculated and compared with the growth of the rotor measured during the commissioning of the rig in Table 6.1. Good agreement between both values is found.

Mass flow measurements for the labyrinth seal characterised in Chapter 5 showed that no changes in leakage performance occurred with varying rotational speed. This surprising difference in the behaviour of the mass flow rate between the two types of seal can be explained by looking at de the design of both the test rig and the testing prototypes. First, the

rotor radial growth changes along the axial span of the rotor due to its recessed cross-section design (see Figure 3.28). Additionally, the axial position of the flow restrictions with respect to the rotor surface is different for each seal, making the non-uniform growth of the rotor affect the behaviour of each design differently.

Figure 6.10 shows the discharge coefficient calculated as per Eq. 4.17 in Chapter 4 accounting for the growth of the rotor. The data proves that the discharge coefficient calculated in this way is independent of rotor speed. This is further evidence that the change in mass flow rate with rotational speed is due to the growth of the rotor. Additionally, Figure 6.10 shows the discharge coefficient of the labyrinth seal presented in Chapter 5 for comparison. The discharge coefficient of the Rayleigh-step annular seal is approximately 0.8, which is twice as large as the discharge coefficient of the labyrinth seal. This means that, for the same clearance height, rotor diameter and operating conditions, the labyrinth seal is more efficient in restricting the flow.

Both the effective clearance and the discharge coefficient plateau beyond the choked conditions, as expected.

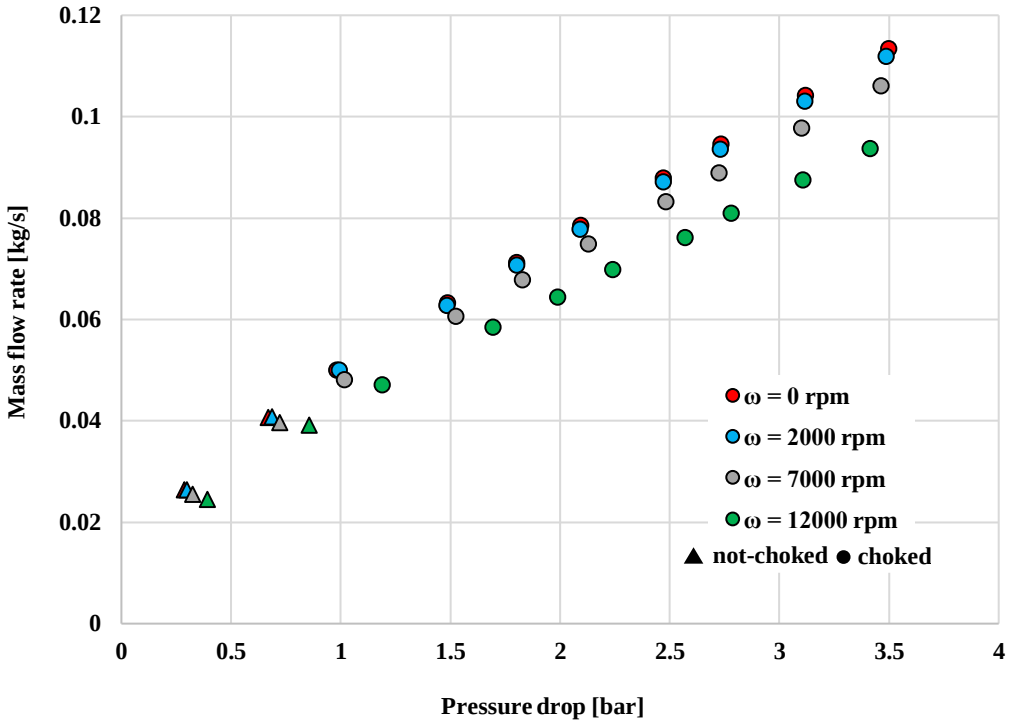

Figure 6.8. Variation of mass flow rate with pressure difference for four rotational speeds.

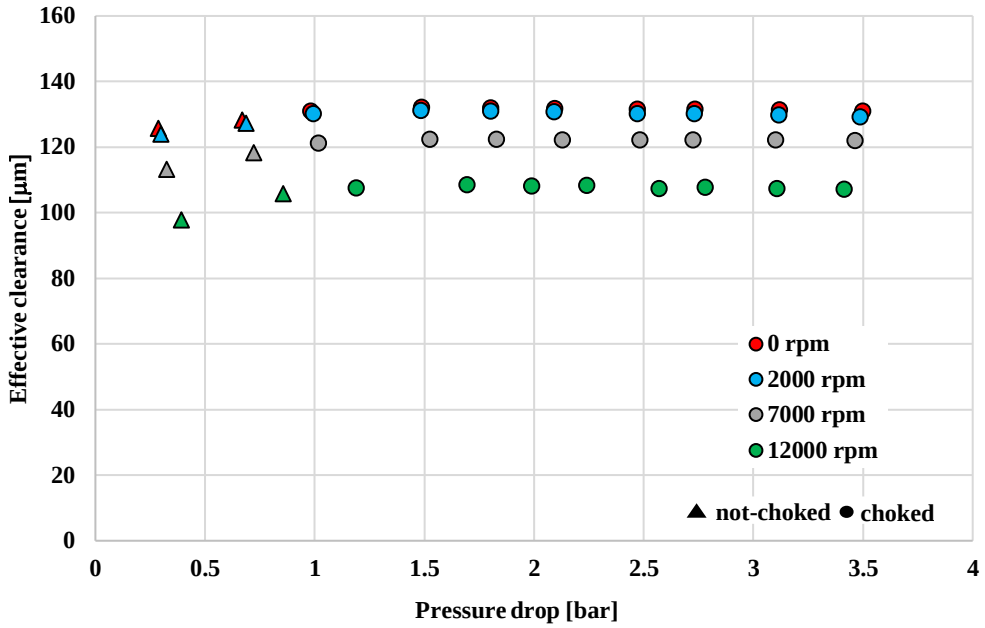

Figure 6.9. Variation of effective clearance with pressure difference for four rotational speeds.

Table 6.1. Comparison between the difference of effective clearance between the rotating tests and the static one with the measured rotor growth.

rotational speed [rpm]	0	2000	7000	12000
Δ effective clearance [μm]	0	1.4	9.4	23.7
measured growth [μm]	0	2	9	29

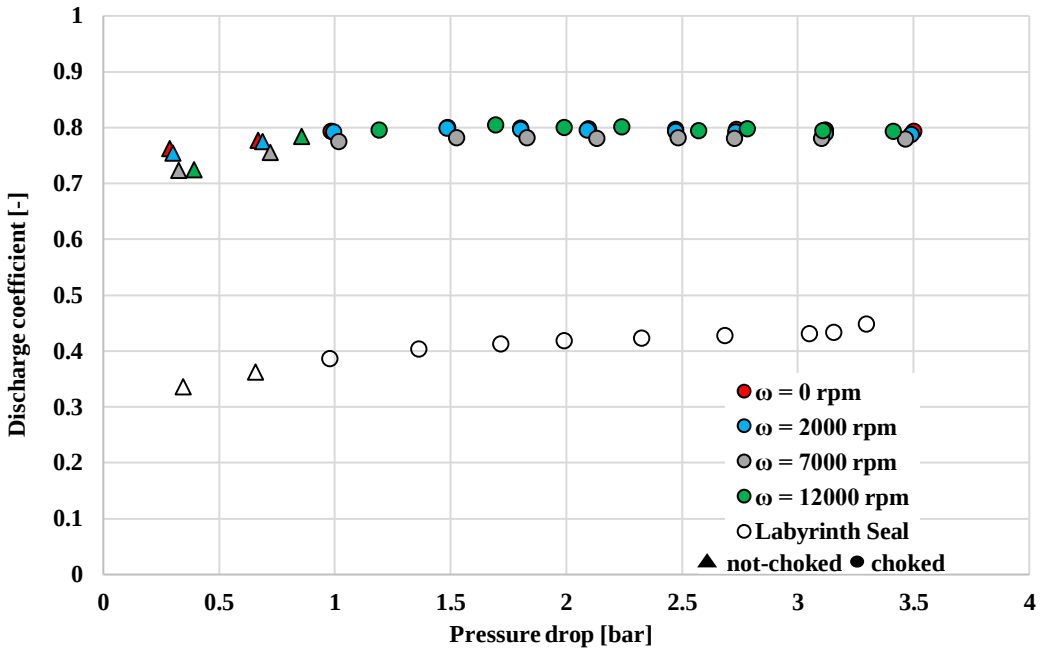

Figure 6.10. Variation of discharge coefficient with pressure difference for four rotational speeds.

6.4 Seal film modelling

The steady state Reynolds equation for gas lubrication may be used to predict the pressure distribution in between the FRPALS runners and the rotor. Integrating this pressure distribution across the runner area yields the forces/moments applied by the clearance fluid film to the seal. Therefore, this tool can be used at the design stage of the FRPALS in order to have a balanced system without the need of expensive experimental iterations. Additionally, the solution of the transient form of the Reynolds equation provides with the perturbations of the forces/moments acting on the runners of the seal, which in turns can be used to calculate the rotordynamic coefficients of the FRPALS. This section shows a solution of the one-dimensional, steady-state Reynolds equation as a stepping-stone towards the final aim of solving the two-dimensional, transient form of the equation. The full derivation of the Reynolds equation for lubrication can be seen in Hamrock *et al.* [2004] The Reynolds equation in its non-dimensional form is shown in Eq. 6.1.

$$\frac{\partial}{\partial \theta}\left(H^3 \frac{\partial P^2}{\partial \theta}\right) + \frac{\partial}{\partial \eta}\left(H^3 \frac{\partial P^2}{\partial \eta}\right) = 2\Lambda \frac{\partial (PH)}{\partial \theta} \qquad \textbf{6.1}$$

where θ is the tangential coordinate, $\eta = z/R$ is the axial coordinate, $P = p/p_a$, $H = h/c$, and the compressibility number is:

$$\Lambda = \frac{6\mu\omega R^2}{p_a c^2} \qquad \textbf{6.2}$$

In terms of the new variable $Q = P^2 H^2$, Eq. 6.1 can be rearranged to give:

$$\frac{\partial^2 Q}{\partial \theta^2} + \frac{\partial^2 Q}{\partial \eta^2} - \frac{1}{H}\left(\frac{\partial H}{\partial \theta} + \frac{\Lambda}{\sqrt{Q}}\right)\frac{\partial Q}{\partial \theta} - \frac{2}{H}\frac{\partial^2 H}{\partial \theta^2} = 0 \qquad \textbf{6.3}$$

The iterative method developed by Castelli and Pirvics [1967] can be used to solve the Reynolds equation numerically for compressible lubrication. In this method, the 2-D space defined by the tangential and axial axes of the seal is divided into a rectangular mesh in which all functions in Eq. 6.3 are represented by their values at the nodes. The derivatives of Q and H are discretised by a three-point central difference scheme, which enables Eq. 6.3 to be written in terms of algebraic relationships.

The *j*-axis of the finite difference grid coincides with the θ-direction, while the *i*-axis is in the negative η-direction. With this definition of the frame of reference, $j = 1$ at $\theta = \theta_1$, $j = m$ at $\theta = \theta_2$, $i = 1$ at $\eta = L/R$ and $i = n$ at $\eta = 0$, the finite difference increments are $\Delta\theta =$

$(\theta_2 - \theta_1)/m$ and $\Delta\eta = L/nR$. The general form of the algebraic approximation of Eq. 6.3 can be written in matrix notation as follows:

$$[\boldsymbol{A_j}]\{\boldsymbol{\phi_j}\} + [\boldsymbol{B_j}]\{\boldsymbol{\phi_{j-1}}\} + [\boldsymbol{C_j}]\{\boldsymbol{\phi_{j+1}}\} = \{\boldsymbol{R_j}\} \qquad \textbf{6.4}$$

for $j = 1,2, \dots, m$, where $\{\boldsymbol{\phi}_j\}$ is the vector of the unknown function, Q, at the *j*-th column of the grid and $\{\boldsymbol{R}_j\}$ is the vector of right-hand sides at the *j*-th column of the grid. The *i*-th elements of $\{\boldsymbol{\phi}_j\}$ and $\{\boldsymbol{R}_j\}$ are denoted by ϕ_{ij} and R_{ij}, respectively. The matrices of coefficients $[\boldsymbol{A_j}], [\boldsymbol{B_j}], [\boldsymbol{C_j}]$ are $n \times n$ matrices in which the *ik*-th elements are denoted by $A_{ikj}, B_{ikj}, C_{ikj}$, respectively.

The values of the coefficient matrices and the right-hand side term are calculated as follows:

(a) If (i, j) is a field point:

$$\boldsymbol{A_{i,i,j}} = -\mathbf{2}\left[\frac{\mathbf{1}}{\boldsymbol{\Delta\theta^2}} + \frac{\mathbf{1}}{\boldsymbol{\Delta\eta^2}} + \frac{\mathbf{1}}{\boldsymbol{H}}\left(\frac{\boldsymbol{\partial^2 H}}{\boldsymbol{\partial\theta^2}} + \frac{\boldsymbol{\partial^2 H}}{\boldsymbol{\partial\eta^2}}\right)_{\boldsymbol{ij}}\right]$$

$$\boldsymbol{A_{i,i-1,j}} = \frac{\mathbf{1}}{\boldsymbol{\Delta\eta^2}} + \frac{\mathbf{1}}{\mathbf{2}\boldsymbol{\Delta\eta}}\left(\frac{\boldsymbol{\partial\, ln\, H}}{\boldsymbol{\partial\eta}}\right)_{\boldsymbol{ij}}$$

$$\boldsymbol{A_{i,i+1,j}} = \frac{\mathbf{1}}{\boldsymbol{\Delta\eta^2}} - \frac{\mathbf{1}}{\mathbf{2}\boldsymbol{\Delta\eta}}\left(\frac{\boldsymbol{\partial}\,\mathbf{ln}\,\boldsymbol{H}}{\boldsymbol{\partial\eta}}\right)_{\boldsymbol{ij}}$$

$$\boldsymbol{B_{i,i,j}} = \frac{\mathbf{1}}{\boldsymbol{\Delta\theta^2}} + \frac{\mathbf{1}}{\mathbf{2}\boldsymbol{\Delta\theta}}\left[\left(\frac{\boldsymbol{\partial}\,\mathbf{ln}\,\boldsymbol{H}}{\boldsymbol{\partial\eta}}\right)_{\boldsymbol{ij}} + \frac{\boldsymbol{\Lambda}}{\left(\boldsymbol{HQ}^{\mathbf{1}/\mathbf{2}}\right)_{\boldsymbol{ij}}}\right]$$

$$\boldsymbol{C_{i,i,j}} = \frac{\mathbf{1}}{\boldsymbol{\Delta\theta^2}} - \frac{\mathbf{1}}{\mathbf{2}\boldsymbol{\Delta\theta}}\left[\left(\frac{\boldsymbol{\partial}\,\mathbf{ln}\,\boldsymbol{H}}{\boldsymbol{\partial\eta}}\right)_{\boldsymbol{ij}} + \frac{\boldsymbol{\Lambda}}{\left(\boldsymbol{HQ}^{\mathbf{1}/\mathbf{2}}\right)_{\boldsymbol{ij}}}\right]$$

The remaining elements of the coefficient matrices are equal to zero:

$$\boldsymbol{R_{ij}} = \mathbf{0}$$

(b) If (i, j) is a boundary point with a specified value of ϕ_{ij}, then:

$$\boldsymbol{A_{i,i,j}} = \mathbf{1}$$

and all the remaining elements of $[\boldsymbol{A_j}], [\boldsymbol{B_j}], [\boldsymbol{C_j}]$ are zero. Also,

$$\boldsymbol{R_{ij} = \phi_{ij}}$$

Equation 6.4 can be solved using the recurrence relationship introduced by Castelli and Pirvics [1967]:

$$\{\boldsymbol{\phi_{j-1}}\} = [\boldsymbol{D_{j-1}}]\{\boldsymbol{\phi_j}\} + \{\boldsymbol{E_{j-1}}\} \quad \textbf{6.5}$$

The influence coefficients $[\boldsymbol{D_j}]$ and $\{\boldsymbol{E_j}\}$ can be calculated by substituting Eq. 6.5 into Eq. 6.4, starting with $j = 2$ through to $j = m - 1$:

$$[\boldsymbol{D_j}] = -([\boldsymbol{A_j}] + [\boldsymbol{B_j}][\boldsymbol{D_{j-1}}])^{-1}[\boldsymbol{C_j}] \quad \textbf{6.6}$$

$$\{\boldsymbol{E_j}\} = ([\boldsymbol{A_j}] + [\boldsymbol{B_j}][\boldsymbol{D_{j-1}}])^{-1}(\{\boldsymbol{R_j}\} - [\boldsymbol{B_j}]\{\boldsymbol{E_{j-1}}\}) \quad \textbf{6.7}$$

Once $[\boldsymbol{D_j}]$ and $\{\boldsymbol{E_j}\}$ are known and using the boundary condition $\{\boldsymbol{\phi}_m\}$, the solution vector $\{\boldsymbol{\phi}_j\}$ is calculated using Eq. 6.5 by varying j from m to 2.

6.4.1 Validation

The model described above was first validated with results by Faria and San Andrés from the solution of the Reynolds equation for gas lubrication for the plane slider bearing represented in Figure 6.11. For a bearing number of $\Lambda = 1000$ and a zero pressure drop imposed across the bearing, Figure 6.12 show the non-dimensional pressure distribution along the clearance of the bearing at three different values of the inlet to outlet channel height ratio (h_1/h_2). The same solution as the one given by Faria and San Andrés [1999] is found. It should be mentioned that the data from Faria and San Andrés [1999] is from a different solution of the Reynolds equation and the discrete points shown in Figure 6.12 are digitised points from a continuous curve.

A second validation of the model is made with the seal geometry used by Cross Manufacturing to statically test the FRPALS concept (Kirk *et al.* [2016]). A two-dimensional segment of the seal was tested in a pressurised chamber. The pressure distribution in the direction of the flow at the centreline of the testing segment was measured; Figure 6.13 shows the experimental setup with the pressure measurement locations. The plate underneath the seal segment runner was fitted with 14 staggered pressure taps to measure the pressure variation along the flow direction. The readings of these pressure taps for eight different upstream pressures ranging between 3.5 and 1 bar-g are plotted in Figure 6.14 against the predictions calculated with the method described above. In this case, there is no relative movement between the two surfaces that form the flow channel, i.e. the bearing number is zero ($\Lambda = 0$).

Overall, good agreement can be seen in both the measured and predicted pressure distributions. Poorer agreement is seen in the region where the Rayleigh step is located. Here the measurements show a sudden pressure drop immediately downstream of the Rayleigh step followed by flat behaviour of the pressure, while the modelled pressures show a gradual decrease until matching the downstream pressure level. Similarly, the measured pressure experiences a sharp drop as the channel narrows at the film-riding region of the clearance and then progressively decreases down to the discharge pressure level. However, the predicted pressures do not show the initial pressure drop. This mismatch between the experiments and the predictions is thought to be due to the model working under the assumption that the pressure variation across the height of the channel is zero. This is assumption applies along most of the length of the clearance except in these two regions where the geometry changes abruptly. Here the flow is likely to separate creating a vena contracta effect and causing the pressure to drop.

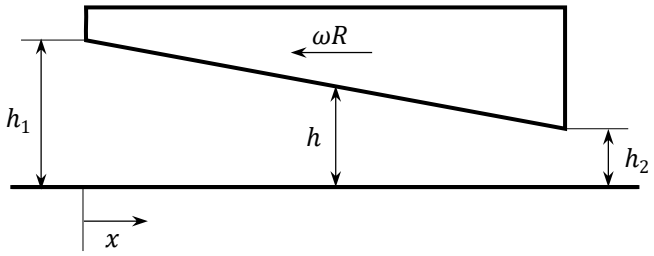

Figure 6.11. Schematic view of the plane slider bearing used by Faria and San Andrés [1999].

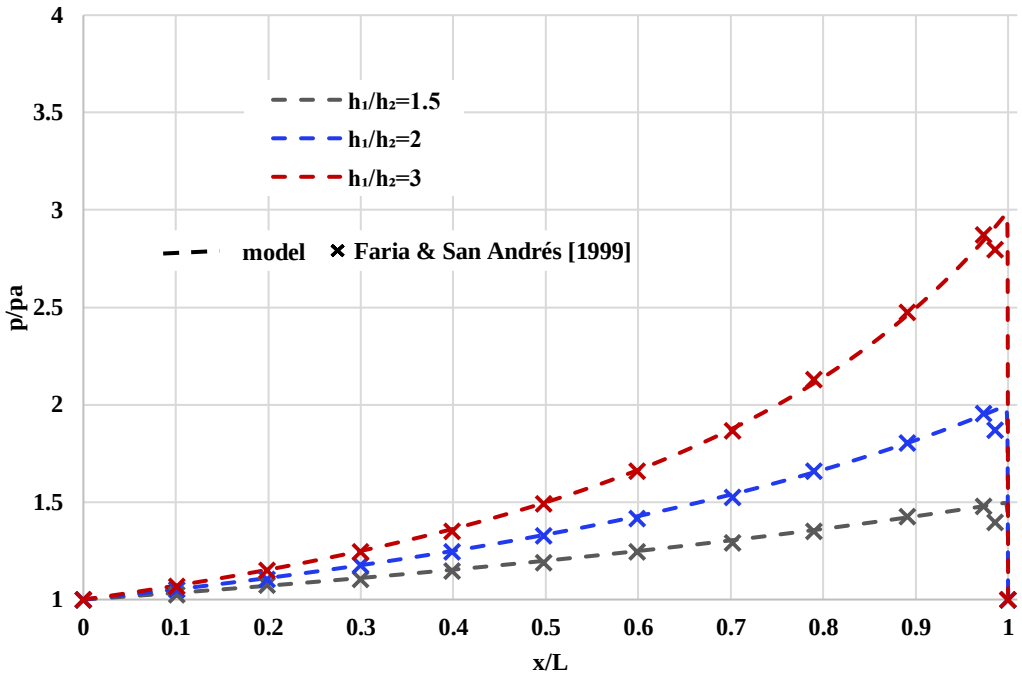

Figure 6.12. Dimensionless pressure distribution along a plane slider bearing. Comparison with the results by Faria and San Andrés [1999].

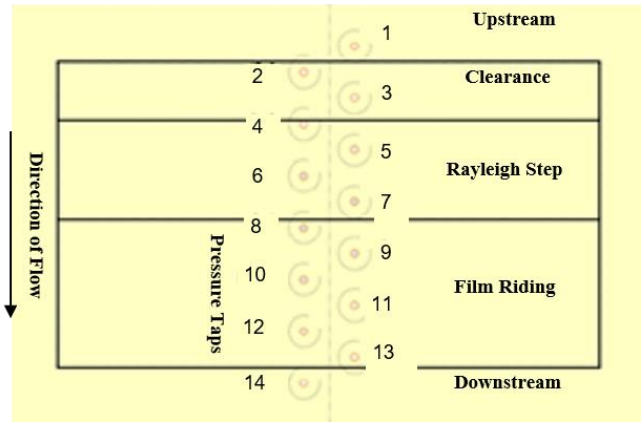

Figure 6.13. Pressure taps arrangement used to measure the pressure distribution along the seal clearance by Kirk *et al.* [2016].

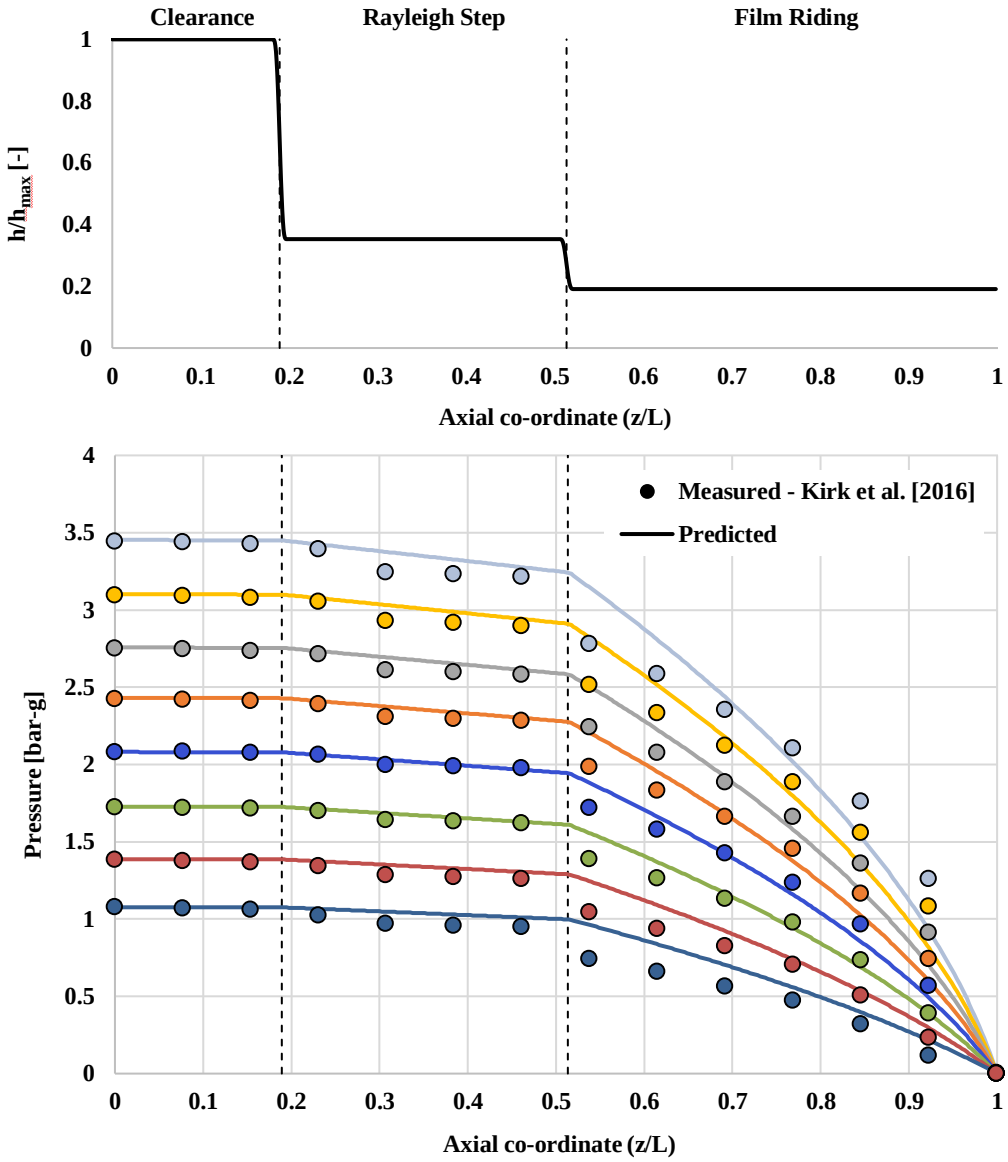

Figure 6.14. Dimensionless geometry and pressure distribution of the clearance of the 2D FRPALS tested by Cross Manufacturing at different upstream pressure levels.

6.5 Axial pressure distribution

In this section, the pressure distribution along the axial direction of the seal measured using the pressure taps shown in Figure 6.2 is discussed. Figure 6.15 shows the non-dimensional geometry of the seal clearance. Additionally, it depicts the three different areas in which the channel is divided and the location of the pressure taps, for reference. Both the measured and predicted pressure distributions are plotted together. Good agreement between both methods is shown for the Rayleigh step section of the clearance. Similar to the second validation case presented in section 6.4.1, at the beginning of the film-riding region the measured pressure reduces at a greater rate than the modelled one. As the channel broadens (clearance region), the flow expands at the backward-facing step, featuring a separation region just downstream of the step. This is reflected in the negative values of the measured pressure. The model does not predict this feature of the flow as it does not account for pressure variations across the height of the channel.

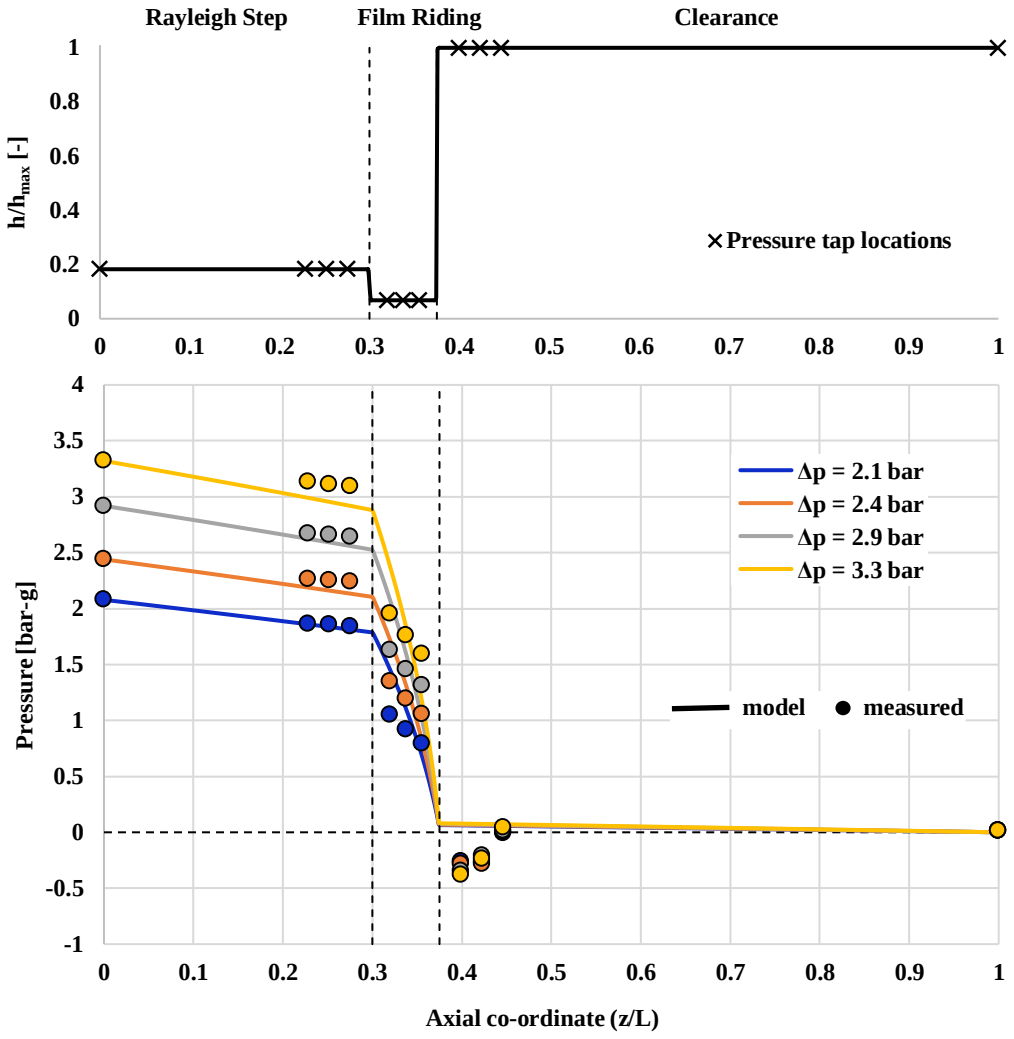

Figure 6.15. Dimensionless geometry and pressure distribution of the clearance of the Rayleigh-step annular seal tested at stationary conditions for four different pressure drops.

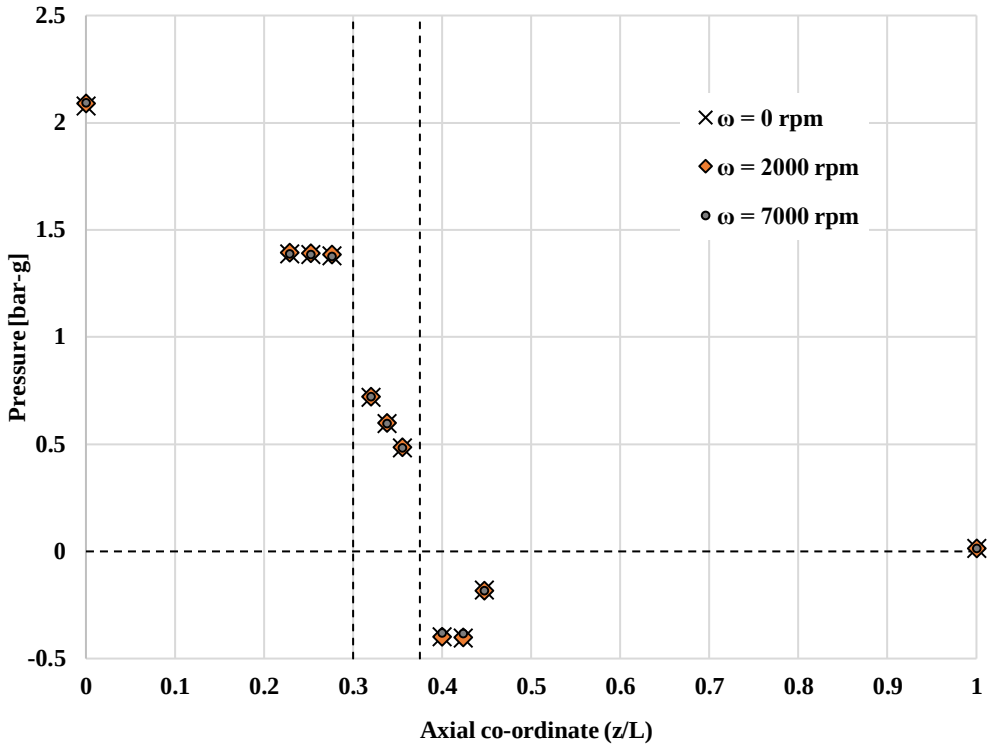

Figure 6.16. Pressure distribution along the axial direction of the clearance of the Rayleigh-step annular seal tested at a pressure drop of 2 bar and three different rotational speeds.

The effect of rotation was also investigated. The axial pressure distribution was measured for three different rotational speeds at a pressure drop of 2 bar and zero eccentricity. Figure 6.16 shows the results of these tests. No changes in the axial pressure distribution were observed. This result can be expected as the hydrodynamic-journal-bearing theory (Hamrock *et al.* [2004]) predicts that the variation of pressure in the tangential (rotational) direction is caused by changes in the film thickness, which are zero for the centred case of the seal under investigation.

When an eccentricity different to zero exists between the rotor and the stator, then the pressure of the thin fluid film experiences a gradient along the circumference of the seal clearance that is proportional to the rotational speed of the shaft. However, this effect has not been established as during the testing at zero eccentricity the rotor rubbed against the seal wearing it out.

The variation of pressure due to changes in eccentricity for the static case was measured before the prototype was damaged at four different pressure drops. Figure 6.17 shows the results for the 2 bar pressure drop case. Changes in eccentricity cause the pressure level at the measurement locations to be shifted. This shift applies to the whole axial length of the

clearance. The pressure increases as the channel narrows (eccentricity decreases), and vice versa.

To be able to predict the effect of both the eccentricity and the rotational speed in the pressure of the seal thin film of air, the complete Reynolds equation for gas lubrication (Eq. 6.1) must be solved. Up to now, and within the scope of this research, only the one-dimensional solution of this equation has been obtained and the upgraded two-dimensional model is left as part of the future work. Additionally, the final aim is to solve the transient form of the Reynolds equation in order to predict the rotordynamic coefficients of the seal.

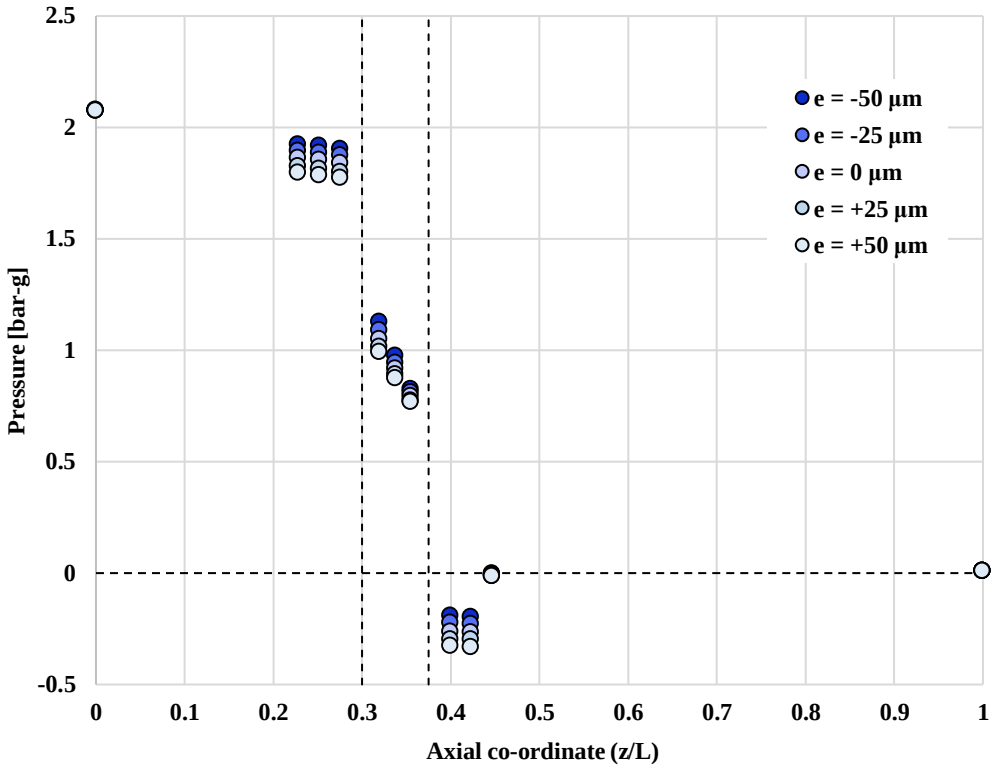

Figure 6.17. Pressure distribution along the axial direction of the clearance of the Rayleigh-step annular seal tested at a pressure drop of 2 bar and five different eccentricity values.

6.6 Summary

This chapter presented measurements of rotordynamic coefficients for a Rayleigh-step annular seal. The direct stiffness is positive and over 1.5 times larger than the direct stiffness of the labyrinth seal tested in Chapter 5. It increased as pressure drop increased and no changes with rotational speed were found. The cross-coupled stiffness is positive, i.e. has a destabilising effect, and is larger in magnitude than the cross-coupled stiffness of the labyrinth seal. Its dependency with rotational speed is small. Similar values to the labyrinth seal for

direct damping were found. Direct comparison of the effective damping of both types of seals suggests that the labyrinth seal is superior to the Rayleigh-step seal from a stability point of view.

The leakage mass flow rate of the seal was also measured showing that the Rayleigh-step annular seal leakage decreased as rotational speed increased due to changes in clearance area caused by rotor growth. Agreement between changes in effective clearance and direct measurements of the rotor growth demonstrated this. The discharge coefficient of Rayleigh-step seal was double than that of the labyrinth seal.

The iterative solution of the Reynolds equation for gas lubrication developed by Castelli and Pirvics [1967] has been used to predict the pressure distribution of the thin film of air in the clearance of the seal. A validation with published data for a linear wedge bearing was performed showing good agreement. Additionally, experimental pressure data from tests performed on a two-dimensional segment of the FRPALS at Cross was used as a second validation. Overall good agreement was found between the measurements and the predictions. However, the model failed to predict the flow features due to the vena contracta effect in the regions of the seal where the clearance reduces abruptly.

The model was also used to predict the pressure distribution in the clearance of the Rayleigh-step annular seal under study. Comparison with pressure measurements showed the model is not capable of predicting the separation of the flow in the backward-facing step feature in the clearance of the seal. In spite of the regions were the assumption of zero pressure gradient along the height of the channel does not hold, the model the pressure predictions match well with experimental data.

Measurements of pressure in the clearance of the seal were also taken with rotation and eccentricity. No changes in pressure were seen for the case in which the seal was concentric to the rotor and rotational speeds of up to 7,000 rpm. In contrast, for eccentricities ranging between +/- 50 μm and zero rotor speed, it was found that the pressure rose for decreasing values of seal clearance. The effect of the rotational speed and eccentricity were not predicted with the model; this, together with solution of the transient Reynolds equation, is left for future work.

Chapter 7: Characterisation of a FRPALS prototype

In previous chapters, the design of a test rig designed for turbomachinery shaft seal research has been described. The leakage performance and rotordynamic coefficients of a labyrinth seal has been measured in the aforementioned rig in order to prove its capability. Additionally, a Rayleigh-step annular seal has been characterised with the intention of building knowledge of seals featuring such a clearance profile. A solution of the steady-state Reynolds equation for gas lubrication which predicts the pressure distribution in the clearance of gas seals has been validated against measurements performed in the Rayleigh-step annular seal, finding good agreement between the modelled and experimental pressures. All these steps have been performed towards the final aim of testing a first prototype of the novel, compliant, film-riding seal referred to as FRPALS, which was described in the Chapter 1.

This chapter gives the geometric parameters of the FRPALS prototype tested and explains the forces that act on each of the sealing elements that comprise the seal. The experimental setup used to track the movement of the runners under the effect of changing pressure drops is explained and the results from such experiments are discussed. The solutions applied to the issues encountered in the blow down process of the FRPALS are then given. Finally, the leakage performance of the seal and the prediction of the pressure in the clearance fluid film are presented.

7.1 FRPALS testing prototype

The seal prototype tested was designed and manufactured by Cross Manufacturing. A description of the final assembly is given in the following paragraphs, and its dimensions are summarised in Table 7.1 and Figure 7.1.

Table 7.1: FRPALS dimensions

Seal Diameter	254 mm
Cold-Build Clearance	0.75 mm
Runner Axial Length	44.14 mm
Rayleigh Step Height	0.127 mm
Film Riding Length	3.81 mm
Rayleigh Step Length	15.24 mm
Leaf Length	31.75 mm
Leaf Angle	35°
Leaf Thickness	0.381 mm

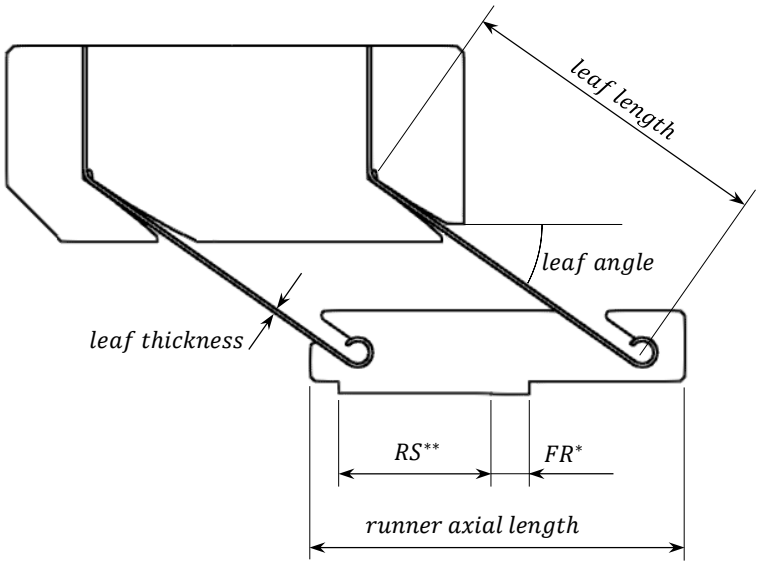

$* FR: film\ riding$
$** RS: Rayleigh\ step$

Figure 7.1. FRPALS parameters.

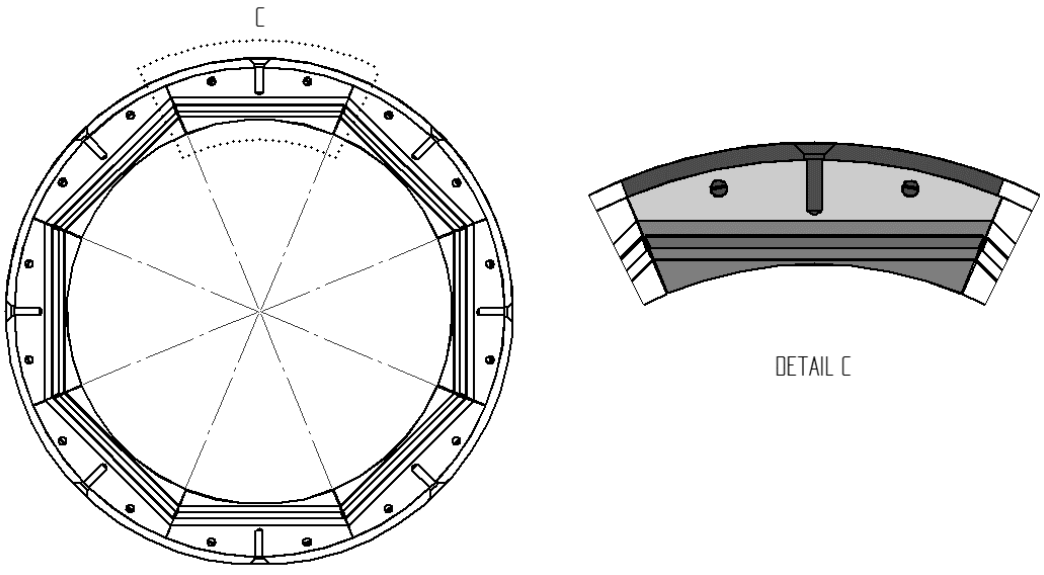

(a) **(b)**

Figure 7.2. (a) Front view of the FRPALS prototype and (b) detail of a seal segment.

The leaves are made from Inconel 718 nickel-chromium alloy and the runners from Nitronic 60 steel; all other components are manufactured from aluminium alloy. The seal is divided in to eight segments, as shown in Figure 7.2, in order to allow radial closure of the leaves. The backing ring assembly design allows for the change in cold build clearance of the seal by using different backing rings, with the inner diameter varying +/- 254 μm from the nominal value.

In the cold built of the seal, a gap between each of the eight segments shown in Figure 7.2 is needed in order to leave room for the movable parts to close towards the rotor. From the CAD model of the seal assembly, this gap is estimated to have an average width of 0.3 mm when the seal is open, which yields a secondary leakage area of 74.61 mm^2 when considering the eight segments of the seal. The calculated leakage area under the Rayleigh step of the seal is 101.4 mm^2 in the closed position. This translates into 57 % of the air flow passing through the primary leakage path of the seal and the remaining 43 % through the secondary air path.

The FRPALS design investigated in this research is referred to as the *reverse design*, as opposed to the original design introduced in Grondahl and Dudley [2010]. The reverse design was chosen because it is more compact. The differences between both designs are depicted in Figure 7.3. From the assembly point of view, the leaves of the original design form an acute angle with respect to the positive axial direction. In contrast, this angle is obtuse for the reverse design. Also, the role of each row of leaves is interchanged between the designs. In the reverse design, the upstream row of leaves forms the positioning set because the upstream air has to be allowed into the interleaf cavity to pressurise the top surface of the runner to enable the seal to close. Note that the set of leaves that bears the pressure difference is the sealing set of leaves for both designs.

Figure 7.4 shows the forces acting on the runner of the seal. The reaction forces of the leaves on the runners can be projected in the radial and axial (flow) direction. The magnitude of these forces changes from one set of leaves to another as only the sealing set of leaves withstands the pressure difference (DP) created across the seal. The leakage air also exerts a direct force onto the runners. In the radial direction, there are two pressure forces of opposed sign; one is due to the high-pressure acting on the top surface of the runner (F_{Rp}) and the other due to the pressure distribution in the film created between the rotor and the seal (F_{Rpi}). Likewise, in the direction of the flow, two forces appear due to the effect of the leakage flow, namely, the hydrostatic pressure acting on the front face of the runner (F_{zp}) and the hydrodynamic drag generated as the air passes through the seal clearance ($Drag$).

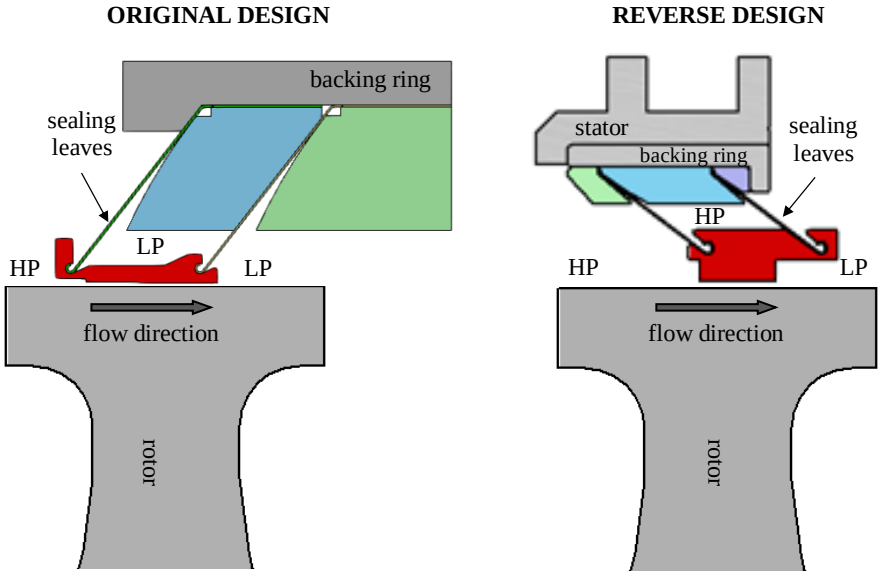

Figure 7.3. Cross section of the original and reverse designs of a FRPALS segment.

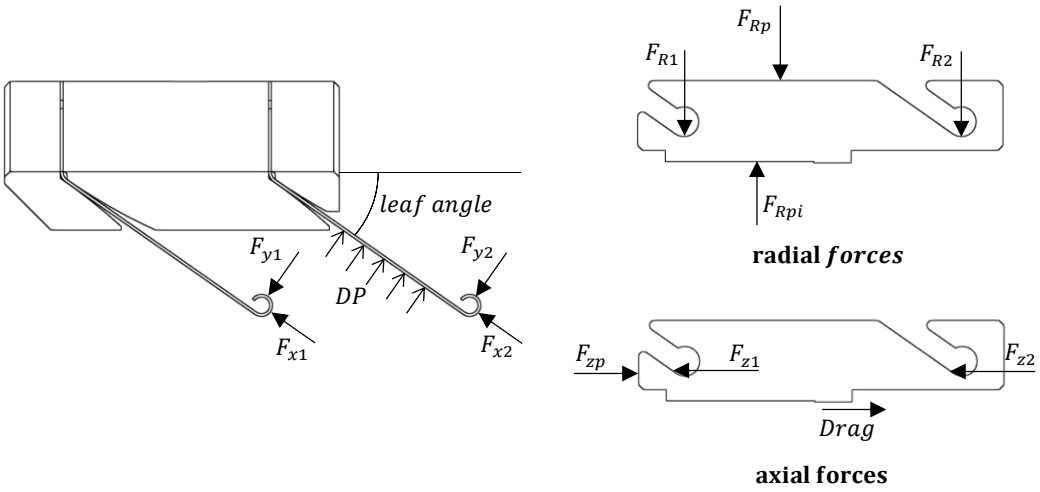

Figure 7.4. Force diagram for the leaves and runner of the reverse FRPALS design.

7.1.1 Prototype predevelopment

A first geometry of the FRPALS runners was tested with the intention of confirming that the seal closed when a pressure drop was applied to it. This test was performed at Cross Manufacturing premises in a chamber designed to pressurise the upstream region of the seal, while leaving the downstream side open to atmosphere. It was found that with this geometry the seal did not close. Visual inspection indicated that the gap between the seal and the rotor did not decrease. No measurements of the geometric clearance of the seal could be performed with this experimental set up. However, mass flow rate measurements showed that, for this configuration, the effective clearance of the seal increased as the applied pressure drop was

raised, indicating that the seal was opening. The plots depicted as *P1-original* in Figure 7.5 and Figure 7.6 shows this behaviour of the initial geometry of the seal (see Figure 7.7).

The forces acting on the runner were reviewed by Cross and mismatch was found between the forces calculated at the design stage and those in reality. The most straight forward way to modify the force equilibrium on the runners was to change the Rayleigh step axial position. The original position of the Rayleigh step within the runner was located too far downstream and, therefore, the high pressure upstream of the seal was acting on a surface of the clearance that was too large, causing the runner to lift up. It was decided to make the runners adjustable in order to test the four different positions of the Rayleigh step shown in Figure 7.7 and determine which one was the optimum.

Mass flow rate tests showed that when the Rayleigh step was positioned at *P1* and *P2* (see Figure 7.5 and Figure 7.6) the runners do not close. What is more, the effective clearance in Figure 7.6 increases with applied pressure drop, which indicates that the runners are actually moving away from the rotor. With the Rayleigh step at *P3* and *P4* the effective clearance is kept constant after the blow down process at 0.3 bar. However, the value of effective clearance for the two positions is different, which means that *P4* closed more than *P3*. Results of effective clearance for *P4* are closer to the target effective clearance (127 μm) of the design and, therefore, this position of the Rayleigh step is chosen to manufacture a second set of runners.

It is worth mentioning that these experiments were carried out with the gap between leaves of adjacent segments (see Figure 7.2) sealed by means of tape and, hence, with the secondary leakage path of the seal blocked. This will be discussed further in Section 7.4, where final mass flow measurements are presented.

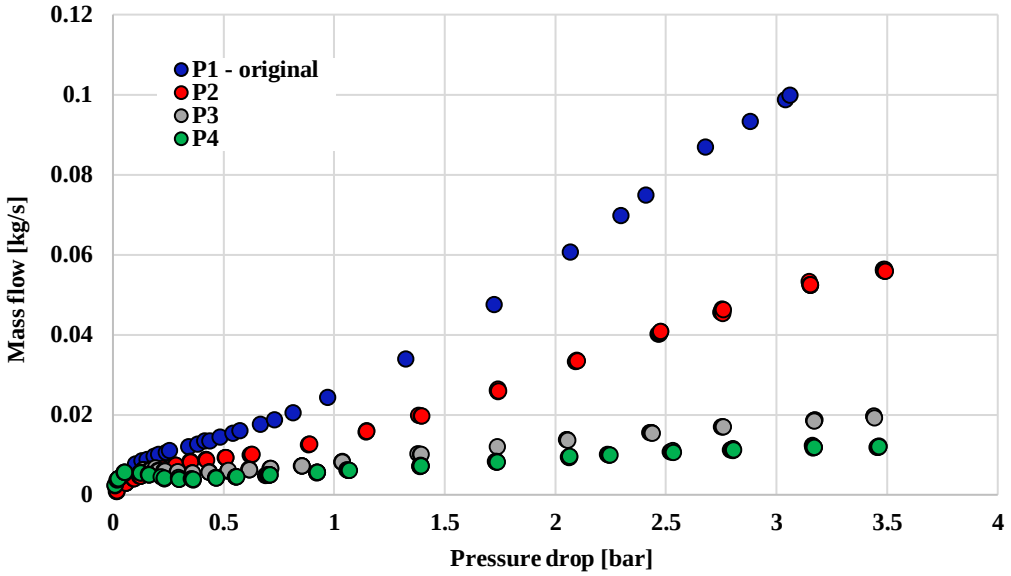

Figure 7.5. Mass flow leakage of the FRPALS measured at four different axial positions of the Rayleigh step.

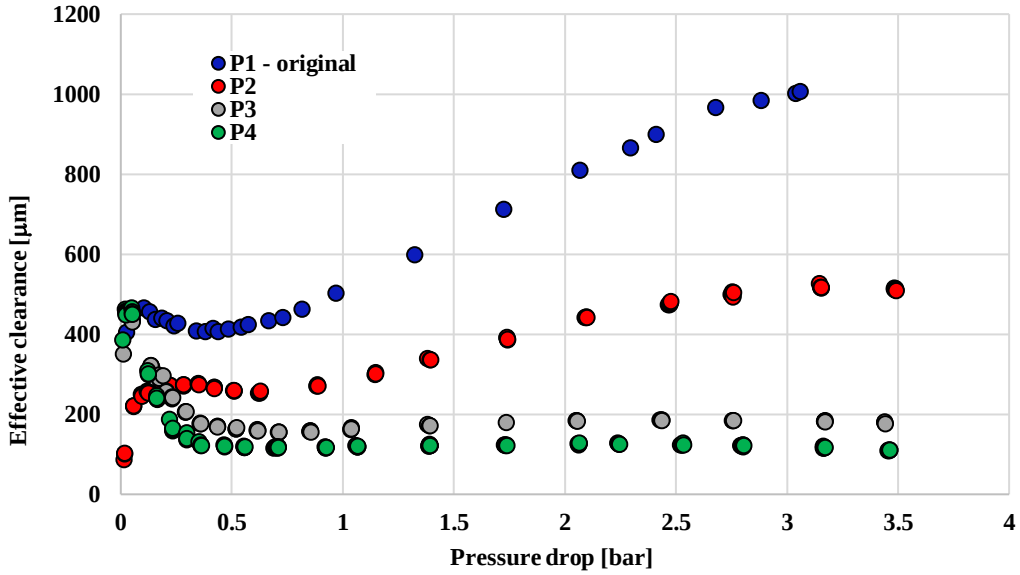

Figure 7.6. Effective clearance of the FRPALS calculated from mass flow data measured at four different axial positions of the Rayleigh step.

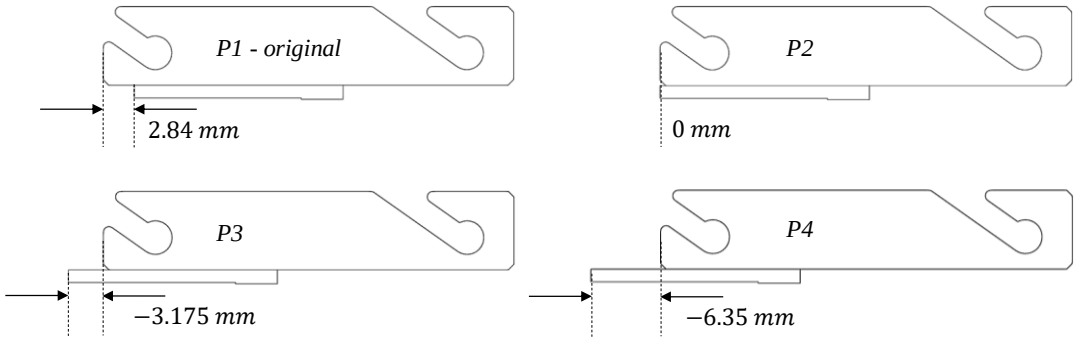

Figure 7.7. Different positions of the Rayleigh step tested.

7.2 FRPALS instrumentation

The axial and radial displacement of the seal pads were monitored by eddy-current displacement transducers. The position of these transducers relative to the rig is shown in Figure 7.8. The axial and radial movement of the two segments highlighted in Figure 7.9, out of the eight segments constituting the seal, could be monitored and they are referred to as *top* and *side segments.* This terminology will be used throughout the discussion of the results. Additionally, the top runner was installed with a Kulite^{TM} transducer in order to measure pressure in the region where the film thickness between the rotor and the seal is smallest.

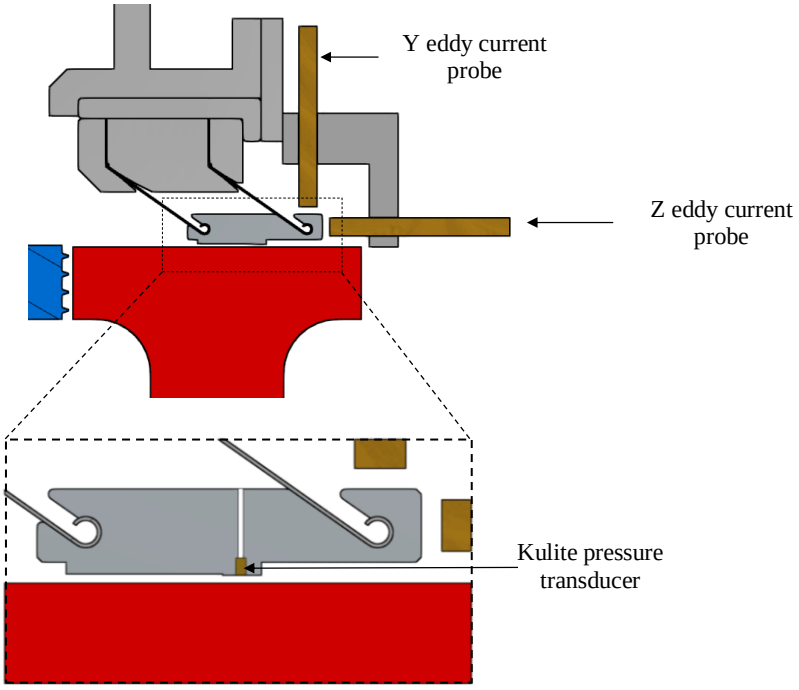

Figure 7.8. Close-up view of the FRPALS and the proximity probes used to characterise the seal.

The radial displacement was measured at the two circumferential extremes of a seal pad, shown in Figure 7.10. The two measurement probes were separated by 104 mm (x) and were targeted on the flat upper surface of the runner. The displacement of the runner, y, is determined with respect to an initial offset, y_0. The active clearance of the FRPALS, c, is therefore equal to the cold-build clearance, c_0, minus the displacement under pressure:

$$c = c_0 - y \tag{7.1}$$

The rock angle of the runner, α, is determined as follows:

$$\alpha = \operatorname{atan}\left(\frac{y_2 - y_1}{x}\right) \tag{7.2}$$

where y_1 and y_2 are the displacements of the runner measured by Probes 1 and 2, respectively.

The axial displacement of the runner is measured using a third displacement transducer, targeting the downstream edge of the seal (Figure 7.11). Here, the axial displacement, z, is measured relative to the cold-build state, z_0.

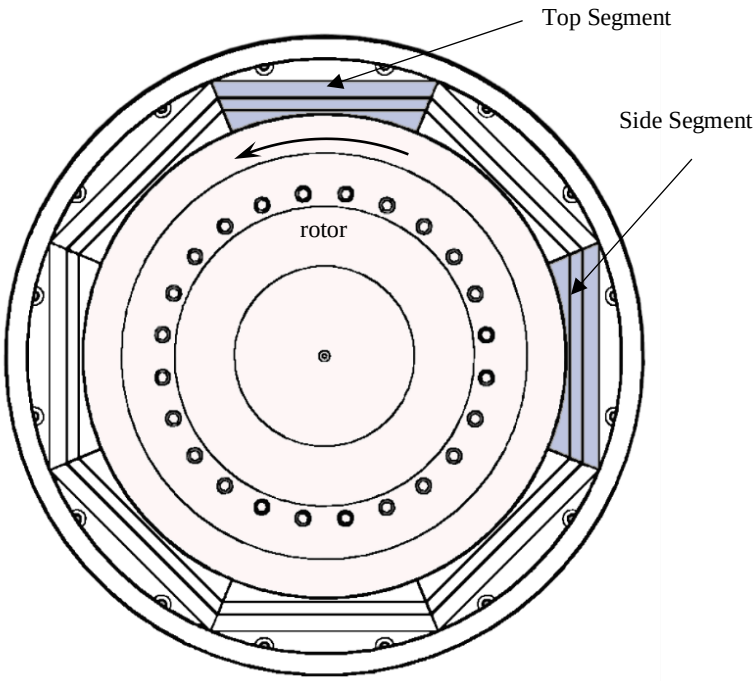

Figure 7.9. FRPALS assembly around the test rotor with the instrumented segments highlighted.

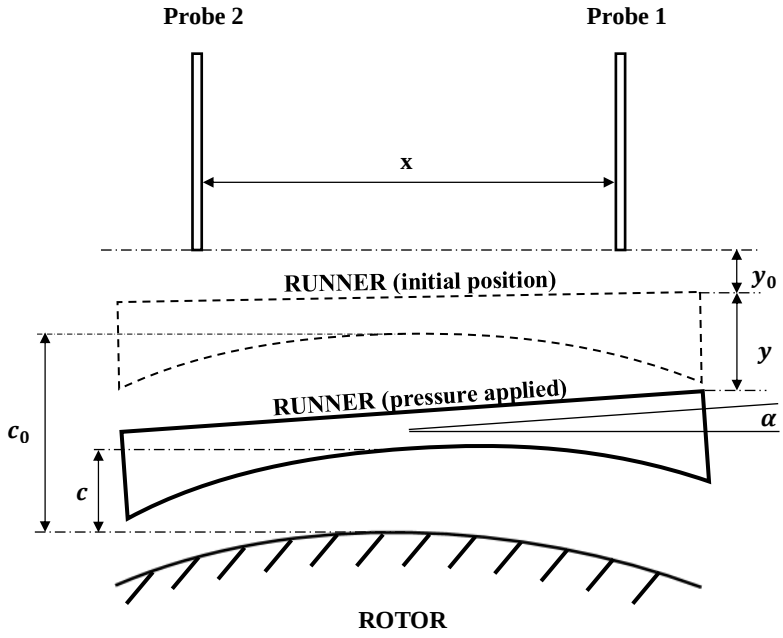

Figure 7.10. Instrumentation measuring the radial displacement of the runner.

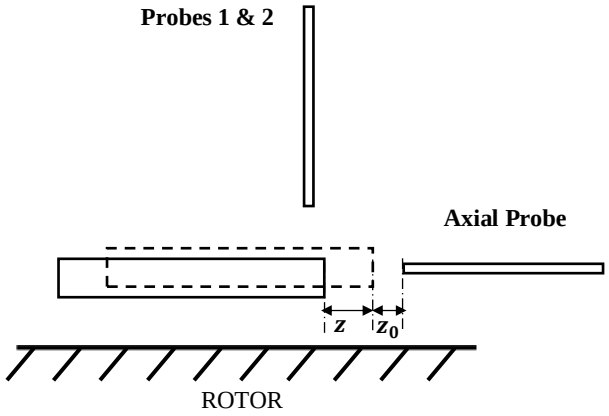

Figure 7.11. Instrumentation measuring the axial displacement of the runner.

7.3 Pressurisation of the FRPALS

This section presents experimental data from the FRPALS test facility. The blow-down process was investigated by measuring the displacement of the seal runners under pressure. The rotor was stationary in all tests reported here.

The pressurisation tests were conducted by two methods: a *stepped approach*, in which the pressure was raised in increments (stabilising after each augmentation), and a *fast transient*, in which the pressurisation to 3.5 bar occurred within two seconds. In order to capture the transient effects, the proximity probe signals were recorded at a sampling frequency of 8 kHz.

A typical pressurisation test is presented in Figure 7.12, shown here for a *fast transient* experiment. Here, positive values of radial movement indicate that the seal is closing towards the shaft. The data from Probe 1 (green) and Probe 2 (yellow) suggest an eccentric displacement in the radial direction; the data also exhibit a pronounced hysteresis when the FRPALS undergoes depressurisation. Figure 7.12 shows that the movement is larger during the depressurisation part of the curves; as the pressure drop is decreased, the pressure in the clearance between the runners and the rotor might decrease at a greater rate than in the upper surface of the runner, hence, the pressure forces push the runners further downwards. The data from the two probes can be averaged (shown in black) to give an indication of the general movement of the runner under pressure.

Figure 7.12 compares the radial displacement of both instrumented runners. It can be seen that the average movement of the side runner is only two thirds of the displacement of the top runner. This indicates that the different segments that constitute the seal behave differently. Additionally, the data from Probe 2 (yellow) of the top runner (Figure 7.12 (a)) is greater than

the design cold-built clearance of the seal (750 μm), which is not feasible unless the actual cold-built clearance is larger than the nominal one. These two findings may be due to a lack of repeatability during the manufacturing process of the leaves, as they are plastically deformed by hand.

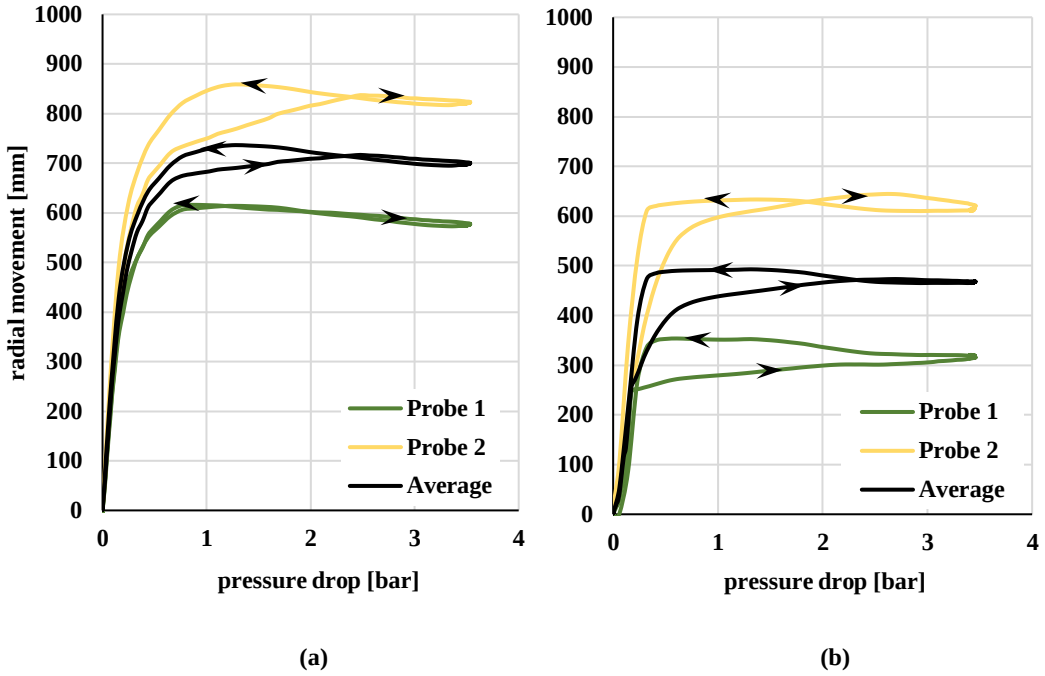

Figure 7.12. Radial displacement of the (a) top runner and (b) side runner of the FRPALS, measured at the two geometric extremes of the runner.

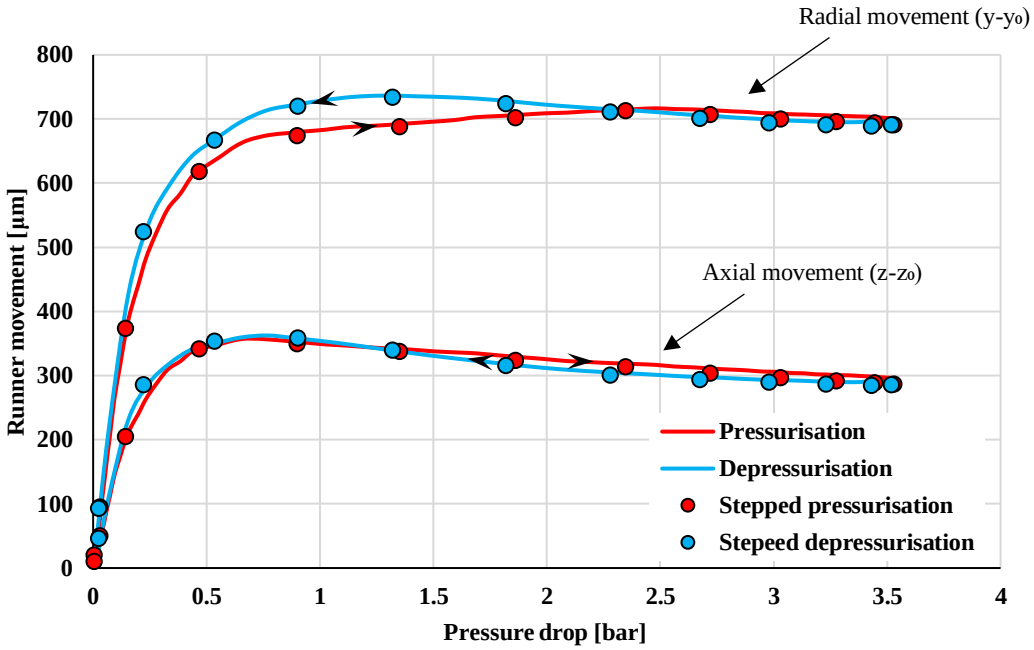

Figure 7.13. Axial and radial movement of the FRPALS top runner under pressurisation (lines are from a fast transient pressurisation; symbols denote a stepped approach).

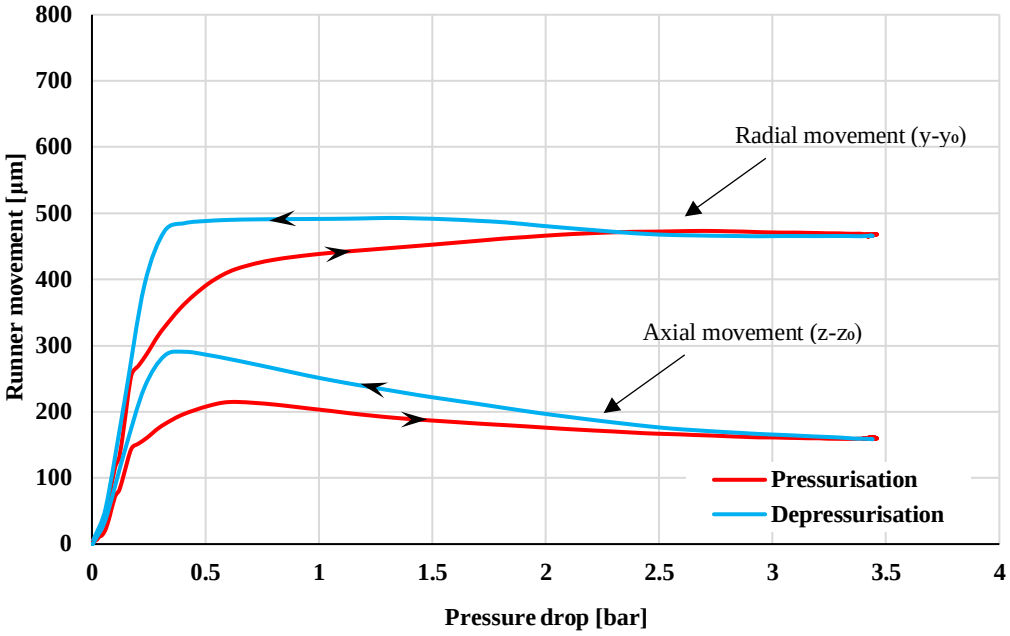

Figure 7.14. Axial and radial movement of the FRPALS side runner under pressurisation.

The averaged dataset from Figure 7.12 (a) is reproduced in Figure 7.13 in order to aid direct comparison with data acquired using the *stepped approach* to pressurisation. The axial displacement is also shown. It can be seen that the blow-down performance of the FRPALS is independent of the rates of pressurisation and depressurisation.

Consideration of the relative displacement in the radial and axial directions yields an approximate ratio of 2:1 (i.e. $(y - y_0) \approx 2 \times (z - z_0)$). The operating envelope for the top segment under a pressurisation to 3.5 bar spans 350 µm and 750 µm for the axial and radial displacements, respectively. The maximum displacement is attained for a pressure drop between 0.5 and 1 bar, after which the magnitude of the movement reduces until finding a stable position at 2.5 bar, approximately. However, it is not clear whether this asymptotic value in the displacement is an indication that the pressure forces acting on the runner have reached equilibrium or it simply means that the runners are in contact with the rotor.

Similar behaviour can be seen in Figure 7.14 for the side segment: the displacement of the runner stabilises for pressure drop values greater than 2.5 bar, and the ratio between the radial and axial displacements is approximately 2:1. However, the operating envelope of the side segment when pressurised up to 3.5 bar spans 280 µm and 500 µm for the axial and radial displacements, respectively, which is less than the top segment.

The rock angle is determined using Eq. 7.1. The effect of pressurisation on the rocking angle of the FRPALS runners is shown in Figure 7.15; again, hysteresis occurs when the seal is subsequently depressurised. The maximum rock angle experienced under a fast transient

pressurisation to 3.5 bar is 0.135 degrees for the top runner and 0.19 degrees for the side runner. This is larger than the 0.05 degree rocking angle measured by Kirk *et al.* [2016] for the two-dimensional segment of the FRPALS.

Figure 7.16 shows the average *geometric* clearance of the runner calculated using Eq. 7.1 and radial displacement data; discussion of the *effective* clearance is taken up in Section 7.4. Data in Figure 7.16 (a) suggest that the FRPALS top runner has, in effect, closed for pressure drops above 1 bar. This surprising result was in contrast to the design clearance which was intended to be 127 μm. Unlike the top runner, data in Figure 7.16 (b) indicates that the geometric clearance between the side runner and the rotor is positive. The measured data were corroborated by inserting a feeler gauge into the seal gap; the runner was indeed in contact with the rotor at multiple positions around the circumference of the disc.

Similar to the bind-up tests described by Proctor and Delgado [2008], the pressure at which the seal completely locks-up the rotor was assessed by increasing the pressure drop across the seal by small increments and spinning the rotor by hand until rotation is no longer possible. It was found that the rotor was stopped by the seal at pressure drops around 0.5 bar.

In the same manner that the difference in range of motion between the top and side runners was thought to be caused by poor repeatability during the manufacturing process of the leaves, the rocking angle being too large could be due to the same reason. Additionally, the possibility of the friction between adjacent runners having an effect in the mechanics of the seal has also been considered as a cause for the reported behaviour of the FRPALS.

The results from the first pressurisation trials of a FRPALS prototype have been analysed in this section. The new seal has shown to have the radial deflection functionality of the design closing down towards the rotor when a pressure drop is applied to it. These first tests have given valuable information about the behaviour of the seal and can be considered as a stepping stone in its development. The list below summarises the challenges found during this test campaign; the efforts made to overcome some of them, together with recommendations for future work, are discussed in the following subsection:

- The two instrumented segments have a different range of motion, indicating non-axisymmetric behaviour.
- The rocking angle of the runners is greater than that reported for the static test prototype by Kirk *et al.* [2016].
- Probe 2 for the top runner has measured radial displacements greater than the nominal cold-built clearance.
- The seal touches and binds-up the rotor, making tests under rotation not feasible yet.

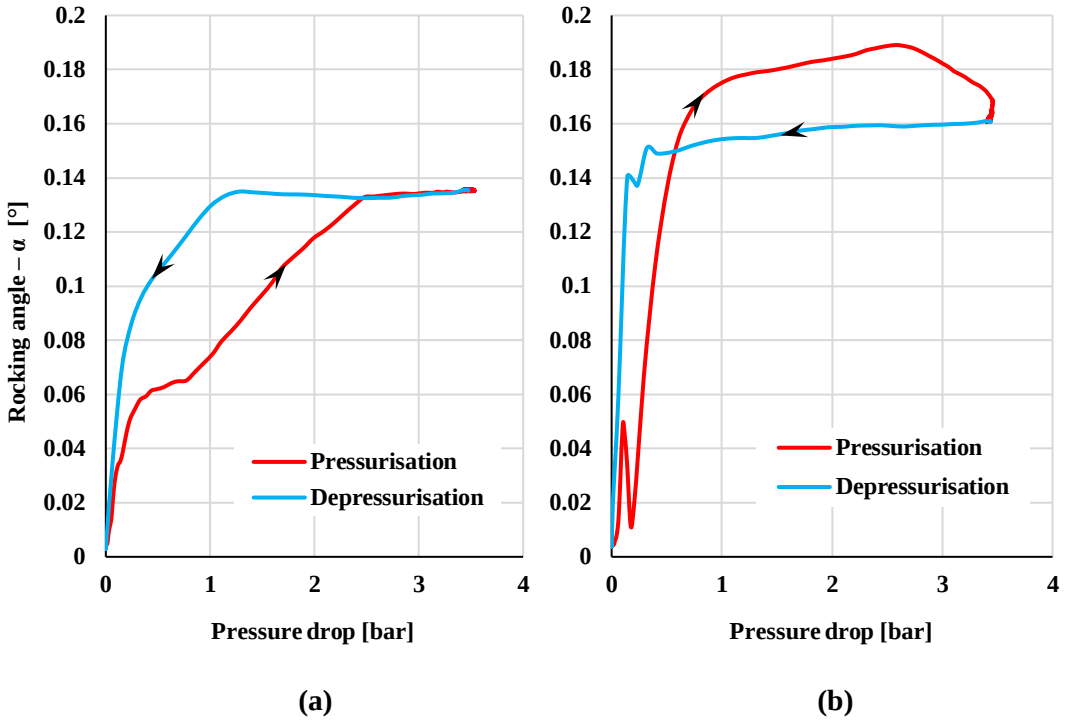

Figure 7.15. Rocking angle of the (a) top runner and (b) side runner of the FRPALS under pressurisation.

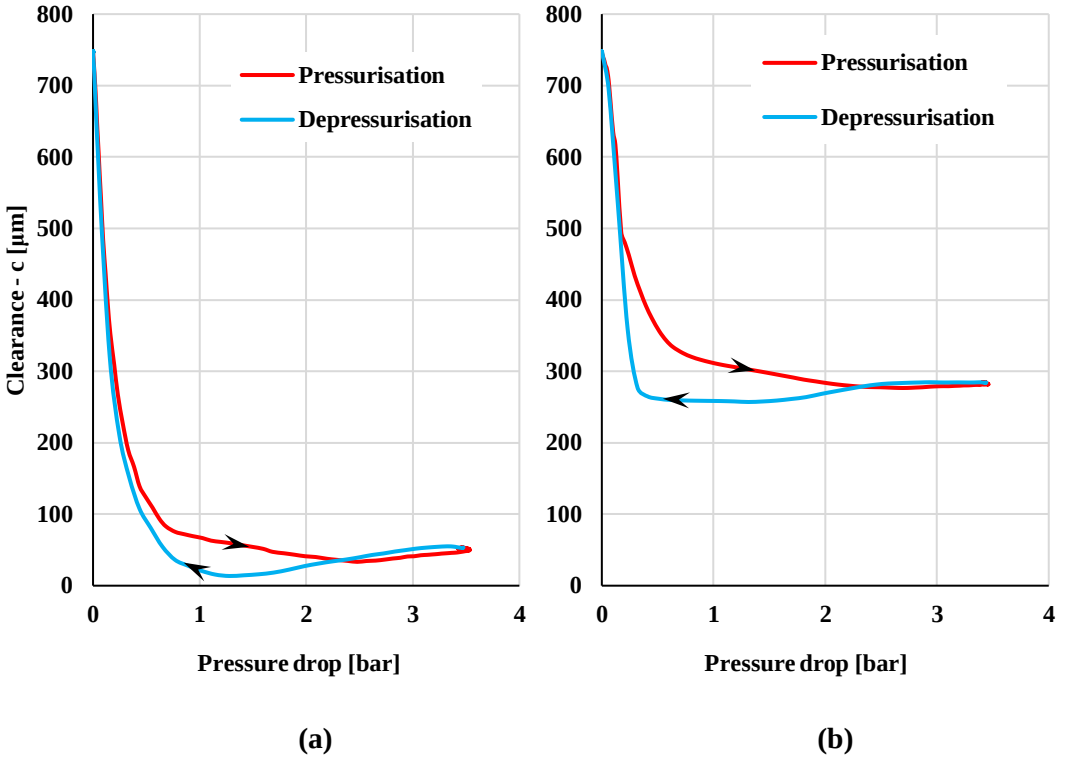

Figure 7.16. Average *geometric* clearance of the (a) top runner and (b) side runner of the FRPALS under pressurisation.

7.3.1 Further development

In an effort to solve the rocking issue found with the movement of the runners, a tapered pin 10 mm long with a maximum diameter of 2.1 mm was installed at both ends of the downstream ankle of the FRPALS segments. Figure 7.17 shows the geometry of the pins and the position within the segments in which they were installed. It was thought that the pins would cause the rolled-up end of the leaves to expand and, hence, to remove the existing slack between the leaf and the runner. In turn, this would help reduce the rocking movement of the runners. However, no improvement was found. Figure 7.18 compares the rocking angle measured at the top segment shown in Figure 7.15 (a) with no pins installed with the results of the tests performed on the same segment after fitting the pins. It can be seen that the rocking angle of the top runner with the pins installed is greater than with the original configuration.

The fact that the rotor was locked by the seal was interpreted as the seal closing too much and therefore the previous, adjustable set of runners was installed back in the FRPALS assembly to be tested at position *P3* using the Bath test rig. Measurements of the top runner radial displacement for the two positions of the Rayleigh step *P4* and *P3* are shown in Figure 7.19. The plots of Figure 7.19 indicate that the runners close with the Rayleigh step at any of the two positions shown. However, the displacement corresponding to *P3* is much smaller than that measured for *P4*; this was expected from the experimental effective clearance results shown in Figure 7.6. Additionally, the signal of the movement for *P3* is 'noisy', which may be an indication of the runner slightly fluttering due to the forces acting on it being on the edge of equilibrium.

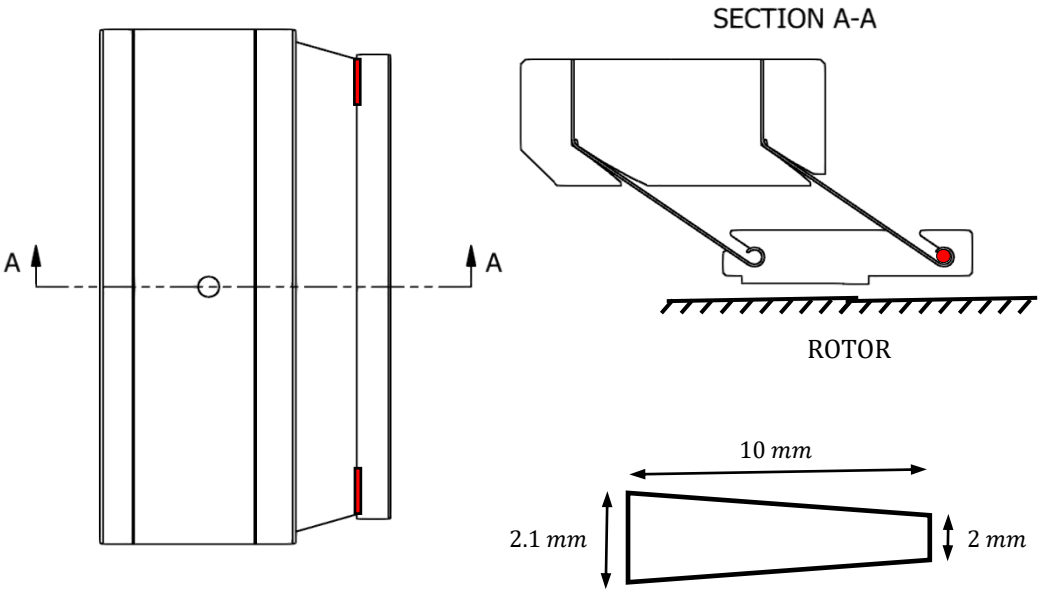

Figure 7.17. Geometry of the pins and their location within the segments of the FRPALS.

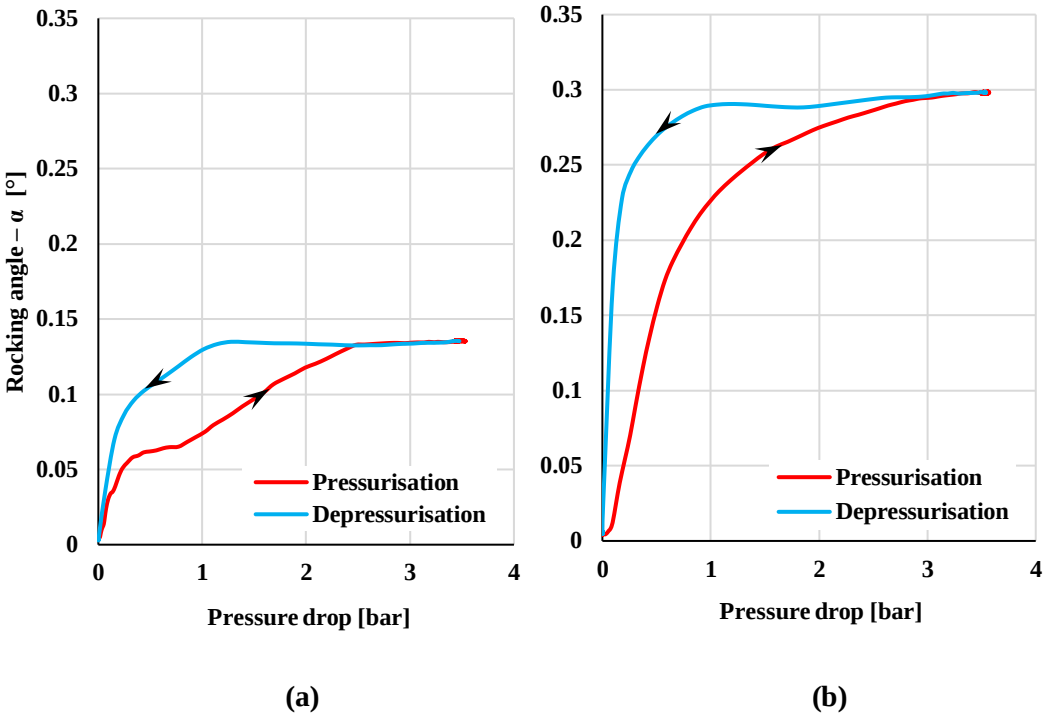

Figure 7.18. Comparison of the rocking angle of the FRPALS top runner when tested (a) without pins installed and (b) with one pin installed at each end of the downstream ankle of the runner.

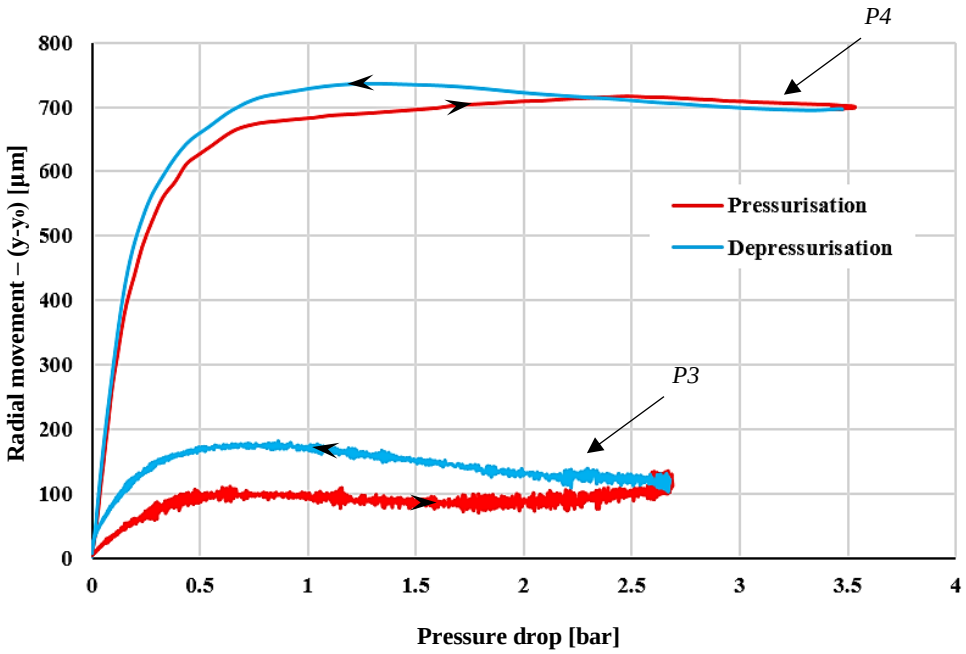

Figure 7.19. Comparison of the radial movement of the FRPALS top runner for the two axial positions of the Rayleigh step tested, P3 and P4.

Even though the displacement was smaller at *P3*, the seal eventually touched the rotor, indicating that some parts of the seal, presumably other segments different to the measured one, were closing further or had a large rocking angle. However, during bind-up tests, it was

found that the pressure drop at which the rotor was completely locked-up by the seal was approximately 2 bar, considerably larger than the 0.5 bar reported for the runner with the Rayleigh step at *P4*.

The review of the existing literature on compliant seals given in Chapter 2 revealed that during the development of other film-riding seals, researchers concluded that the equilibrium of the forces acting on the sealing elements is crucial for expected behaviour of the seal. Further investigation of the equilibrium of the forces acting on the runners of the FRPALS would be beneficial for the understanding of the seal behaviour and moving towards a more tuned prototype.

Using prediction tools for the forces on the runners together with experiments to explore the design space between *P3* and *P4*, could give an optimum axial position of the Rayleigh step for which the runners film-ride without touching the rotor. This optimised design should be accompanied by improvements in the manufacturing tolerances if the rocking movement of the runners is to be diminished.

Gaining deeper insight on the effect of the friction between runners in their movement towards the rotor during the pressurisation event and finding a mitigating solution for this issue is also recommended.

7.4 Leakage performance

Figure 7.20 shows the effect of pressure drop on the leakage mass flow-rate through the FRPALS; a slight hysteresis can be seen at low values of pressure drop. The hysteresis found in the leakage characteristics of the FRPALS is in line with the hysteresis captured by the eddy current transducers in the displacement of the seal runners and shown in Section 7.3.

Further evidence to indicate that the friction between runners has an effect on the blow down of the seal is found in the leakage data. The highlighted area of the mass flow rate measurements of Figure 7.20 is shown in Figure 7.21 with an expanded scale. In Figure 7.21, it can be seen that at a specific point in the pressurisation process of the FRPALS, when the control valve is open to increase the pressure drop across the seal, both the measured pressure drop and leakage decreased with respect to the previous point acquired during the test. This is interpreted as the increase in pressure drop, and effectively in upstream pressure, causing an increment of the downward forces acting on the runners large enough to overcome the friction, allowing the seal to close further, hence the decrease in measured leakage.

Figure 7.22 shows the effective clearance of the FRPALS over the tested range of pressure drops, evaluated using Eq. 4.16 from Chapter 4. The maximum effective clearance observed

in the tests was 400 μm. This value takes into account not only the leakage path between the rotor and the runners, but also the secondary leakage flow between adjacent leaves.

The mass flow rate data gathered at Cross with the inter-leaf gaps blocked with tape (plot P4 in Figure 7.6) has been plotted in Figure 7.22 as a preliminary assessment of the difference between the overall leakage of the seal and the one purely due to the rotor-to-seal clearance. Direct comparison of the red and green plots in Figure 7.22 yields a maximum difference of 280 μm, i.e. the mass flow rate through the secondary air path contributes a 60% of the overall seal leakage. This last figure does not match with the calculated percentage of leakage share between the primary and secondary leakage paths from flow area calculations shown in Section 7.1. This mismatch is attributed to the fact that the actual leakage area between segments may be different from the one in the CAD model. Additionally, the fact that the runners touch the rotor is an indication that the total flow area under the Rayleigh step has decreased with respect the desing value.

Calculation of a discharge coefficient for the FRPALS lacks sense as there is not a well-defined, reference clearance to be used. However, Figure 7.22 reveals that, for the same conditions and the same rotor diameter, the FRPALS overall effective clearance is over three times greater than the found for the labyrinth seal of Chapter 5. This is, again, due to the secondary leakage path. Therefore, a means to control the gap between leaves is needed in order to reduce the leakage of the seal.

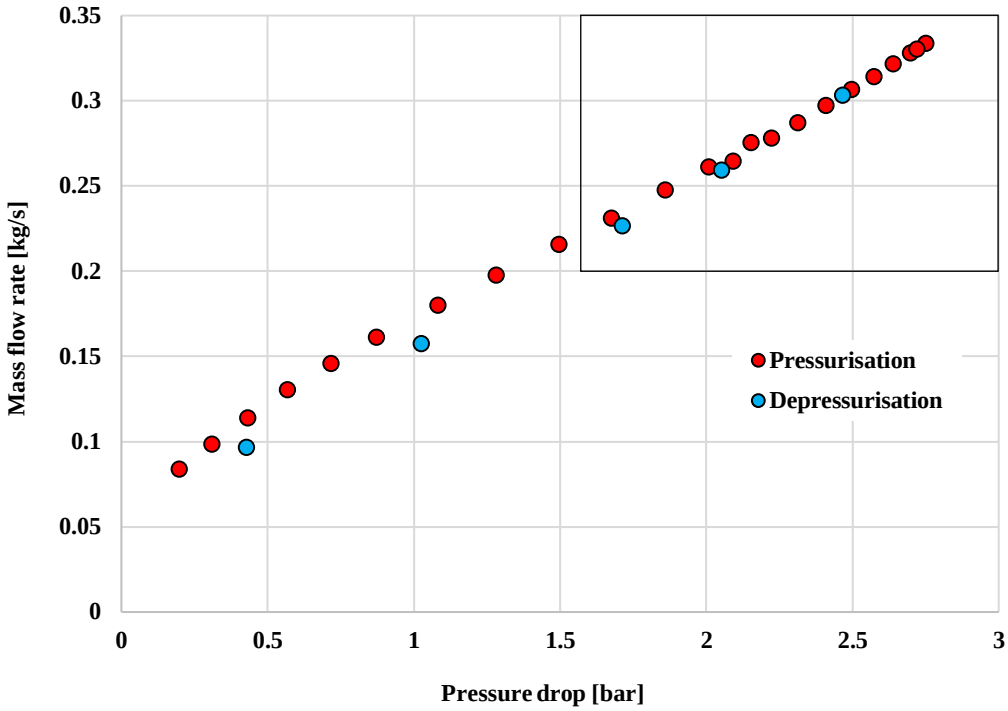

Figure 7.20. Leakage characteristics of the FRPALS with respect to pressure drop across the seal.

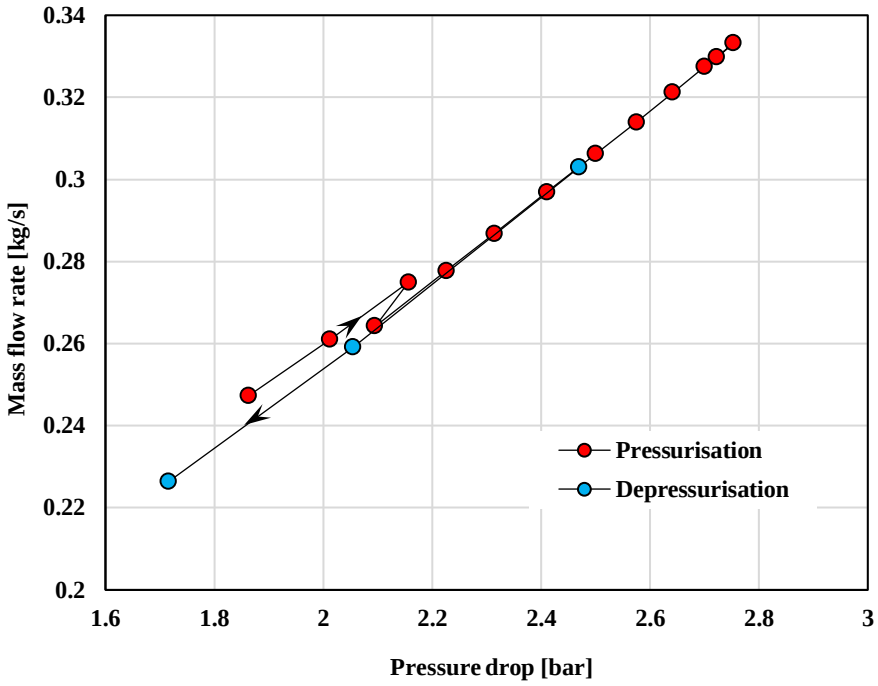

Figure 7.21. Detail of the leakage characteristics of the FRPALS.

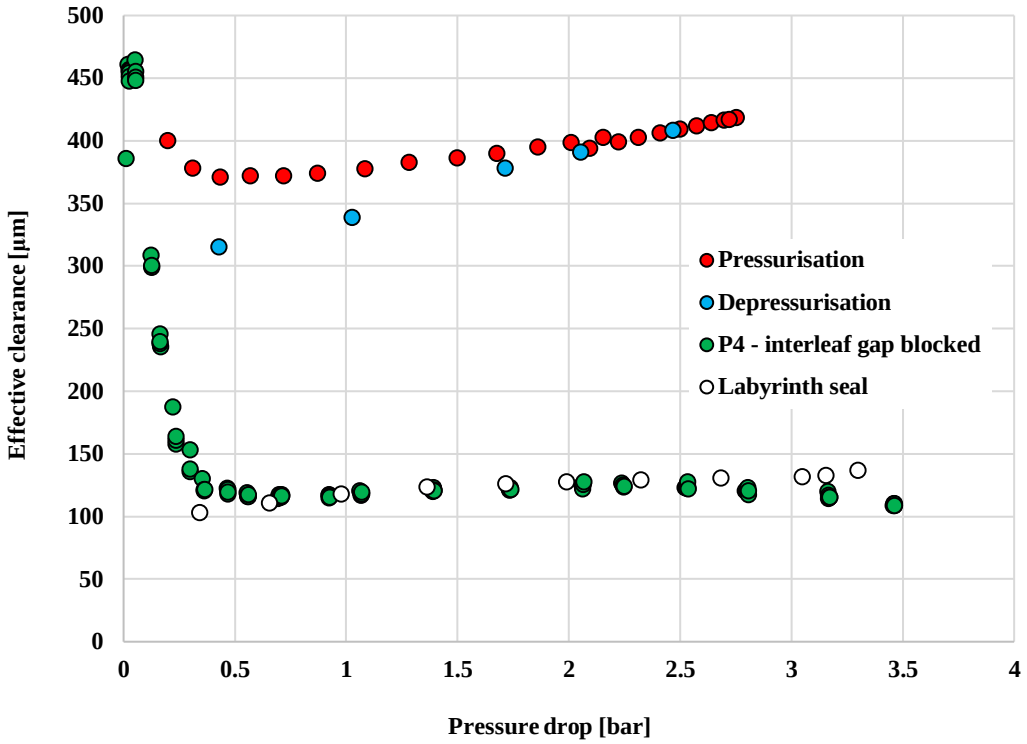

Figure 7.22. Effective clearance of the FRPALS with respect to pressure drop across the seal. Comparison with the effective clearance of the Labyrinth seal results from Chapter 5.

7.5 Thin film pressure modelling

Further validation of the pressure predictions was undertaken in the experiments described in Section 7.2. The Kulite pressure transducer (Figure 7.8) was installed in the Ryleigh-step region (Figure 7.23) of the top segment of the FRPALS prototype under investigation. The readings from this sensor were compared with the values predicted by the solution of the Reynolds equation described in Chapter 6. Figure 7.23 shows good agreement between the measured and computed results for five different upstream pressures. However, from the measurements taken for the Rayleigh-step annular seal of Chapter 6, the flow undergoes separation at the backward-facing step immediately downstream of the film riding region; this flow feature is not predicted by the model.

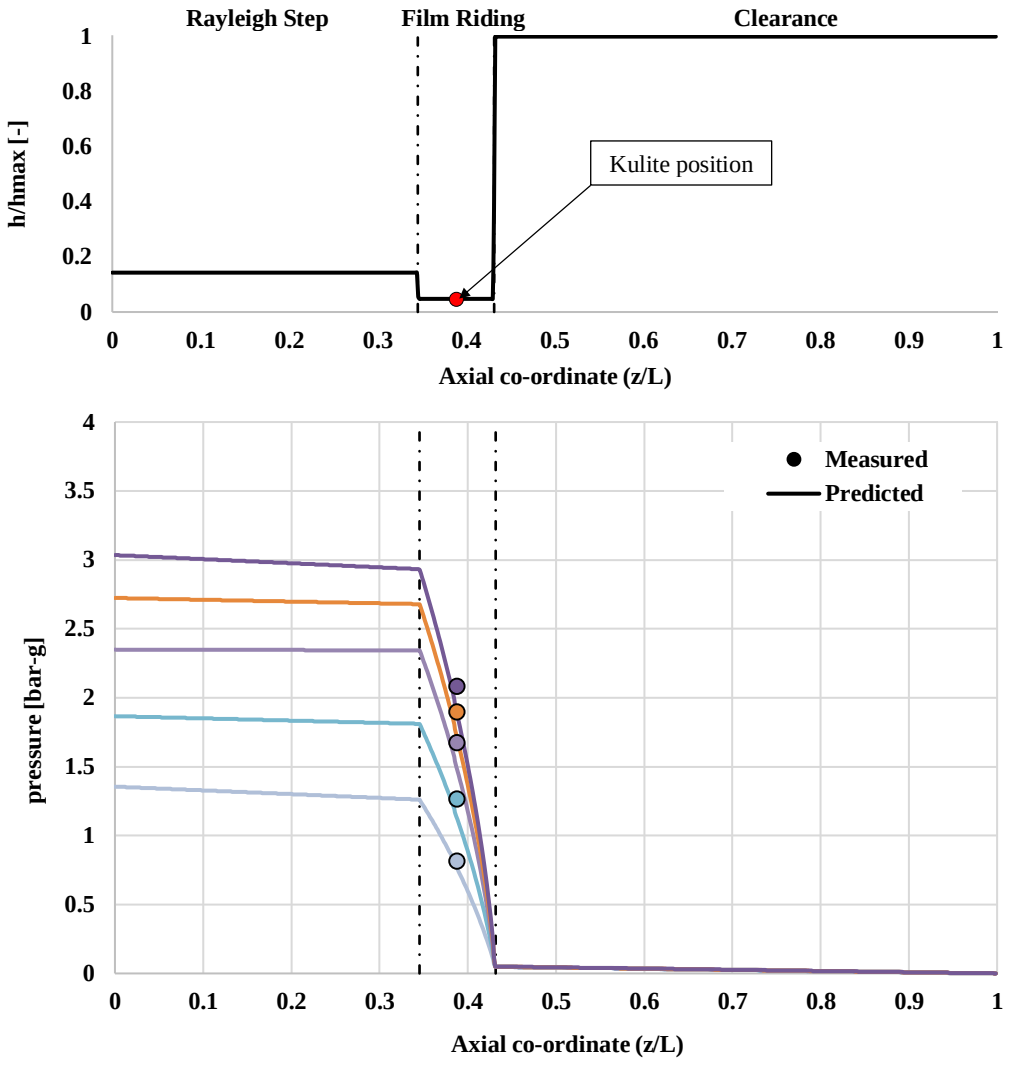

Figure 7.23. Dimensionless geometry and pressure distribution of the clearance of the prototype FRPALS under investigation for stationary conditions.

7.6 Summary

This chapter presents the experimental results of the first full FRPALS prototype ever tested. Before showing the measurement data, the geometry of the prototype is shown together with the forces acting on the runners of the seal.

Preliminary tests performed in a pressurised chamber indicated that with the initial geometry the leaves did not deflect and, hence, the seal did not close. The axial position of the Rayleigh step feature on the lower surface of the runners was moved further upstream of its original position until the seal closed.

The FRPALS with the modified runners' geometry from the preliminary tests was investigated using the test rig presented in Chapter 3. Measurements of the radial and axial displacement of two runners were taken with eddy-current proximity probes during the pressurisation and depressurisation of the seal. The main conclusions from the gathered data are as follows:

- The seal blow down process experienced hysteresis, i.e. the path followed by the runners is different during the pressurisation and depressurisation events.
- The radial movement of the segments was reported to be twice as large as the axial displacement.
- The range of motion of one of the measured pads was approximately 1.5 times larger than the other, indicating that the seal does close heterogeneously.
- From the point of view of the clearance, one of the segments was found to have zero clearance, i.e. it touched the rotor, whereas the other had a positive clearance for the full range of pressure drops tested.
- The rocking angle of the runners was reported to be larger compared with results from tests in a single-segment, two-dimensional prototype.
- The seal locked-up the rotor for pressure drops greater than 0.5 bar.

Given these results, changes were applied to the FRPALS prototype in order to make the seal close more evenly and, hence, to prevent it from touching the rotor. The ankle of the downstream leaf was pinned to remove the slack between the leaf and the runner, thus, reducing the rocking angle. Measurements of the runners' displacement with the pins installed showed that no reduction of the runners rocking angle was obtained.

A different axial position of the Rayleigh step was tested for comparison with the previous results. It was found that for a Rayleigh step positioned further downstream, the FRPALS

closed towards the rotor, but less than in the previous case. The rotor could be rotated for larger pressure drops, but it eventually touched the rotor at a pressure drop of 2 bar.

Mass flow rate measurements also detected the hysteresis of the blow-down process. A sudden change in the mass flow rate with increasing pressure drop suggested that friction between adjacent runners might be one of the causes of this hysteresis. Comparison of the FRPALS mass flow rate when measured with and without the interleaf gap area blocked estimated that the secondary air leakage passing through the space between neighbouring leaves represents approximately 60% of the total seal leakage mass flow. The FRPALS leakage performance was shown to be three times lower than the labyrinth seal investigated in this research.

The pressure predictions calculated with the procedure described in Chapter 6 was found to be in good agreement with the pressure measured at the film-riding section of the FRPALS top runner by means of a Kulite pressure transducer.

Chapter 8: Conclusions

8.1 Design of a new test facility for shaft seals research

A new high-speed rotating test facility capable of accommodating different turbomachinery shaft seals was designed, built and commissioned. The rig was specifically designed for the testing and development of novel non-contacting adaptive seals. It featured a 254 mm diameter rotor that was able to rotate up to a maximum speed of 15,000 rpm (200 m/s rotor tangential velocity) by means of a 15 kW electric motor. A maximum pressure drop of 3.5 bar can be applied across the testing seal.

Two pressure transducers and a thermal mass flow meter were used to measure the pressure drop created across seal under investigation and its leakage performance, respectively. Additional instrumentation such as thermocouples, a motor speed encoder and an optical speed measurement device were also included.

A vibration test was applied to the test seal in order to measure its rotordynamic coefficients. The casing, which holds the seal around the rotor and hangs from three pairs of pre-tensioned cables, was excited by means of an electromagnetic shaker capable of moving its payload at a maximum force of 3,000 N and a maximum frequency of 4,000 Hz. The force applied to the stator assembly by the shaker was measured by a load cell and its movement was tracked by eddy-current proximity probes and accelerometers installed in both the direction of excitation and the orthogonal direction, within the plane of rotation.

8.2 Labyrinth seal

Measurements of rotordynamic coefficients for rotational speeds of up to 14,600 rpm and pressure differences of up to 3.3 bar were performed in a short (L/D = 1/5) labyrinth seal with four cavities and a nominal clearance of 0.375 mm. These experiments were intended to demonstrate the capability of the new test facility and to fill a gap identified in the literature for rotordynamic coefficients of labyrinth seals with less than five cavities.

The rotordynamic measurements showed that the three coefficients increased with increasing pressure drop, although this dependency was weaker for the cross-coupled stiffness. The direct stiffness was positive and slightly decreased with increasing rotational speed. Both the direct damping and the cross-coupled stiffness decreased as the rotational speed was augmented. The positive direct damping combined with the negative cross-coupled stiffness yielded negative values of tangential reaction forces of the seal, i.e. the labyrinth seal under

study was demonstrated to have a stable behaviour. An inverse dependency of the coefficients with ambient temperature has been found.

The contribution of the cross-coupled damping to the radial seal reaction force was calculated to be just 6% of the direct stiffness. Also, the experimental uncertainty was demonstrated to be greater than 10% of the value of the coefficient, therefore no further discussion of the cross-coupled damping was given. Although direct comparison with data from the literature was not possible, the relative order of magnitude between the rotordynamic coefficients was found to be consistent with the published data for seals with different geometries and operating conditions.

The variation of leakage mass flow rate with pressure difference for the labyrinth seal was shown to be independent of rotational speed for values of up to 12,000 rpm. The trend of the mass flow rate with pressure was found to be linear, matching the predictions of the ideal mass flow rate equation. In agreement with Wittig *et al.* [1987], a discharge coefficient of 0.4 was calculated for the labyrinth seal.

8.3 Rayleigh-step annular seal

A Rayleigh-step annular seal was also characterised in terms of its stability behaviour and leakage performance. Measurements of rotordynamic coefficients showed that the direct stiffness was positive and larger than that of the short labyrinth seal. Increments in pressure drop translated into increasing direct stiffness, whereas no significant changes were seen with variations of rotational speed. Unlike the case of the labyrinth seal, the cross-coupled stiffness of the Rayleigh-step annular seal was positive, thus having a destabilising effect on the behaviour of the seal. The direct damping was found to have values similar to that of the labyrinth seal and decreased as rotational speed increased.

The effective damping of both the labyrinth and the Rayleigh-step seals was compared for a pressure drop of 2.9 bar. In general, the Rayleigh-step seal was less stable than the labyrinth seal. This difference was larger for lower values of the rotational speed and it decreased, until becoming negligible, as rotational speed increased.

Mass flow rate measurements showed that the leakage of the seal decreased with increasing rotational speed. It was demonstrated that this variation was due to the clearance closing as the rotor grew under rotation. The Rayleigh-step seal was found to be less efficient in restricting the flow than the labyrinth seal; a discharge coefficient slightly lower than 0.8 was calculated for the Rayleigh-step annular seal as opposed to 0.4 discharge coefficient of the labyrinth seal.

In order to calculate the pressure distribution in the clearance of the seal, the steady-state Reynolds equation for gas lubrication has been solved. The predicted pressure has been compared with pressure measurements in two different seal clearances profiles. These two test cases have shown that accurate predictions can be obtained with the presented solution of the Reynolds equation. However, the model fails to predict the flow features caused by sudden changes in the geometry such as forward and backward-facing steps.

Measurements of the pressure distribution along the clearance of the Rayleigh-step annular seal with rotation have shown that the rotational speed has no effect in the results for values of up to 7,000 rpm. In contrast, changes in the eccentricity between the rotor and the stator demonstrated that the pressure increased as the channel height decreased.

8.4 FRPALS

A prototype of the FRPALS has been investigated. Tests with an initial geometry of the seal runners showed that the seal did not close, therefore changes in the clearance geometry were studied until a closing solution was found. This process highlighted the role that the forces acting on the seal components have in a compliant, film-riding seal. The changes in geometry consisted in varying the axial position of the Rayleigh step within the clearance of the seal.

Once a closing seal was obtained, the blow down-process of the FRPALS was demonstrated through measurements of displacement, pressure and leakage in the absence of rotation for pressure drops of up to 3.5 bar. The principal conclusions are as follows:

- The FRPALS runners were shown to displace radially and axially under an applied pressure.
- The maximum displacement was reached in both directions at pressure drops close to 1 bar, after which the displacement decreased. For pressure drops greater than 2.5 bar the displacement stabilised, indicating that the seal was either touching the rotor or operating in a stable condition.
- A hysteresis was observed in the blow-down process when the pressure was applied and relieved.
- The ratio between the radial and axial movement was found to be approximately 2.
- The range of motion of the two monitored segments differed by a factor of 1.5, which translates into a non-uniform blow-down process.

- The FRPALS runner was shown to exhibit an eccentric displacement in the radial direction under loading. The maximum rock angle experienced under a fast, transient pressurisation is 0.14 degrees.
- Bind-up tests showed that the seal stopped the rotor from moving at pressure drops greater than 0.5 bar.

In the light of these findings, pins were installed in the downstream ankle of the runners in order to tighten the leaf-runner joint and prevent the runners from rocking. However, displacement measurements with this configuration demonstrated that no improvement was achieved. Additionally, the displacement of the runners with the Rayleigh step in a more downstream position was measured. It was found that the seal closed, however, the range of the movement was smaller than in the previous case. During bind-up tests, the rotor was free to spin for pressure drops of up to 2 bar.

The leakage mass flow rate of the FRPALS was measured to be three times larger than the labyrinth seal studied in Chapter 5. This is because an additional leakage flow path exists in the design of the FPRALS in the gap between adjacent segments. Comparison of the mass flow rate when measured with and without this secondary air path blocked indicated that the leakage through the rotor-to-seal clearance constitutes only 30 % of the overall leakage of the seal.

The pressure distribution along the clearance of the FRPALS was predicted with a solution for the Reynolds equation for gas lubrication from the open literature. Good agreement was reported between the measured pressure at the Rayleigh step of the runner and the results obtained from the model.

8.5 Future work

The next stage of the development of the FRPALS is to investigate the causes that make the runners touch the rotor and change the design and/or the manufacturing processes in order to have film riding segments that close evenly towards the rotor. This can be achieved by testing an isolated segment with the test arrangement shown in Figure 8.1; seven segments are removed from the FRPALS assembly and a labyrinth seal cut to fit the remaining segment is bolted on the outer ring. The labyrinth seal is cut in such a way that the testing runner does not touch the edges of the labyrinth section and, therefore, the friction between adjacent runners is removed.

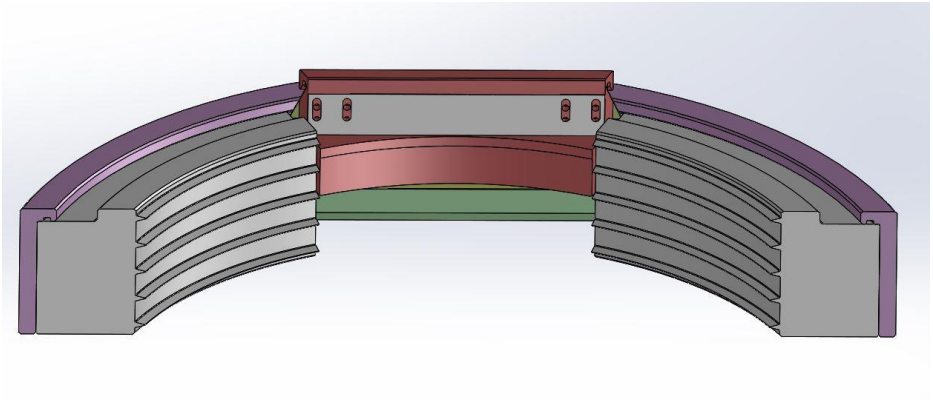

Figure 8.1: Schematic of the labyrinth seal under investigation

With this debugging configuration, the runners with an adjustable Rayleigh step position can be tested. This will give insight into the role that the profile of the clearance geometry has on the behaviour of the seal until an equilibrium of the forces acting on the runners is found. Analytical calculations of these forces can aid the development process; this can be one by using the solution of the steady-state Reynolds equation introduced in this thesis, or more sophisticated methods such as CFD models.

Once a FRPALS prototype operating under rotating conditions is achieved, the following step in the development of the seal is to assess its dynamic behaviour by measuring the rotordynamic coefficients using the test rig described in this thesis and taking into account the considerations given in Section 8.5.1.

The solution of the two-dimensional, transient Reynolds equation for gas lubrication will provide the forces and moments acting on the runners of the FRPALS which, in turn, will yield a prediction of the rotordynamic coefficients. Validating the effect of rotation and eccentricity with the two-dimensional, steady-state solution is the first step towards obtaining the solution of the full equation. The final aim is to be able to calculate the rotordynamic coefficients of the seal and validate the results with the experimental data.

References

Arora, G. K., 1998, "Noncontacting finger seal with hydrodynamic foot portion," US Patent 5755445.

Arora, G.K., Proctor, M., Steinetz, B., and Delgado, I., 1999, "Pressure balanced, low hysteresis, finger seal test results," Proc. 35th AIAA/ASMlE/SAE/ASEE Joint Propulsion Conference and Exhibit, Paper No.99-2686.

Arthur, S. P., and Childs, D. W., 2015, "Measured Rotordynamic and Leakage Characteristics of a Tooth-on-Rotor Labyrinth Seal With Comparisons to a Tooth-on-Stator Labyrinth Seal and Predictions," Proc. ASME Turbo Expo 2015. Paper No. GT2015-43242.

Aslan-zada, F. E., Mammadov, V. A., and Dohnal, F., 2013, "Brush seals and labyrinth seals in gas turbine applications," Proceedings of the institution of mechanical engineers, Part A: Journal of Power and Energy, 227(2), pp. 216-230.

Bayley, F. J. and Owen, J. M., 1969, "Flow Between a Rotating and a Stationary Disc."Aeronautical Quarterly 20: pp. 333 -354.

Beermann, L. S., Höfler, C., and Bauer, H.-J., 2015, "Design of a High-Speed Rotating Test Rig for Adaptive Seal Systems," Proc. ASME Turbo Expo 2015, Paper No. GT2015-42329.

Beermann, L., Wilhelm, J., Schwitzke, C., and Bauer, H.-J., 2018, "Experimental investigation of the sealing performance of a new adaptive seal system," Proceedings of GPPS Forum 18, Paper No. GPPS-2018-0005,.

Bowsher, A., Crudgington, P., Grondahl, C. M., Dudley, J. C., Kirk, T., and Pawlak, A., 2015, "Pressure Activated Leaf Seal Technology Readiness Testing," J. Eng. Gas. Turbines Power-Trans. ASME, 137(6), p. 10.

Braun, M. J., Choy, F., and Pierson, H., 2003a "Structural and dynamic considerations towards the design of padded finger seals," Proc. 39th AIAA/ASME/SAE/ASEE Joint Propulsion Conference and Exhibit, Paper No. 2003–4698.

Braun, M., Kudriavtsev, V., Steinetz, B., and Proctor, M., 2003b, "Two-and three-dimensional numerical experiments representing two limiting cases of an in-line pair of finger seal components," International Journal of Rotating Machinery, 9(3), pp. 171-179.

Braun, M., Pierson, H., and Deng, D., 2005, "Thermofluids considerations and the dynamic behavior of a finger seal assembly," Tribology transactions, 48(4), pp. 531-547.

Burcham, R., and Keller Jr, R., 1978, "Liquid rocket engine turbopump rotating-shaft seals."

Cangioli, F., Vannini, G., Pennacchi, P., Ciuchicchi, L., Nettis, L., and Chatterton, S., 2019, "Rotordynamic characterization of a staggered labyrinth seal: experimental test data and comparison with predictions," Journal of Engineering for Gas Turbines and Power, 141(1), p. 011009.

Castelli, V., and Pirvics, J., 1967, "Equilibrium Characteristics of Axial-Groove Gas-Lubricated Bearings," Journal of Lubrication Technology, 89(2), pp. 177-193.

Childs, D., and Scharrer, J. K., 1986, "An Iwatsubo-based solution for labyrinth seals: comparison to experimental results," Journal of Engineering for Gas Turbines and Power, 108(2), pp. 325-331.

Childs, D., Elrod, D. A., and Hale, K., 1988, "Rotordynamic coefficient and leakage test results for interlock and tooth-on-stator labyrinth seals," Proc. ASME 1988 International Gas Turbine and Aeroengine Congress and Exposition, ASME Paper No. 88-GT-87

Childs, D., 1993, Turbomachinery Rotordynamics: Phenomena, Modeling, and Analysis, John Wiley & Sons.

Childs, D., and Hale, K., 1994, "A Test Apparatus and Facility to Identify the Rotordynamic Coefficients of High-Speed Hydrostatic Bearings," Journal of Tribology, 116(2), pp. 337-343.

Childs, D., and Vance, J. M., 1997 "Annular Gas Seals and Rotordynamics of Compressors and Turbines," Proc. Proceedings of the 26th Turbomachinery Symposium, Texas A&M University Turbomachinery Laboratories.

Chupp, R. E., Hendricks, R. C., Lattime, S. B., and Steinetz, B. M., 2006, "Sealing in turbomachinery," J. Propul. Power, 22(2), pp. 313-349.

Chupp, R. E., Hendricks, R. C., and Steinetz, B. M., 2010, "Gas Turbine Engines: Seals," Encyclopedia of Aerospace Engineering.

Cloutier, D., Avitabile, P., Bono, R., and Peres, M., 2009, "Shaker/stinger effects on measured frequency response functions," Proc. Proceedings of the 27th International Modal Analysis Conference.

Conner, K., and Childs, D. W., 1993, "Rotordynamic coefficient test results for a four-stage brush seal," J. Propul. Power, 9(3), pp. 462-465.

Crudgington, P., 1998, "Brush seal performance evaluation," Proc. 34th AIAA/ASME/SAE/ASEE Joint Propulsion Conference and Exhibit, Paper No. 98- 3172.

Crudgington, P., 2001, "Recent Brush Seal and Testing Development at Cross," AIAA Paper No. 2001-3480.

Crudgington, P., and Bowsher, A., 2003 "Brush seal blow down," Proc. 39th AIAA/ASME/SAE/ASEE Joint Propulsion Conference and Exhibit, Paper No. 2003-4697

Crudgington, P.F., and Bowsher, A., 2002 "Brush seal pack hysteresis," Proc. 38th AIAA/ASME/SAE/ASEE Joint Propulsion Conference & Exhibit, Paper No. 2002-3794.

Cumpsty, N., 1997, "Jet Propulsion, Cambridge Engine Technology Series," Cambridge University Press, Cambridge, UK.

Davison, A. C., 2003, Statistical models, Cambridge University Press.

Dawson, M. P., Childs, D. W., Holt, C. G., and Phillips, S. G., 2002, "Measurements Versus Predictions for the Dynamic Impedance of Annular Gas Seals—Part I: Test Facility and Apparatus," Journal of Engineering for Gas Turbines and Power, 124(4), pp. 958-962.

Delgado, A., San Andrés, L., and Justak, J. F., 2005, "Measurements of Leakage, Structural Stiffness and Energy Dissipation Parameters in a Shoed Brush Seal," Sealing Technology, 2005(12), pp. 7-10.

Dell'Era, G., Mersinligil, M., and Brouckaert, J., 2015, "Assessment of Unsteady Pressure Measurement Uncertainty - Part I: Single Sensor Probe." ASME. J. Eng. Gas Turbines Power. April 2016; 138(4): 041601.

Deo, H. V., 2012, "Compliant plate seals: Testing and validation," Proc. ASME Turbo Expo 2012, ASME Paper No. GT2012-69356.

Dessornes, O., Landais, S., Valle, R., Fourmaux, A., Burguburu, S., Zwyssig, C., and Kozanecki, Z., 2014, "Advances in the Development of a Microturbine Engine," Journal of Engineering for Gas Turbines and Power, 136(7), p. 071201.

El-Gamal, H. A., Awad, T., and Saber, E., 1996, "Leakage from labyrinth seals under stationary and rotating conditions," Tribology International, 29(4), pp. 291-297.

Ewins, D. J., 1984, Modal testing: theory and practice, Research studies press Letchworth.

Faria, M. T. C., and Andrés, L. S., 1999, "On the numerical modeling of high-speed hydrodynamic gas bearings," J. Trib., 122(1), pp. 124-130.

Ferguson, J., 1988, "Brushes as High Performance Gas Turbine Seals," Proc. ASME 1988 International Gas Turbine and Aeroengine Congress and Exposition, Paper No. 88-GT-182.

Flower, R., 1990, "Brush seal development system," 26th Joint Propulsion Conference, American Institute of Aeronautics and Astronautics, AIAA Paper No. 90-2143

Floyd, C., 1986, "Gas seals for rotating shafts," Tribology international, 19(4), pp. 204-211.

Gary, K., Childs, D. W., and Ramirez, M. A., 2018, "Measurements of the Leakage and Rotordynamic Performance of Interlocking Labyrinth Seals," Proc. ASME Turbo Expo 2018, GT2018-75885.

Gaszner, M., Pugachev, A. O., Georgakis, C., and Cooper, P., 2013, "Leakage and Rotordynamic Coefficients of Brush Seals With Zero Cold Clearance Used in an Arrangement With Labyrinth Fins," J. Eng. Gas. Turbines Power-Trans. ASME, 135(12), p. 11.

Gillespie, D., Pekris, M., Franceschini, G., Jones, T., and Owen, A., 2016, "Analytical modeling and experimental validation of heating at the leaf seal/rotor interface.", Heat Transfer, ASME, Vol5A, p. V05AT15A026.

Grondahl, C. M, 2005, "Pressure actuated leaf seals for improved turbine shaft sealing," AIAA Paper No. 2005-3985.

Grondahl, C. M., 2009, "Pressure Actuated Leaf Seals Feasibility Study and Demonstration," AIAA Paper No. 2009-5167.

Grondahl, C. M., and Dudley, J. C., 2010, "Film Riding Leaf Seals for Improved Shaft Sealing", Proc. ASME Turbo Expo 2010, Paper No GT2010-23629.

Grondahl, C. M., Smith, R. L., and Dudley, J. C., 2011, "Film riding pressure actuated leaf seal assembly," US Patent 8474827 B2.

Gülen, S. C., 2018, "Beyond Brayton Cycle: It is Time to Change the Paradigm," Journal of Engineering for Gas Turbines and Power, 140(11), p. 111703, Paper No. V003T08A015.

Hamrock, B. J., Schmid, S. R., and Jacobson, B. O., 2004, Fundamentals of fluid film lubrication, CRC press.

Harris, D. M., and Bush, J. W., 2015, "Generating Uniaxial Vibration With an Electrodynamic Shaker and External Air Bearing," Journal of Sound and Vibration, 334, pp. 255-269.

Hendricks, R., Carlile, J., and Liang, A., 1993, "Brush seal low surface speed hard-rub characteristics," AIAA Paper No. 93-2534.

Herrmann, N., Dullenkopf, K., and Bauer, H.-J., 2013, "Flexible seal strip design for advanced labyrinth seals in turbines," ASME PaperNo. GT2013-95424.

Hunt, R., 2011, "The history of the industrial gas turbine (part 1 the first fifty years 1940-1990)," The Institution of Diesel and Gas Turbine Engineers, Bedford Heights, Manton Lane, Bedford MK41 7PH, publication: 582, 2011.

Iwatsubo, T., 1980, "Evaluation of instability forces of labyrinth seals in turbines or compressors.", Proc. Rotordynamic Instability Problems in High Performance Turbomachinery, NASA CP-2133, Texas A&M University, pp.139–167

Jahn, I. H., Gillespie, D., and Cooper, P., 2013, "Hydrodynamic air-riding in leaf seals," Proc. ASME Turbo Expo 2013, Paper No. GT2013-95585

Jahn, I. H., Owen, A. K., Franceschini, G., and Gillespie, D., 2008, "Experimental characterisation of the stiffness and leakage of a prototype leaf seal for turbine applications," Proc. ASME Turbo Expo 2008, Paper No GT2008-51206.

Justak, J. F., 2002, "Robust hydrodynamic brush seal," US Patent 6428009 B2.

Justak, J. F., 2008, "Hydrodynamic brush seal," US Patent 7410173 B2.

Justak, J. F., and Crudgington, P. F., 2006, "Evaluation of a Film Riding Hybrid Seal," AIAA Paper No. 2006-4932.

Justak, J. F., and Doux, C., 2009, "Self-Acting Clearance Control for Turbine Blade Outer Air Seals," Proc. ASME Turbo Expo 2009, Paper No GT2009-59683.

Kerrebrock, J. L., 1992, Aircraft engines and gas turbines, MIT press Cambridge, MA.

Kirk, T., Bowsher, A., Crudgington, P., Grondahl, C., Dudley, J., and Pawlak, A., 2016, "Film riding pressure activated leaf seal proof of concept," Proc. 52nd AIAA/SAE/ASEE Joint Propulsion Conference, Paper No. AIAA-2016-4920.

Mahler, F. H., 1972, "Advanced Seal Technology," Pratt and Whitney Aircraft East Hartford Conn.

Matsushita, O., Tanaka, M., Kanki, H., Kobayashi, M., and Keogh, P., 2017, Vibrations of rotating machinery, Springer.

Messenger, A., Williams, R., Ingram, G., Hogg, S., Tibos, S., and Seaton, J., 2015, "A Dynamic Clearance Seal for Steam Turbine Application." Proceedings of the ASME Turbo Expo 2015, Paper No. GT2015-43471.

Messenger, A., Williams, R., Ingram, G., Hogg, S., Tibos, S., Seaton, J., and Charnley, B., 2016, "Experimental and Numerical Development of a Dynamic Clearance Seal for Steam Turbine Application." Proceedings of the ASME Turbo Expo 2016, Paper No. GT2016-56995.

Messenger, A., Williams, R., Ingram, G., Hogg, S., Tibos, S., Seaton, J., and Charnley, B., 2017, "Demonstration of a Dynamic Clearance Seal in a Rotating Test Facility." Proceedings of the ASME Turbo Expo 2017, Paper No. GT2017-64285.

Messenger, A., Williams, R., Ingram, G, Hogg, S, and Reggentin, P., 2019, "Demonstration of a Dynamic Clearance Seal in a Rotating Steam Test Facility." Proceedings of the ASME Turbo Expo 2019, Paper No. GT2019-91605

Nakane, H., Maekawa, A., Akita, E., Akagi, K., Nakano, T., Nishimoto, S., Hashimoto, S., Shinohara, T., and Uehara, H., 2004, "The development of high-performance leaf seals," J. Eng. Gas. Turbines Power-Trans. ASME, 126(2), pp. 342-350.

Owen, J. M., Haynes, C. M. and Bayley, F. J. (1974). "Heat Transfer from an Air-Cooled Rotating Disk." Proceedings of the Royal Society of London. Series A, Mathematical and Physical Sciences 336(1607): pp. 453-473.

Pasch, J., and Stapp, D., 2018 "Testing of a New Turbocompressor for Supercritical Carbon Dioxide Closed Brayton Cycles." Proceedings of the ASME Turbo Expo 2018, Paper No. GT2018-77044.

Pekris, M. J., Franceschini, G., Jahn, I. H. J., and Gillespie, D. R. H., 2015, "Experimental Investigation of a Leaf Seal Prototype at Engine-Representative Speeds and Pressures," Journal of Engineering for Gas Turbines and Power, 138(7), pp. 072502-072502.

Peletti, J., and Childs, D., 1991 "A Comparison of Theoretical Predictions for the Rotordynamic Coefficients of Short (1/D= 1/6) Labyrinth Seals," Proc. Rotating Machinery

and Vehicle Dynamics, Proceedings of the 13th Vibration Conference, Miami, FL, ASME, New York, DE, pp. 69-76.

Picardo, A., and Childs, D. W., 2005, "Rotordynamic coefficients for a tooth-on-stator labyrinth seal at 70 bar supply pressures: measurements versus theory and comparisons to a hole-pattern stator seal," Journal of engineering for gas turbines and power, 127(4), pp. 843-855.

Proctor, M. P, and Delgado, I. R., 2008, "Preliminary Test Results of Non-Contacting Finger Seal on Herringbone-Grooved Rotor," Proc. 44th AIAA/ASME/SAE/ASEE Joint Propulsion Conference & Exhibit, Paper No. 2008-4506.

Proctor, M. P., and Delgado, I. R., 2004, "Leakage and power loss test results for competing turbine engine seals," Proc. ASME Turbo Expo 2004, Paper No GT2004-53935.

Proctor, M. P., and Steinetz, B. M., 2004, "Noncontacting finger seal," US Patent 6811154 B2.

Proctor, M. P., Kumar, A., and Delgado, I. R., 2002, "High-speed, high-temperature finger seal test results," Proc. 38th AIAA/ASME/SAE/ASEE Joint Propulsion Conference & Exhibit, Paper No. 2002-3793.

Rolls-Royce, 2015, The jet engine, John Wiley & Sons.

Rouvas, C., and Childs, D. W., 1993, "A Parameter Identification Method for the Rotordynamic Coefficients of a High Reynolds Number Hydrostatic Bearing," Journal of Vibration and Acoustics, 115(3), pp. 264-270.

San Andrés, L., and Anderson, A., 2014, "An All-Metal Compliant Seal Versus a Labyrinth Seal: A Comparison of Gas Leakage at High Temperatures," (45738), p. V05CT16A014.

San Andrés, L., Baker, J., and Delgado, A., 2009, "Measurements of Leakage and Power Loss in a Hybrid Brush Seal," J. Eng. Gas. Turbines Power-Trans. ASME, 131(1), p. 6.

San Andrés, L., Baker, J., and Delgado, A., 2010, "Rotordynamic Force Coefficients of a Hybrid Brush Seal: Measurements and Predictions," Journal of Engineering for Gas Turbines and Power, 132(4).

Saravanamuttoo, H. I., Rogers, G. F. C., and Cohen, H., 2001, Gas turbine theory, Pearson Education.

Scobie, J. A., 2014, "An Experimental Study of Gas Turbine Rim Seals." University of Bath PhD Thesis

Scobie, J.A., Sangan, C.M., Keogh, P.S., Lock, G.D., Bowsher, A., and Crudgington, P.F., 2015, . "Development of a film riding pressure actuated leaf seal". Grant proposal

Silvey, S. D., 2017, Statistical inference, Chapman & Hall/CRC.

Tiwari, R., Lees, A., and Friswell, M., 2004, "Identification of dynamic bearing parameters: a review," Shock and Vibration Digest, 36(2), pp. 99-124.

Vannini, G., Cioncolini, S., Calicchio, V., and Tedone, F., 2011, "Development of a high pressure rotordynamic test rig for centrifugal compressors internal seals characterization," Proc. Proceedings of the 40th Turbomachinery Symposium, Texas A&M University. Turbomachinery Laboratories.

Vannini, G., Cioncolini, S., Del Vescovo, G., and Rovini, M., 2014, "Labyrinth seal and pocket damper seal high pressure rotordynamic test data," Journal of Engineering for Gas Turbines and Power, 136(2), p. 022501.

Vullo, V., and Vivio, F., 2013, Rotors: Stress analysis and design, Springer Science & Business Media.

Wittig, S., Schelling, U., Kim, S., and Jacobsen, K., 1987, "Numerical predictions and measurements of discharge coefficients in labyrinth seals," Proc. ASME 1987 International Gas Turbine Conference and Exhibition, Paper No. 87-GT-188.

Wu, T., Barajas-Rivera, J., Zhang, J., and Kawashita, R., 2019, "Leakage and Cavity Pressures in an Interlocking Labyrinth Gas Seal: Measurements Versus Predictions," Journal of Engineering for Gas Turbines and Power, 141, pp. 101007-101001.

Appendix A: Testing facility design calculations

A.1 Casing Weight

The amplitude of the acceleration of a sinusoidal movement with a stroke of $s = 0.065\ mm$, which is approximately half of the clearance of the testing seal, and a frequency of 250 Hz is:

$$\boldsymbol{y = s \cdot \sin \omega t \rightarrow \frac{\partial^2 y}{\partial t^2} = -s\omega^2 \cdot \sin \omega t}$$
$$\boldsymbol{a = s\omega^2 = 0.65 \cdot 10^{-4} \cdot (250 \cdot 2\pi)^2 = 160\ m/s^2} \quad \text{A.1}$$

For a maximum force delivered by the shaker (3000 N) and the maximum acceleration to be achieved during the test, Newton's second law applied to the casing gives a value of 18.7 kg for the maximum mass that the shaker can excite.

$$\boldsymbol{\vec{F} = m \cdot \vec{a}}$$
$$\boldsymbol{m = \frac{F}{a} = 18.7\ kg} \quad \text{A.2}$$

A.2 Rotor stresses

The expressions of the radial and tangential (hoop) stresses and radial displacement for a constant thickness rotating disc are given Eq. A.3 as functions of the radial co-ordinate and the material properties. These expressions are derived from elastic theory and the whole derivation can be seen in Vullo and Vivio [2013].

$$\boldsymbol{\sigma_r = \frac{3+\nu}{8} \rho\omega^2 \cdot (1 - r^2)}$$
$$\boldsymbol{\sigma_t = \frac{3+\nu}{8} \rho\omega^2 \cdot \left(1 - \frac{1+3\nu}{3+\nu} \cdot r^2\right)} \quad \text{A.3}$$
$$u = \frac{1}{E} \cdot r \cdot \frac{3+\nu}{8} \rho\omega^2 \cdot \left[(1-\nu) - r^2 \cdot \frac{1-\nu^2}{3+\nu}\right]$$

where:

- ν is Poisson's ratio
- ρ is the density of the rotor's material
- ω is the angular velocity
- E is Young's modulus

A.3 Rotor windage

The power dissipated by the rotor into the surrounding air due to friction is calculated using the equations given by Owen *et al.* [1974] for the moment coefficient of a free disc:

$$\boldsymbol{P = M\Omega} \tag{A.4}$$

$$\boldsymbol{C_m = \frac{M}{\frac{1}{2}\rho\Omega^2 r^5}} \tag{A.5}$$

where:

- M is the disc moment
- ρ is the density of the air
- r is the radius of the rotor
- Ω is the angular velocity

According to the correlation presented by Bayley and Owen [1969], the value for the moment coefficient can be estimated from the Reynolds number based on the rotor surface speed for turbulent flow over a disc:

$$\boldsymbol{C_m = 0.0655\, Re_\phi^{-0.186}} \tag{A.6}$$

This value of the moment coefficient can be used in Eq. A.5 to solve for the moment, which is then used in Eq. A.4 together with the maximum value of the angular speed of the rotor to calculate a lower limit of the power required run the disc.

The expression of the rotational Reynolds number reads:

$$\boldsymbol{Re_\phi = \frac{\rho\Omega r^2}{\mu}} \tag{A.7}$$

A.4 Axial force on the rotor

Figure A.1 shows the distribution of the pressure along the secondary labyrinth seal. During the design stage, this pressure distribution was assumed to be linear in order to have an estimation of the force acting on the face of the rotor. The pressure is parametrised as per Eq. A.7 and the integral of this expression along the axial surface of the rotor yields the value of the axial force on the bearings (Eq. A.8):

$$\boldsymbol{p = p(r) = p_{max}\frac{(r - R_1)}{(R_2 - R_1)}} \quad \text{A.8}$$

$$\boldsymbol{F = \int_{R_1}^{R_2} p(r) \cdot 2\pi r dr = \int_{R_1}^{R_2} p_{max}\frac{(r - R_1)}{(R_2 - R_1)} \cdot 2\pi r dr = 2646N} \quad \text{A.9}$$

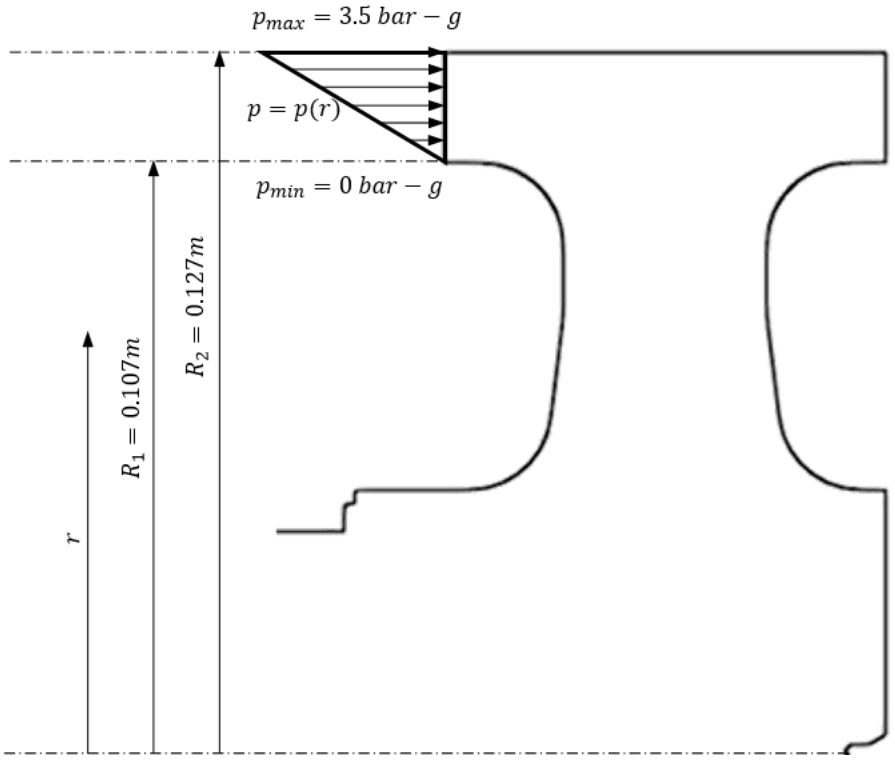

Figure A.1: Schematic of the parametrisation of the pressure distribution along the secondary labyrinth seal.

A.5 Shaker stinger

The equations used by Harris and Bush [2015] to mathematically express the criteria to be fulfilled by the stinger in terms of length and diameter, for a given maximum testing frequency and a given material, are summarised in this section. Table A.1 groups all the geometric and material properties of the stinger. As the length of the stinger is given by the distance between the shaker and the casing, the value to be determined is the diameter of the stinger. An initial guess is given and the criteria are checked.

Table A.1: Geometric and material properties of the drive rod

Parameter	Meaning	Value
E	Young's modulus	$205\ GPa$
ρ	Density	$7830\ kg/m^3$
σ_e	Endurance limit	$515\ MPa$
d	Diameter	$10\ mm$
L	Length	$400\ mm$
A	$= \pi d^2/4$, Cross-sectional area	$78.54\ mm^2$
I	$= \pi d^4/64$, Area moment of inertia	$490.87\ mm^4$
k	$= 12EI/L^3$, Lateral stiffness	$18.9\ N/mm$
κ	$= 4EI/L$, Moment stiffness	$1006.29\ N\cdot/deg$
M	Mass of casing	$15\ kg$
m	Mass of entire payload on the shaker	$15.5\ kg$
f_m	Maximum frequency	$200\ Hz$
a	Acceleration amplitude	$588.6\ m/s^2$

A.5.1 Fatigue-induced failure

The maximum axial stress should be lower than the endurance limit of the material:

$$\frac{\pi d^2}{4}\sigma_e > M \cdot a \tag{A.10}$$

Solving the inequality for the diameter, it gives the minimum diameter the stinger should have in order to not fail under periodic loading:

$$10\ mm = d > \sqrt{\frac{4Ma}{\pi\sigma_e}} = 4.7\ mm \tag{A.11}$$

A.5.2 Buckling

The maximum compressive load acting on the drive rod is the sum of the force due to the vibrating acceleration and the weight of the mass of the payload.

$$F_c = M \cdot (a + g) \tag{A.12}$$

This load should be smaller than the buckling load. Assuming a clamped-clamped beam, the buckling load reads:

$$P_b = \frac{4\pi^2 EI}{L^2} \tag{A.13}$$

Again, comparing both the maximum compressive load withstood by the rod and the critical buckling load gives a critical length that represents an upper limit for the length of the stinger:

$$\mathbf{400\ mm} = L < \frac{d^2}{4}\sqrt{\frac{\pi^3 E}{M(a+g)}} = L_b = \mathbf{665\ mm} \quad \text{A.14}$$

A.5.3 Axial resonance

In order to consider the longitudinal resonance of the drive rod, it is assumed that a uniform rod behaves like a linear spring with stiffness $k_a = EA/L$ when subjected to an axial force. The system composed by the casing and the rod can be considered as a mass-spring system which natural frequency, in Hertz, is:

$$f_a = \frac{1}{2\pi}\sqrt{\frac{\pi E d^2}{4LM}} \quad \text{A.15}$$

Imposing the maximum testing frequency to be smaller than the resonance frequency $(f_m < f_a)$ and solving for the length:

$$\mathbf{400\ mm} = L < \frac{Ed^2}{16\pi M f_m^2} = L_a = \mathbf{680\ mm} \quad \text{A.16}$$

A.5.4 Transverse resonance

The expression for the frequency of the first mode of lateral vibration reads:

$$f_{l,0} = \frac{\lambda_1^2}{2\pi L^2}\sqrt{\frac{EI}{\rho A}} \quad \text{A.17}$$

where λ_1 has a value of 22.4 for a clamped -clamped beam.

The value of this lateral frequency is modified by the presence of the static, constant axial load due to the gravity acting on the casing, $P_s = -M \cdot g$:

$$f_l = \beta \cdot f_{l,0}\ ; \beta = \sqrt{1 + \frac{P_s}{P_b}} = \sqrt{1 - \frac{g}{a+g}} \quad \text{A.18}$$

Once again, making sure that the test frequency is less than the lateral resonance frequency $(f_m < f_l)$ and solving for *L*:

$$\mathbf{400\ mm = L < \sqrt{\frac{\beta\lambda_1^2 d}{8\pi f_m}}\left(\frac{E}{\rho}\right)^{1/4} = L_l = 2251\ mm} \quad \text{A.19}$$

A.6 Crimped wires selection and tests

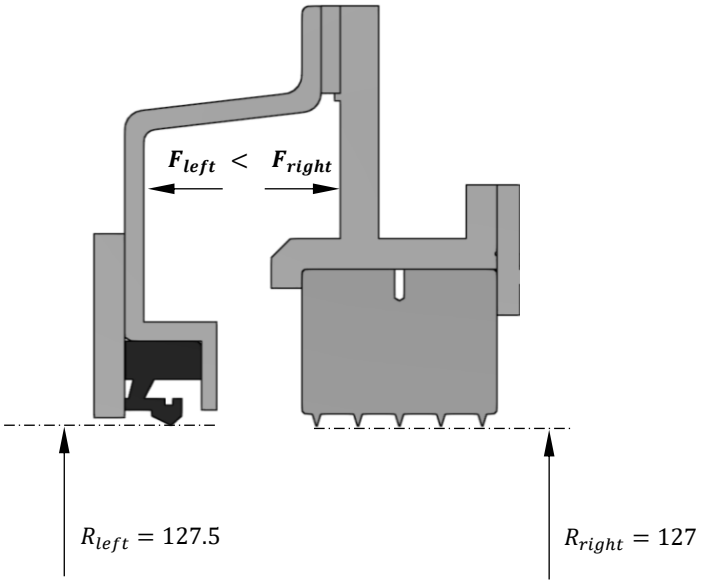

Figure A.2: Difference in area translates into a difference in force.

Figure A.2 shows that the radius of the left hand side of the upstream cover is larger than the radius of the right hand side. This difference in radius, means that there is a non-zero resultant force on the casing due to the pressurised air acting in surfaces of different area (see Eq. A.20). In addition to the difference in area due to the difference in radius, Eq. A.21 takes into account the fact that the left hand side wall of the upstream cover contains the pipes, which results in a further reduction of the area of this surface.

$$\mathbf{F_1 = p_{max} \cdot \pi\left(R_{left}^2 - R_{right}^2\right) = 140\ N} \quad \text{A.20}$$

$$\mathbf{F_{pipes} = Npipes\ \times \pi r_{pipe}^2 = 1390\ N} \quad \text{A.21}$$

The sum of the two forces calculated above is 1,530 N. A value of the limit load of the crimped wires is chosen to have a safety factor of two.

Figure A.3 shows the tensile strength test of the crimped wires. Load is plotted against the extension of the wire for two load cycles with a maximum load of 3,000 N. Both load-unload loops fall on top of each other indicating no plastic deformation of the specimen. The load-to-

failure test is shown in Figure A.4. A change in slope of the load curve can be seen in the proximity of 12,000 N. This point can be considered the yield point of the crimped wire system. Finally, the wire breaks at 17,500 N.

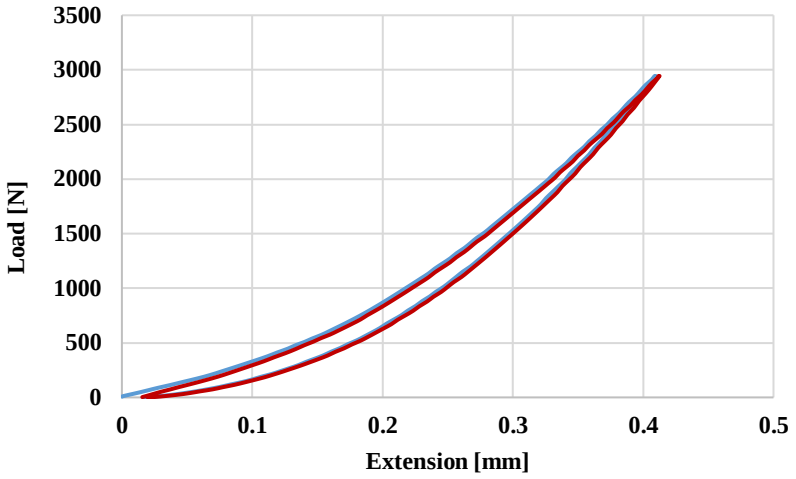

Figure A.3: Tensile strength test – up to a maximum load of 3,000 N.

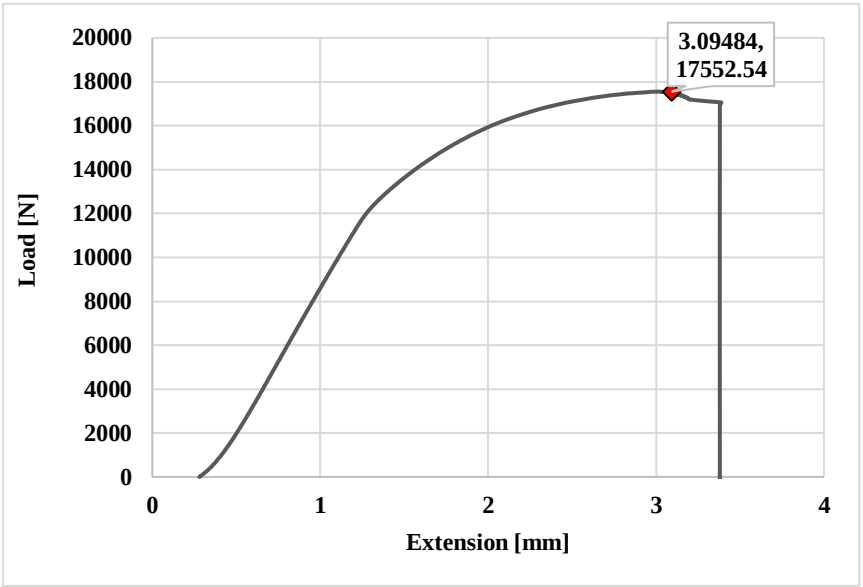

Figure A.4: Tensile strength test until failure.

Figure A.5 shows the change in length of the tested crimped wire for fatigue. After 3,000 cycles up to the rated load no change in extension can be appreciated.

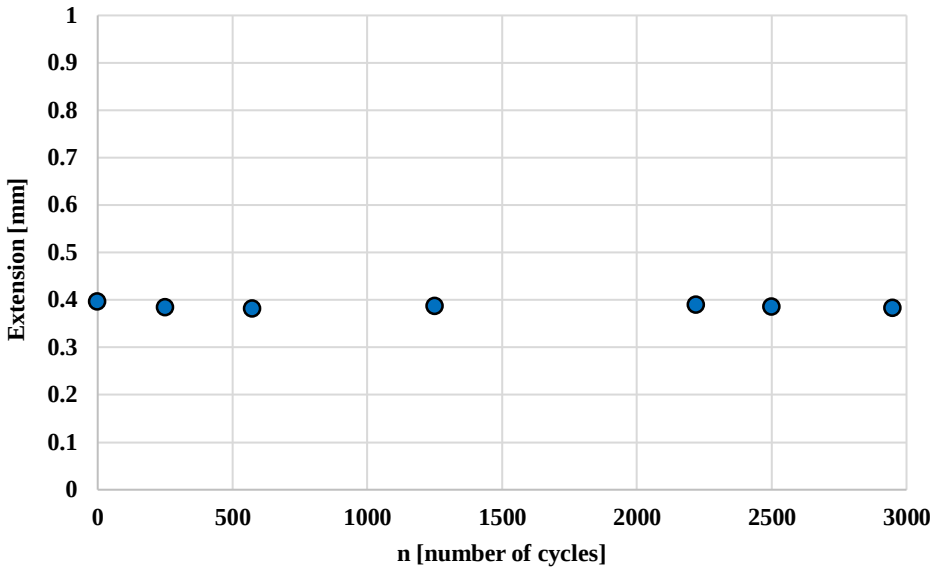

Figure A.5: Change in length of the crimped wire prototype for different number of load cycles applied

Appendix B: Photographs of the testing facility

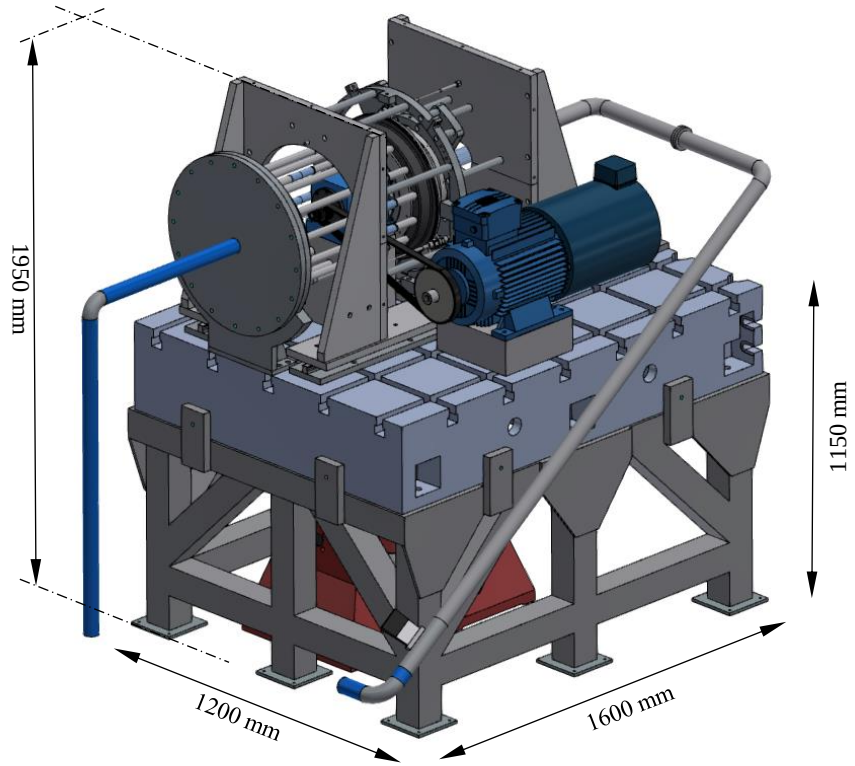

Figure B.1: Overall dimensions of the test rig.

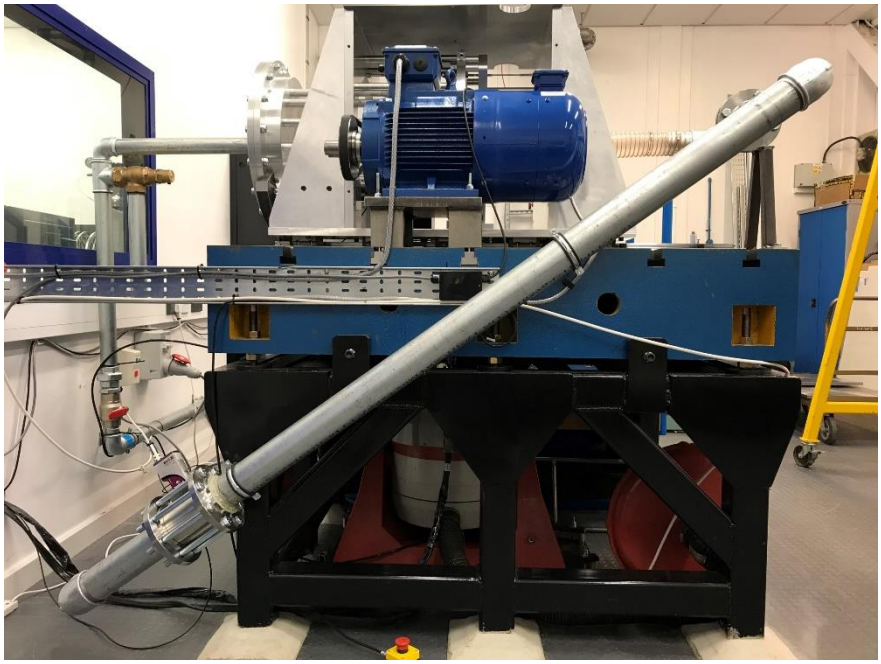

Figure B.2: Side view of the full assembly.

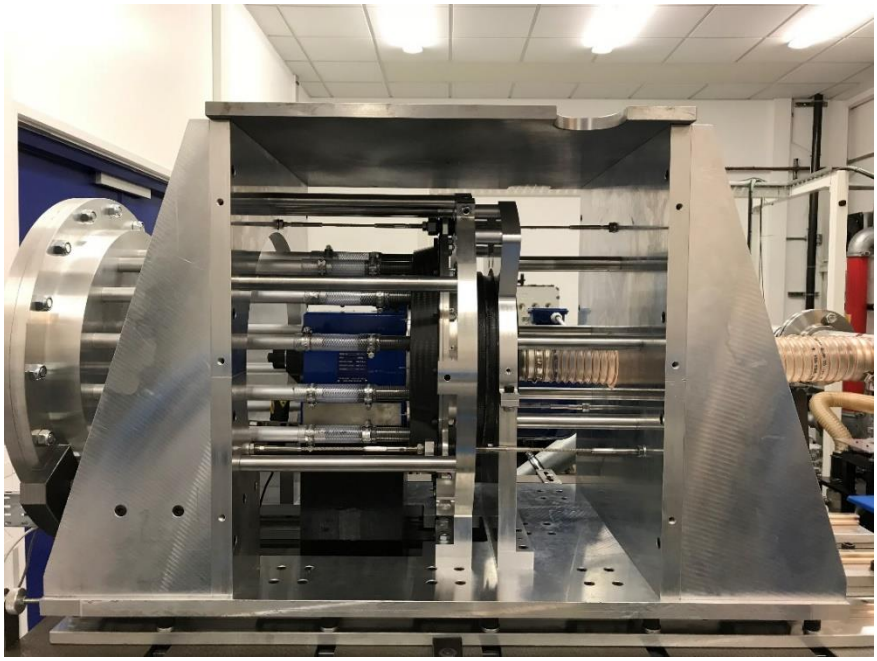

Figure B.3: Close-up view of the test section.

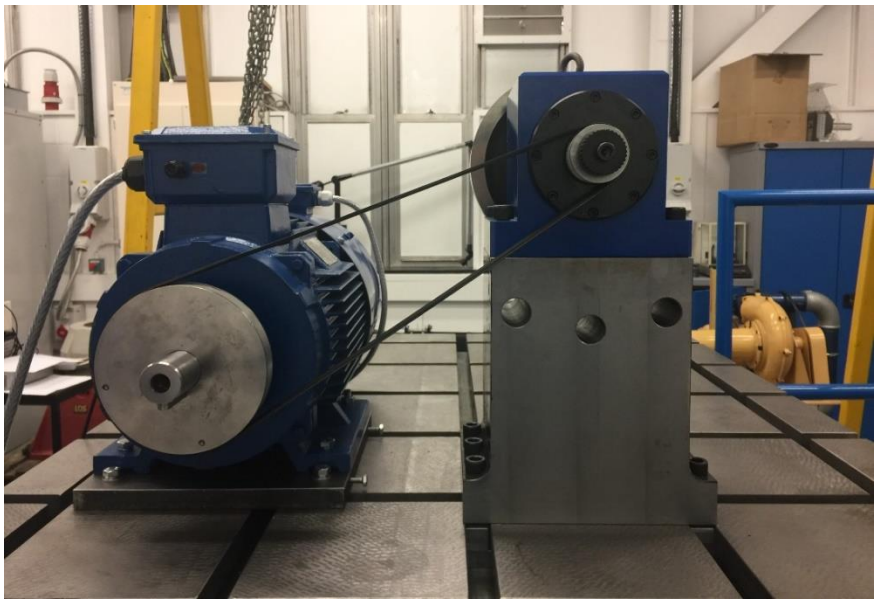

Figure B.4: Drivetrain subassembly during commissioning of the rig.

Appendix C: Instrumentation uncertainty

The uncertainty of the instruments used to measure the results presented in this thesis has been calculated by following the guidelines by Dell'Era *et al.* [21].

The eddy current probes and pressure transducers were calibrated in-house. The calibration points of each sensor were approximated by a linear fit. The random uncertainty of the fit was calculated as the standard estimate of the error of the calibration fit, $SEE_{\mathbb{C}}$, divided by the square root of the number of points used in the calibration, N.

$$\boldsymbol{SEE_{\mathbb{C}}} = \sqrt{\frac{\sum_{i=1}^{N}(\mathbb{C}_i - \mathbb{C}_{fit,i})^2}{N-K}} \qquad \boldsymbol{s_{\bar{\mathbb{C}}}} = \frac{\boldsymbol{SEE_{\mathbb{C}}}}{\sqrt{N}} \tag{C.1}$$

The measured calibration points are referred to as $\mathbb{C}_i$ and the values calculated from the data fit are denoted by $\mathbb{C}_{fit,i}$. K refers to the numbers of coefficients of the fit.

The reference instruments for both the pressure transducers and eddy current probes are digital instruments. Therefore, the bias uncertainty introduced by them was calculated as the standard deviation of a rectangular distribution with an interval equal to the resolution of the instrument.

The total uncertainty of the sensors was calculated by taking into account both the random and bias uncertainties using Eq. C.2:

$$\boldsymbol{\partial_T} = \sqrt{\sum_i (\boldsymbol{b_i})^2 + \sum_i (\boldsymbol{s_i})^2} \tag{C.2}$$

Finally, the expanded uncertainty for a 95% confidence interval is calculated by multiplying the total uncertainty times the value of the two-sided t-distribution for a 95% confidence interval.

$$\boldsymbol{\partial_{95}} = \boldsymbol{t_{95}} \cdot \boldsymbol{\partial_T} \tag{C.3}$$

Table C.1 summarises the expanded uncertainties for the sensors used.

Table C.1. Sensor uncertainties.

Sensor	∂_{95}
EC Probe 1	$\pm$ 6.3 µm
EC Probe 2	$\pm$ 5.8 µm
EC Probe Axial	$\pm$ 5.7 µm
Upstream Pressure Transducer	$\pm$ 1.2 mbar
Downstream Pressure Transducer	$\pm$ 1.2 mbar
Kulite Pressure Transducer	$\pm$ 1.2 mbar